SIMULTANEOUS MITIGATION OF SUBSYNCHRONOUS RESONANCE AND SUBSYNCHRONOUS INTERACTION USING FULL-SCALE FREQUENCY CONVERTER- AND DOUBLY-FED INDUCTION GENERATOR-BASED WIND FARMS

A Thesis

Submitted to the College of Graduate Studies and Research

In Partial Fulfillment of the Requirements

For the Degree of Master of Science

In the Department of Electrical and Computer Engineering

University of Saskatchewan

Saskatoon, Saskatchewan

By

Xuan Gao

PERMISSION TO USE

I agree that the Library, University of Saskatchewan, may make this thesis freely available for inspection. I further agree that permission for copying of this thesis for scholarly purpose may be granted by the professor or professors who supervised the thesis work recorded herein or, in their absence, by the Head of the Department or the Dean of the College in which the thesis work was done. It is understood that due recognition will be given to me and to the University of Saskatchewan in any use of the material in this thesis. Copying or publication or any other use of this thesis for financial gain without approval by the University of Saskatchewan and my written permission is prohibited.

Request for permission to copy or to make any other use of the material in this thesis in whole or part should be addressed to:

Head of the Department of Electrical and Computer Engineering
University of Saskatchewan
57 Campus Drive
Saskatoon, Saskatchewan S7N 5A9
Canada

ABSTRACT

Subsynchronous Resonance (SSR) is one of the major obstacles for the wide spread of high degrees (60% and higher) of series capacitor compensation. Recently, a new obstacle, namely Subsynchronous Interaction (SSI) has been added to the list after the Zorillo Gulf wind farm incident in Texas in October 2009. SSI is due to the interaction between large Doubly-Fed Induction Generator (DFIG)-based wind farms and series capacitor compensated transmission systems.

In integrated power systems incorporating series capacitor compensated transmission lines and high penetration of wind energy conversion systems, especially DFIG-based wind farms, SSR and SSI could occur concurrently as a result of some system contingences. Therefore, mitigating SSR and SSI is an important area of research and development targeting at developing practical and effective countermeasures.

This thesis reports the results of digital time-domain simulation studies that are carried out to investigate the potential use of Full-Scale Frequency Converter (FFC) and DFIG-based wind farms for simultaneous mitigation of SSR and SSI. This is achieved through introducing supplemental control signals in the reactive power control loops of the grid side converters of the DFIG and/or the FFC wind turbines. In this context, two supplemental controls designated as Supplemental Controls 1 and 2 are examined. Supplemental Control 1 introduces a signal in the grid side converter of the FFC wind turbines to damp both SSR and SSI oscillations. On the other hand, Supplemental Control 2 introduces a signal in the grid side converter of the FFC wind turbines for damping SSR oscillations and another signal in the grid side converters of the DFIG wind turbines for damping SSI oscillations.

Time-domain simulations are conducted on a benchmark model using the ElectroMagnetic Transients program (EMTP-RV). The results of the investigations have demonstrated that the presented two supplemental controls are very effective in mitigating the SSR and SSI phenomena at different system contingencies and operating conditions.

ACKNOWLEDGEMENTS

Foremost, I would like to express my sincere gratitude to my supervisor Dr. S.O. Faried, for his enthusiasm, motivation, patience, encouragement and immense knowledge. His guidance helped me through all the time over my classes, research and the writing of my thesis.

I offer my acknowledgement to my graduate study teachers, Dr. Rajesh Karki, Dr. N.A. Chowdhury and Dr. Daniel Chen for strengthening my knowledge on reliability, mathematics and control engineering. I also would like to appreciate Dr. Ulas Karaagac for providing some of the models used in this thesis.

Besides that, I would like to thank my lab partners: Emmanuel Ogemuno, Qi Zhao, Linh Pham and Jiping Zhang, for the discussions, inspirations and time we were working together. I also would like to thank my friend Federica Giannelli for helping me edit the references.

Last but not the lease, I would like to thank my family: my parents Jianzhang Gao and Xianglan Yin, for supporting me spiritually and financially all through my time living and studying in University of Saskatchewan.

TABLE OF CONTENTS

LIST OF FIGURES

LIST OF TABLES

LIST OF SYMBOLS

A	blade sweep area (m^2)
C	capacitor
C_f	wind turbine blade design constant
C_p	power coefficient of the blade
D	damping coefficient in p.u.
D_E, D_g, D_B, D_A, D_I, D_H	damping coefficient of the corresponding inertia
d	direct axis
e_d, e_q	d- and q- axis components of the stator voltage
e_{fd}	filed voltage
f_n	subsynchronous natural frequency
GSC	grid side converter
I_{L1}, I_{L2}	line currents
i_d, i_q	d- and q- axis components of the stator current
i_{fd}	field winding current
i_{1d}	d-axis damper winding current
i_{1q}, i_{2q}	q-axis damper winding currents
i_{sd}, i_{sq}	d- and q- axis components of the stator current
i_{ds}, i_{qs}	DFIG q- and d- axis components of the stator current
i_s, i_r	steady-state DFIG stator and rotor current
k	degree of compensation
K	stiffness in p.u.
K_{Eg}, K_{gB}, K_{BA}, K_{AI}, K_{IH}	stiffness of the connecting shafts
K_1, K_2, K_i	constants

K_{shaft}	speed deviation damping
L	inductance
L_s, L_r	stator and rotor inductances
L_d, L_q	d- and q- axis components of the stator inductance
L_{ad}	d-axis magnetizing inductance
L_{aq}	q-axis magnetizing inductance
L_{ffd}	self-inductance of the field winding
L_{ls}, L_{lr}	DFIG stator and rotor linkage inductance
L_{11d}	self-inductance of the d-axis damper winding
L_{11q}, L_{22q}	self-inductances of the q-axis damper winding
M_E, M_g, M_B, M_A, M_I, M_H	inertia constants of exciter, generator, two low-pressure turbines, intermediate-pressure turbine and high-pressure turbine respectively
M_i	inertia constant of the i^{th} rotating mass
M	mutual inductance between rotor and stator
MPT	maximum power tracking point
MSC	PSMG side converter
P	real power
P_A, P_B, P_I, P_H	power of the stages of the turbine
PMSG	permanent-magnet synchronous generator
PI	proportional integral
P_r, P_g	active power of the RSC and GSC
P_m	Pulse-width-modulation index
$P_{grid\text{-}Ref}$	real power reference for GSC
P_{Load}	load real power
ρ	air density (kgm^{-3})
Q	reactive power
Q_{Load}	load reactive power

$Q_{grid\text{-}Ref}$	reactive power reference for RSC
$Q_{GSC\text{-}Ref}$	reactive power reference for GSC
q	quadrature axis
R_ω	rotor radius of the wind turbine
R_a	armature resistance
R_s	synchronous generator stator resistance
R_r	resistance in the rotor circuits
RSC	rotor side converter
R_L	resistance of the series capacitor compensated transmission line
R_{fd}	field winding resistance
R_{1d}	d-axis damper winding resistance
R_{1q}, R_{2q}	q-axis damper winding resistances
r_s	resistance of the RC snubber circuit
r_r	resistance of the rotor side
s	Laplace transformation operator
^{T}	superscript to denote matrix transpose
t	time
T_e	electromagnetic torque
T_{MECH}	mechanical torque
T_C	fault clearing time
T_F	total simulation time
T_{ai}, T_{bi}	time constants
u_{sd}, u_{sq}	PMSG d- and q- components of the stator voltage
U_{AC}, U_{DC}	AC- and DC- voltages
V_{dc}	dc link capacitor voltage
$V_{dc\text{-}Ref}$	reference signal

V_C	voltage across the series capacitor of the compensated transmission line
V_{Cd}, V_{Cq}	voltages across the series capacitor in the d-q reference frame
V_R	voltage across the resistance of the series capacitor compensated transmission line
V_L	voltage across the inductance of the series capacitor compensated transmission line
V_{Ld}, V_{Lq}	voltages across the inductance in the d-q reference frame
v_{qg}, v_{dg}	quadrature and direct axis GSC voltages
V_b	infinite-bus voltage
V_{bd}, V_{bq}	d- and q- axis components of the infinite-bus voltages
v_s, v_r	stator and rotor side voltages
V_t	generator terminal voltage
V_{td}, V_{tq}	d- and q- axis components of the generator terminal voltages
V_{Rd}, V_{Rq}	voltages across the resistance in the d-q reference frame
v_{qs}, v_{ds}	quadrature and direct axis GSC voltages
v_{qr}, v_{dr}	quadrature and direct axis RSC voltages
V_ω	wind speed (m/s)
V_{Load}	load voltage
X_C	series capacitor reactance
X_L	inductive reactance of the series capacitor compensated transmission line
X_l	synchronous generator leakage reactance
X_0	synchronous generator zero-sequence reactance
Z, Z_{L1}, Z_{L2}	impedance of the transmission line
Z_{Load}	load impedence
Ψ_d, Ψ_q	d- and q- axis components of the stator flux linkages

Ψ_{fd}	field winding flux linkage
Ψ_{1d}	d-axis damper winding flux linkage
Ψ_{1q}, Ψ_{2q}	q-axis damper winding flux linkages
Ψ_{sd}, Ψ_{sq}	PMSG d- and q-axis components of the stator flux linkage
Ψ_{PM}	permanent magnet flux
δ	generator power (load) angle
δ_E, δ_B, δ_A, δ_I, δ_H	rotor angles of exciter, two low-pressure turbines, intermediate-pressure turbine and high-pressure turbine respectively
λ	wind turbine blade tip speed ratio
λ_S, λr	stator and rotor side flux linkages
λ_{dm}, λ_{qm}	d- and q- axis components of the magnetizing flux linkages
λ_{ds}, λ_{qs}	DFIG stator d- and q-axis components of the flux linkage
λ_{dr}, λ_{qr}	DFIG rotor d- and q-axis components of the flux linkage
Ω_m	mechanical angular velocity (rad/s)
ω	angular velocity
ω_{gen}	turbine-generator rotating mass speeds
$\omega_{gen\text{-}Ref}$	turbine-generator rotating mass speeds reference
ω_E, ω_B, ω_A, ω_I, ω_H	angular velocity of exciter, two low-pressure turbines, intermediate-pressure turbine and high-pressure turbine respectively
ω_n	natural frequency
ω_0 (f_0)	synchronous frequency (337 rad/sec)
$\Delta\omega_m$	modal speed deviation matrix
ω_m	speed deviation matrix of the turbine-generator rotating masses
ω_s, ω_r	stator and rotor angular frequency

θ	blade pitch angle
Φ_i	phase compensations
$\Delta Y'$	the output of the band pass filters

1. INTRODUCTION

1.1 Wind Energy

Wind energy has become one of the most popular renewable technologies around the world. Compared to fossil fuels, it is clean, widely distributed, plentiful and environmentally friendly. World wind generation capacity more than quadrupled between 2000 and 2006, doubling about every three years. There are now over 200,000 wind turbines operating around the world, with a total capacity of 282,482 MW as of the end of 2012 [1]. Owing to the rapidly increasing use of wind power, the aspect of integrating high levels of wind power into the grid is becoming more and more reality. Examples of large wind farms are the 5000 MW Gansu wind farm in China, the 781.5 MW Roscoe wind farm in Texas, the 845 MW Shepherds Flat wind farm in Oregon, and the 1550 MW Alta wind farm being developed in California [2].

1.2 Series Capacitive Compensation

Series capacitive compensation of power transmission lines using capacitor banks is the most economical way for increasing power transfer capability and improving system stability, especially when large amounts of power must be transmitted through long transmission lines. However, one of the hindering factors for increased utilization of series capacitive compensation is the potential risk of Subsynchronous Resonance (SSR) and Subsynchronous Interaction (SSI) [3], [4]. Figure 1.1 shows a typical time response of a turbine-generator shaft torsional torque (High-Pressure turbine to Low-Pressure turbine shaft section, (HP-LP)) during and after clearing a fault in a series capacitive compensated transmission system in the presence of the SSR phenomenon. It is worth noting here that this shaft is designed to withstand a maximum torsional torque of 0.75 per unit (on the generator base MVA). On the other hand, Figure 1.2 shows a typical time response of the terminal voltage (root mean square) of a large Doubly-Fed Induction Generator (DFIG)-based wind farm during and after clearing a fault in a series capacitive compensated transmission system in the presence of the SSI phenomenon. As it can be seen from this figure, the wind farm terminal voltage exhibits sustained oscillations.

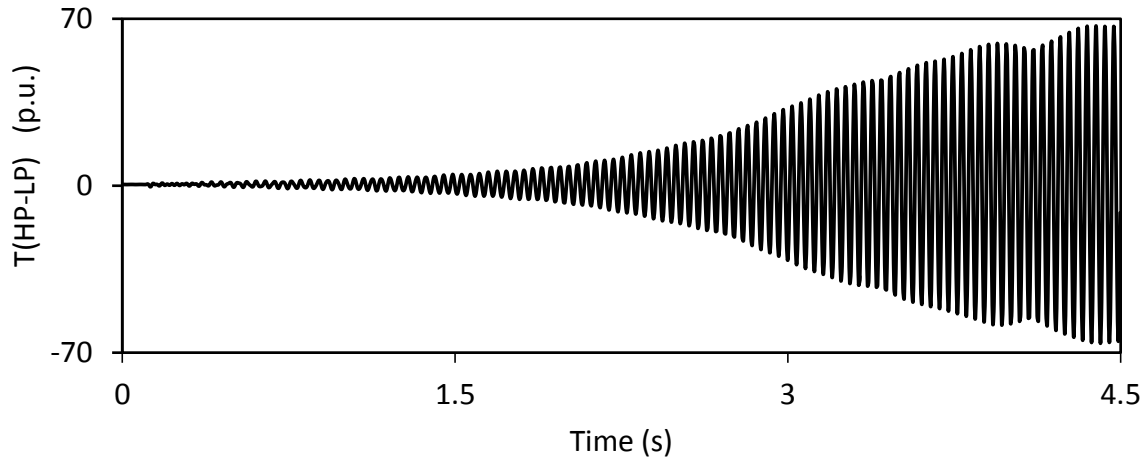

Figure 1.1: Transient time response of a turbine-generator shaft torsional torque during and after clearing a system fault on a series capacitive compensated transmission line.

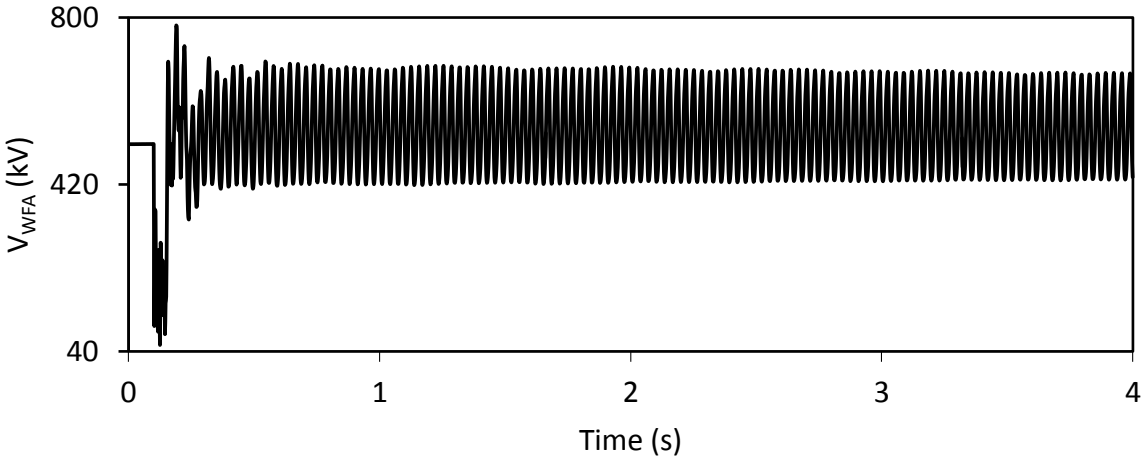

Figure 1.2: Transient time response of a large DFIG-based wind farm terminal voltage (root mean square) during and after clearing a system fault on a series capacitive compensated transmission line.

1.3 Transmission Line Series Compensation

The main purpose of series compensation of a transmission line is the virtual reduction of the line inductive reactance in order to enhance power system stability and increase the loadability of transmission corridors [5]. The principle is based on the compensation of the distributed line reactance by the insertion of a series capacitor. The reactive power generated by the capacitor is continuously proportional to the square of the line current. This means that the series capacitor has a self-regulating effect. When the system loading increases, the reactive power generated by

the series capacitor increases as well. The response of the series capacitor is automatic, instantaneous and continuous as long as the capacitor current remains within the specified operating limits. The following are some of the major benefits of incorporating series capacitors in transmission systems:

1.3.1 Increase the power transfer capability by raising the first swing stability limit

A substantial increase in the stability margin is achieved by installing a series capacitor. The series compensation will improve the situation in two ways: it will decrease the initial generator load angle corresponding to a specific power transfer and it will also shift the power-load angle (P-δ) characteristic upwards. This will result in increasing the transient stability margin.

1.3.2 Increase in power transfer

The increase in the power transfer capability as a function of the degree of compensation for a transmission line can be illustrated using the circuit and the vector diagram shown in Figure 1.3. The power transfer on the transmission line is given by:

$$P = \frac{|V_t||V_b|}{X_L - X_c}\sin\delta = \frac{|V_t||V_b|}{X_L(1-k)}\sin\delta \tag{1.1}$$

where *k* is the degree of compensation defined as

$$k = \frac{X_C}{X_L}$$

The effect on the power transfer when a constant load angle difference is assumed is shown in Figure 1.4. Practical compensation degree ranges from 20 to 60 percent and, therefore, doubling the transmission capability is achievable in practice.

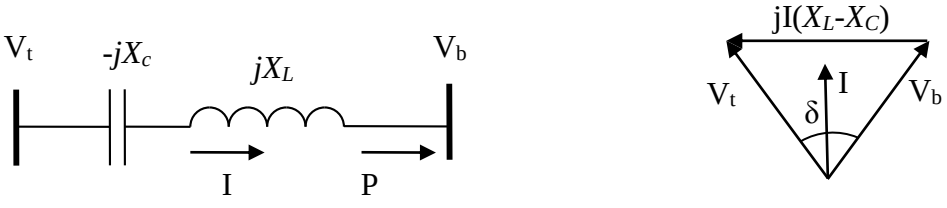

Figure 1.3: A transmission line with a series capacitor.

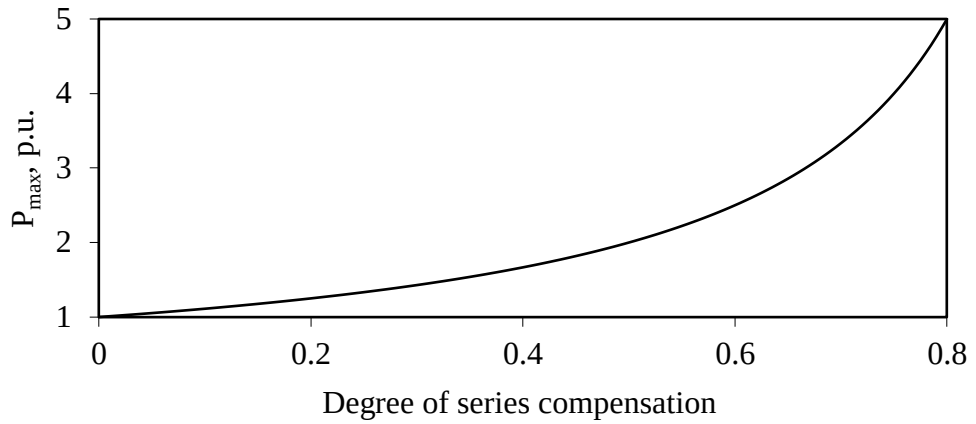

Figure 1.4: Maximum power transmitted over a transmission line as a function of the degree of series compensation ($|V_t| = |V_b| = 1$ *p.u.*, $X_L = 1$ *p.u.*).

1.3.3 Active load sharing between parallel circuits

When two transmission lines are connected in parallel, the natural power sharing between them is dictated by their respective impedances. If the two lines are of different configurations (and consequently of different thermal ratings), their impedances could still be very close. Therefore, the power transmitted in each line will be similar. The voltage drop in both circuits is identical, and therefore, the relationship between the line currents I_{L1} and I_{L2} can be expressed as:

$$I_{L1}Z_{L1} = I_{L2}Z_{L2} \tag{1.2}$$

If overloading the lower thermal rating line, (L_2, Figure 1.5) is to be avoided (i.e. $I_{L2} \leq I_{L2max}$), then the full power capacity of the other line, L_1, will never be reached (i.e. $I_{L1} \leq I_{L1max}$). For example, consider the case when L_1 is a four conductor bundle (quad) circuit configuration, whereas L_2 has a two conductor bundle (twin) circuit configuration. If the conductors of the two bundles are identical, then L_1 has twice rating of L_2. The inductive reactance of the two lines, however, are very close. If a series capacitor is installed in the higher thermal rating line, both transmission lines can operate at their maximum capacity when the appropriate degree of compensation is provided (50% in this case) [6].

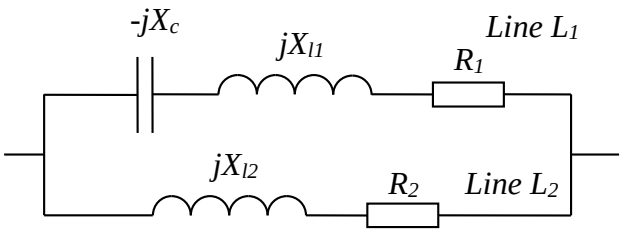

Figure 1.5: Adjusting the power sharing between two parallel lines using a series capacitor.

1.4 Subsynchronous Resonance (SSR)

SSR is a dynamic phenomenon in the power system which has certain special characteristics. The definitions of subsynchronous oscillation and SSR are given by the IEEE as [7], [8]:

> "*Subsynchronous oscillation* is an electric power system condition where the electric network exchanges significant energy with a turbine-generator at one or more of the natural frequencies of the combined system below the synchronous frequency of the system following a disturbance from equilibrium. The above excludes the rigid body modes of the turbine-generator rotors."

> "*Subsynchronous Resonance (SSR)* encompasses the oscillatory attributes of electrical and mechanical variables associated with turbine-generators when coupled to a series capacitor compensated transmission system where the oscillatory energy interchange is lightly damped, undamped, or even negatively damped and growing."

1.4.1 SSR: basic phenomenon

Consider the simple power system shown in Figure 1.6. It consists of a large turbine-generator which is connected to an infinite-bus system through a series capacitor compensated transmission line. The generator is driven by a multi-stage turbine, where the various stages of the turbine (HP, IP and LP) and the generator rotor (GEN) are coupled by elastic shafts.

The natural resonance frequency for the electrical system is given by

$$\omega_n = \frac{1}{\sqrt{LC}} = \frac{\omega_0}{\sqrt{(\omega_0 L)(\omega_0 C)}} = \omega_0 \sqrt{\frac{X_C}{X_L}} \quad \text{rad/s} \tag{1.3}$$

or

$$f_n = f_0\sqrt{\frac{X_C}{X_L}} \quad \text{Hz} \tag{1.4}$$

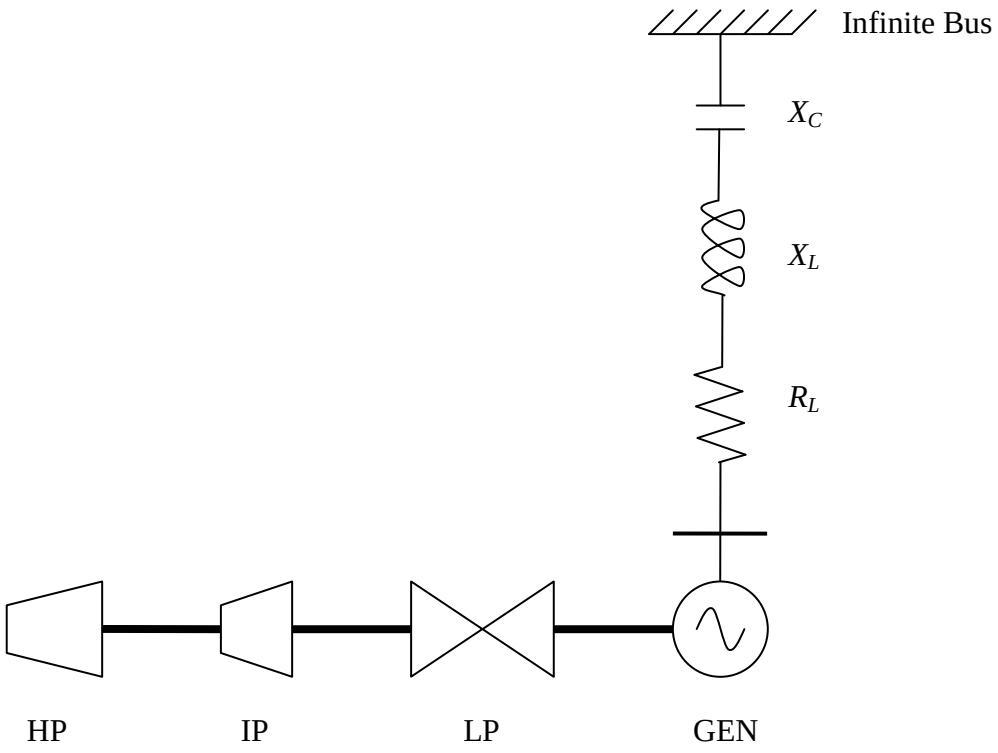

Figure 1.6: A turbine-generator connected to an infinite-bus system through a series capacitor compensated transmission line.

where ω_n is the natural frequency, f_0 is the synchronous frequency in Hz, and $\omega_0 = 2\pi f_0\, rad/s$, $f_0 = 60\ Hz$, X_C is the capacitive reactance and X_L is the transmission line inductive reactance.

In practice, f_n is always below the synchronous frequency f_0 since the compensation degrees of transmission lines are usually less than 100%. For this reason, f_n is called the subsynchronous natural frequency of the electrical system.

The shaft system of the turbine-generator has (N-1) natural torsional frequencies where N is the number of the rotating masses. These torsional frequencies are functions of the inertia of the different masses and the stiffness of the connected shafts. Due to the physical properties of the

shaft materials and the mechanical design of the turbine-generator shaft system, the torsional natural frequencies are also subsynchronous. Thus, the basic interaction between the electrical and mechanical systems is due to the closeness of f_n to the natural torsional frequencies of the turbine-generator shaft system. SSR can occur in the following three forms [3], [8]:

(1) Torsional Interaction: this is due to an interaction and exchange of energy between the series compensated electrical system and the turbine-generator mechanical system. This can lead to growing shaft torque oscillations at one of the natural torsional frequencies of the turbine-generator shaft system. Torsional interaction can occur when the generator is connected to a series compensated electrical system that has one or more natural frequencies, which are the synchronous frequency complements of one or more of the spring-mass natural frequencies. Generally, shaft torques due to torsional interaction can be expected to build up at a relatively slow rate such that damaging torque levels would not be reached in less than a minute or so.

(2) Induction Generator Effect: this is a pure electrical phenomenon that is due to the fact that, when subsynchronous currents flow in the armature circuit of a synchronous generator, the generator appears as a negative-resistance circuit at the prevailing subsynchronous frequencies. If the apparent resistance is greater than the inherent positive resistance of the circuit at one of the natural frequencies of the electrical circuit, growing subsynchronous voltages and currents will be expected in the system and at the generator. This could result in voltages and currents large enough to be damaging to the generator and power system equipment. In addition, if the subsynchronous currents in the generator armature are at the frequency corresponding to one of the turbine-generator spring-mass modes, large oscillatory shaft torques may result. As in the case of torsional interaction, a relatively slow oscillation growth rate would be expected.

(3) Torque Amplification: this phenomenon occurs when a fault on a series compensated power system, and its subsequent clearing, results in a high-energy storage in the series capacitor banks, which then discharge their energy through a generator in the form of a current having a frequency that corresponds to one of the natural torsional frequencies of the turbine-generator mechanical system. Unlike torsional interaction and induction generator effect, the growth rate for torque amplification is high and oscillating shaft torques might be expected to reach a damaging level within 0.1 second.

The ultimate hazard of SSR is a shaft fraction at full load and rated speed. The damage of such an occurrence cannot be accurately predicted, but extensive equipment damage could occur with a safety hazard to personnel. A more likely most-severe hazard would be a crack initiation at the surface of one of the turbine-generator shafts, indicating fatigue and requiring shaft replacement, resulting in a unit outage of 90 days or more.

1.5 Doubly-fed Induction Generator Wind Turbine

The basic structure of a doubly-fed induction generator (DFIG) wind turbine is shown in Figure 1.7. The stator of the induction machine is directly connected to the grid and the wound rotor windings are connected to the grid through slip rings and an indirect ac-ac converter system which controls both the rotor and the grid currents. The ac-ac converter system consists of two three-phase pulse-width modulated (PWM) Voltage-Sourced Converters (VSC) (Rotor-Side Converter (RSC) and Grid-Side Converter (GSC)) connected by a dc bus. A line inductor and an ac filter are used at the GSC to improve the power quality. A crowbar is also used to protect the RSC against over-currents and the dc capacitor against over-voltages [9].

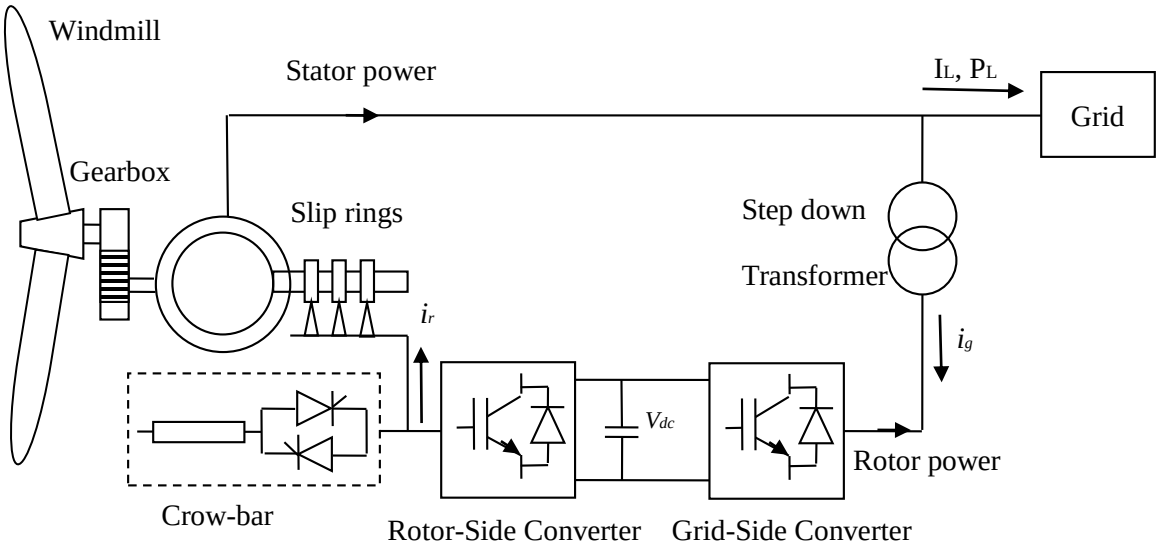

Figure 1.7: Schematic diagram of a DFIG wind turbine.

The control of the DFIG is realized by controlling the RSC and GSC using vector control techniques. The function of the RSC is to control the active and reactive powers delivered to the grid, and to follow a tracking characteristic to adjust the generator speed for optimal power generation depending on the wind speed. On the other hand, the function of the GSC is to keep the dc bus voltage constant and to support the grid with reactive power during system faults [4]. Details on DFIG wind turbine controls are given in [10].

The main advantage of the DFIG is the low cost of its converters as their rating is typically 25% to 30% of the DFIG rated power. As a result, the cost of the converters and electromagnetic interference (EMI) filters is also reduced.

1.6 Subsynchronous Interaction Phenomenon in DFIG-Based Wind Farms

Recent studies have identified the vulnerability of DFIG wind turbines to subsynchronous resonance interaction (SSI). This has been confirmed in October 2009 by the Zorillo Gulf wind farm incident in Texas which can be regarded as the first event of SSI between a DFIG-based wind farm (485 MW) and a series capacitor compensated transmission line [4], [10]. As a result of clearing a fault on a transmission line connected to the Zorillo Gulf wind farm, the wind farm became radially connected to the grid through a series capacitor compensated transmission line (the Rio Hondo line: 345 kV, 80 miles and a 50% compensation degree). Severe subsynchronous growing currents and voltages were recorded and damage occurred in the DFIG-wind turbine electrical and control systems.

Comprehensive studies of the SSI phenomenon using linearized techniques and eigenvalue analysis have attributed the "main cause" of the problem to the fast rotor current controller of the Rotor Side Converter (RSC) of the DFIG wind turbine [10]. Such a controller tends to move the subsynchronous electrical modes to the right-hand side of the s-plane causing system instability when its gain is increased. In other words, the rotor current controller changes the rotor resistance in such a way that it is seen from the stator side as a negative resistance. This occurs over a wide range of slip frequencies and can be classified as an Induction Generator Effect (IGE).

It is worth noting here that the Torsional Interaction (TI) phenomenon in DFIG wind turbine shaft systems is of a little concern. This is due to the fact that the natural torsional frequencies of oscillations of the shaft system (turbine, turbine-blades, gear box, generator rotor)

are in the range of 1 Hz to 3 Hz. Very high and impractical degrees of series capacitive compensation (90% and higher) are required to excite these torsional modes.

1.7 Full-Scale Frequency Converter Wind Turbine

Full-scale frequency converter (FFC) wind turbines are becoming popular in wind farms, since they can meet the stringent grid code requirements more easily than DFIG turbines. This is because FFC wind turbine has full control capability for real and reactive power output, with the generator decoupled from the grid.

The FFC wind turbine employs a permanent–magnet synchronous generator (PMSG) that has a large number of poles; hence a gear box is not required. This is also known as a direct-drive wind turbine generator where the synchronous machine rotates at the slow turbine speed and generates electrical power with frequency well below that of the gird (the synchronous frequency). The increased generator weight is offset by the absence of the gearbox. Further, the reliability and maintenance considerations for a gearbox are eliminated. Hence, this concept is particularly attractive for offshore locations [11].

Figure 1.8 shows a FFC PMSG wind turbine connected to the grid through an ac-ac converter system. Depending on the size of the wind turbine, the PMSG side converter (MSC) can be either a diode rectifier or a VSC. On the other hand, the GSC is typically a VSC. In the studies conducted in this thesis, the back-to-back (BtB) VSC topology is adopted. In addition, the gearbox can be eliminated, such that [12].

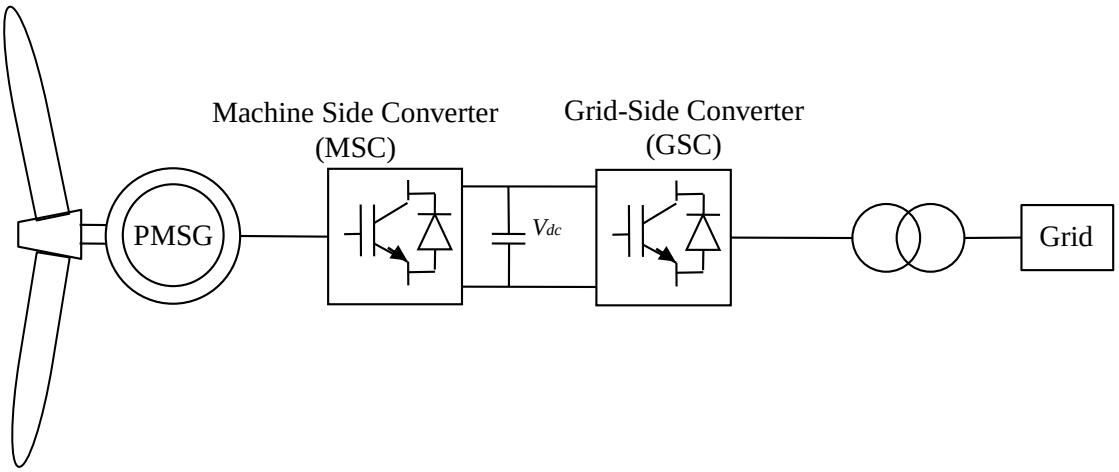

Figure 1.8: Schematic diagram of a FFC wind turbine.

Similar to the DFIG, the control of the FFC is realized by controlling the MSC and GSC using also vector control techniques [4]. The MSC controls the active power delivered by the PMSG, and follows a tracking characteristic to adjust the PMSG speed for optimal power generation depending on wind speed. The function of GSC is maintaining the dc bus voltage at its desired level, i.e. transmitting the active power delivered to the dc link by the MSC. GSC also controls the reactive power delivered to the grid.

1.8 Research Objective and Scope of the Thesis

In integrated power systems incorporating series capacitor compensated transmission lines and high penetration of wind energy conversion systems, especially DFIG-based wind farms, SSR and SSI could occur concurrently as a result of some system contingences. Therefore, mitigating SSR and SSI is an important area of research and development targeting at developing practical and effective countermeasures.

As most large wind farms in North America employ DFIG and FFC wind turbines, their voltage-sourced converter-based back-to-backs (BtBs) offer independent control of the real and reactive power. The use of these control capabilities have been recently proposed for damping power swings as well as inter-area oscillations [13]-[16]. Very little research has been reported on utilizing DFIG- and FFC-based wind farms for damping SSR [17], [18] and virtually, no research has been reported on simultaneous mitigation of SSR and SSI using large wind farms.

The main objective of this research work is to investigate the potential use of FFC- and DFIG-based wind farms for simultaneous mitigation of SSR and SSI. This is achieved through introducing supplemental control signals in the reactive power control loops of the grid side converters of the DFIG wind turbines or the grid side converter of the FFC wind turbines. In this context, two supplemental controls designated as Supplemental Controls 1 and 2 are examined. Supplemental Control 1 introduces a signal in the grid side converter of the FFC wind turbines to damp both SSR and SSI oscillations. On the other hand, Supplemental Control 2 introduces a signal in the grid side converter of the FFC wind turbines for damping SSR oscillations and another signal in the grid side converters of the DFIG wind turbines for damping SSI oscillations.

The thesis is organized in four chapters, a list of references section and two appendices. Chapter 1 introduces some fundamental benefits of series compensation of transmission lines. Brief introductions to SSR and SSI are also presented. The objective of the research is also presented in this chapter.

In Chapter 2, the system used for the investigations conducted in this thesis is described and the detailed dynamic models of its individual components are also presented in this chapter. The results of the digital time-domain simulations of a case study for the system during a three-phase fault are presented at the end of this chapter.

Chapter 3 demonstrates the effectiveness of the presented two supplemental controls in damping SSR and SSI oscillations through time-domain simulation studies. The supplemental controls performance at different system contingencies and operating conditions is also investigated.

Chapter 4 summarizes the research described in this thesis and presents some conclusions.

The data of the systems under investigations are given in Appendix A. Supplemental controls 1 and 2 output SSR and SSI signals for the case studies reported in Chapters 2 and 3 are given in Appendix B.

2. MATHEMATICAL MODELING OF POWER SYSTEMS INCORPORATING FFC- AND DFIG-BASED WIND FARMS FOR LARGE DISTURBANCE STUDIES

2.1 Introduction

In this chapter, the system used for the studies reported in this thesis is described and the mathematical models of its various components are presented. A digital time-domain and a frequency spectrums simulation of the system during a three-phase fault are presented at the end of this chapter.

2.2 System under Study

The system used in the investigations of this thesis is shown in Figure 2.1. It consists of a generating station and two wind farms designated as wind farms A and B. The generating station and wind farm A are connected to each other through two transmission lines (Lines 3 and 4) as well as to an infinite-bus system through two series capacitor compensated transmission lines (lines 1 and 2, each with a 60% compensation degree except for the sample case study in Section 2.4 where the compensation degree in both lines is 30%). Wind farm B is connected to the generating station and wind farm A through lines 3, 4 respectively and to the infinite-bus system through two transmission lines (lines 5 and 6). The generating station comprises two turbine-generators, G1 (600 MVA, 22 kV) and G2 (700 MVA, 22 kV). The shaft system of G1 comprises high and low-pressure turbines (HP1, LP1), the generator rotor and an exciter (EXC). The shaft system of G2 comprises high and low-pressure turbines (HP2, LP2) and the generator rotor. The frequencies of the natural torsional modes of oscillations of G1 and G2 shaft systems are 24.65 Hz, 32.39 Hz, 51.1 Hz and 24.65 Hz, 44.99 Hz respectively. The data of G1 and G2 are taken from the IEEE second benchmark model for computer simulation of SSR. Wind farm A comprises 300 $\times$1.5 MW DFIG wind turbines. Wind farm B is a FFC wind farm of 100 $\times$2 MW wind turbines.

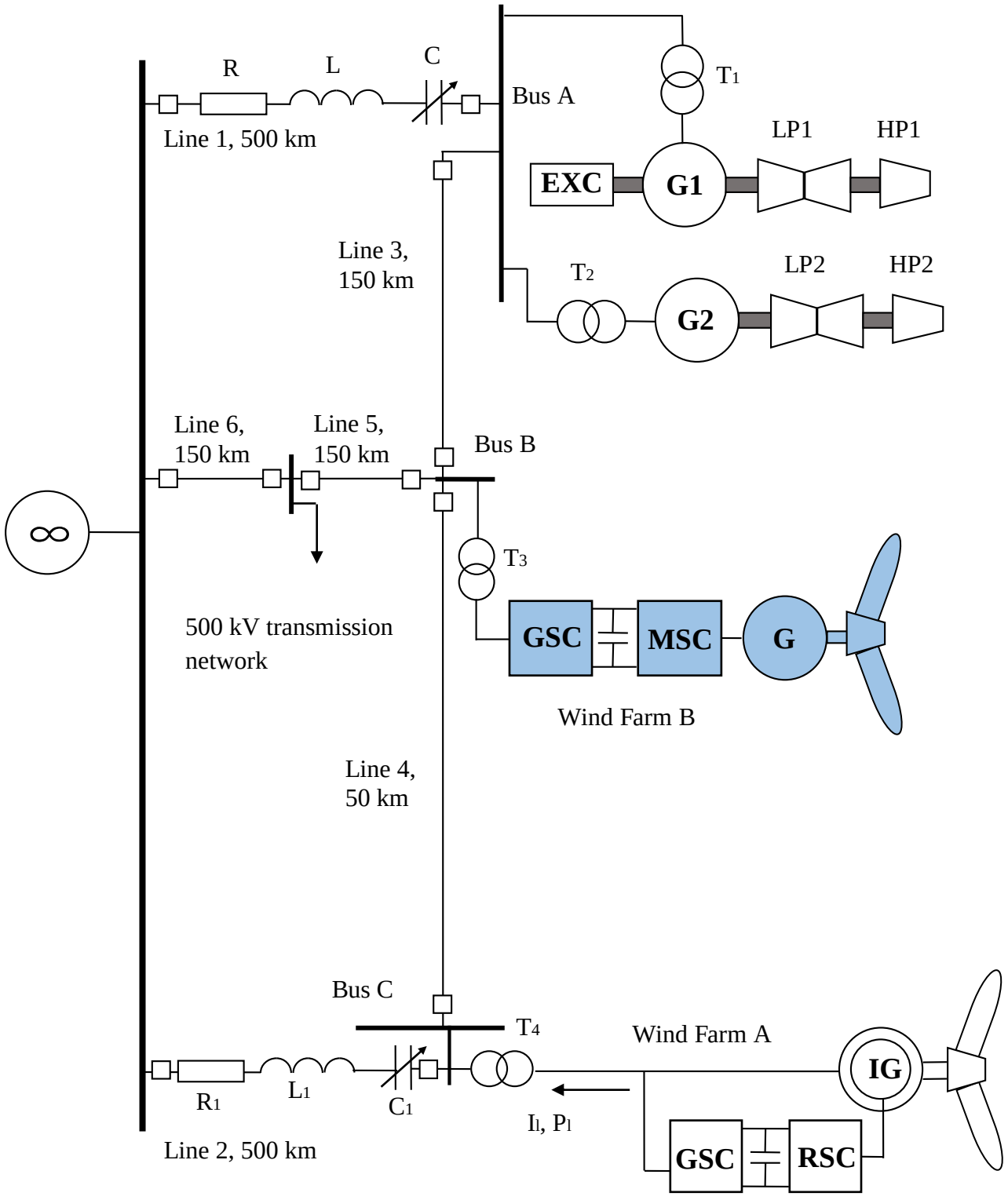

Figure 2.1: System under study.

The operating wind speeds and power outputs of the two wind farms are given in Table 2.1. The medium voltage collector grid is represented with its equivalent PI circuit model [19]. Faults are assumed to occur on Lines 4 and 5 and to be cleared by circuit breaker operations at both ends of the line.

Table 2.1: Wind speeds and wind farm outputs.

Wind farm	Operating speed and output power
A (DFIG-based wind farm)	Wind speed = 11 m/s, ≈ 425 MW
B (FFC-based wind farm)	Wind speed = 15 m/s, ≈ 200 MW

2.3 Power System Modeling

The nonlinear differential equations of the system under study are derived by developing individually the mathematical models which represent the various components of the system, including the synchronous generator, the generator turbine, the transmission line, the transformer, the system load, the wind turbine aerodynamic model, the DFIG-based wind turbine and its BtB converter controllers, as well as the FFC-based wind turbine and its BtB converter controllers. Knowing the mutual interaction among these models, the system of differential equations can be formed.

2.3.1 Modeling of the synchronous generator

In a conventional synchronous machine, the stator circuit consisting of a three-phase winding produces a sinusoidally space distributed magnetomotive force. The rotor of the machine carries the field (excitation) winding which is excited by a dc voltage. The electrical damping due to the eddy currents in the solid rotor and, if present, the damper winding is represented by three equivalent damper circuits; one on the direct axis (d-axis) and the other two on the quadrature axis (q-axis). The performance of the synchronous machine can be described by the equations given below in the d-q reference frame (Figure 2.2) [20]. In these equations, the convention adopted for the signs of the voltages and currents is that v is the impressed voltage at the terminals and that the direction of positive current i corresponds to generation. The sign of the currents in the equivalent damper windings is taken positive when they flow in a direction similar to that of the positive field current.

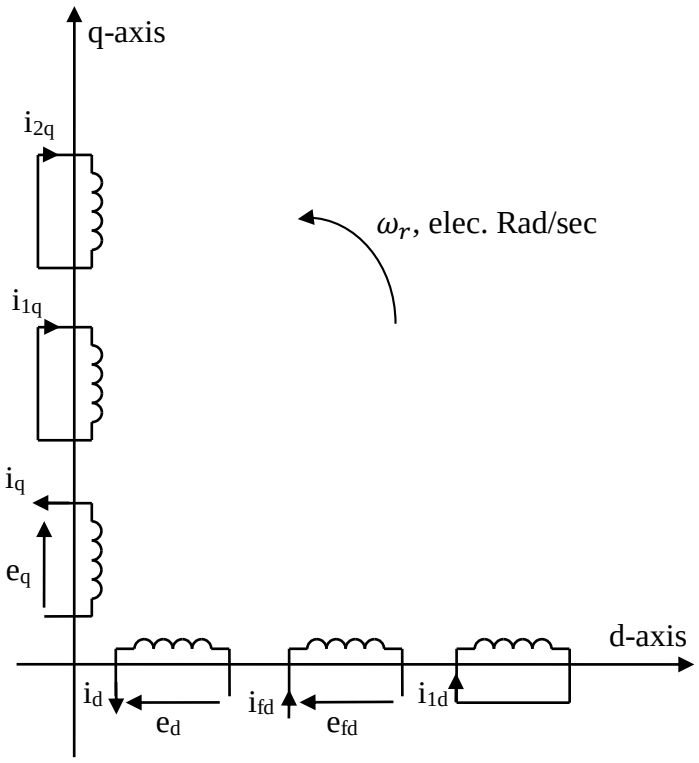

Figure 2.2: Modeling of the synchronous machine in the d-q reference frame.

With time t expressed in seconds, the angular velocity ω expressed in rad/s ($\omega_0 = 377 rad/\text{sec}$) and the other quantities expressed in per unit, the stator equations become:

$$e_d = \frac{1}{\omega_0}\frac{d\Psi_d}{dt} - \frac{\omega}{\omega_0}\Psi_q - R_a i_d \tag{2.1}$$

$$e_q = \frac{1}{\omega_0}\frac{d\Psi_q}{dt} + \frac{\omega}{\omega_0}\Psi_d - R_a i_q \tag{2.2}$$

The rotor equations:

$$e_{fd} = \frac{1}{\omega_0}\frac{d\Psi_{fd}}{dt} + R_{fd} i_{fd} \tag{2.3}$$

$$0 = \frac{1}{\omega_0}\frac{d\Psi_{1d}}{dt} + R_{1d} i_{1d} \tag{2.4}$$

$$0 = \frac{1}{\omega_0}\frac{d\Psi_{1q}}{dt} + R_{1q} i_{1q} \tag{2.5}$$

$$0 = \frac{1}{\omega_0}\frac{d\Psi_{2q}}{dt} + R_{2q}i_{2q} \tag{2.6}$$

The stator flux linkage equations:

$$\Psi_d = -L_d i_d + L_{ad} i_{fd} + L_{ad} i_{1d} \tag{2.7}$$

$$\Psi_q = -L_q i_q + L_{aq} i_{1q} + L_{aq} i_{2q} \tag{2.8}$$

The rotor flux linkage equations:

$$\Psi_{fd} = L_{ffd} i_{fd} + L_{ad} i_{1d} - L_{ad} i_d \tag{2.9}$$

$$\Psi_{1d} = L_{ad} i_{fd} + L_{11d} i_{1d} - L_{ad} i_d \tag{2.10}$$

$$\Psi_{1q} = L_{11q} i_{1q} + L_{aq} i_{2q} - L_{aq} i_q \tag{2.11}$$

$$\Psi_{2q} = L_{aq} i_{1q} + L_{22q} i_{2q} - L_{aq} i_q \tag{2.12}$$

The electromagnetic torque equation:

$$T_e = \Psi_d i_q - \Psi_q i_d \tag{2.13}$$

The overall differential equations which describe the transient performance of the synchronous machine are given by the following matrix equation:

$$\left[\frac{dX_{syn}}{dt}\right] = \left[At_{syn}\right]\left[X_{syn}\right] + \left[Bt_{syn}\right]\begin{bmatrix} V_{td} \\ V_{tq} \\ e_{fd} \end{bmatrix} \tag{2.14}$$

where

$$\left[X_{syn}\right] = [i_d \quad i_q \quad i_{fd} \quad i_{1q} \quad i_{1d} \quad i_{2q}]^T$$

$$\left[At_{syn}\right] = [L]^{-1}[Qt]$$

$$\left[Bt_{syn}\right] = [L]^{-1}[Rt]$$

$$[L] = \begin{bmatrix} -L_d & 0 & L_{ad} & 0 & L_{ad} & 0 \\ 0 & -L_q & 0 & L_{aq} & 0 & L_{aq} \\ -L_{ad} & 0 & L_{ffd} & 0 & L_{ad} & 0 \\ 0 & -L_{aq} & 0 & L_{11q} & 0 & L_{aq} \\ -L_{aq} & 0 & L_{ad} & 0 & L_{11d} & 0 \\ 0 & -L_{aq} & 0 & L_{aq} & 0 & L_{22q} \end{bmatrix} \tag{2.15}$$

$$[Qt] = \begin{bmatrix} \omega_0 R_a & -\omega L_q & 0 & \omega L_{aq} & 0 & \omega L_{aq} \\ \omega L_d & \omega_0 R_a & -\omega L_{ad} & 0 & -\omega L_{ad} & 0 \\ 0 & 0 & -\omega_0 R_{fd} & 0 & 0 & 0 \\ 0 & 0 & 0 & -\omega_0 R_{1q} & 0 & 0 \\ 0 & 0 & 0 & 0 & -\omega_0 R_{1d} & 0 \\ 0 & 0 & 0 & 0 & 0 & -\omega_0 R_{2q} \end{bmatrix}$$

$$[Rt] = \begin{bmatrix} \omega_0 & 0 & 0 \\ 0 & \omega_0 & 0 \\ 0 & 0 & \omega_0 \\ 0 & 0 & 0 \\ 0 & 0 & 0 \\ 0 & 0 & 0 \end{bmatrix}$$

Here, the superscript ^{T} means matrix transpose.

The synchronous machine swing equation can be written as:

$$\frac{M}{\omega_0}\frac{d\omega}{dt} = T_{MECH} - T_e \tag{2.16}$$

$$\frac{d\delta}{dt} = \omega - \omega_0 \tag{2.17}$$

In the above two equations (2.16 and 2.17), ω is in radians per second, the inertia constant M is in seconds, and the load angle δ is in radians, ω_0 is the synchronous frequency (377 rad/sec) and the mechanical and electrical torques T_{MECH} and T_e are in per unit.

In developing the equations of multi-machine systems, the equations of each synchronous machine expressed in its own d-q reference frame which rotates with its rotor must be expressed in a common reference frame. Usually, a reference frame rotating at synchronous speed is used as

the common reference. Axis transformation equations are used to transform between the individual machine (d-q) reference frames and the common (R-I) reference frame [20].

2.3.2 Modeling of the turbine-generator mechanical system

Figure 2.3 illustrates a typical representation of the mechanical system of a large turbine-generator which consists of a high-pressure turbine (HP), an intermediate-pressure turbine (IP), two low-pressure turbines (LPA & LPB), the generator rotor (GEN) and the exciter (EXC). Such a system can be modeled by a six-mass-spring system [21].

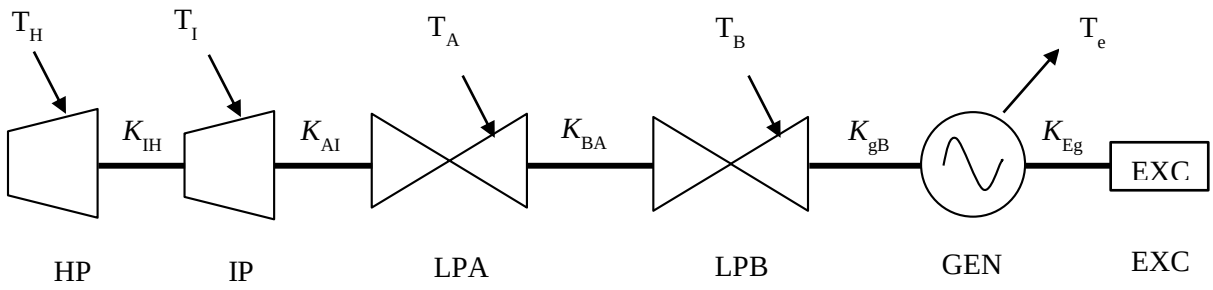

Figure 2.3: Representation of a typical turbine-generator shaft system.

Assuming that M is the inertia constant in seconds, D is the damping coefficient in p.u. torque/p.u. speed for each rotating mass and K is a stiffness in p.u. torque/rad for each shaft section, the equations of the i^{th} mass of an N-mass spring system shown in Figure 2.4 are given by

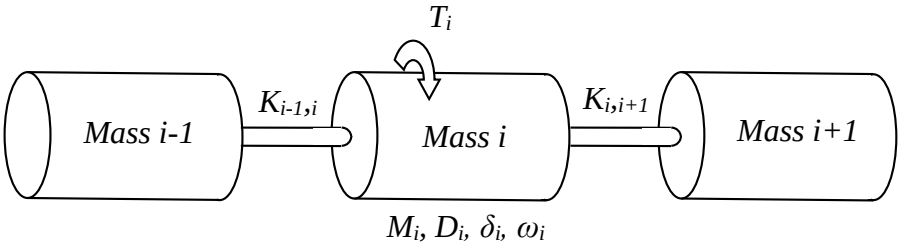

Figure 2.4: The i^{th} mass of an N-mass spring system.

$$\frac{M_i}{\omega_0}\frac{d\omega_i}{dt} = T_i + K_{i-1,i}(\delta_{i-1} - \delta_i) - K_{i,i+1}(\delta_i - \delta_{i+1}) - \frac{D_i}{\omega_0}(\omega_i - \omega_0) \tag{2.18}$$

$$\frac{d\delta_i}{dt} = \omega_i - \omega_0 \tag{2.19}$$

where

$$K_{i-1,i}|_{i=1} = 0, \qquad K_{i,i+1}|_{i=N} = 0, \tag{2.20}$$

As an example, when Equations (2.18) to (2.20) are applied to the linear six-mass-spring system of Figure 2.3, the shaft system equations are written as:

$$\frac{M_E}{\omega_0}\frac{d\omega_E}{dt} = K_{Eg}(\delta - \delta_E) - \frac{D_E}{\omega_0}(\omega_E - \omega_0)$$

$$\frac{d\delta_E}{dt} = \omega_E - \omega_0$$

$$\frac{M_g}{\omega_0}\frac{d\omega}{dt} = -T_e + K_{gB}(\delta_B - \delta) - K_{Eg}(\delta - \delta_E) - \frac{D_g}{\omega_0}(\omega - \omega_0)$$

$$\frac{d\delta}{dt} = \omega - \omega_0$$

$$\frac{M_B}{\omega_0}\frac{d\omega_B}{dt} = \frac{\omega_0}{\omega_B}P_B + K_{BA}(\delta_A - \delta_B) - K_{gB}(\delta_B - \delta) - \frac{D_B}{\omega_0}(\omega_B - \omega_0)$$

$$\frac{d\delta_B}{dt} = \omega_B - \omega_0 \tag{2.21}$$

$$\frac{M_A}{\omega_0}\frac{d\omega_A}{dt} = \frac{\omega_0}{\omega_A}P_A + K_{AI}(\delta_I - \delta_A) - K_{BA}(\delta_A - \delta_B) - \frac{D_A}{\omega_0}(\omega_A - \omega_0)$$

$$\frac{d\delta_A}{dt} = \omega_A - \omega_0$$

$$\frac{M_I}{\omega_0}\frac{d\omega_I}{dt} = \frac{\omega_0}{\omega_I}P_I + K_{IH}(\delta_H - \delta_I) - K_{AI}(\delta_I - \delta_A) - \frac{D_I}{\omega_0}(\omega_I - \omega_0)$$

$$\frac{d\delta_I}{dt} = \omega_I - \omega_0$$

$$\frac{M_H}{\omega_0}\frac{d\omega_H}{dt} = \frac{\omega_0}{\omega_H}P_H - K_{IH}(\delta_H - \delta_I) - \frac{D_H}{\omega_0}(\omega_H - \omega_0)$$

$$\frac{d\delta_H}{dt} = \omega_H - \omega_0$$

The overall shaft equations are given by the following matrix equation

$$\left[\frac{dX_{ms}}{dt}\right] = [At_{ms}][X_{ms}] + [Bt_{ms}][U_{tms}] \tag{2.22}$$

where

$$[X_{ms}] = [\delta_E \quad \delta \quad \delta_B \quad \delta_A \quad \delta_I \quad \delta_H \quad \omega_E \quad \omega \quad \omega_B \quad \omega_A \quad \omega_I \quad \omega_H]^T$$

$$[U_{tms}] = [\omega_0 \quad P_H \quad P_I \quad P_A \quad P_B \quad T_e]^T$$

$$[At_{ms}] = \begin{bmatrix} 0_{6\times6} & I_{6\times6} \\ As1 & As2 \end{bmatrix}$$

$$[As1] = \omega_0 \begin{bmatrix} -\frac{K_{Eg}}{M_E} & \frac{K_{Eg}}{M_E} & 0 & 0 & 0 & 0 \\ \frac{K_{Eg}}{M_g} & -\frac{K_{gB}+K_{Eg}}{M_g} & \frac{K_{gB}}{M_g} & 0 & 0 & 0 \\ 0 & \frac{K_{gB}}{M_B} & -\frac{K_{BA}+K_{gB}}{M_B} & \frac{K_{gB}}{M_B} & 0 & 0 \\ 0 & 0 & \frac{K_{BA}}{M_A} & -\frac{K_{AI}+K_{BA}}{M_A} & \frac{K_{AI}}{M_A} & 0 \\ 0 & 0 & 0 & \frac{K_{AI}}{M_I} & -\frac{K_{HI}+K_{AI}}{M_I} & \frac{K_{HI}}{M_I} \\ 0 & 0 & 0 & 0 & \frac{K_{HI}}{M_H} & -\frac{K_{HI}}{M_H} \end{bmatrix}$$

$$[As2] = \begin{bmatrix} -\frac{D_E}{M_E} & 0 & 0 & 0 & 0 & 0 \\ 0 & -\frac{D_g}{M_g} & 0 & 0 & 0 & 0 \\ 0 & 0 & -\frac{D_B}{M_B} & 0 & 0 & 0 \\ 0 & 0 & 0 & -\frac{D_A}{M_A} & 0 & 0 \\ 0 & 0 & 0 & 0 & -\frac{D_I}{M_I} & 0 \\ 0 & 0 & 0 & 0 & 0 & -\frac{D_H}{M_H} \end{bmatrix} \tag{2.23}$$

$$[Bt_{ms}] = \begin{bmatrix} -1_{6\times1} & 0_{6\times1} & 0_{6\times1} & 0_{6\times1} & 0_{6\times1} & 0_{6\times1} \\ \frac{D_E}{M_E} & 0 & 0 & 0 & 0 & 0 \\ \frac{D_g}{M_g} & 0 & 0 & 0 & 0 & -\frac{\omega_0}{M_g} \\ \frac{D_B}{M_B} & 0 & 0 & 0 & \frac{\omega_0^2}{\omega_B M_B} & 0 \\ \frac{D_A}{M_A} & 0 & 0 & \frac{\omega_0^2}{\omega_B M_B} & 0 & 0 \\ \frac{D_I}{M_I} & 0 & \frac{\omega_0^2}{\omega_I M_I} & 0 & 0 & 0 \\ \frac{D_H}{M_H} & \frac{\omega_0^2}{\omega_H M_H} & 0 & 0 & 0 & 0 \end{bmatrix}$$

Here, the $[I_{n\times n}]$ is an *n* by *n* identity matrix, $0_{m\times n}$ is an *m* by *n* matrix with all elements zero, and $-1_{6\times1}$ is a 6 by 1 matrix with all elements -1.

2.3.3 Modeling of the transmission line

A series capacitor-compensated transmission line may be represented by the *RLC* circuit shown in Figure 2.5 [21]. In the voltage phasor diagram shown in Figure 2.6, the rotor angle δ is the angle (in elec. rad) by which the q-axis leads the infinite-bus (reference) voltage V_b. The differential equations for the circuit elements, after applying Park's transformation [21], can be expressed in the d-q reference frame by the following matrix expressions.

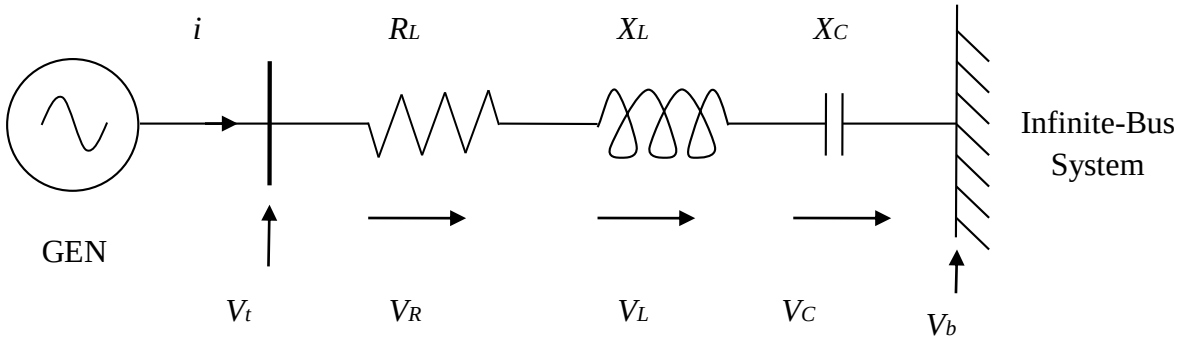

Figure 2.5: A series capacitor-compensated transmission line.

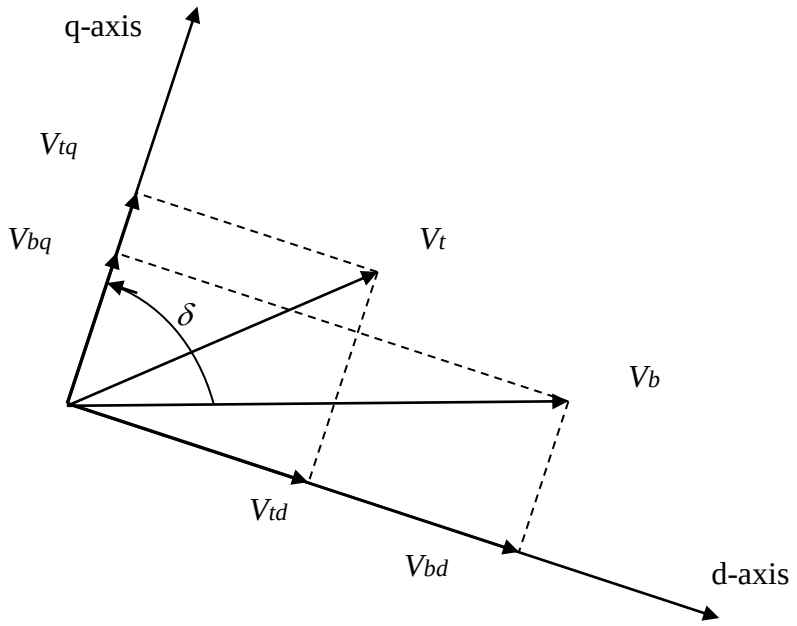

Figure 2.6: Voltage phasor diagram.

The voltage across the resistance:

$$\begin{bmatrix} V_{Rd} \\ V_{Rq} \end{bmatrix} = \begin{bmatrix} R_L & 0 \\ 0 & R_L \end{bmatrix} \begin{bmatrix} i_d \\ i_q \end{bmatrix} \tag{2.24}$$

The voltage across the inductance:

$$\begin{bmatrix} V_{Ld} \\ V_{Lq} \end{bmatrix} = \begin{bmatrix} 0 & -\frac{\omega}{\omega_0} X_L \\ \frac{\omega}{\omega_0} X_L & 0 \end{bmatrix} \begin{bmatrix} i_d \\ i_q \end{bmatrix} + \begin{bmatrix} \frac{X_L}{\omega_0} & 0 \\ 0 & \frac{X_L}{\omega_0} \end{bmatrix} \begin{bmatrix} \frac{di_d}{dt} \\ \frac{di_q}{dt} \end{bmatrix} \tag{2.25}$$

The voltage across the capacitor:

$$\begin{bmatrix} \frac{dV_{Cd}}{dt} \\ \frac{dV_{Cq}}{dt} \end{bmatrix} = \begin{bmatrix} \omega_0 X_C & 0 \\ 0 & \omega_0 X_C \end{bmatrix} \begin{bmatrix} i_d \\ i_q \end{bmatrix} + \begin{bmatrix} 0 & \omega \\ -\omega & 0 \end{bmatrix} \begin{bmatrix} V_{Cd} \\ V_{Cq} \end{bmatrix} \tag{2.26}$$

The overall equations of the transmission line can be written as

$$\begin{bmatrix} \frac{dV_{Cd}}{dt} \\ \frac{dV_{Cq}}{dt} \\ V_{td} \\ V_{tq} \end{bmatrix} = [Att]\begin{bmatrix} V_{Cd} \\ V_{Cq} \end{bmatrix} + [Rt1]\begin{bmatrix} \frac{di_d}{dt} \\ \frac{di_q}{dt} \end{bmatrix} + [Rt2]\begin{bmatrix} i_d \\ i_q \end{bmatrix} + [Btt][V_b] \tag{2.27}$$

where

$$[Att] = \begin{bmatrix} 0 & \omega \\ -\omega & 0 \\ 1 & 0 \\ 0 & 1 \end{bmatrix}$$

$$[Rt1] = \begin{bmatrix} 0 & 0 \\ 0 & 0 \\ \frac{X_L}{\omega_0} & 0 \\ 0 & \frac{X_L}{\omega_0} \end{bmatrix}$$

$$[Rt2] = \begin{bmatrix} \omega_0 X_C & 0 \\ 0 & \omega_0 X_C \\ R_L & -\frac{\omega}{\omega_0} X_L \\ \frac{\omega}{\omega_0} X_L & R_L \end{bmatrix} \tag{2.28}$$

$$[Btt] = \begin{bmatrix} 0 \\ 0 \\ \sin\delta \\ \cos\delta \end{bmatrix}$$

2.3.4 Modeling of transformer

The three-phase transformer is constructed by using three single-phase transformers connected in Delta (LV side)/Y ground (HV side). The connection type, both sides of the voltage, as well as the winding resistance and winding reactance are represented in the model.

2.3.5 Modeling of system loads

The system loads are modeled in these studies by constant impedances. The formula, which is used in calculating the load impedances, is given by [22]:

$$Z_{Load} = \frac{|V_{Load}|^2}{P_{Load} - jQ_{Load}} \tag{2.29}$$

where

$$Z_{Load} = \text{load impedence}$$

$$V_{Load} = \text{load voltage}$$

$$P_{Load} = \text{load real power}$$

$$Q_{Load} = \text{load reactive power}$$

2.3.6 Wind turbine aerodynamic model

The dynamic output mechanical torque of the wind turbine is expressed as [10]

$$T_{MECH} = \frac{1}{2}\rho \mathrm{A} R_{\omega} C_p V_{\omega}^2 / \lambda \tag{2.30}$$

where ρ is the air density (kgm^{-3}), A is the blade sweep area (m^2), R_{ω} is the rotor radius of wind turbine (m), and V_{ω} is the wind speed ($\mathrm{m/s}$). C_p is the power coefficient of the blade which is a function of the blade pitch angle θ and the tip speed ratio λ according to the following equation:

$$C_p = \frac{1}{2}\left(\frac{R_{\omega} C_f}{\lambda} - 0.022\theta - 2\right) e^{-0.255\frac{R_{\omega} C_f}{\lambda}} \tag{2.31}$$

where C_f is the wind turbine blade design constant and the tip speed ratio λ is given by

$$\lambda = \frac{\Omega_m R_{\omega}}{V_{\omega}} \tag{2.32}$$

where Ω_m is the mechanical angular velocity (rad/s).

The power rotating speed, wind speed and the pitch angle relationships are illustrated in Figure 2.7.

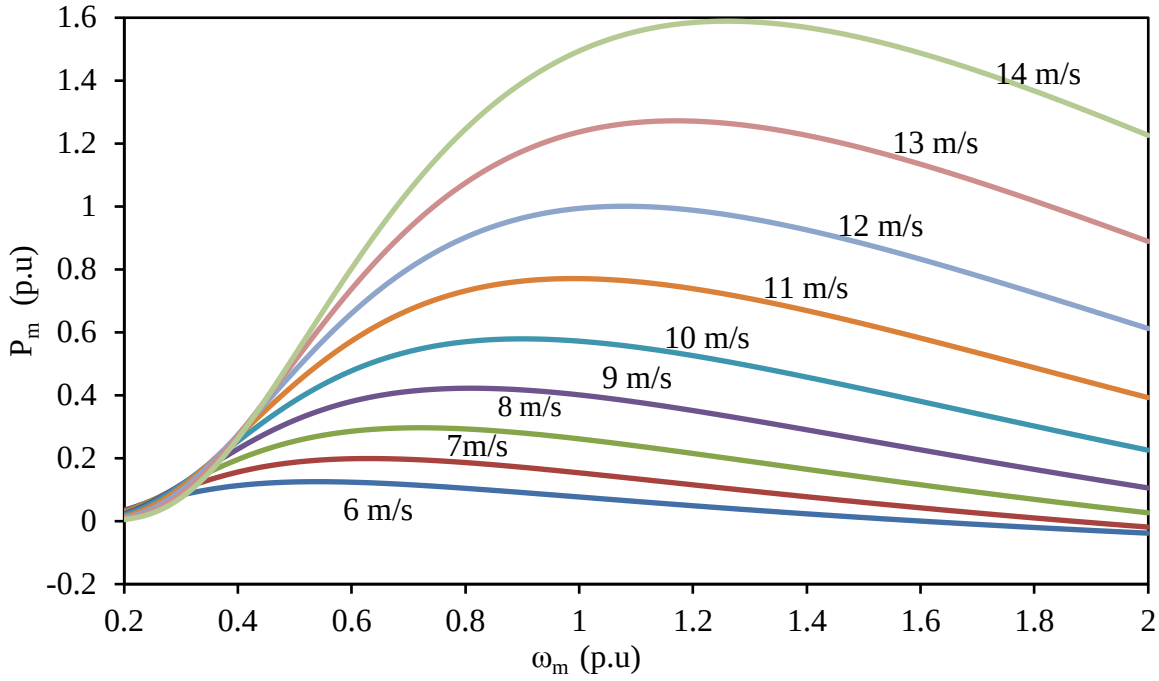

Figure 2.7: Mechanical power, rotor speed and wind speed relationships.

2.3.7 Modeling of the DFIG

Figure 2.8 shows the equivalent circuit of a DFIG in the synchronous *qd* reference frame, where the *q*-axis leads the *d*-axis by 90˚. The stator and rotor voltage equations in the *qd* reference frame can be written as follows:

$$\begin{cases} v_s = r_s i_s + j\omega_s \lambda_s + \frac{d\lambda_s}{dt} \\ v_r = r_r i_r + j(\omega_s - \omega_r)\lambda_r + \frac{d\lambda_r}{dt} \end{cases} \tag{2.33}$$

where $v_s = v_{qs} - jv_{ds}$ and $v_r = v_{qr} - jv_{dr}$. The flux linkage expressions are given as follows:

$$\begin{cases} \lambda_s = L_s i_s + M i_r \\ \lambda_r = L_r i_r + M i_s \end{cases} \tag{2.34}$$

where $L_s = L_{ls} + M$, $L_r = L_{lr} + M$, $\lambda_s = \lambda_{qs} - j\lambda_{ds}$, $\lambda_r = \lambda_{qr} - j\lambda_{dr}$, $i_s = i_{qs} - ji_{ds}$ and $i_r = i_{qr} - ji_{dr}$.

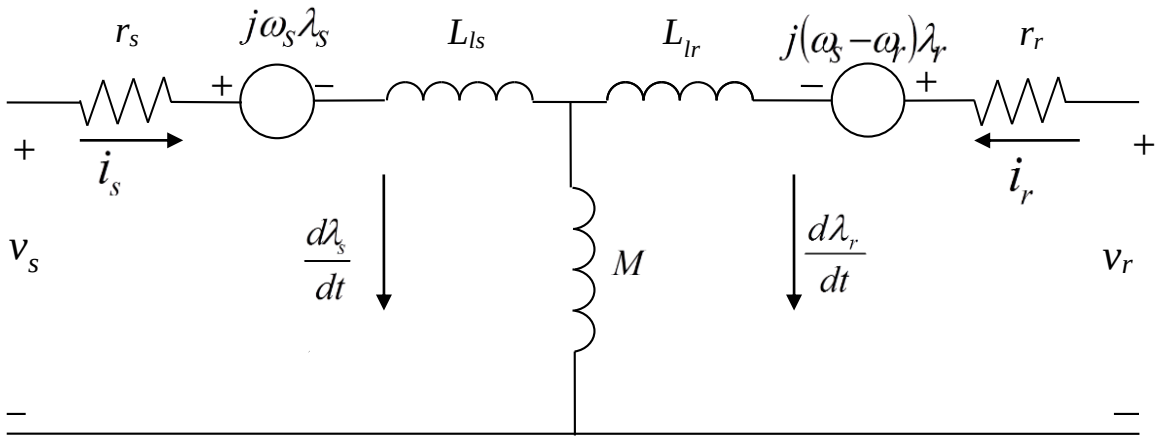

Figure 2.8: Equivalent circuit of the DFIG.

From Equations 2.33 and 2.34, a set of differential equations with the stator and rotor currents are state variables and the stator and rotor voltage as inputs can be established. While the rotor voltages are determined by the RSC control scheme, the stator voltages are determined by the network interface.

The electromagnetic torque T_e can be expressed as follows:

$$T_e = \lambda_{qm} i_{dr} - \lambda_{dm} i_{qr} \tag{2.35}$$

where λ_{qm} and λ_{dm} are, respectively, the *q*-and *d*-axes magnetizing flux linkages defined as

$$\lambda_{qm} = \lambda_{qs} - i_{qs} L_{ls} \tag{2.36}$$

$$\lambda_{dm} = \lambda_{ds} - i_{ds} L_{ls} \tag{2.37}$$

2.3.8 Modeling of the BtB dc capacitor link

The dynamics of the BtB dc capacitor link can be described with the help of the equivalent circuit shown in Figure 2.9 as

$$C \frac{dv_{dc}}{dt} = P_r - P_g \tag{2.38}$$

where

$$\begin{cases} P_r = K_1(v_{qr}i_{qr} + v_{dr}i_{dr}) \\ P_g = K_2(v_{qg}i_{qg} + v_{dg}i_{dg}) \end{cases} \quad (2.39)$$

In Equation 2.39, K_1 and K_2 are constants, P_r, P_g are the active powers of the RSC and the GSC respectively, v_{qr}, v_{dr} are the quadrature- and direct- axes RSC voltage respectively and v_{qg}, v_{dg} are the quadrature- and direct- axes GSC voltage respectively.

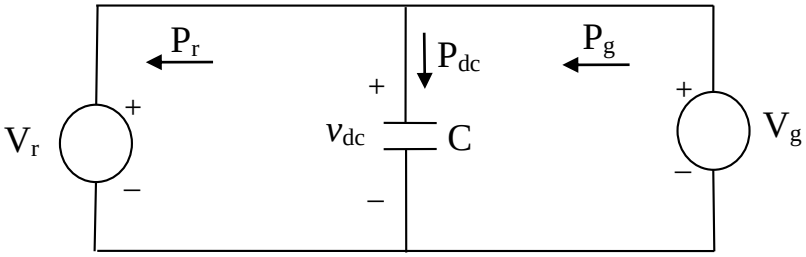

Figure 2.9: Equivalent circuit for the BtB dc capacitor link.

The frequency converters are modeled by a fundamental frequency approach, which is appropriate and sufficient for power system dynamic studies. Assuming an ideal DC-link voltage and an ideal pulse-width modulation [23], the relation between AC- and DC- voltages can be expressed as follows [12]

$$|U_{\mathrm{AC}}| = K_0 P_m U_{\mathrm{DC}} \quad (2.40)$$

P_m, which donates the pulse-width-modulation index, is limited ($0 < P_m \leq 1$) to avoid saturation effects. The factor K_0 depends on the modulation method, e.g. rectangular or sinusoidal modulation. In case of sinusoidal modulation, which is standard in power application, the factor K_0 is defined as

$$K_0 = \frac{\sqrt{3}}{2\sqrt{2}} \quad (2.41)$$

The DC-link capacitor provides an intermediate energy storage, which decouples the generator-side converter and the grid-side converter. The size of the DC-link Capacitor is selected based on a trade-off between voltage ripples, lifetime and fast control of the DC-link [12], [24].

The control of the DFIG wind turbine is achieved by controlling the RSC and GSC utilizing vector control techniques. Vector control allows decoupled control of both the real and reactive

power. The idea is to use a rotating reference frame based on an AC flux or voltage and then to project the currents on this rotating frame. Such projections are usually referred to as the d- and q- components of their respective currents. For flux-based rotating frames, changes in the q-component leads to real power changes, while changes in the d- component leads to reactive power changes. In voltage-based rotating frames (90˚ ahead of flux-based frames), the effect is the opposite.

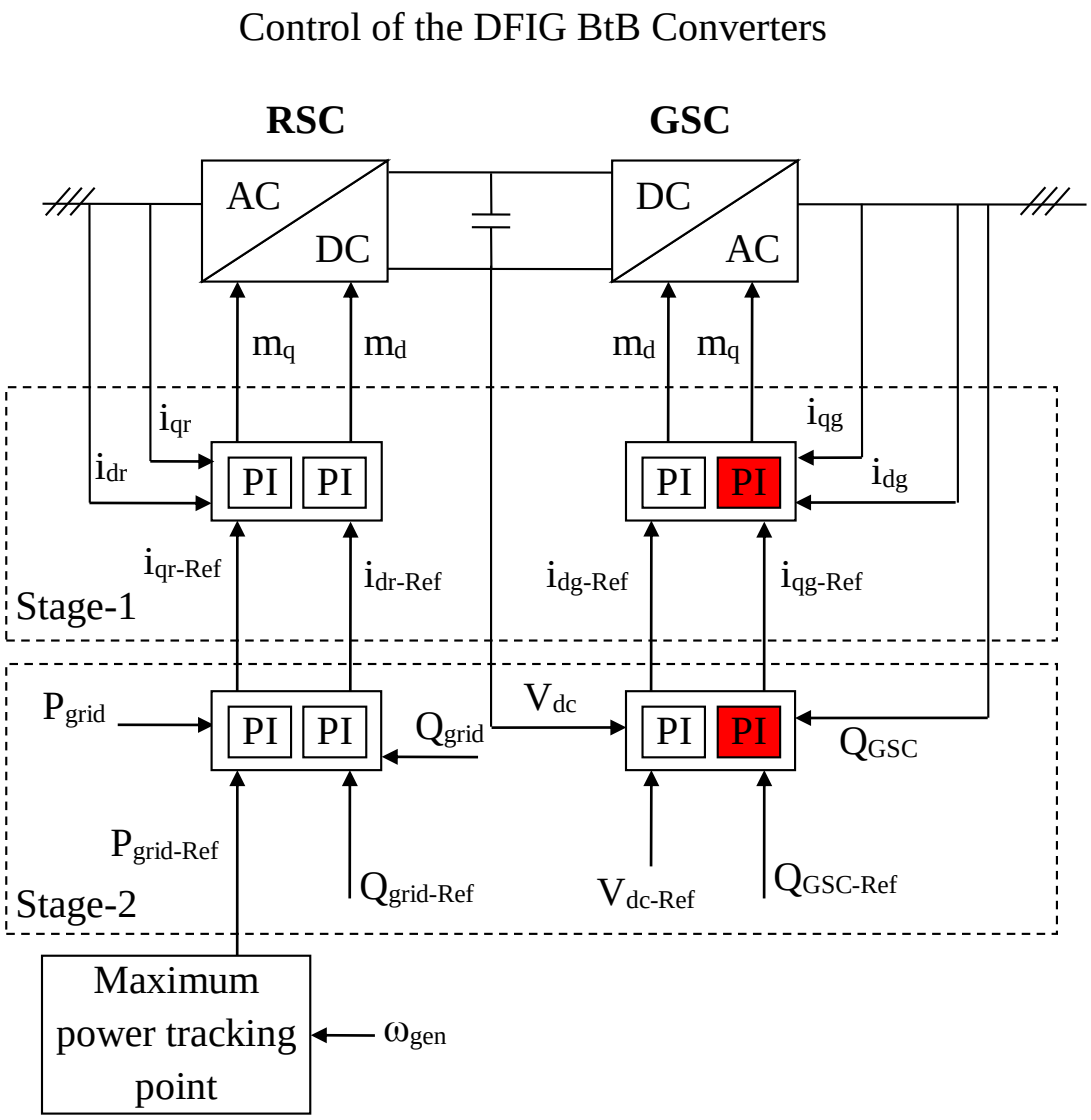

Figure 2.10: Schematic diagram of a general control scheme of DFIG BtB converters.

Figure 2.10 shows a general control scheme for the DFIG BtB converters [25]-[27]. In such a scheme, the RSC operates in the stator flux reference while the GSC operates in the stator

voltage reference frame. The q-axis current of the RSC is used to control the real power while the d-axis current is used for reactive power control. On the other hand, the d-axis current for the GSC is used to control the dc link voltage to a constant level while the q-axis current is used for reactive power control.

As illustrated in Figure 2.10, both RSC and GSC are controlled by a two-stage controller. The first stage consists of very fast current controllers regulating the rotor currents to references values that are specified by slower power controllers (Stage-2). In normal operation, the aim of the RSC is to control independently the real and reactive power on the grid while the GSC has to maintain the dc link capacitor at a set value regardless of the magnitude and direction of the rotor power and to guarantee converter operation with unity power factor (zero reactive power). The reference $P_{grid-Ref}$ for the real power is given by the maximum power tracking point (MPT) lookup table as a function of the optimal generator speed. The reference $Q_{grid-Ref}$ for the reactive power of the RSC can be set to a certain value or to zero according to whether or not the DFIG is required to contribute with reactive power. The reactive power reference for the GSC, $Q_{GSC-Ref}$ is "usually" set to zero. This means that the GSC exchanges only real power with the grid and, therefore, the transmission of reactive power controllability of the GSC can be useful during the process of voltage reestablishment after clearing a system fault. The reference signal V_{dc-Ref} is set to a constant value that depends on the size of the converter, the stator/rotor voltage ratio and the modulation factor of the power converter [27].

2.3.9 Modeling of PMSG

The equations of a PMSG can be expressed directly from the equations of a DC excited synchronous generator, with the simplification that PMSG does not have damper windings. The voltage equations of the generator [20], expressed in the *dq*-reference frame, can be expressed as follows

$$e_d = R_s i_d - \omega\psi_q + \dot{\psi}_d \tag{2.42}$$

$$e_q = R_s i_q + \omega\psi_d + \dot{\psi}_q \tag{2.43}$$

With the stator flux components

$$\psi_d = L_d i_d + \psi_{PM} \tag{2.44}$$

$$\psi_q = L_q i_q \tag{2.45}$$

where e_d and e_q, i_d and i_q, L_d and L_q are the *d*- and *q*-components of the stator voltage, of the stator current and of the stator inductance, respectively. R_s and Ψ_{PM} stand for stator resistance and permanent magnet flux, respectively. In stability studies, the stator transients can be neglected.

The electromagnetic torque equation:

$$T_e = \psi_d i_q - \psi_q i_d \tag{2.46}$$

2.3.10 Modelling of the BtB dc capacitor link

As shown in Figure 2.11, the dynamic of the BtB capacitor link is very similar to that discussed in subsection 2.3.8 if the symbol "r" representing the "rotor" in RSC is replaced by the symbol "m" represent "MSC".

2.3.11 FFC Wind turbine control

Similar to DFIG, the control of the FFC is achieved by controlling the MSC and GSC utilizing vector control techniques [4]. The MSC controls the active power delivered by the PMSG, and follows a tracking characteristic to adjust the PMSG speed for optimal power generation depending on wind speed. The function of GSC is maintaining the dc bus voltage to the dc link by the MSC. GSC also controls the reactive power delivered to the grid [12], [28].

A generic 2 MW, 60 Hz FFC model of EMTP-RV is used in this thesis. The model includes a pitch control, dc chopper and over/under voltage protections. The wind turbine drive system is represented with its two-mass model. The FFC converters are also modeled with their AVMs.

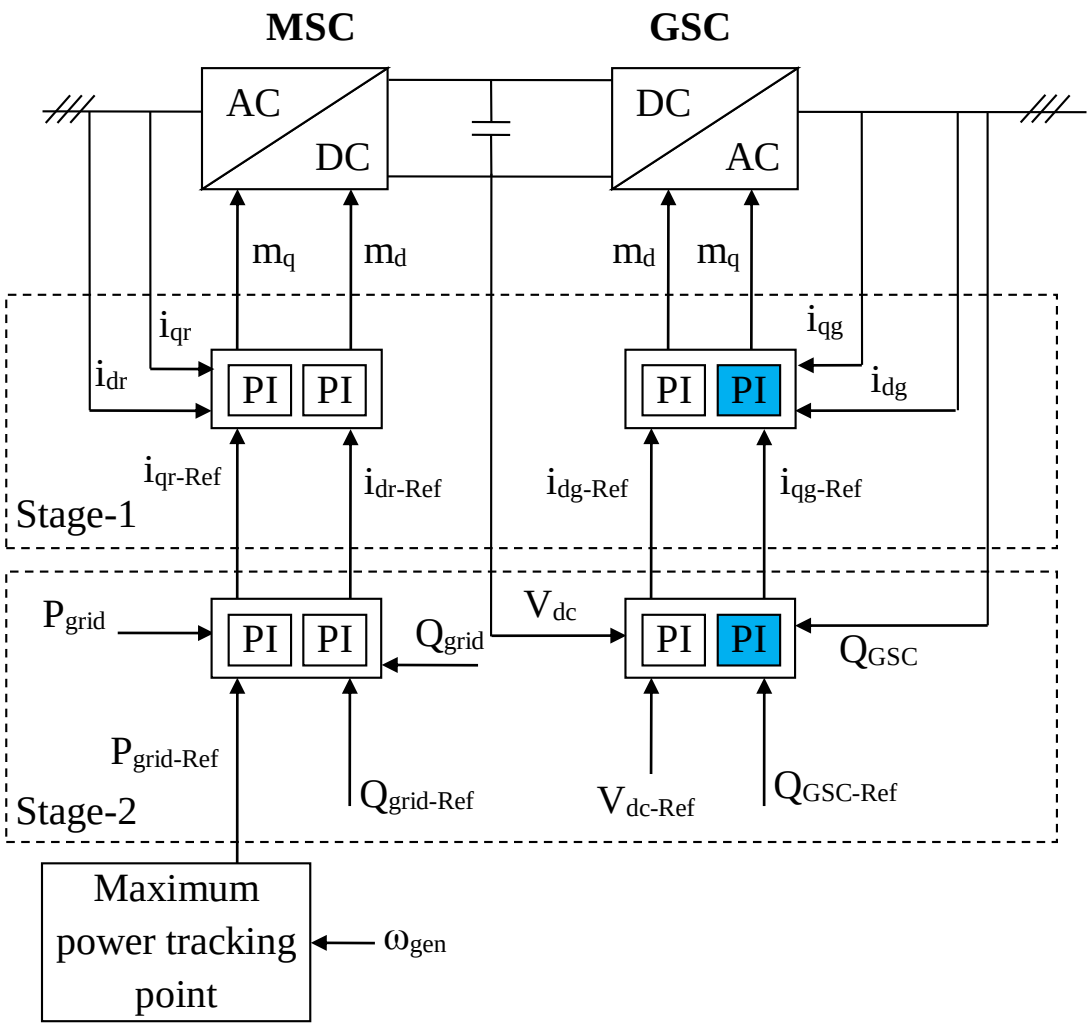

Figure 2.11: Schematic diagram of a general control scheme of FFC BtB converters.

2.4 A Sample Case Study: 30% Compensation Degree in Lines 1 and 2

In the studies conducted in this thesis, the ElectroMagnetic Transient Program (EMTP-RV) is used for modeling the various system components and producing the time-domain simulation results [29]. Moreover, faults are assumed to occur at t = 0.1 second.

Figure 2.12 shows the power flow results for the system bus voltages and transmission line real power flows. The real and reactive powers, terminal voltages and dc capacitor voltages of wind farms A and B during and after clearing a 3-cycle, three-phase fault on Line 5 are shown in

Figures 2.13 and 2.14 respectively. The turbine-generator electrical powers and shaft torsional torques during and after clearing the same fault are shown in Figure 2.15. Moreover, the frequency spectrums (obtained by using Fast Fourier Transform (FFT) analysis) of the turbine-generator shaft torsional torques and the stator current of the DFIG wind turbine are illustrated in Figures 2.16 and 2.17 respectively.

The following observations can be made from examining these figures:

1. The system is stable after fault clearing as the low-frequency oscillations in the turbine-generator electrical powers are damped.
2. It can be seen from Figure 2.15 that the turbine-generator shaft torsional torques are not sinusoidal with a single frequency but contain contributions from all the torsional modes. Moreover, it can be noticed from the same figure that the shaft section between the generators and low-pressure turbines are subjected to the highest stresses.
3. Except for the (GEN1-EXC) shaft torsional torque which exhibits slowly growing oscillations, the other turbine-generator shaft torsional torques are either slightly damped or exhibit sustained oscillations.
4. The frequency spectrums of the turbine-generator shaft torsional torques identify the four natural torsional modes of oscillations of G1 and G2 shaft systems with frequencies 24.65 Hz, 32.39 Hz, 44.99 Hz and 51.1 Hz.
5. At this compensation degree, wind farm A does not exhibit subsynchronous interaction as the oscillations in its real output power and terminal voltages are damped after fault clearing.

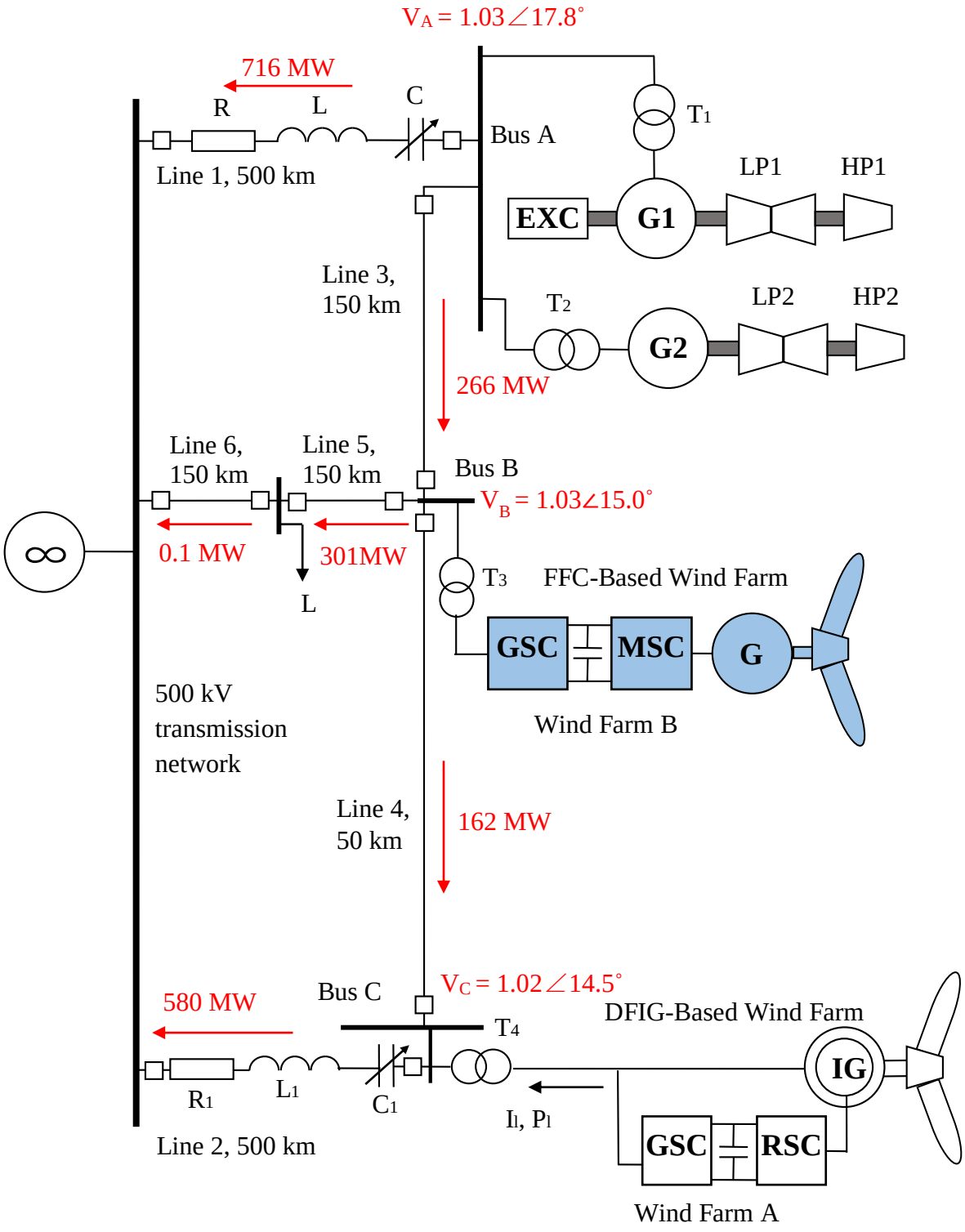

Figure 2.12: Power flow results of bus voltages and transmission line real power flows of the system under study.

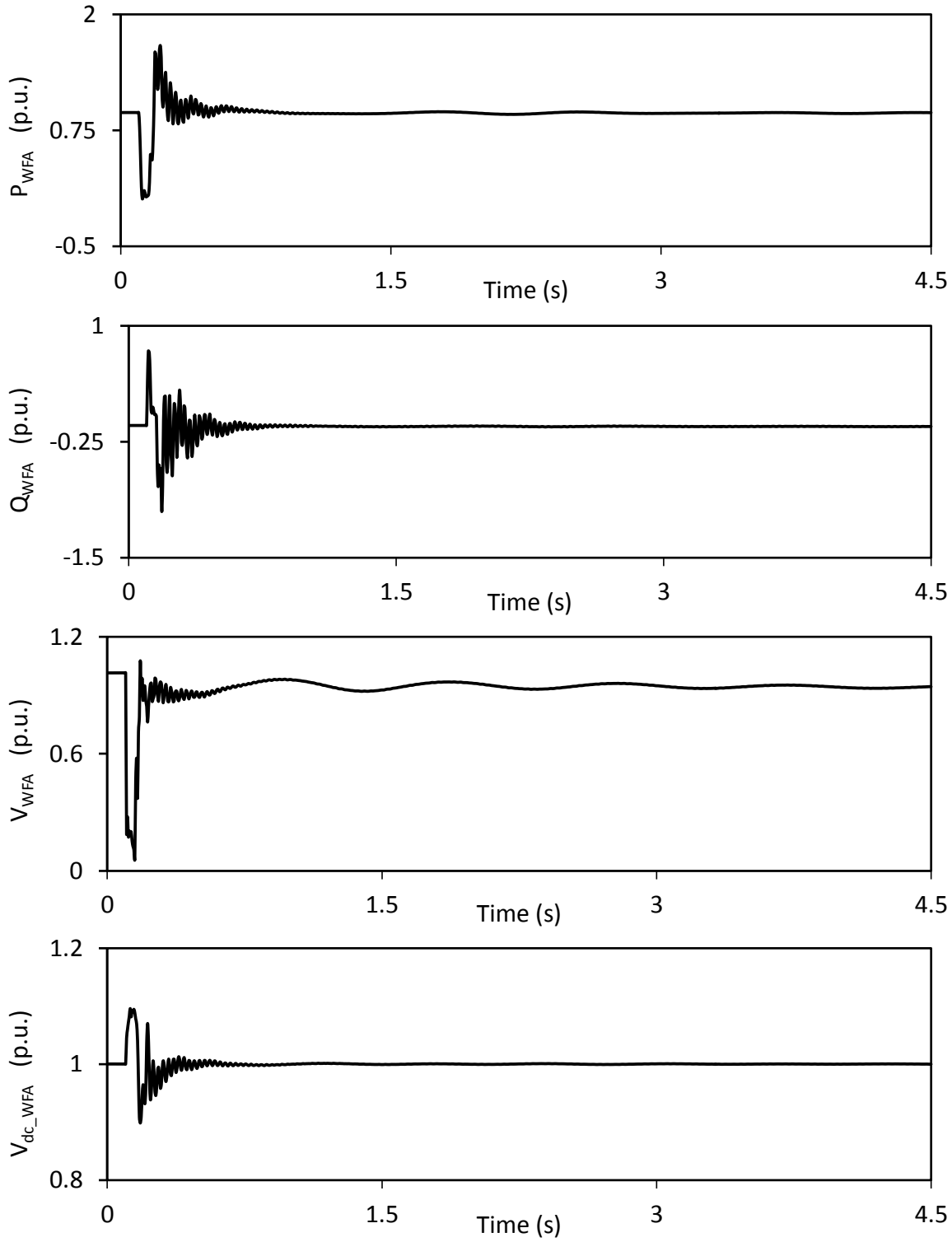

Figure 2.13: Wind farm A real and reactive powers, terminal voltage and dc capacitor voltage during and after clearing a 3-cycle, three-phase fault on Line 5 (30% compensation degree).

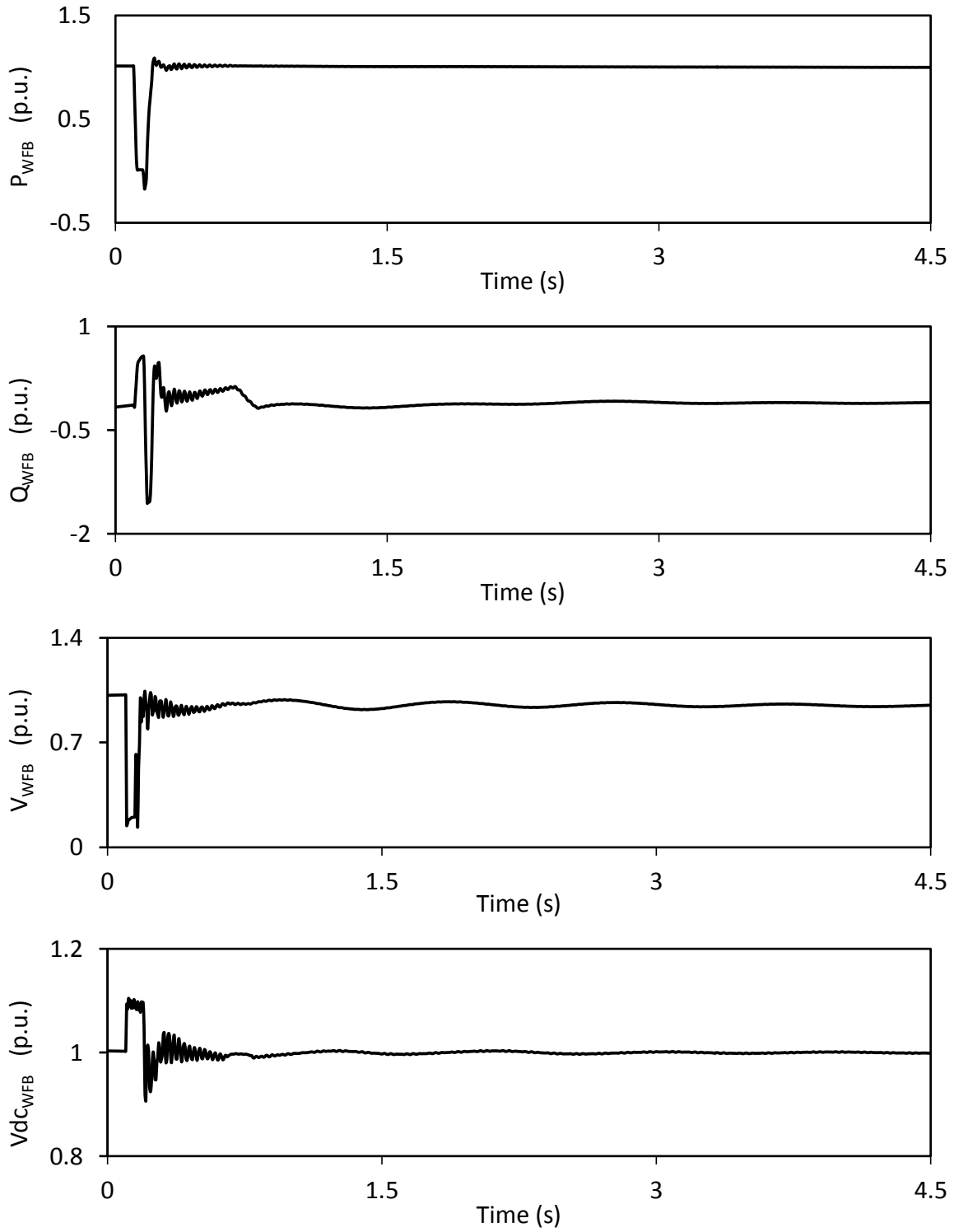

Figure 2.14: Wind farm B real and reactive powers, terminal voltage and dc capacitor voltage during and after clearing a 3-cycle, three-phase fault on Line 5 (30% compensation degree).

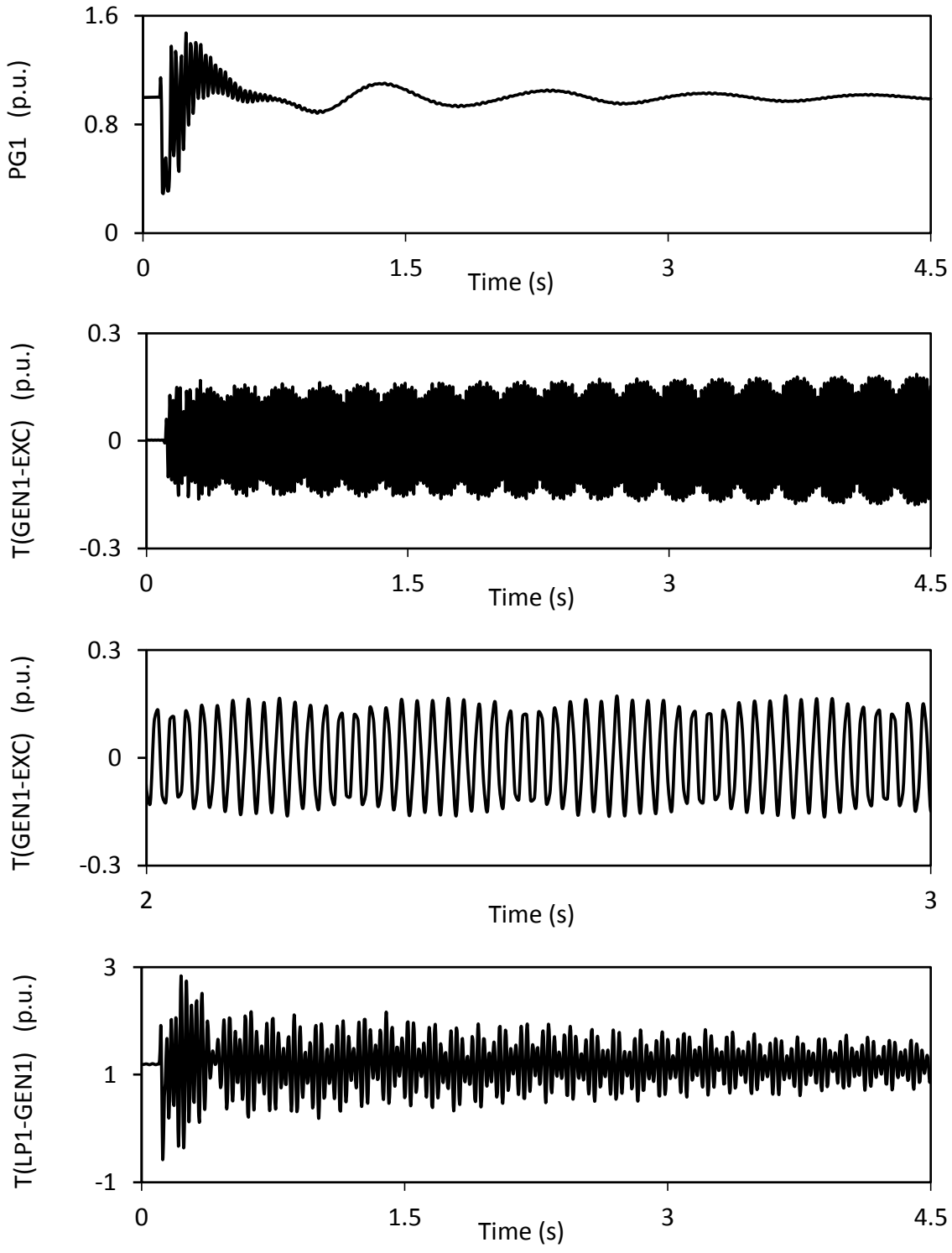

Figure 2.15: Turbine-generator electrical powers and shaft torsional torques during and after clearing a 3-cycle, three-phase fault on Line 5 (30% compensation degree).

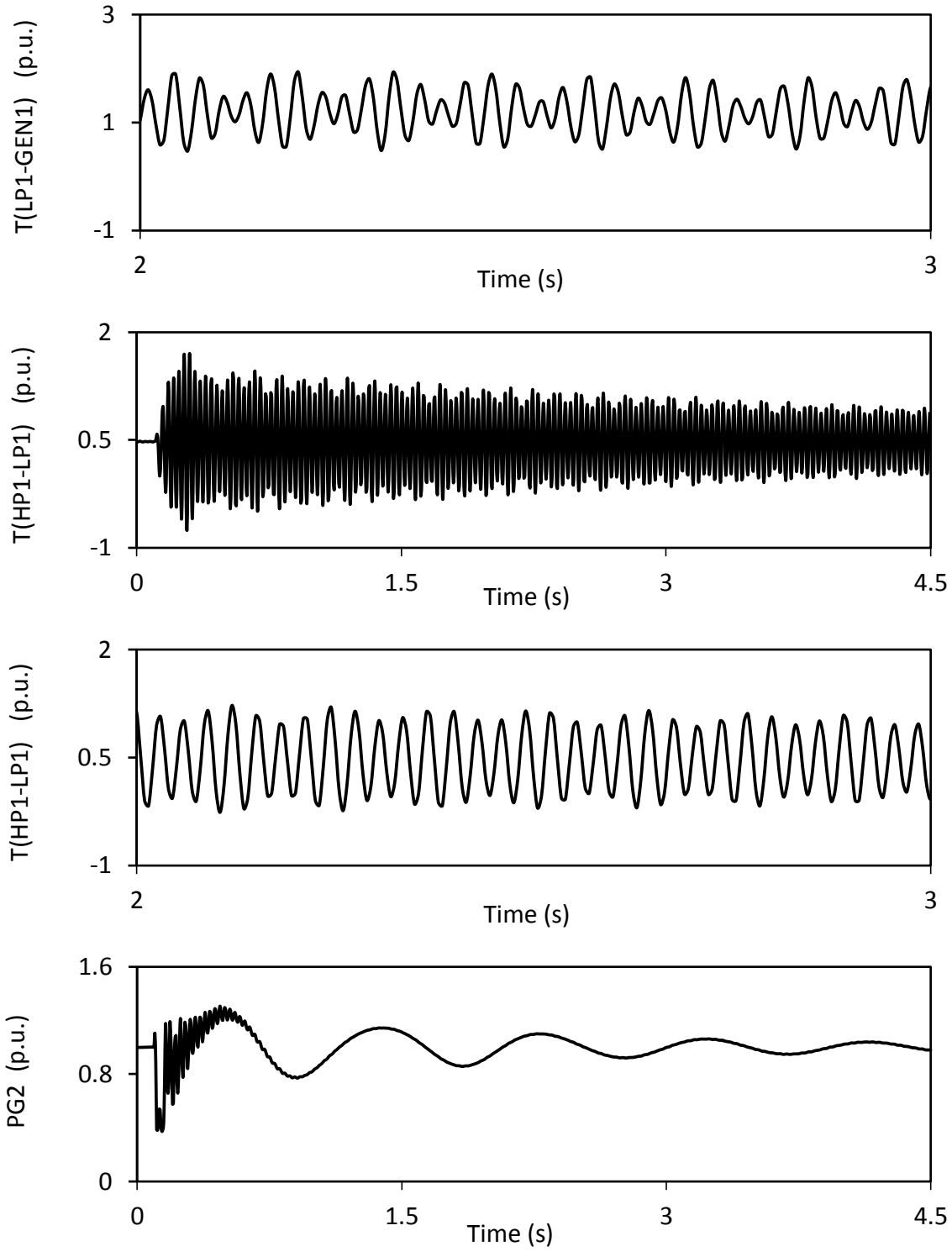

Figure 2.15: Continued.

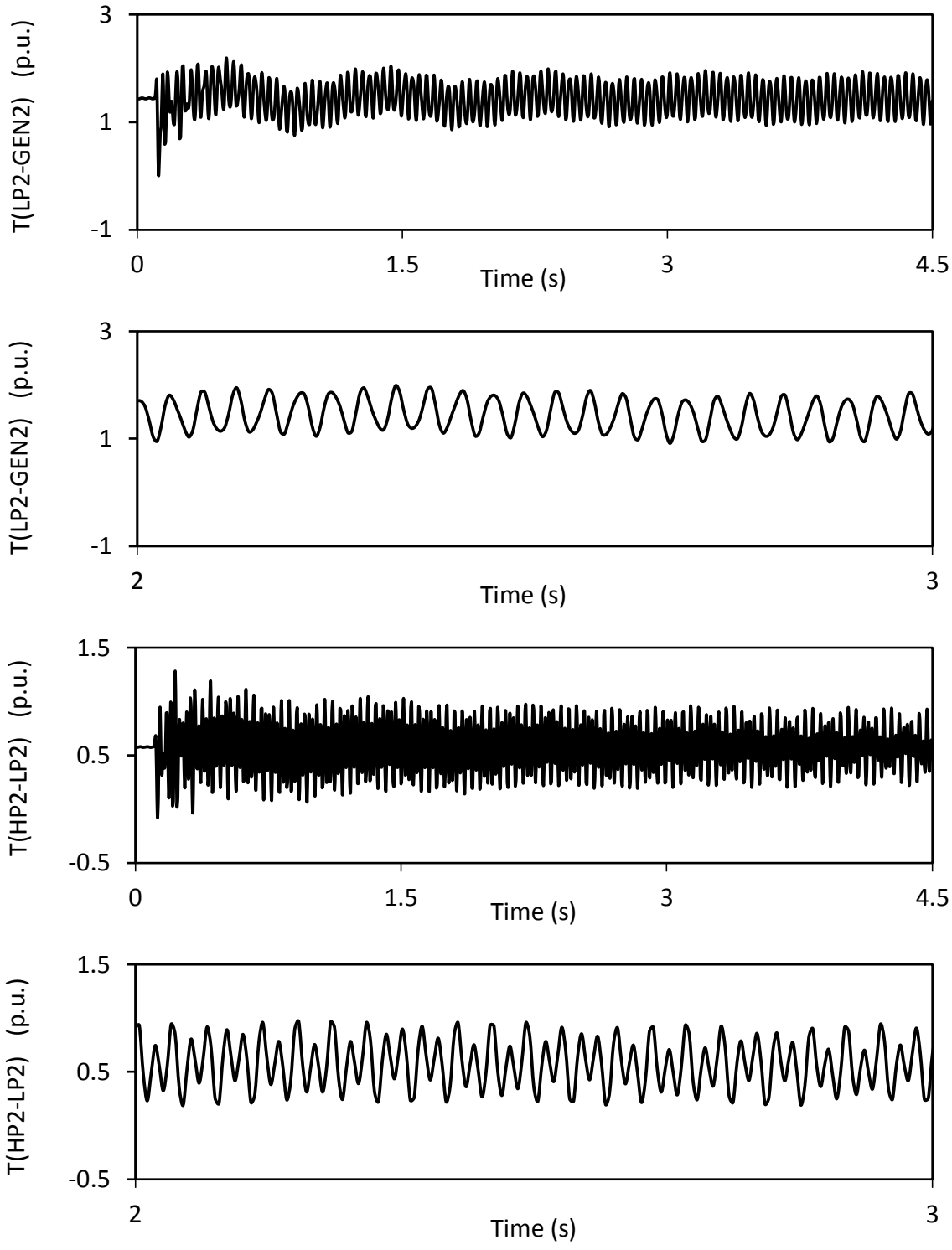

Figure 2.15: Continued.

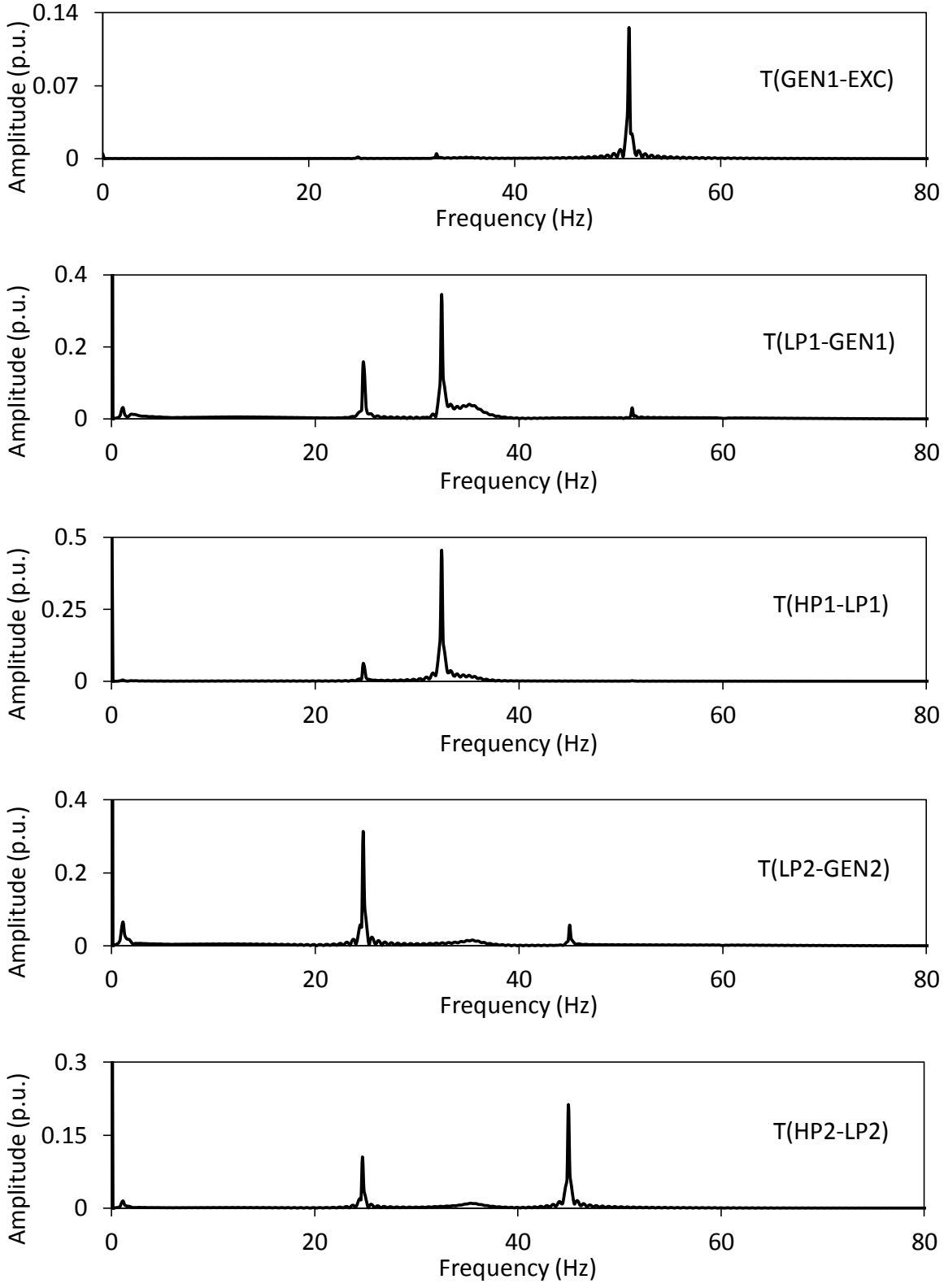

Figure 2.16: Frequency spectrums of the turbine-generator shaft torsional torques during and after clearing a 3-cycle, three-phase fault on Line 5 (30% compensation degree).

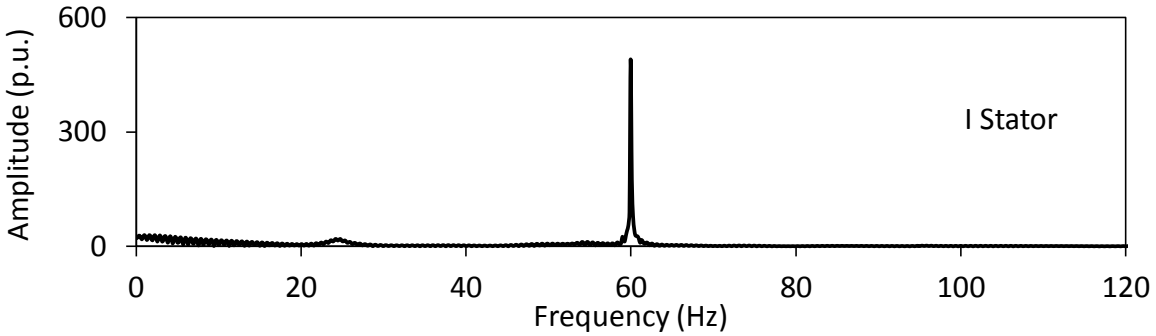

Figure 2.17: Frequency spectrums of the stator current of the DFIG wind turbine.

2.5 Summary

This chapter introduces the system used for the studies reported in this thesis and presents the mathematical models of its various components. A digital time-domain simulation of a case study of the system during a three-phase fault is also presented. The results of this case study show the existence of subsynchronous resonance and the absence of subsynchronous interaction. In the next chapter, supplemental controls are presented for simultaneous mitigation of the two phenomena.

3. SUPPLEMENTAL CONTROLS OF FFC- AND DFIG-BASED WIND FARMS FOR SIMULATANEOUS MITIGATION OF SUBSYNCHRONOUS RESONANCE AND SUBSYNCHRONOUS INTERACTION

3.1 Introduction

In this chapter, two supplemental controls of FFC- and DFIG-based wind farms for simultaneous mitigation of SSR and SSI are introduced. The effectiveness of the two presented controllers in mitigating both phenomena is investigated through several time-domain simulation case studies for different wind farm ratings and system contingences.

3.2 Supplemental Controls of FFC- and DFIG-Based Wind Farms

SSR and SSI damping is achieved through the modulation of the reactive powers of the FFC and DFIG wind turbines. This is attained by introducing supplemental control signals, U_S, in the reactive power control loop of their grid side converters of as shown in Figures 3.1 and 3.2 respectively. In this context, two supplemental controls designated as Supplemental controls 1 and 2 are proposed.

In Supplemental control 1, shown in Figure 3.3, SSR and SSI damping is attained by adding the supplementary control signal $U_S = U_{SSR} + U_{SSI}$ in the reactive power control loop of the GSC of the FFC wind turbines before the PI regulator of the inner control loop as shown in Figure 3.1. On the other hand, in Supplemental control 2, shown in Figure 3.4, SSR and SSI damping is attained by adding supplementary control signals $U_S = U_{SSR}$ and $U_S = U_{SSI}$ in the reactive power control loops of the GSC of the FFC and DFIG wind turbines respectively before the PI regulator of the inner control loop as shown in Figures 3.1 and 3.2.

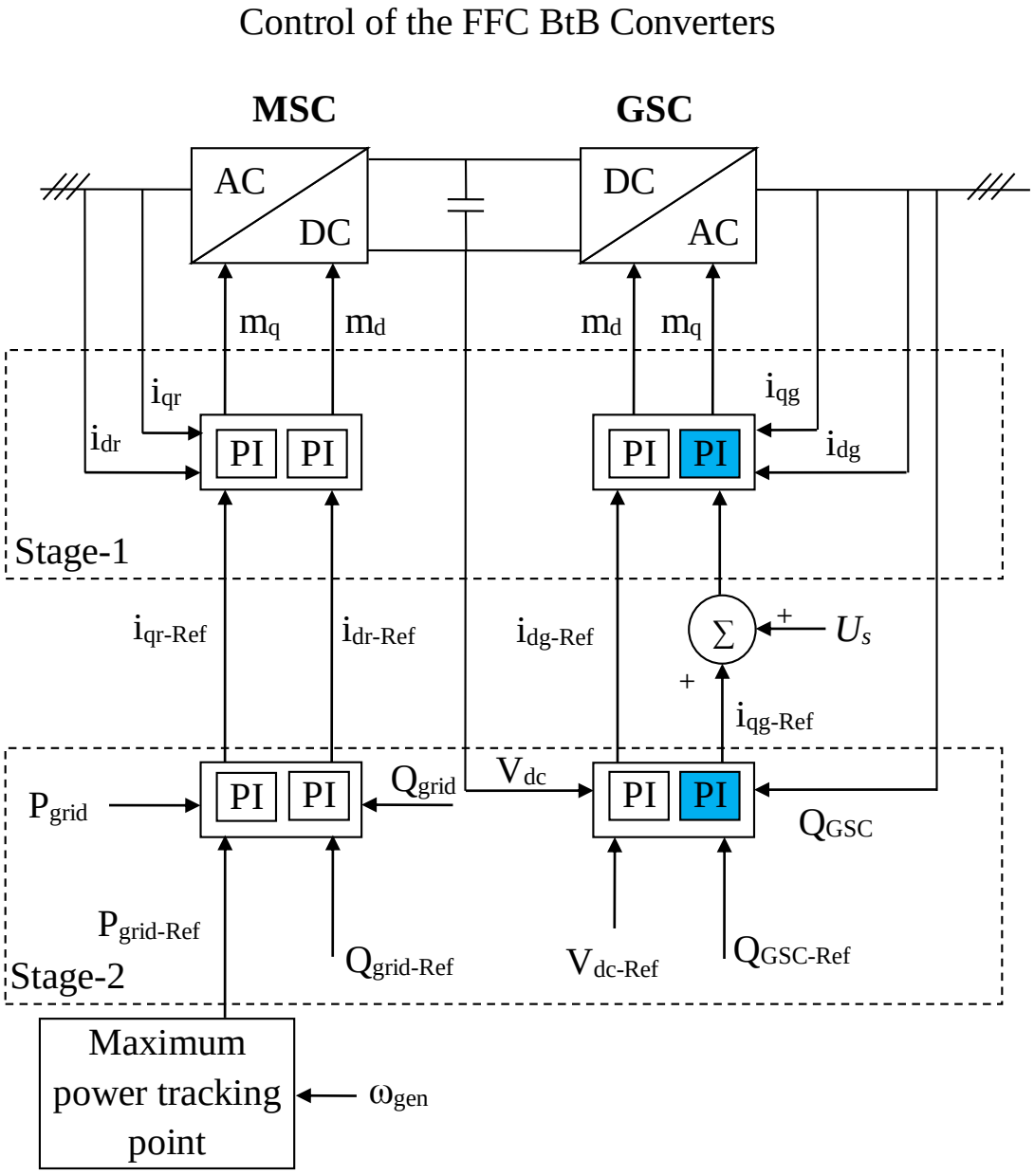

Figure 3.1: Incorporating a supplemental control signal, U_S, in the reactive power control loop of the GSC of FFC wind turbine.

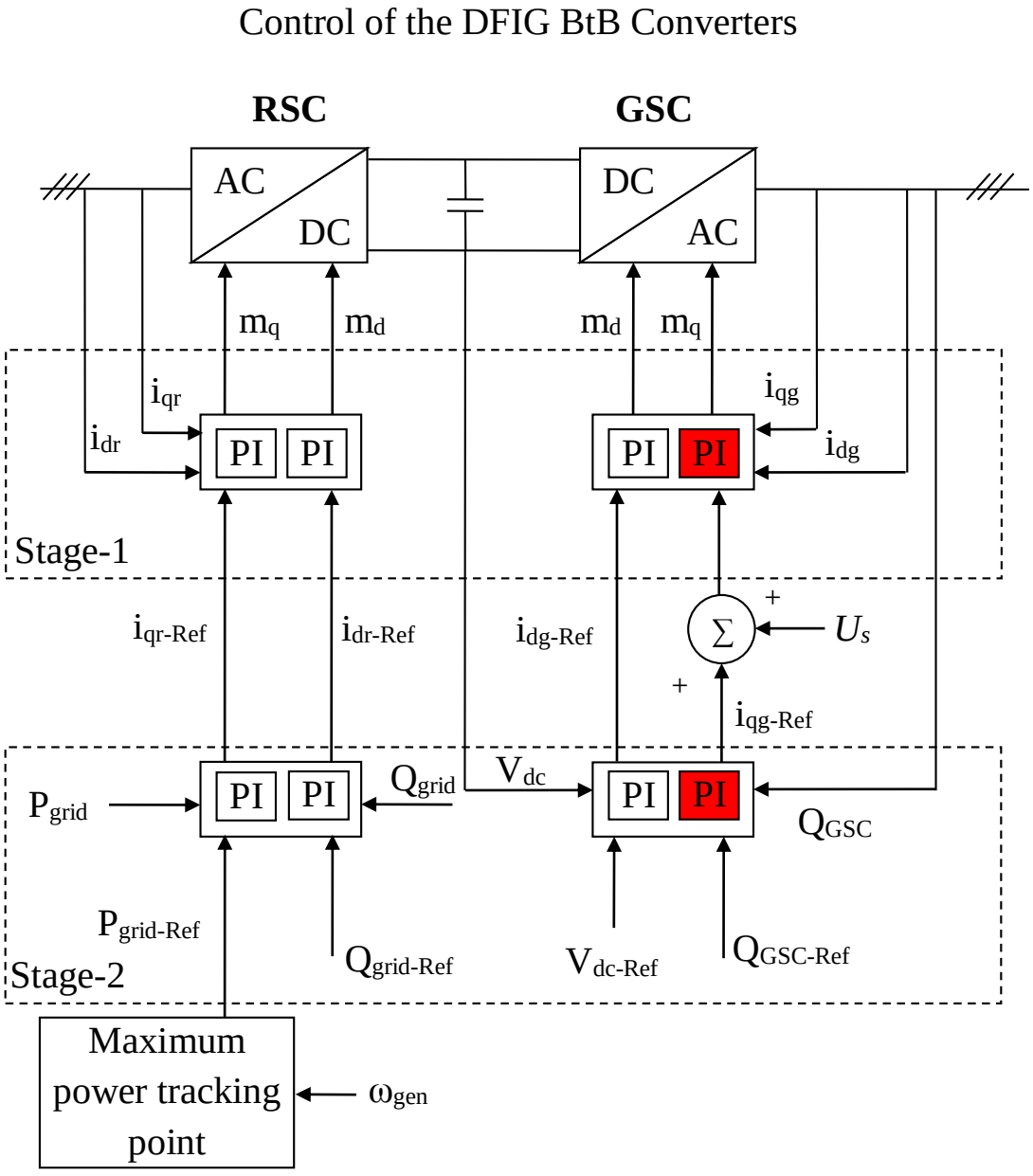

Figure 3.2: Incorporating a supplemental control signal, U_S, in the reactive power control loop of the GSC of DFIG wind turbine.

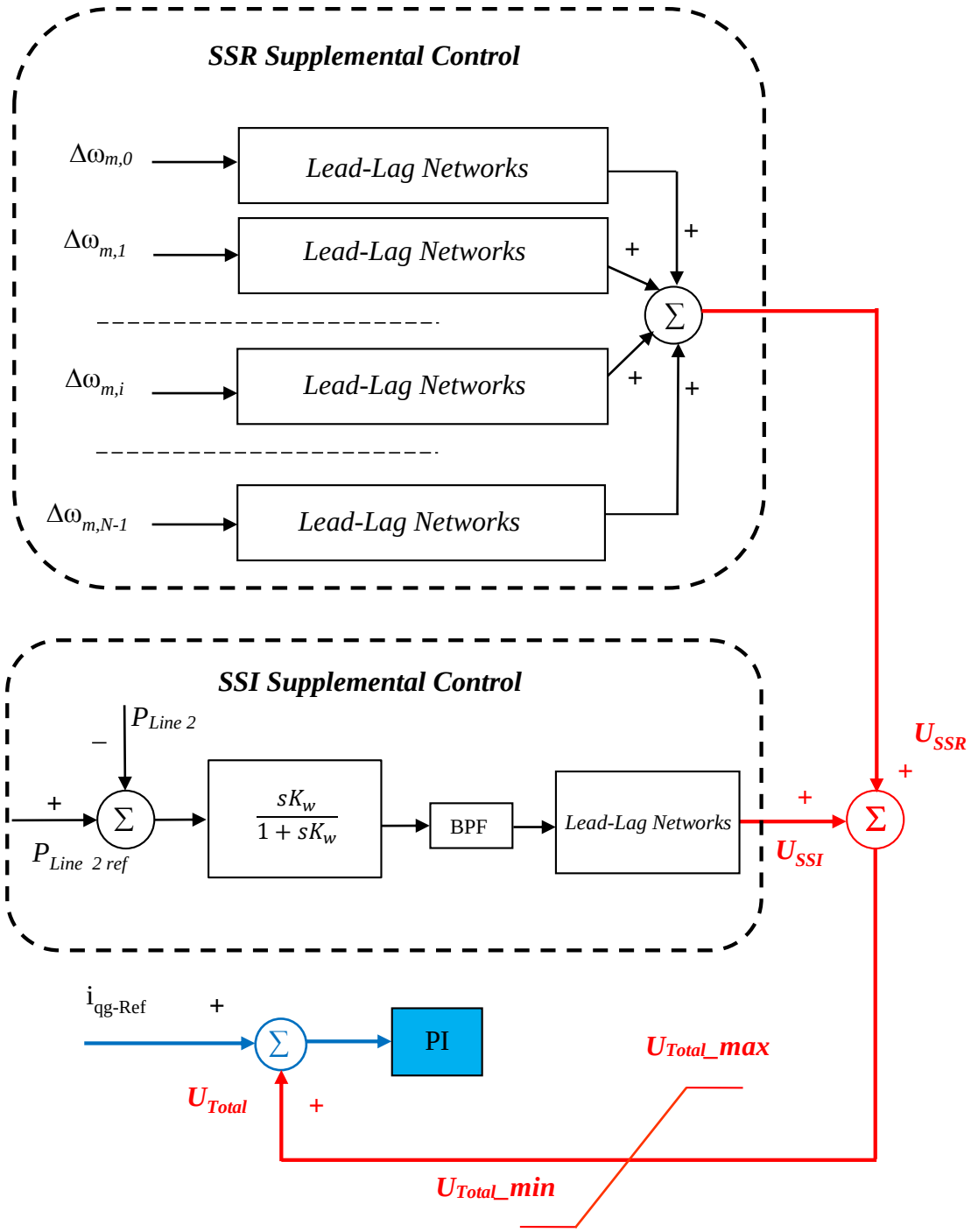

Figure 3.3: Supplemental control 1.

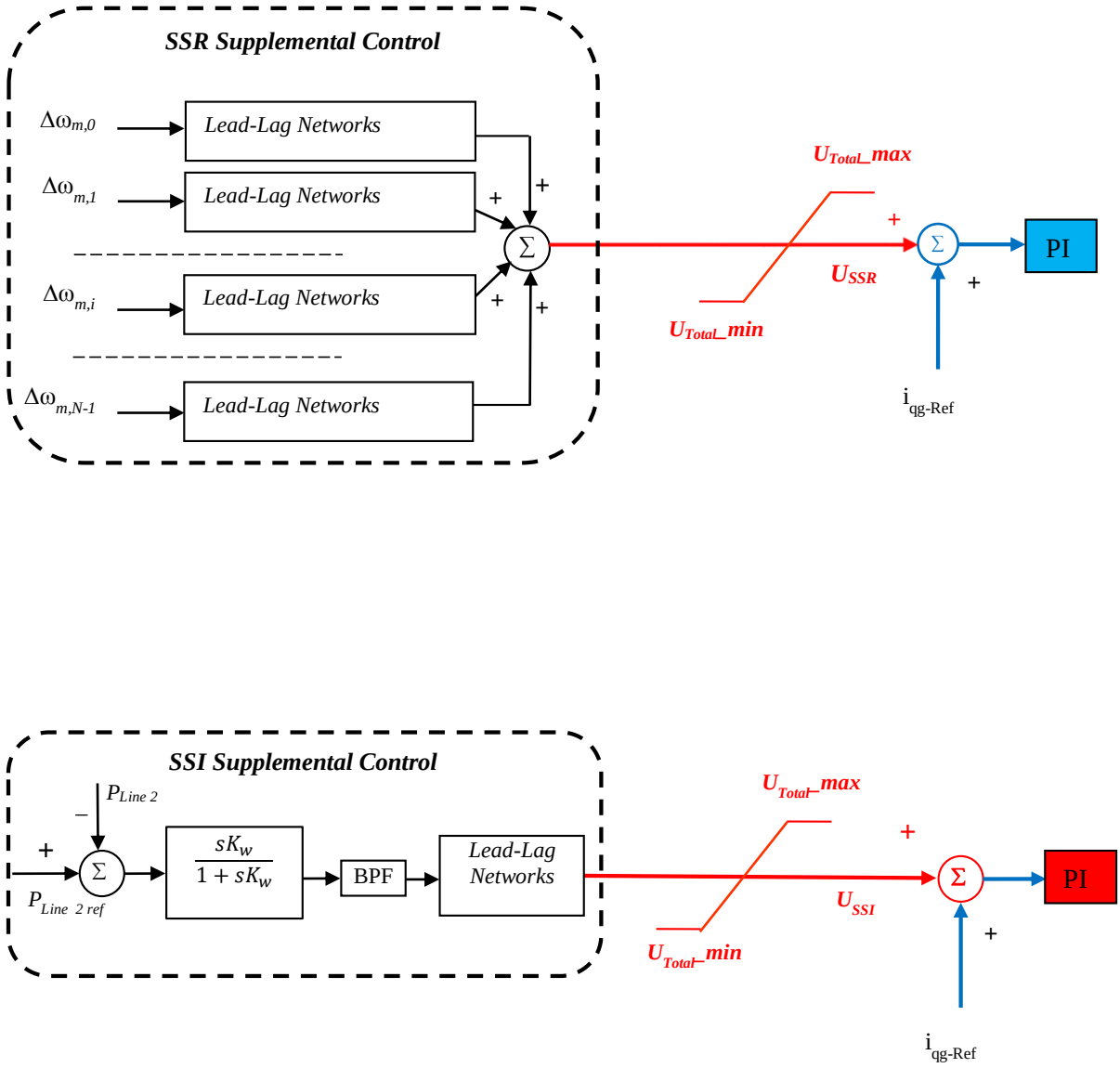

Figure 3.4: Supplemental control 2.

The SSR supplemental control, shown in Figures 3.3 and 3.4 has N-channels (N is the number of turbine-generator shaft system rotating masses) that employ the modal speeds as control signals. These modal speeds are derived from the turbine-generator rotating mass speeds as [30], [31]:

$$[\Delta\omega_m] = [Q]^{-1}[\Delta\omega] \tag{3.1}$$

where, $\Delta\omega_m$ is the modal speed deviation matrix, Q is the eigenvector matrix and $\Delta\omega$ is the speed deviation matrix of the turbine-generator rotating masses. The rotating mass speeds can be obtained using torsional monitor. Each modal speed as presented is separately phase and gain adjusted to provide damping for its corresponding torsional mode. The phase compensations are provided as:

$$\emptyset_i = \frac{1+sT_{ai}}{1+sT_{bi}}, \quad \mathrm{i} = 0,1,\ldots,\mathrm{N}-1 \tag{3.2}$$

The values of the matrices Q for the two turbine-generator shaft systems are given in Appendix A. On the other hand, the SSI supplemental control, shown in Figures 3.3 and 3.4, is an m-stage lead-lag compensation controller incorporating wash-out (high-pass) and band-pass (BPF) filters and utilizes Line 2 real power flow as a control signal.

In Supplemental control 1, a central controller located in wind farm B accepts the remote input signals and sends an output signal U_S to each FFC wind turbine. On the other hand, in Supplemental control 2, there are two central controllers located in wind farms A and B. The central controller in wind farm A accepts a local input signal (Line 2 real power flow) and sends output signal $U_S = U_{SSI}$ to each DFIG wind turbine. The other central controller accepts the remote signals (turbine-generator shaft rotating mass speeds) and sends an output signal $U_S = U_{SSI}$ to each FFC wind turbine. In the investigations reported in this thesis, it is presumed the accessibility of a wide-area network of synchronized phasor measurement units where the supplemental control input signals can be downloaded at the controller in real time without delay. Nevertheless, incorporating the effect of the time delay in computing the phasor quantities and the variable communication network latency for a controller that uses remote synchrophasor data is achievable [32].

A trial-and-error approach is adopted in the investigations conducted in this thesis for

finding appropriate controller gains and time constants that result in an acceptable oscillations damping. The fine-tuning of the controller parameters is achieved by performing repetitive time-domain simulations to minimize the objective functions

$$C_{SSI} = \int_{T_C}^{T_F} (\Delta Y')^2 \mathrm{dt} \tag{3.3}$$

and

$$C_{SSR} = \int_{T_C}^{T_F} \sum_{i=0}^{N-1} \left(\Delta\omega_{m,i}\right)^2 dt \tag{3.4}$$

where T_C is the fault clearing time, T_F is the total simulation time and $\Delta Y'$ is the output of the band pass filters in the controller. The design of optimal supplemental controls using nonlinear control techniques, such as indirect adaptive control, is out of scope of this thesis.

3.3 Performance of Supplemental Control 1 in damping SSR and SSI Oscillations

Figure 3.5 shows the turbine-generator shaft torsional torque time responses during and after clearing a ***3-cycle, three-phase fault on line 5*** for the case when the supplemental control is not activated. Figures 3.6 and 3.7 illustrate respectively the time responses of wind farms A and B active and reactive powers, terminal voltage and the BtB dc voltage for the same case. It can be seen from Figure 3.5 that, at the 60% compensation degree of lines 1 and 2, the turbine-generator shaft torsional torques endure torsional instability. It can also be seen from Figures 3.6 and 3.7 that SSI, which is due to the induction generator effect, is clearly present in wind farm A and that the adverse effects of the simultaneous existence of SSR and SSI extend their impact to the FFC wind farm (wind farm B) performance.

For a clear insight of the excited SSR and SSI mode components and the effectiveness of the supplemental controllers in decreasing these components, Figure 3.8 shows the frequency spectrums of the stator current of the DFIG wind turbines and the turbine-generator shaft torsional torques. It can be seen from Figure 3.8 that the stator current contains frequency components (electrical modes) of 10.37 Hz, 14.8 Hz, 35.09 Hz, 60 Hz, 84.83 Hz, 109.86 Hz and 115.36 Hz. The complements (60 – 10.37 = 49.625 Hz, 60 – 14.8 = 45.2 Hz, 60 – 35.09 =24.91 Hz) of the three electrical modes excite SSI mode (24.5 Hz) as well as the three shaft torsional modes (24.65 Hz, 44.99 Hz, 51.1 Hz).

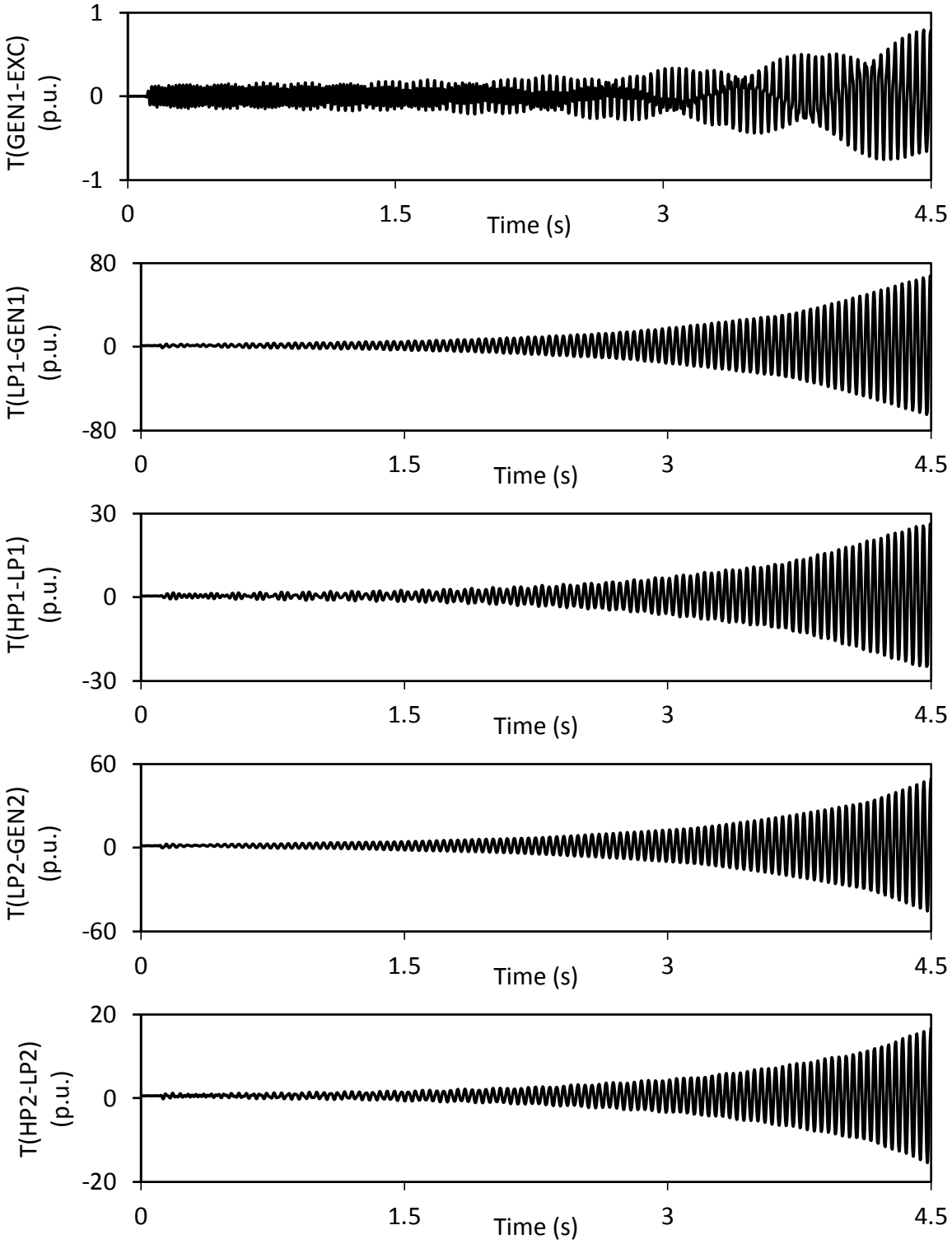

Figure 3.5: Turbine-generator shaft torsional torques during and after clearing a 3-cycle, three-phase fault on Line 5 (60% compensation degree, supplemental control 1 is not activated, wind farm B rating = 200 MW).

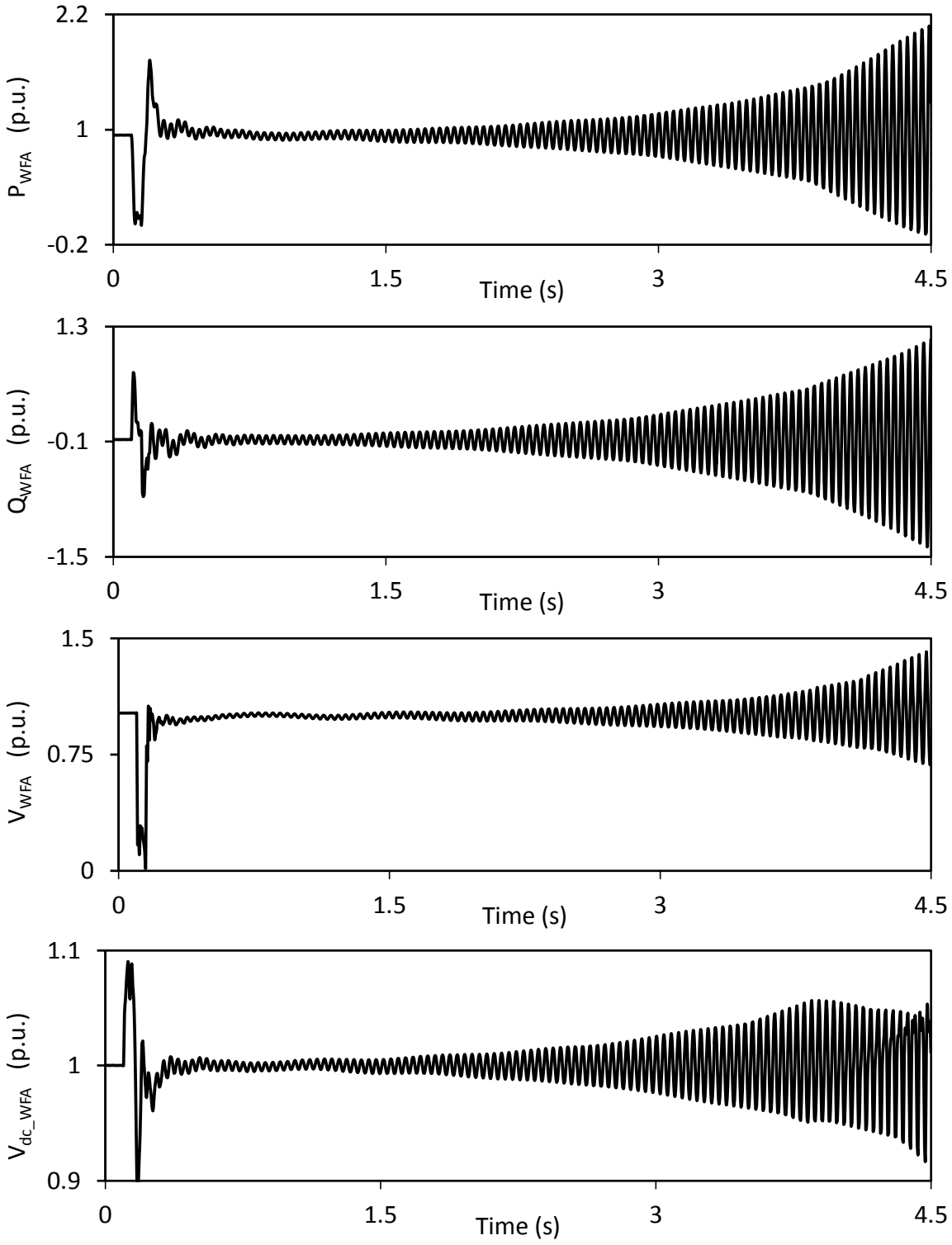

Figure 3.6: Wind farm A real and reactive powers, terminal voltage and dc capacitor voltage during and after clearing a 3-cycle, three-phase fault on Line 5 (60% compensation degree, supplemental control 1 is not activated, wind farm B rating = 200 MW).

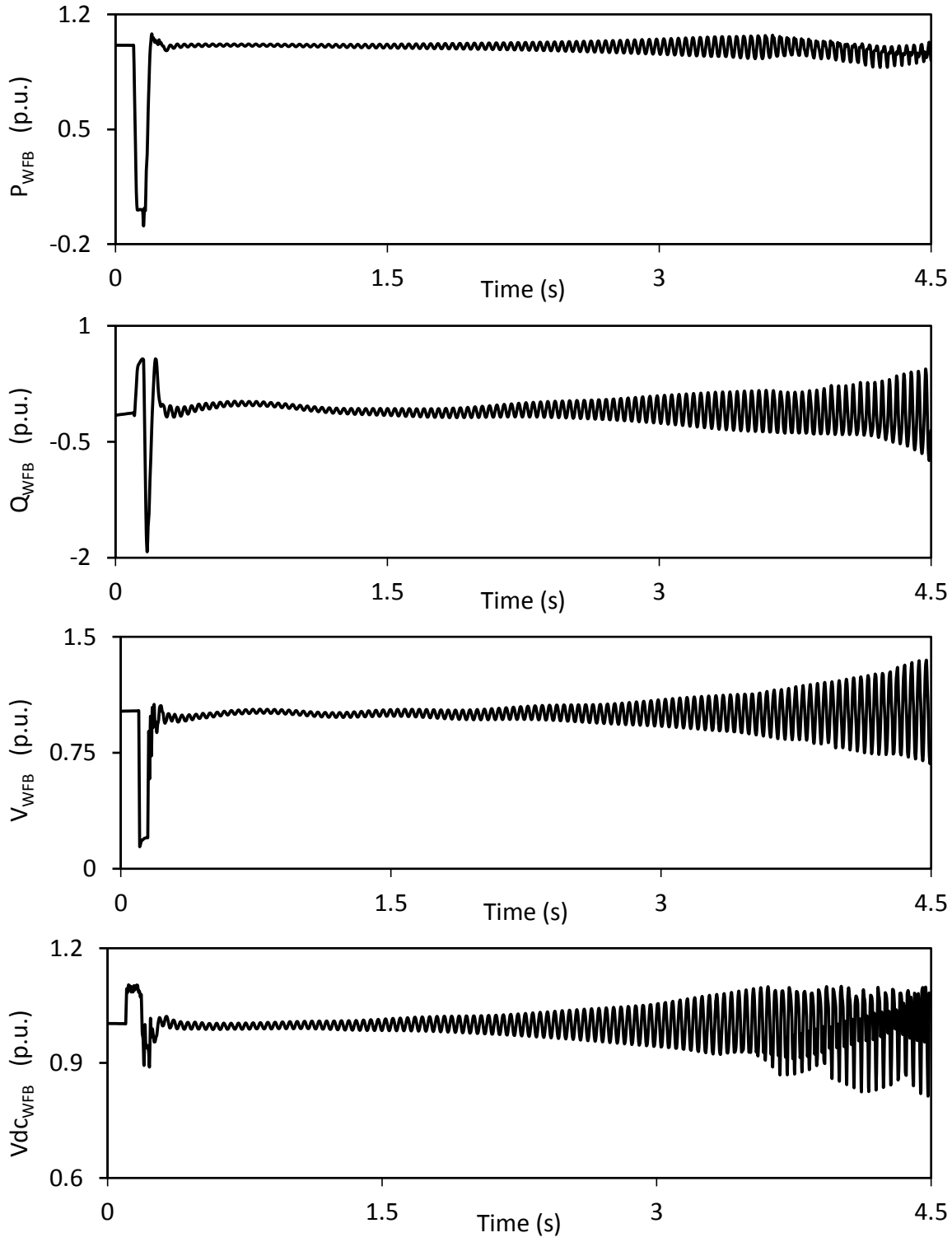

Figure 3.7: Wind farm B real and reactive powers, terminal voltage and dc capacitor voltage during and after clearing a 3-cycle, three-phase fault on Line 5 (60% compensation degree, supplemental control 1 is not activated, wind farm B rating = 200 MW).

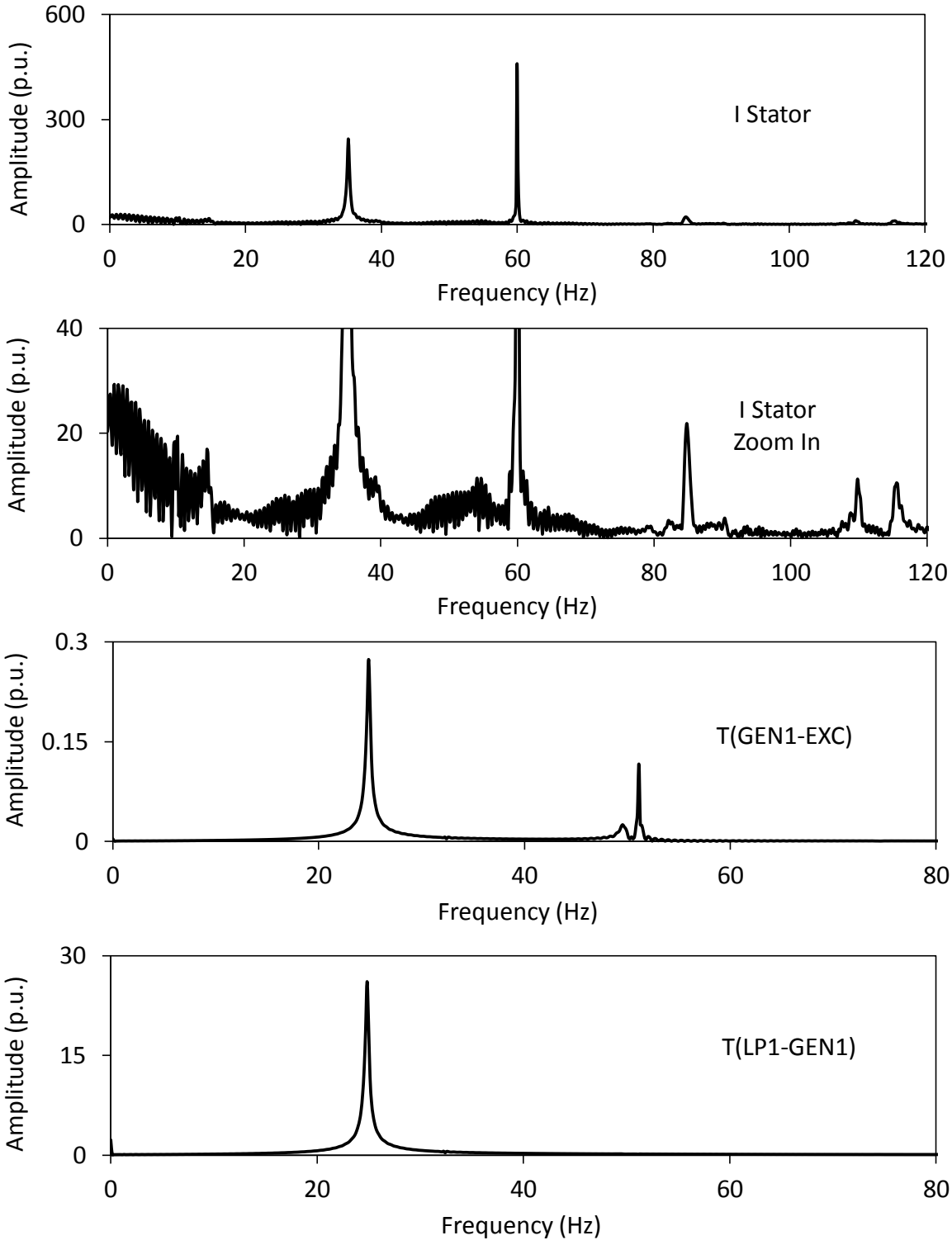

Figure 3.8: Frequency spectrums of the stator current of the DFIG wind turbine and the turbine-generator shaft torsional torques during and after clearing a 3-cycle, three-phase fault on Line 5 (60% compensation degree, supplemental control 1 is not activated, wind farm B rating = 200 MW).

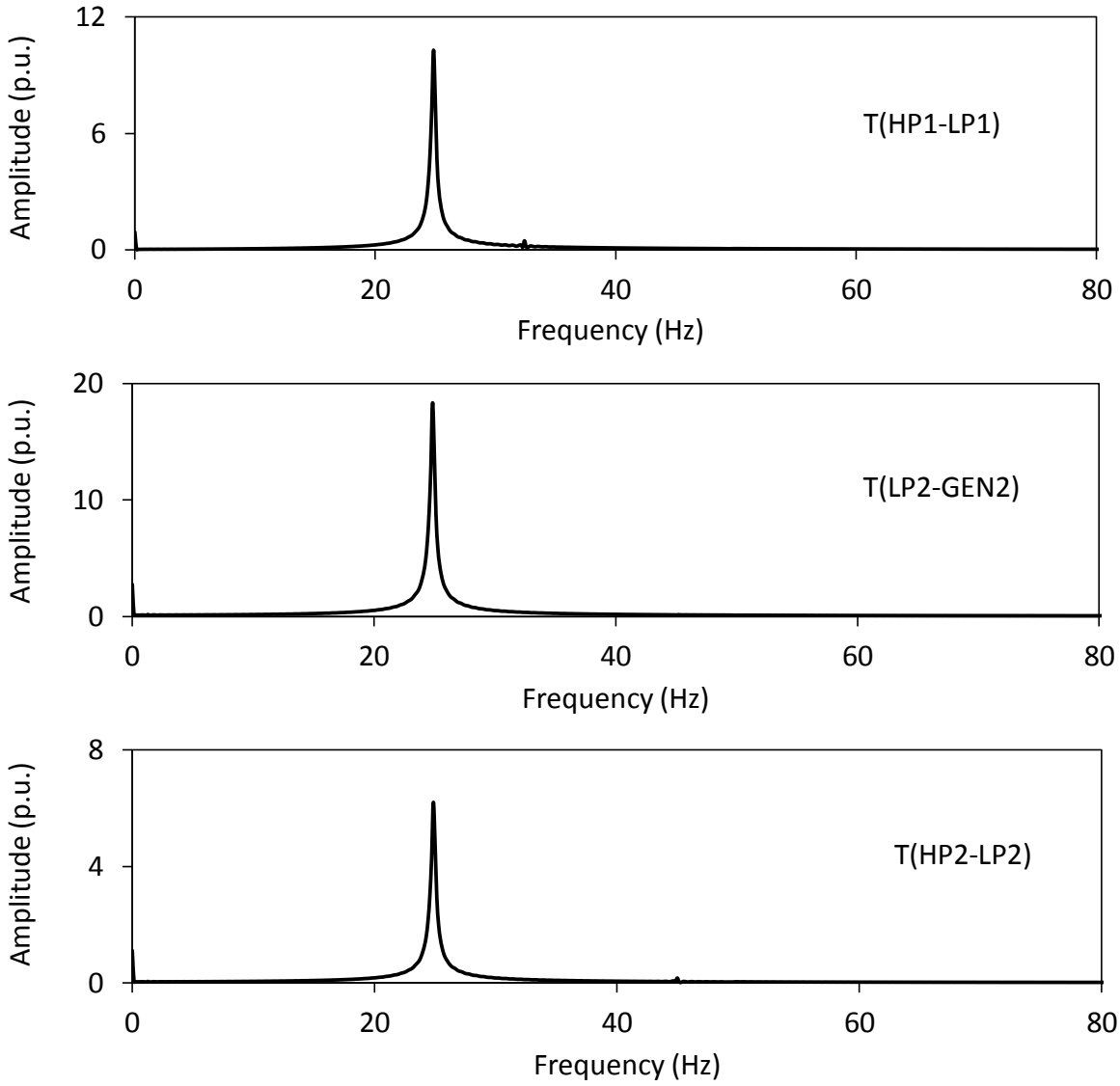

Figure 3.8: Continued.

Figure 3.9 shows turbine-generator shaft torsional torque time responses during and after clearing the same fault for the case when Supplemental control 1 is activated. Figures 3.10 and 3.11 illustrate respectively the time responses of wind farms A and B active and reactive powers, terminal voltage and the BtB dc voltage for the same case. Moreover, Figure 3.12 shows the frequency spectrums of the stator current of the DFIG wind turbines and the turbine-generator shaft torsional torques for the same study case. Furthermore, the transfer functions of Supplemental control 1 are given in Table 3.1. The comparison between the two groups of figures (Figures 3.5, 3.6, 3.7, 3.8) and (Figures 3.9, 3.10, 3.11, 3.12) establishes the effectiveness of Supplemental control 1 in damping the torsional torques in all turbine-generator shaft sections as well as in mitigating SSI in wind farm A. It can also be seen from Figures 3.10 that the dc chopper protection of FFC limits the dc bus voltage at 1.1 p.u.

Table 3.1: Transfer functions of Supplemental control 1 (Wind farm B rating = 200 MW, three-phase fault on Line 5).

Modal speeds	Transfer function
G1, $\Delta_{\omega m0}$	0
G1, $\Delta_{\omega m1}$	$G_{\omega_1}(s) = 2.5\frac{s+300}{s+1}$
G1, $\Delta_{\omega m2}$	$G_{\omega_2}(s) = -2.5\frac{s+1000}{s+1}$
G1, $\Delta_{\omega m3}$	$G_{\omega_3}(s) = 2.5\frac{s+1000}{s+1}$
G2, $\Delta_{\omega m0}$	0
G2, $\Delta_{\omega m1}$	$G_{\omega_1}(s) = 25\frac{s+250}{s+1}$
G2, $\Delta_{\omega m2}$	$G_{\omega_2}(s) = 25\frac{s+1250}{s+1}$
Washout filter	$G(s) = \frac{s}{s+10}$
Band-Pass filter	$G(s) = \frac{62.83s}{s^2+62.83s+35500}$
Lead-Lag compensator	$G(s) = \frac{s+250}{s+1}$
U_{Total_max}, U_{Total_min}	0.33, -0.33

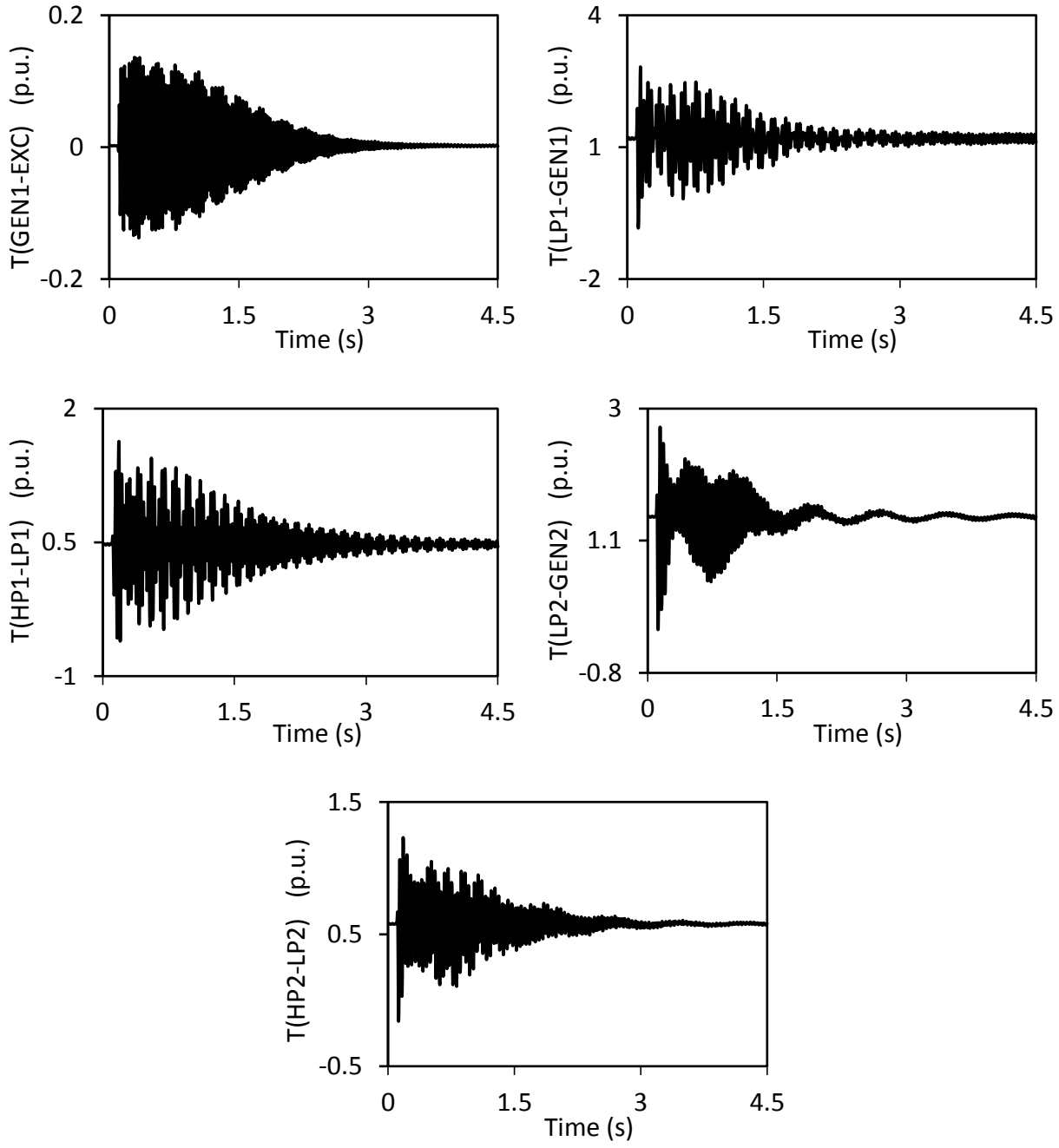

Figure 3.9: Turbine-generator shaft torsional torques during and after clearing a 3-cycle, three-phase fault on Line 5 (60% compensation degree, supplemental control 1 is activated, wind farm B rating = 200 MW).

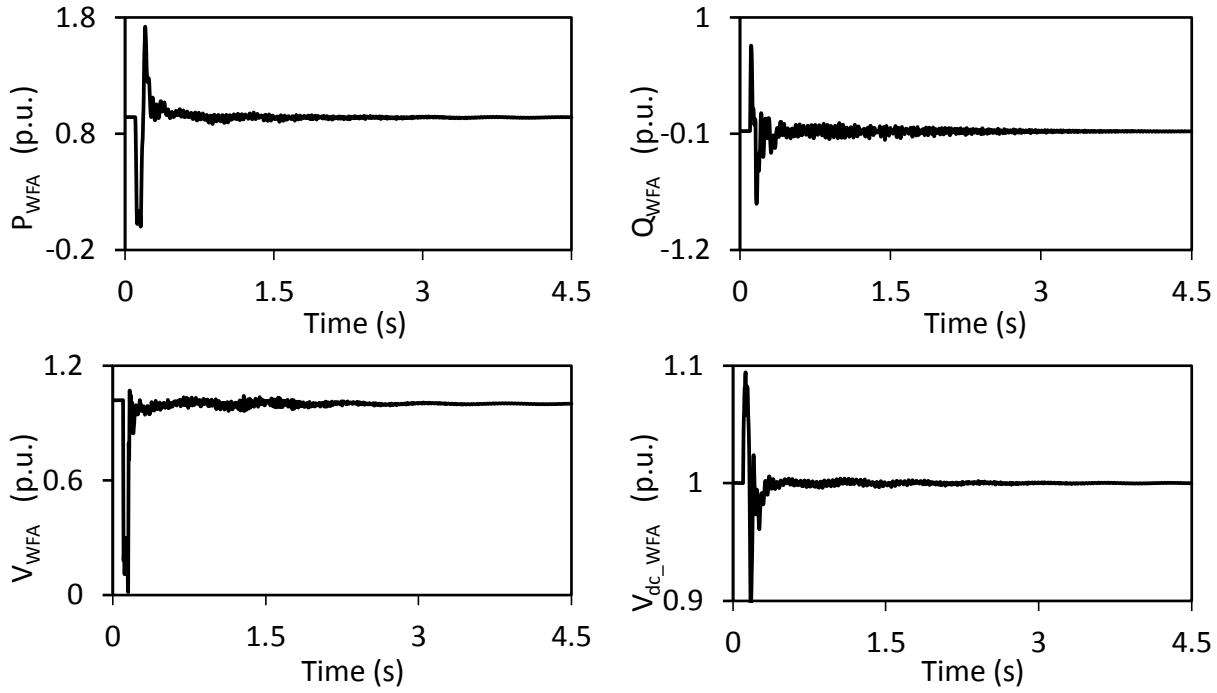

Figure 3.10: Wind farm A real and reactive powers, terminal voltage and dc capacitor voltage during and after clearing a 3-cycle, three-phase fault on Line 5 (60% compensation degree, supplemental control 1 is activated, wind farm B rating = 200 MW).

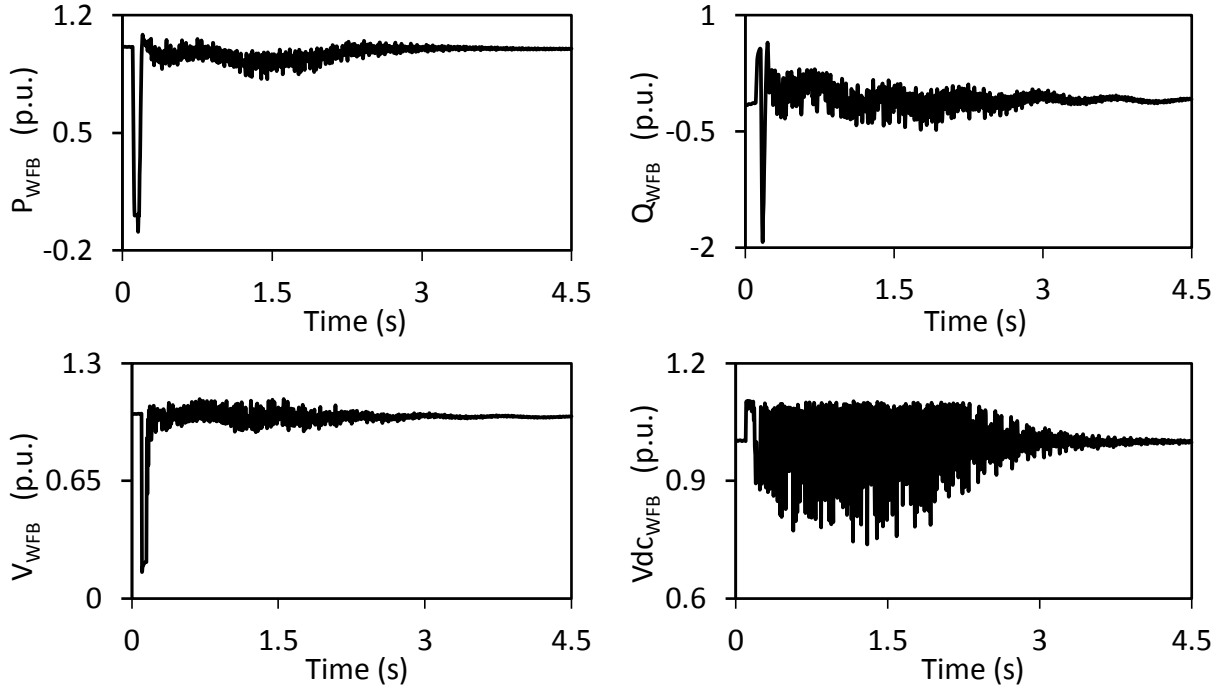

Figure 3.11: Wind farm B real and reactive powers, terminal voltage and dc capacitor voltage during and after clearing a 3-cycle, three-phase fault on Line 5 (60% compensation degree, supplemental control 1 is activated, wind farm B rating = 200 MW).

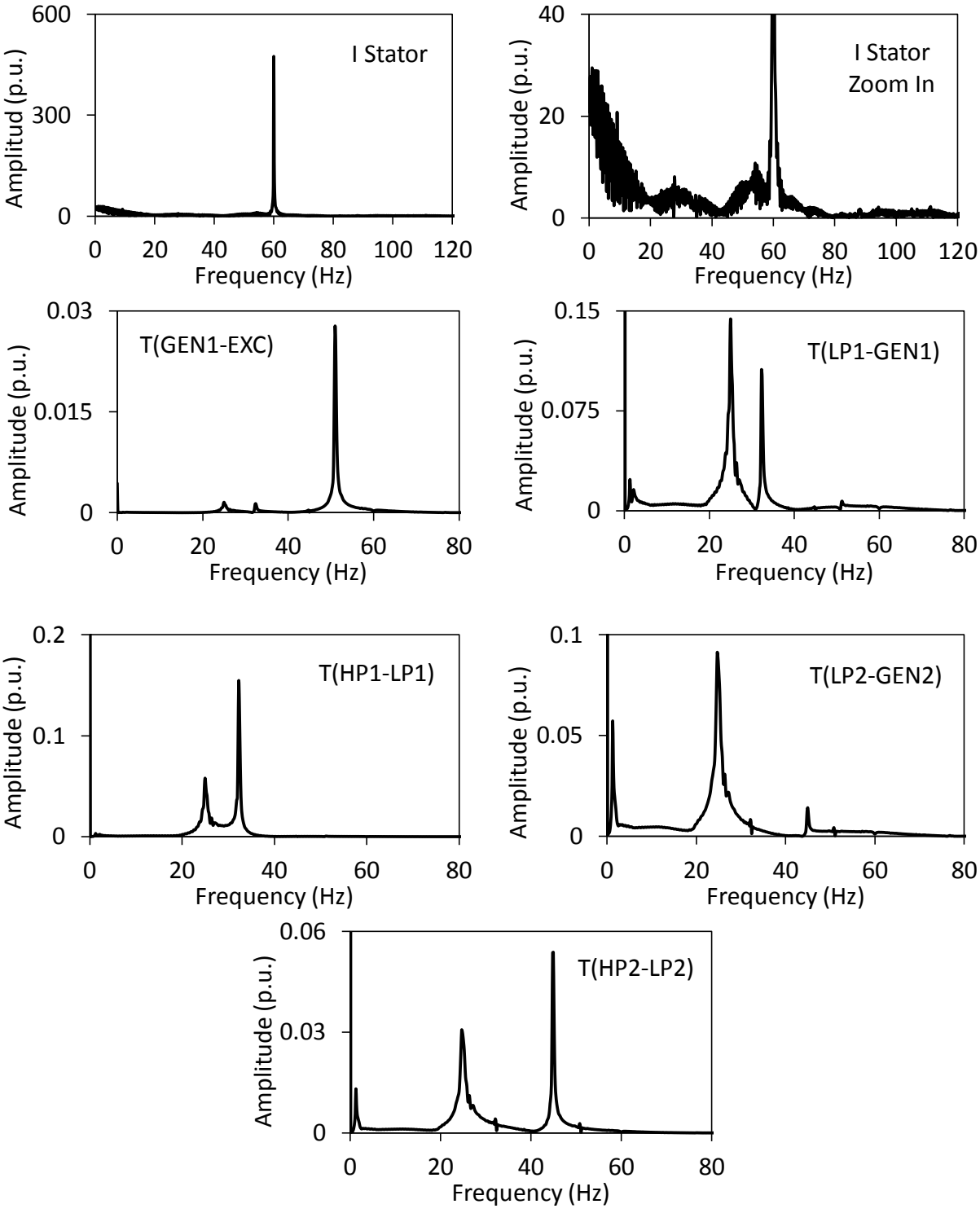

Figure 3.12: Frequency spectrums of the stator current of the DFIG wind turbine and the turbine-generator shaft torsional torques during and after clearing a 3-cycle, three-phase fault on Line 5 (60% compensation degree, supplemental control 1 is activated, wind farm B rating = 200 MW).

3.3.1 Effect of the distance between wind farm B and the turbine-generators

The effect of the distance between wind farm B and the turbine-generators on the performance of Supplemental control 1, especially in mitigating SSR, is examined by changing the length of transmission Line 3. The results of this study are presented in the following three groups of figures:

Group A: Line 3 = 50 km, (Figures 3.13, 3.14, 3.15, 3.16, 3.17, 3.18, 3.19, 3.20)

Group B: Line 3 = 100 km, (Figures 3.21, 3.22, 3.23, 3.24, 3.25, 3.26, 3.27, 3.28)

Group C: Line 3 = 200 km, (Figures 3.29, 3.30, 3.31, 3.32, 3.33, 3.34, 3.35, 3.36)

In each group, the turbine-generator shaft torsional torques, wind farms A and B active and reactive powers, terminal voltage and the BtB dc voltage as well as the frequency spectrums of the stator current of the DFIG wind turbines and the turbine-generator shaft torsional torques are shown for the cases when Supplemental control 1 is disabled and activated respectively. Moreover, the transfer functions of Supplemental control 1 in Groups A and C are given in Tables 3.2 and 3.3 respectively. The transfer functions of Supplemental control 1 in Group B are the same as those in Table 3.1.

Table 3.2: Transfer functions of Supplemental control 1 for Group A (Line 3 length = 50 km).

Modal speeds	Transfer function
G1, $\Delta_{\omega m0}$	0
G1, $\Delta_{\omega m1}$	$G_{\omega_1}(s) = 15\dfrac{s+300}{s+1}$
G1, $\Delta_{\omega m2}$	$G_{\omega_2}(s) = -2.5\dfrac{s+1000}{10s+1}$
G1, $\Delta_{\omega m3}$	$G_{\omega_3}(s) = 2.5\dfrac{s+500}{s+1}$
G2, $\Delta_{\omega m0}$	0
G2, $\Delta_{\omega m1}$	$G_{\omega_1}(s) = 25\dfrac{10s+250}{s+1}$
G2, $\Delta_{\omega m2}$	$G_{\omega_2}(s) = 25\dfrac{s+1250}{s+0.1}$
Washout filter	$G(s) = \dfrac{s}{s+10}$

Band-Pass filter	$G(s) = \frac{62.83s}{s^2 + 62.83s + 35500}$
Lead-Lag compensator	$G(s) = \frac{s + 250}{s + 1}$
U_{Total_max}, U_{Total_min}	0.33, -0.33

Table 3.3: Transfer functions of Supplemental control 1 for Group C (Line 3 length = 200 km).

Modal speeds	Transfer function
G1, $\Delta_{\omega m0}$	0
G1, $\Delta_{\omega m1}$	$G_{\omega_1}(s) = 2.5\frac{10s + 300}{s + 1}$
G1, $\Delta_{\omega m2}$	$G_{\omega_2}(s) = -2.5\frac{s + 1000}{s + 1}$
G1, $\Delta_{\omega m3}$	$G_{\omega_3}(s) = 2.5\frac{10s + 300}{s + 1}$
G2, $\Delta_{\omega m0}$	0
G2, $\Delta_{\omega m1}$	$G_{\omega_1}(s) = 25\frac{50s + 250}{10s + 1}$
G2, $\Delta_{\omega m2}$	$G_{\omega_2}(s) = 25\frac{0.1s + 1250}{s + 1}$
Washout filter	$G(s) = \frac{s}{s + 10}$
Band-Pass filter	$G(s) = \frac{62.83s}{s^2 + 62.83s + 35500}$
Lead-Lag compensator	$G(s) = \frac{s + 250}{s + 1}$
U_{Total_max}, U_{Total_min}	0.33, -0.33

The comparisons between the two sets of figures in Group A, B and C (Set 1: Supplemental control 1 is disabled and Set 2: Supplemental control 1 is activated; e.g. Figures 3.13, 3.14, 3.15, 3.16 and Figures 3.17, 3.18 3.19 and 3.20 in Group A) demonstrate the effectiveness of the supplemental control in mitigating SSR and SSI when it is located at different distances from the turbine-generators and wind farm A.

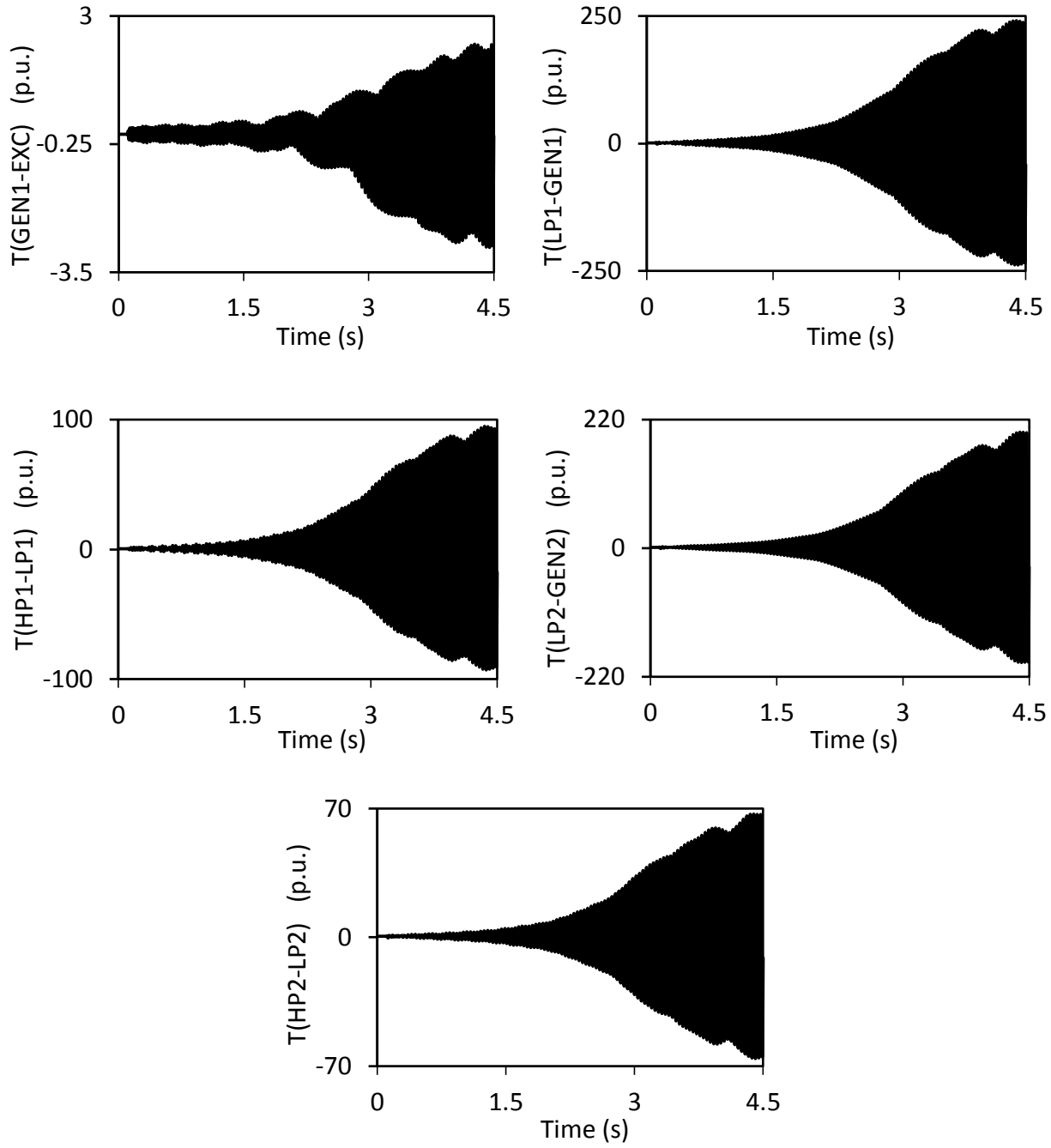

Figure 3.13: Turbine-generator shaft torsional torques during and after clearing a 3-cycle, three-phase fault on Line 5 (60% compensation degree, supplemental control 1 is not activated, Line 3 length = 50 km).

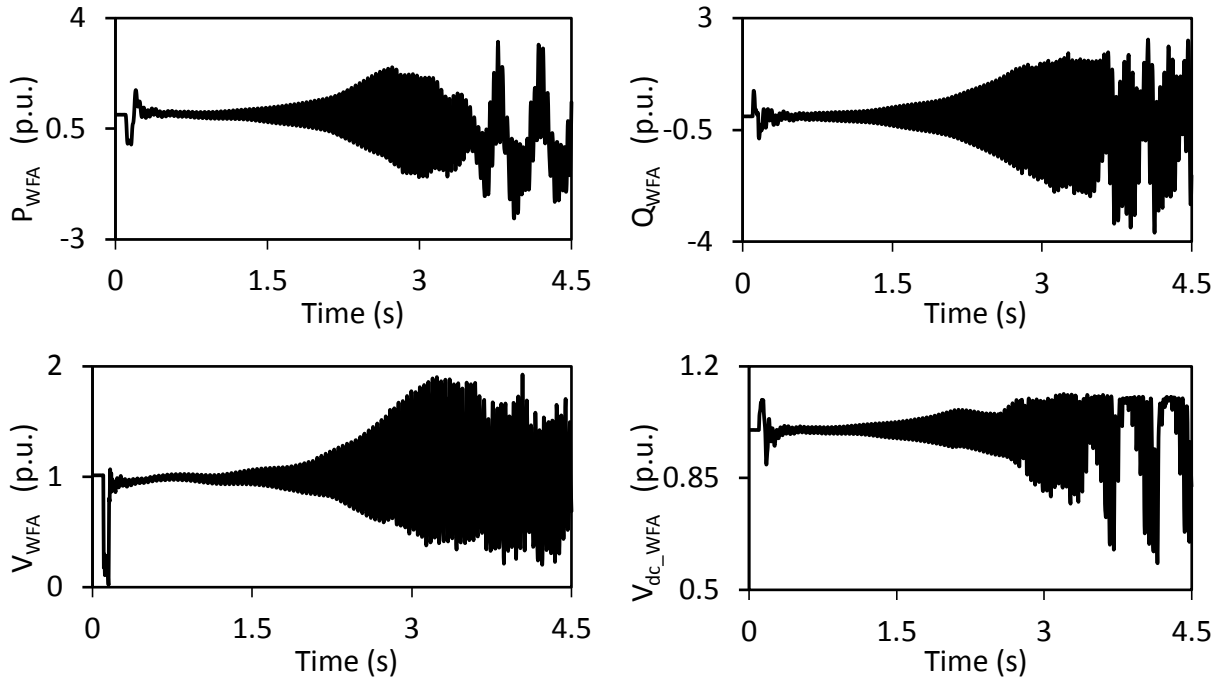

Figure 3.14: Wind farm A real and reactive powers, terminal voltage and dc capacitor voltage during and after clearing a 3-cycle, three-phase fault on Line 5 (60% compensation degree, supplemental control 1 is not activated, Line 3 length = 50 km).

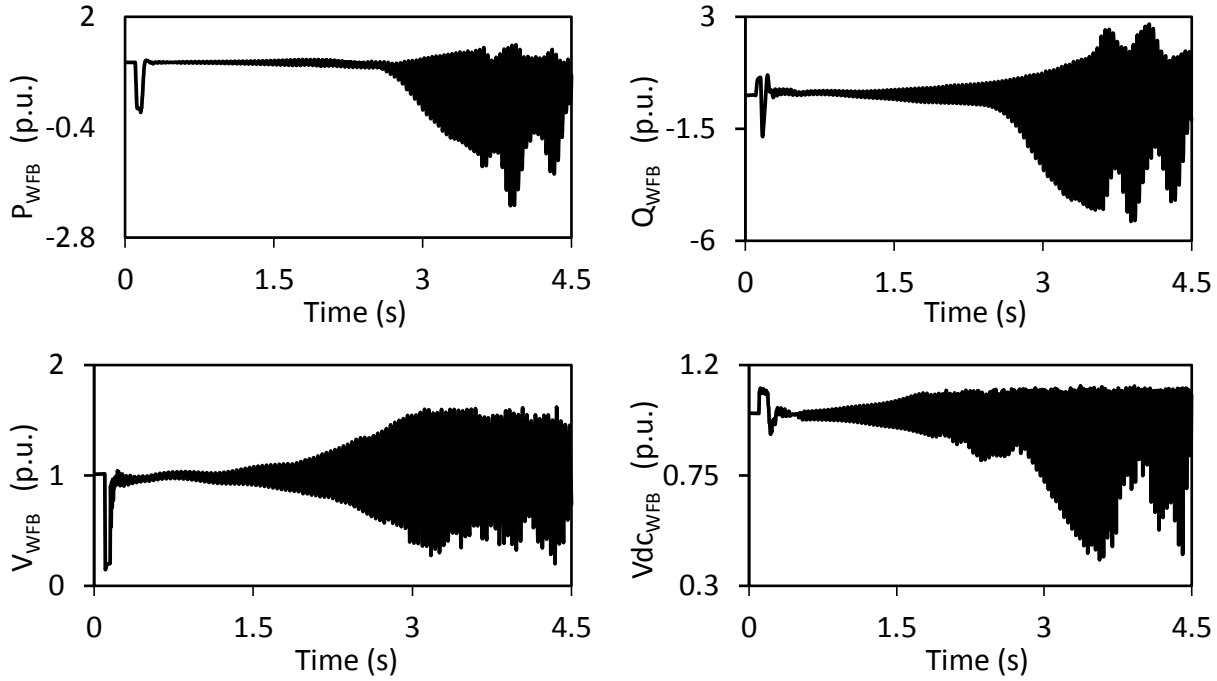

Figure 3.15: Wind farm B real and reactive powers, terminal voltage and dc capacitor voltage during and after clearing a 3-cycle, three-phase fault on Line 5 (60% compensation degree, supplemental control 1 is not activated, Line 3 length = 50 km).

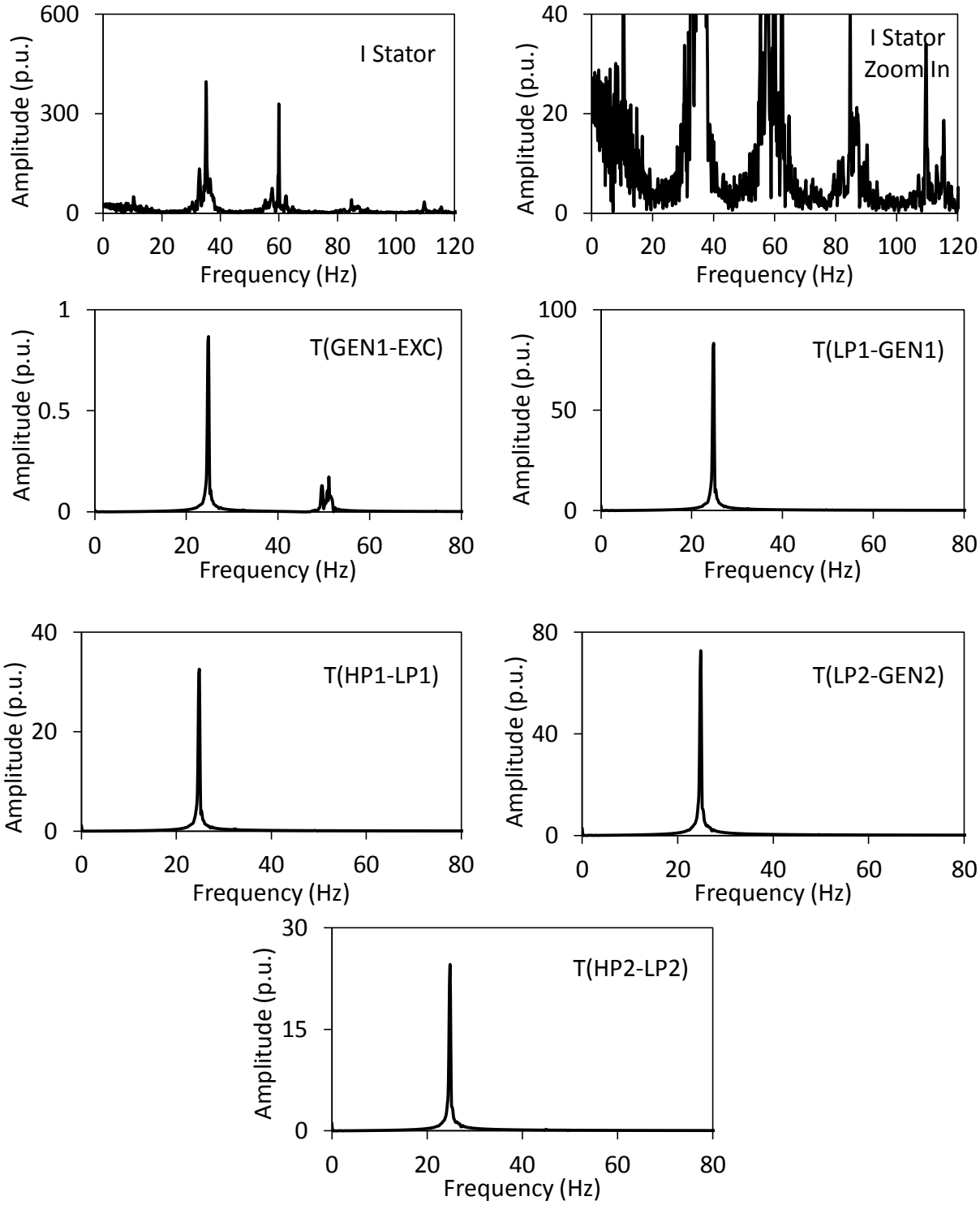

Figure 3.16: Frequency spectrums of the stator current of the DFIG wind turbine and the turbine-generator shaft torsional torques during and after clearing a 3-cycle, three-phase fault on Line 5 (60% compensation degree, supplemental control 1 is not activated, Line 3 length = 50 km).

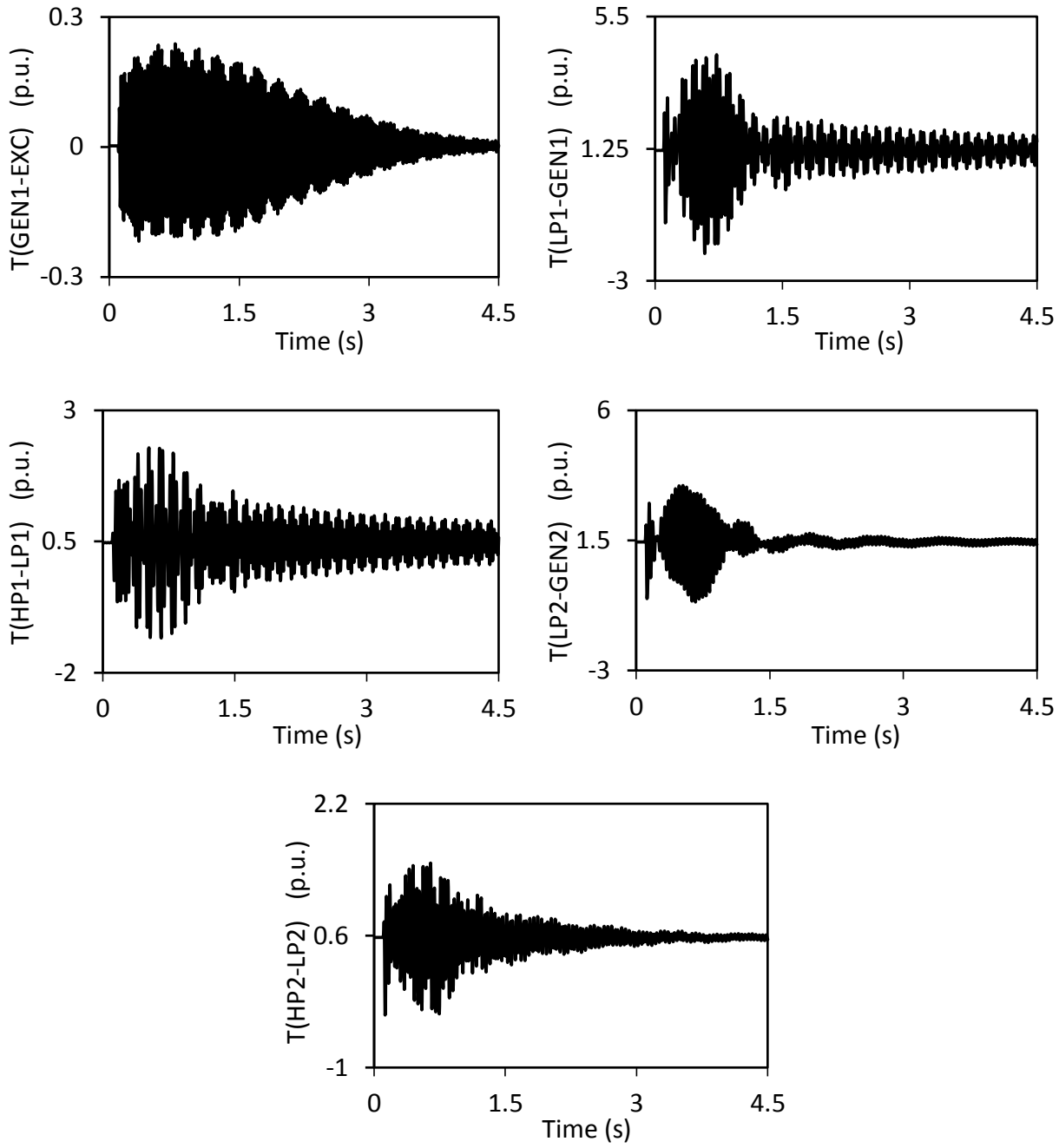

Figure 3.17: Turbine-generator shaft torsional torques during and after clearing a 3-cycle, three-phase fault on Line 5 (60% compensation degree, supplemental control 1 is activated, Line 3 length = 50 km).

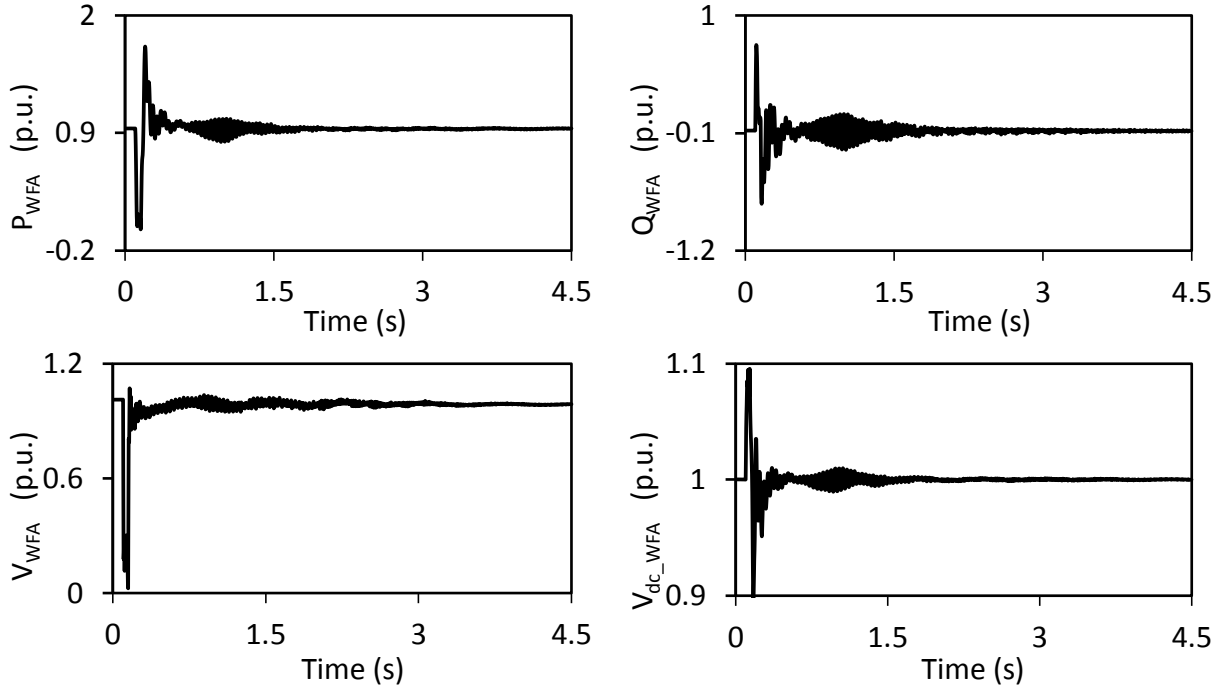

Figure 3.18: Wind farm A real and reactive powers, terminal voltage and dc capacitor voltage during and after clearing a 3-cycle, three-phase fault on Line 5 (60% compensation degree, supplemental control 1 is activated, Line 3 length = 50 km).

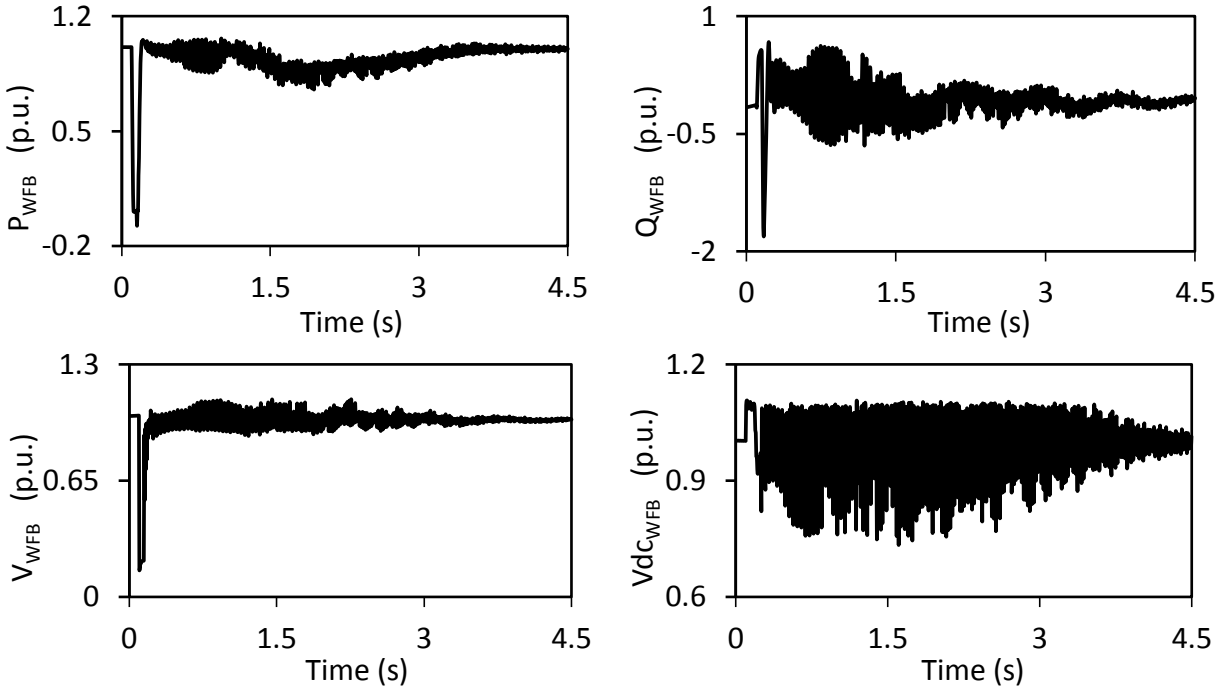

Figure 3.19: Wind farm B real and reactive powers, terminal voltage and dc capacitor voltage during and after clearing a 3-cycle, three-phase fault on Line 5 (60% compensation degree, supplemental control 1 is activated, Line 3 length = 50 km).

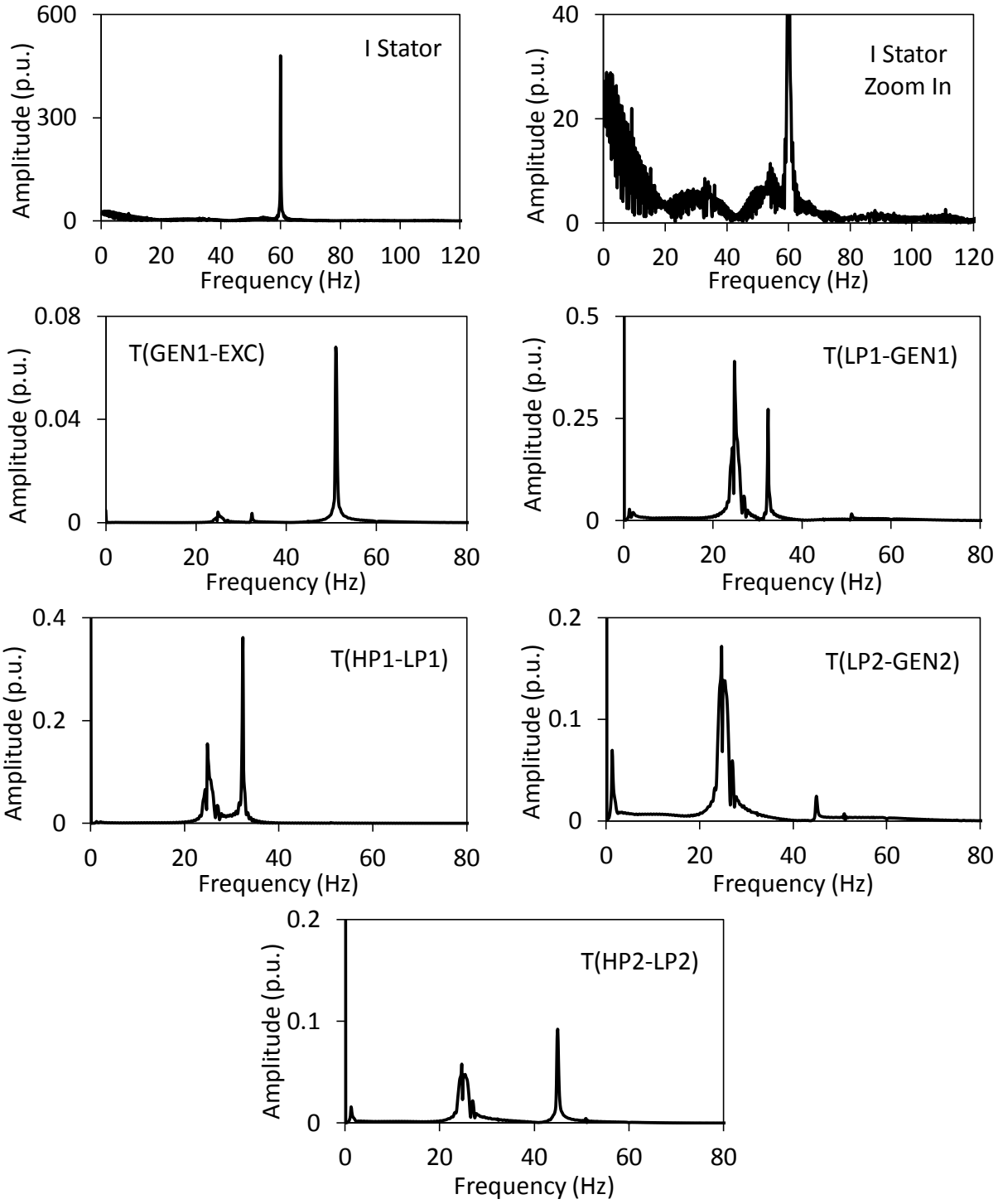

Figure 3.20: Frequency spectrums of the stator current of the DFIG wind turbine and the turbine-generator shaft torsional torques during and after clearing a 3-cycle, three-phase fault on Line 5 (60% compensation degree, supplemental control 1 is activated, Line 3 length = 50 km).

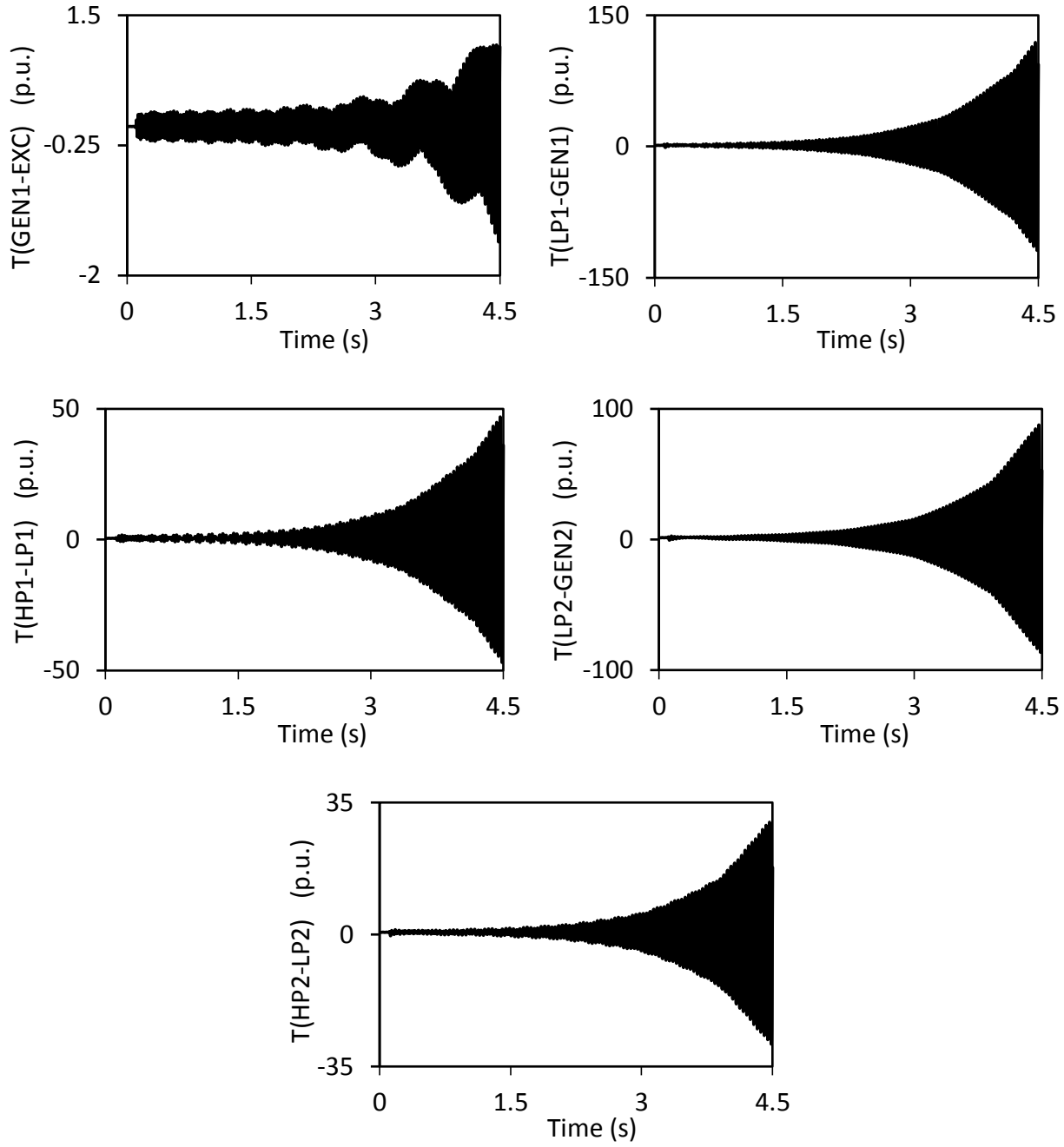

Figure 3.21: Turbine-generator shaft torsional torques during and after clearing a 3-cycle, three-phase fault on Line 5 (60% compensation degree, supplemental control 1 is not activated, Line 3 length = 100 km).

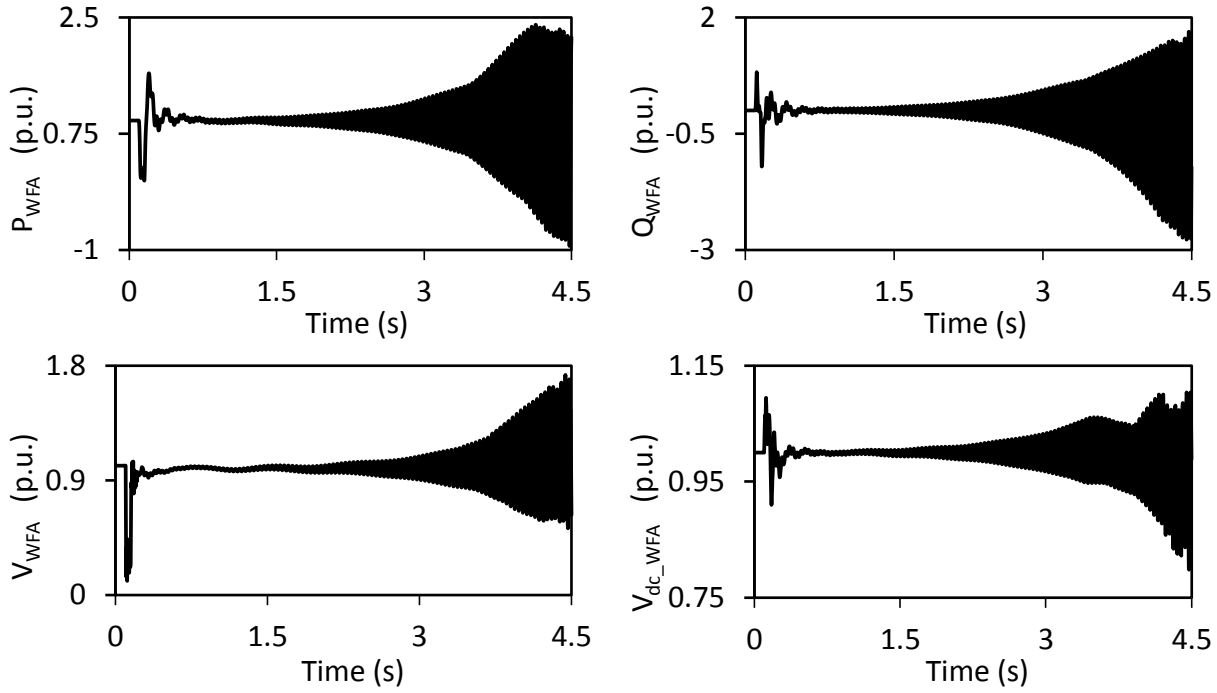

Figure 3.22: Wind farm A real and reactive powers, terminal voltage and dc capacitor voltage during and after clearing a 3-cycle, three-phase fault on Line 5 (60% compensation degree, supplemental control 1 is not activated, Line 3 length = 100 km).

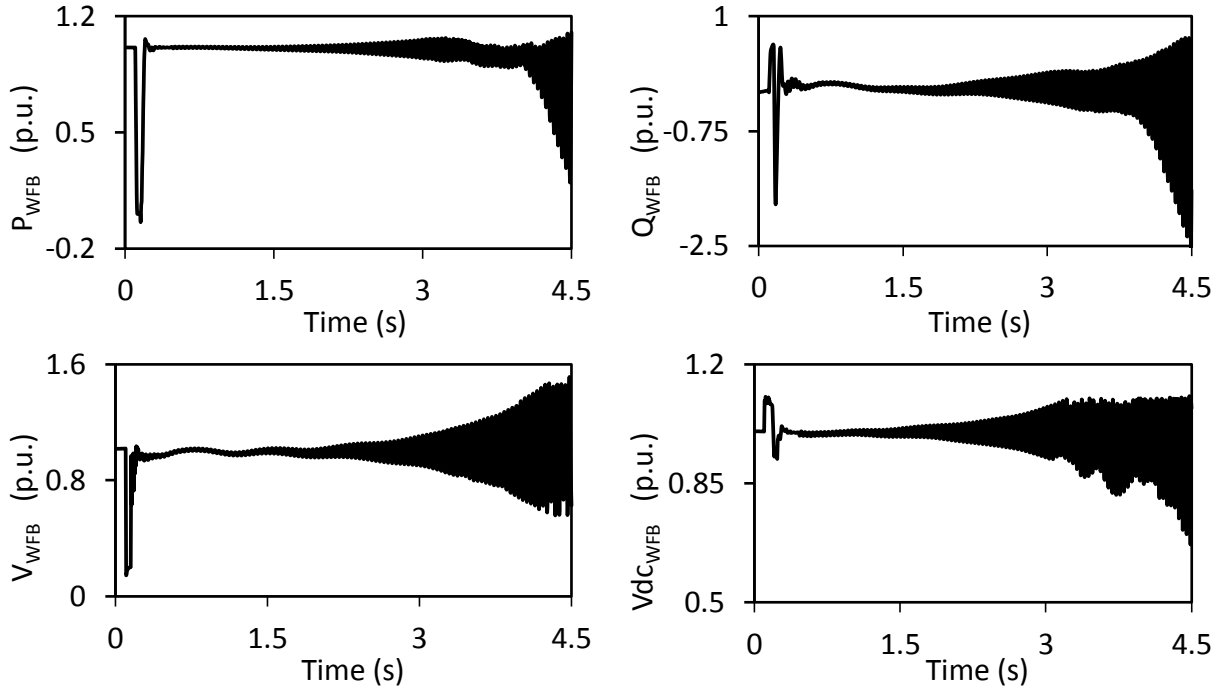

Figure 3.23: Wind farm B real and reactive powers, terminal voltage and dc capacitor voltage during and after clearing a 3-cycle, three-phase fault on Line 5 (60% compensation degree, supplemental control 1 is not activated, Line 3 length = 100 km).

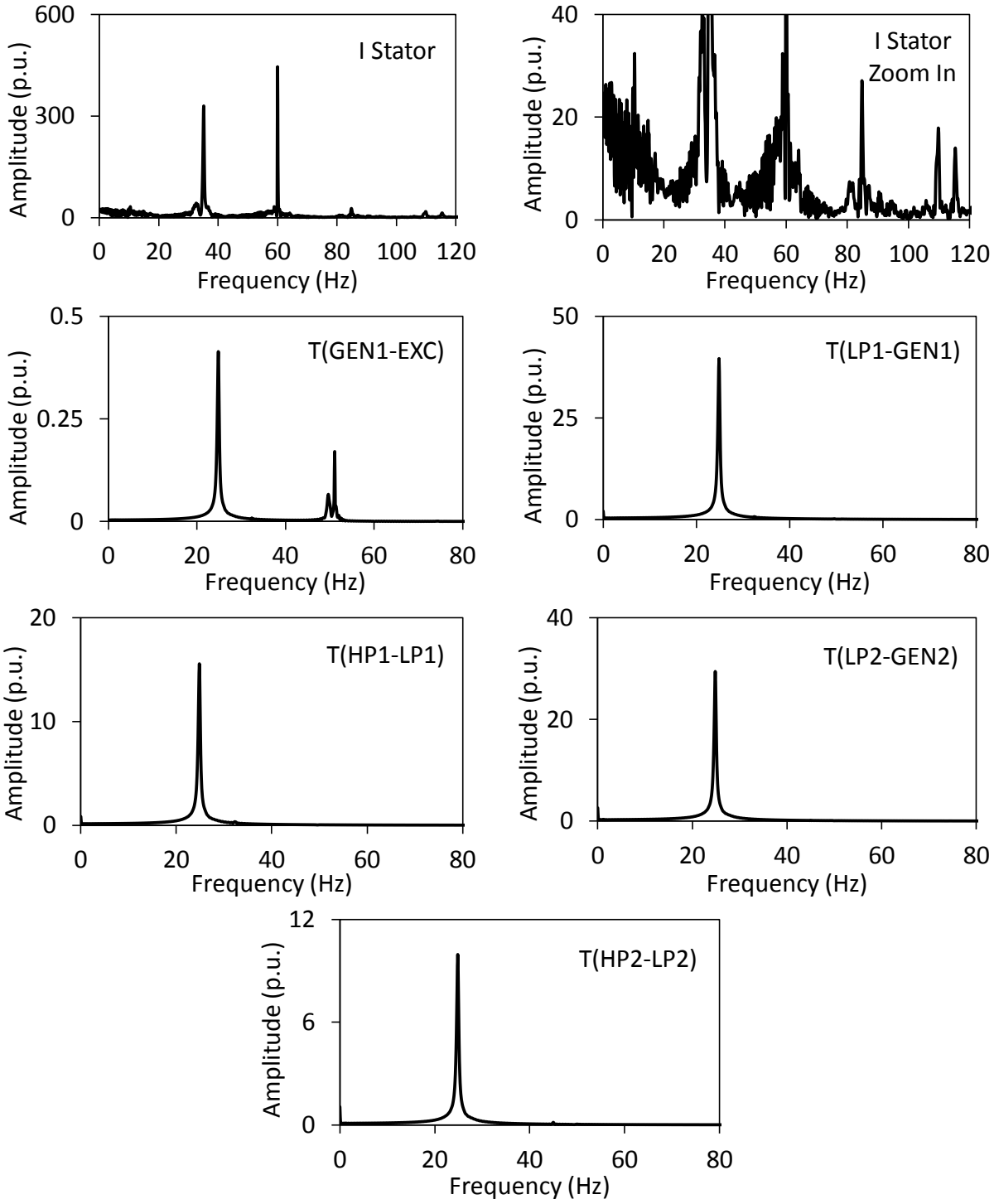

Figure 3.24: Frequency spectrums of the stator current of the DFIG wind turbine and the turbine-generator shaft torsional torques during and after clearing a 3-cycle, three-phase fault on Line 5 (60% compensation degree, supplemental control 1 is not activated, Line 3 length = 100 km).

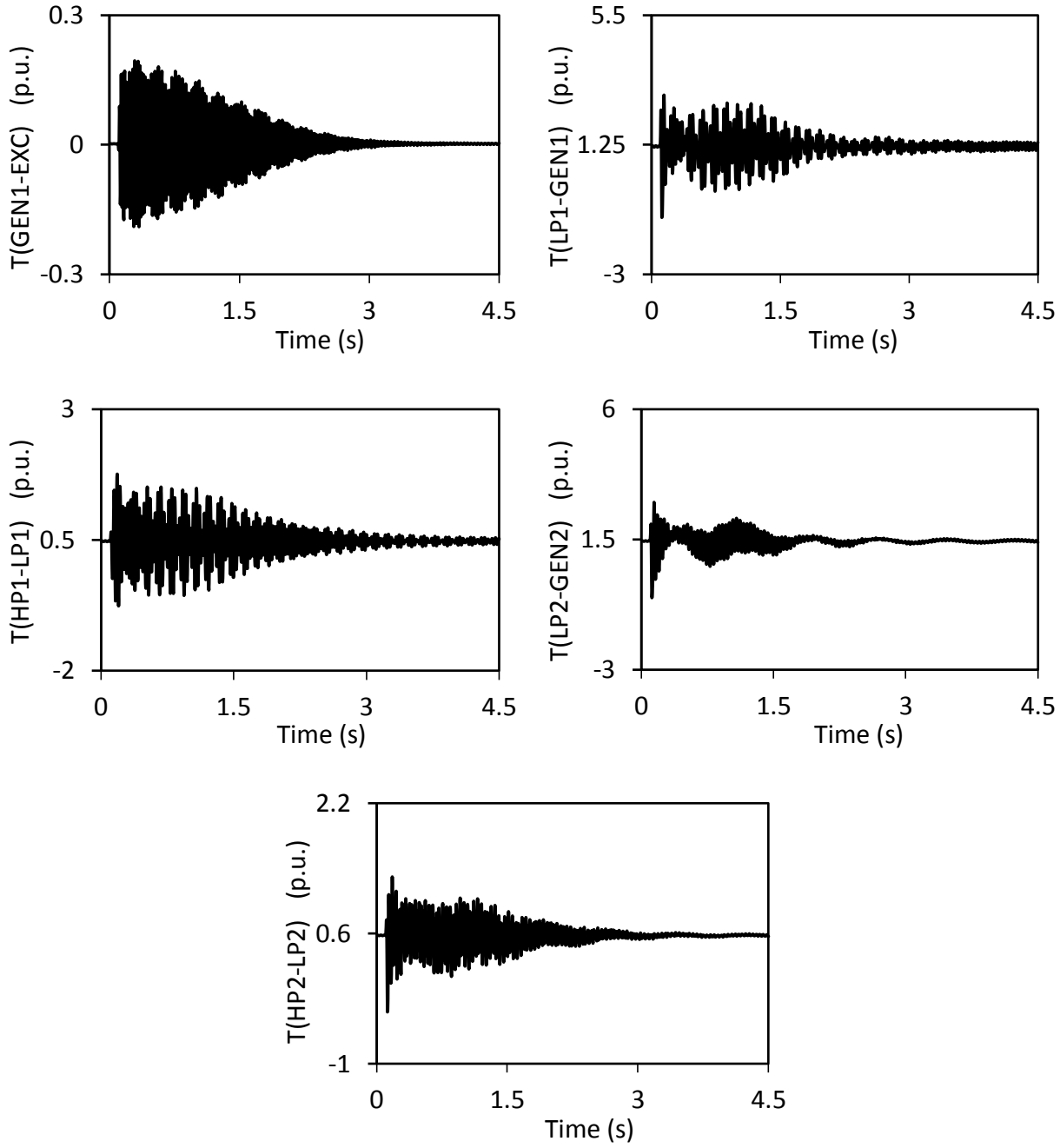

Figure 3.25: Turbine-generator shaft torsional torques during and after clearing a 3-cycle, three-phase fault on Line 5 (60% compensation degree, supplemental control 1 is activated, Line 3 length = 100 km).

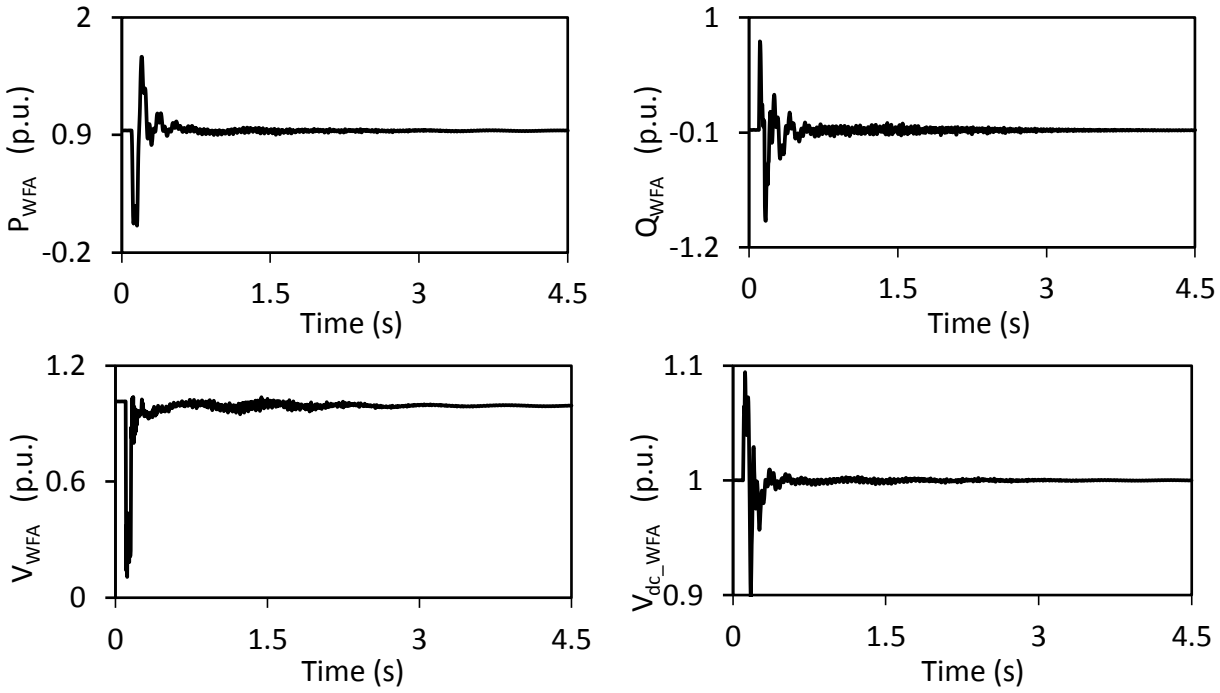

Figure 3.26: Wind farm A real and reactive powers, terminal voltage and dc capacitor voltage during and after clearing a 3-cycle, three-phase fault on Line 5 (60% compensation degree, supplemental control 1 is activated, Line 3 length = 100 km).

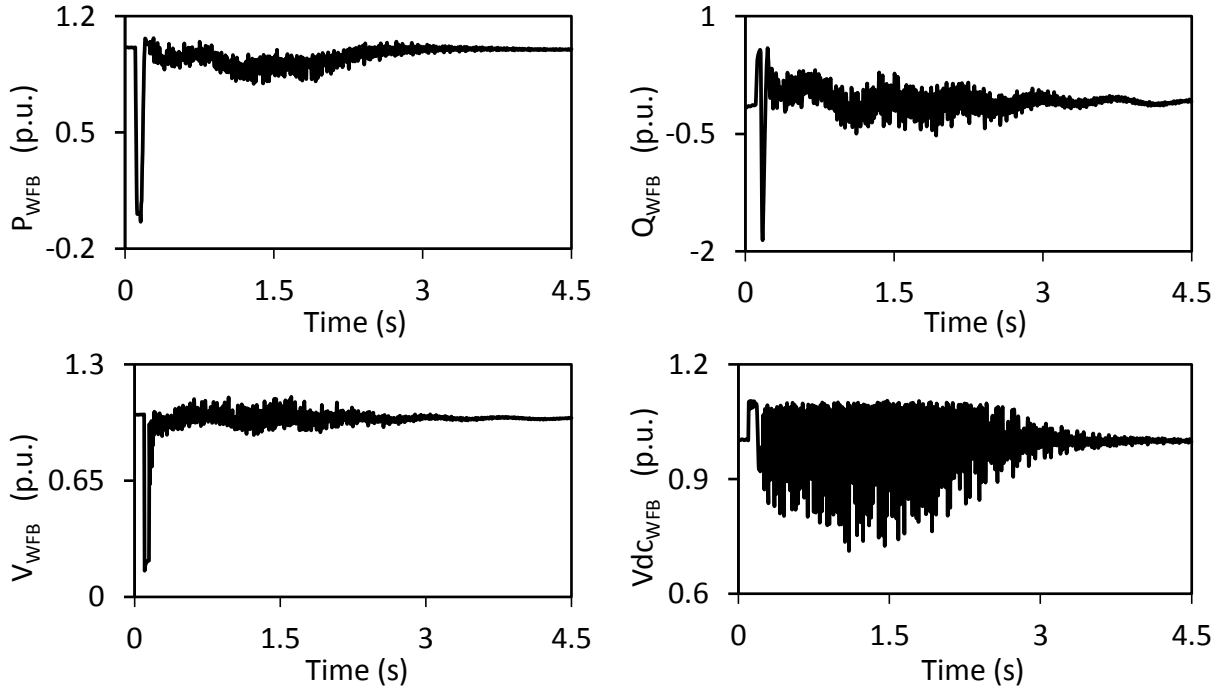

Figure 3.27: Wind farm B real and reactive powers, terminal voltage and dc capacitor voltage during and after clearing a 3-cycle, three-phase fault on Line 5 (60% compensation degree, supplemental control 1 is activated, Line 3 length = 100 km).

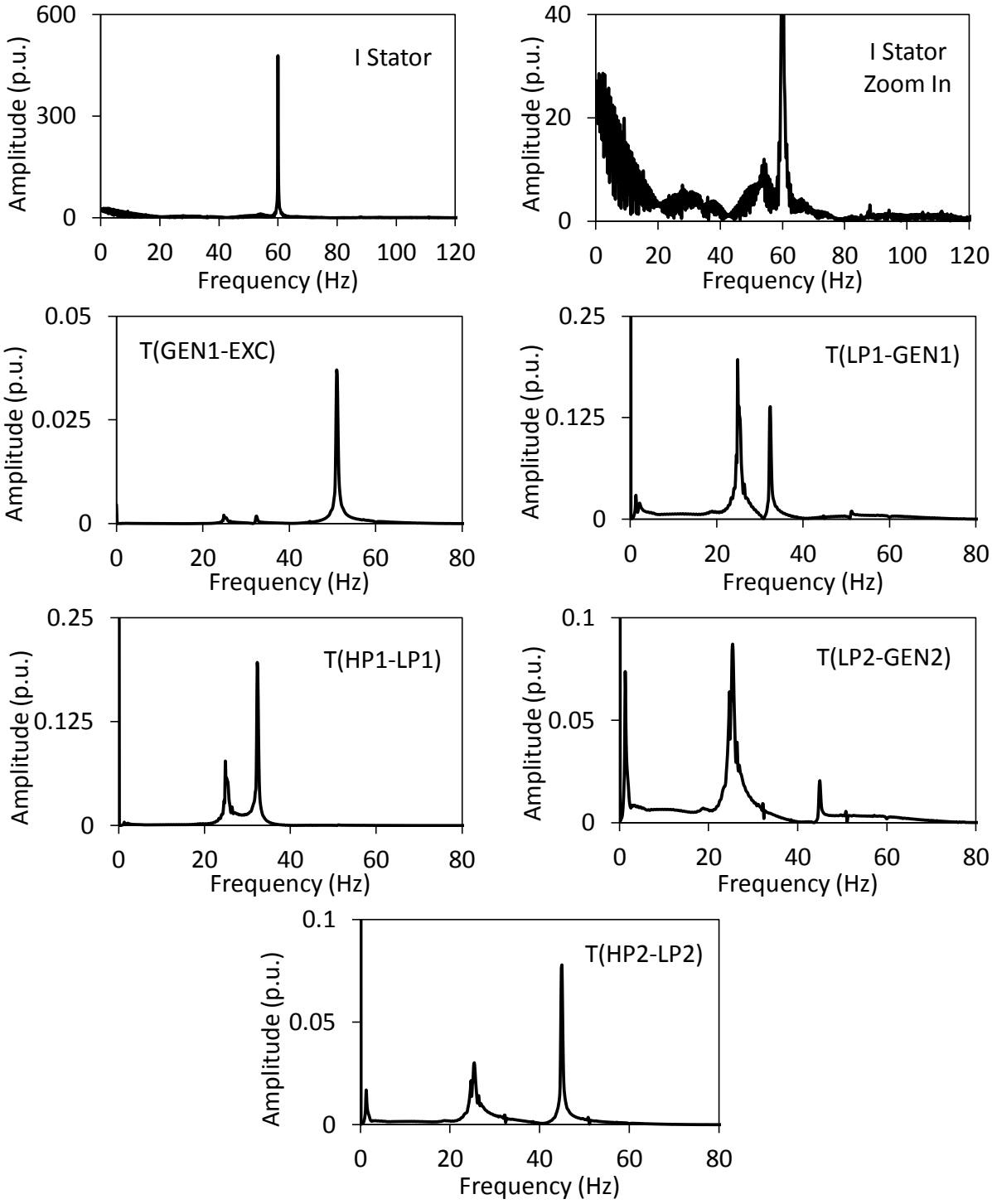

Figure 3.28: Frequency spectrums of the stator current of the DFIG wind turbine and the turbine-generator shaft torsional torques during and after clearing a 3-cycle, three-phase fault on Line 5 (60% compensation degree, supplemental control 1 is activated, Line 3 length = 100 km).

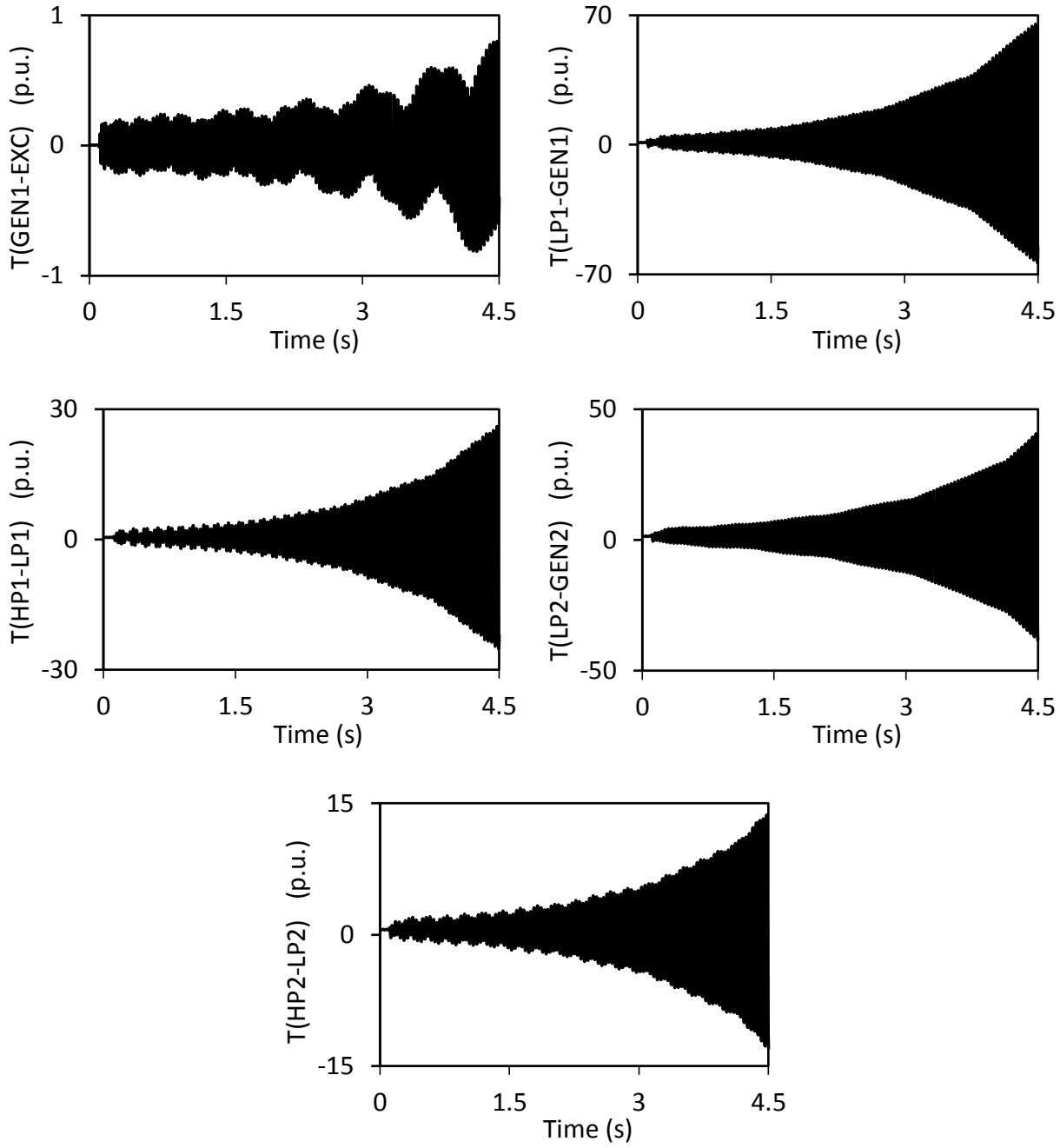

Figure 3.29: Turbine-generator shaft torsional torques during and after clearing a 3-cycle, three-phase fault on Line 5 (60% compensation degree, supplemental control 1 is not activated, Line 3 length = 200 km).

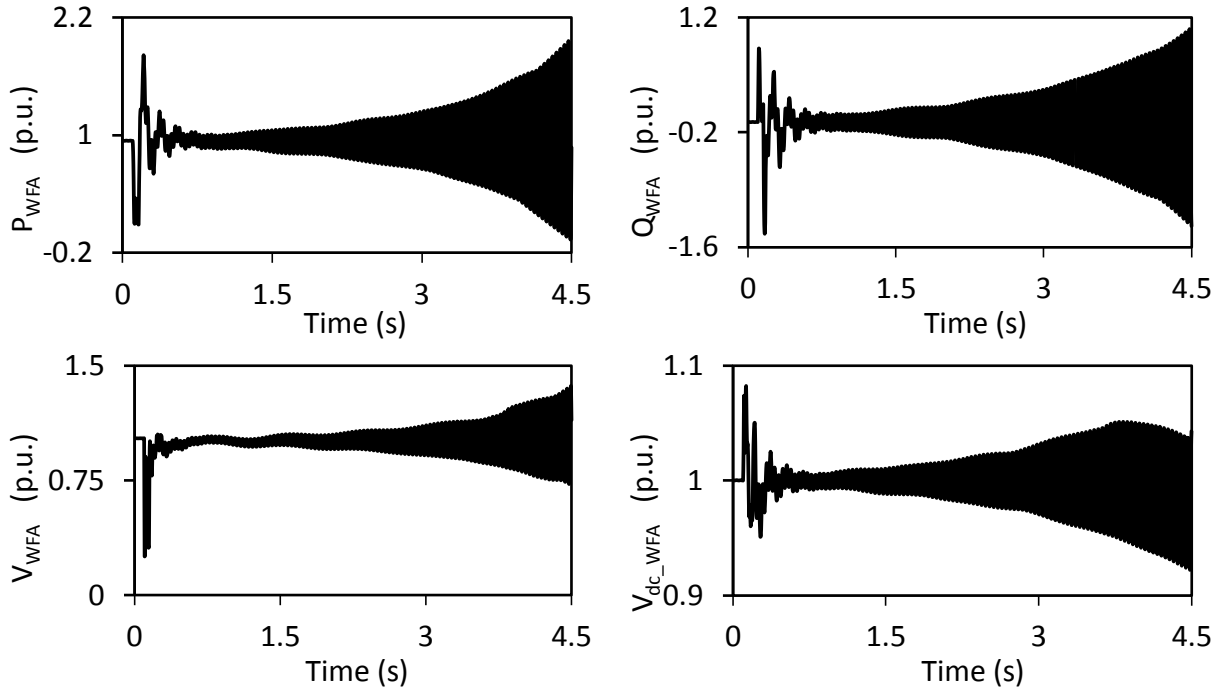

Figure 3.30: Wind farm A real and reactive powers, terminal voltage and dc capacitor voltage during and after clearing a 3-cycle, three-phase fault on Line 5 (60% compensation degree, supplemental control 1 is not activated, Line 3 length = 200 km).

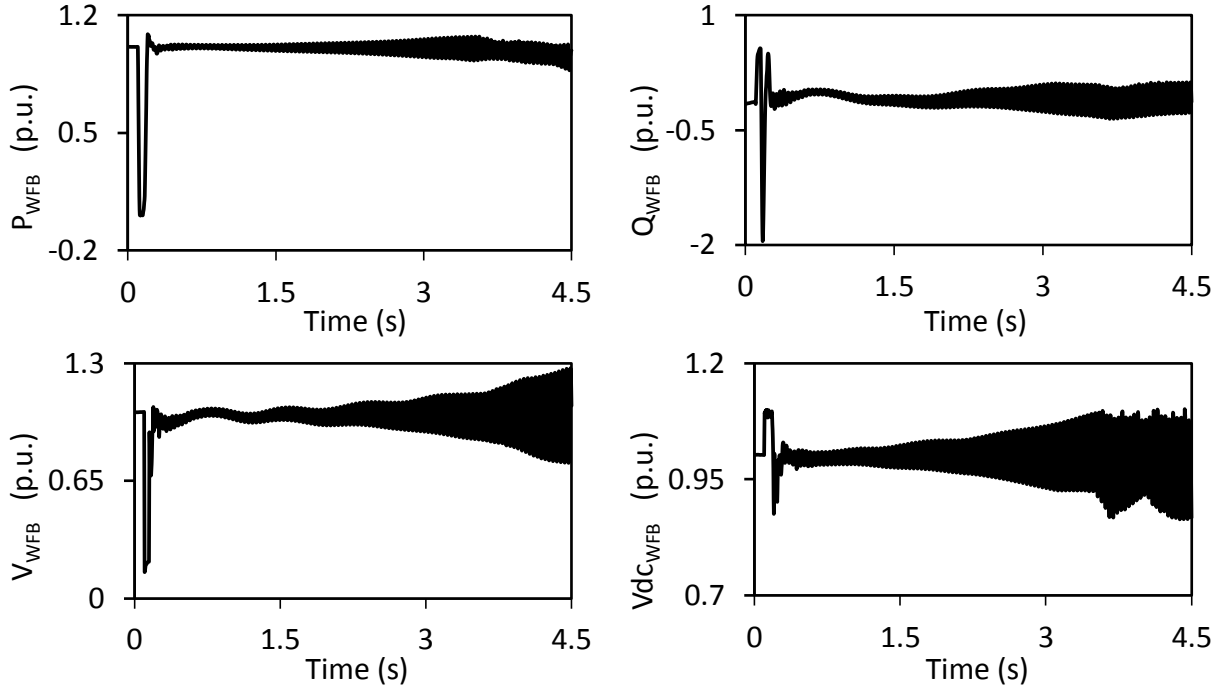

Figure 3.31: Wind farm B real and reactive powers, terminal voltage and dc capacitor voltage during and after clearing a 3-cycle, three-phase fault on Line 5 (60% compensation degree, supplemental control 1 is not activated, Line 3 length = 200 km).

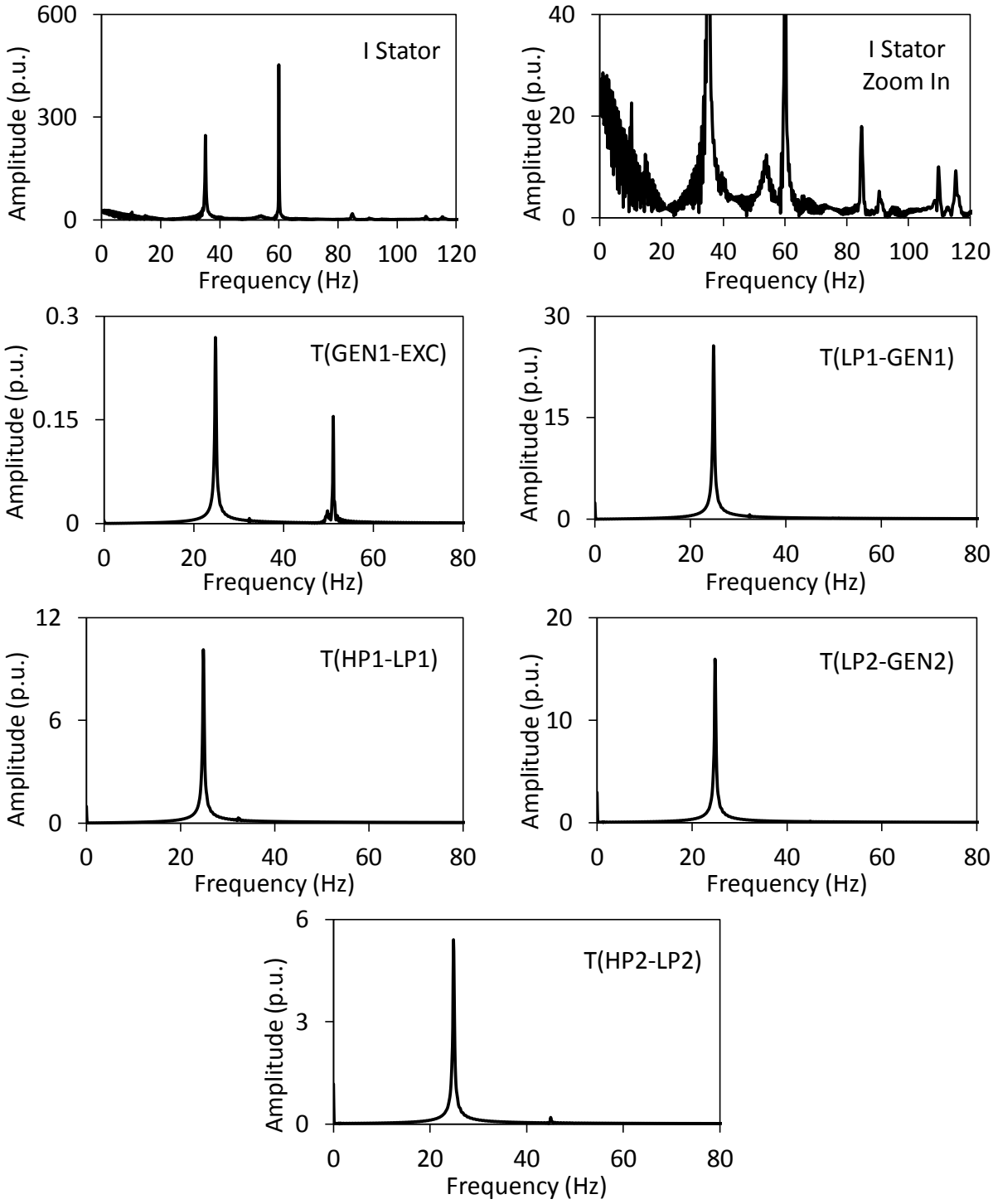

Figure 3.32: Frequency spectrums of the stator current of the DFIG wind turbine and the turbine-generator shaft torsional torques during and after clearing a 3-cycle, three-phase fault on Line 5 (60% compensation degree, supplemental control 1 is not activated, Line 3 length = 200 km).

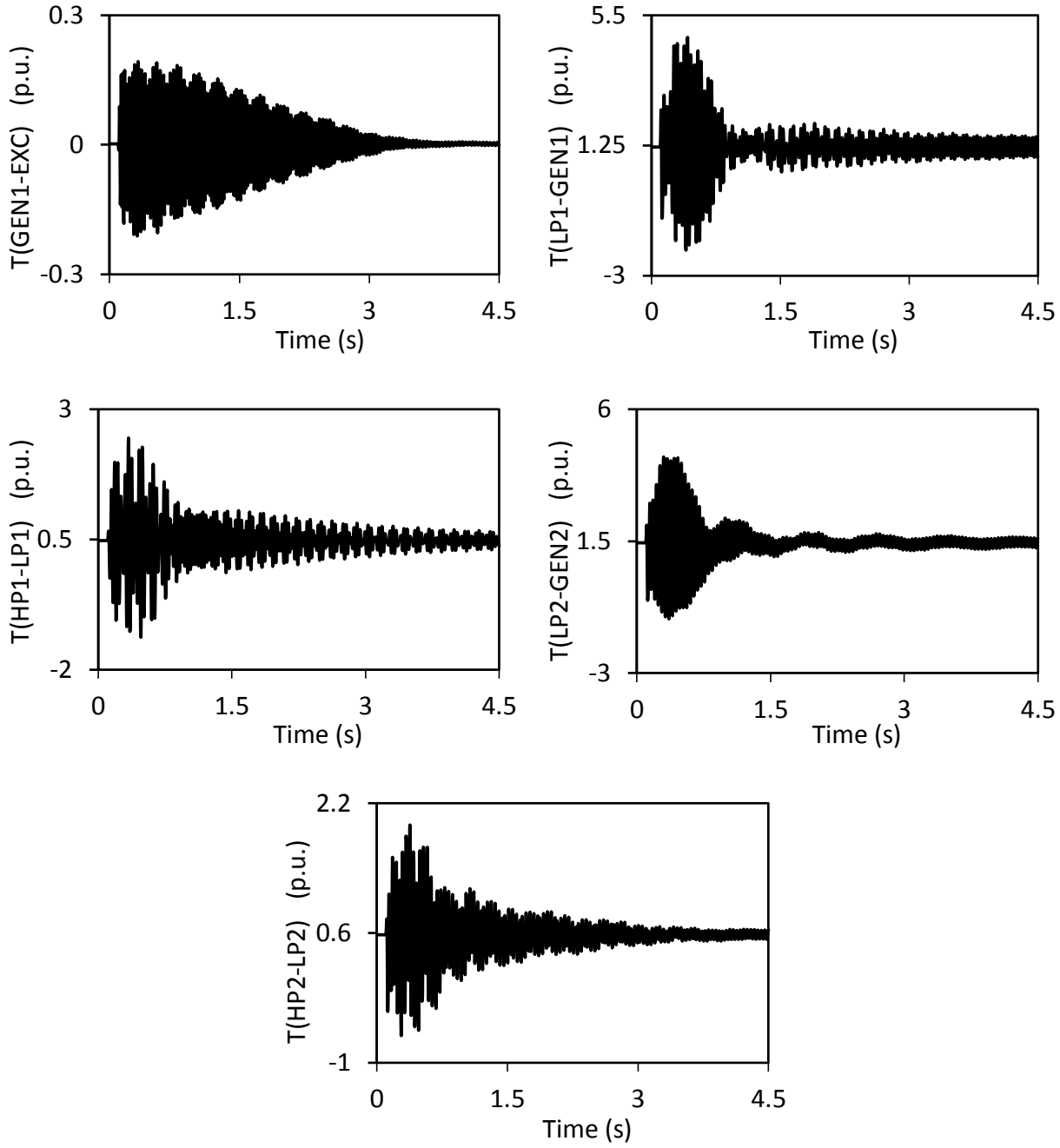

Figure 3.33: Turbine-generator shaft torsional torques during and after clearing a 3-cycle, three-phase fault on Line 5 (60% compensation degree, supplemental control 1 is activated, Line 3 length = 200 km).

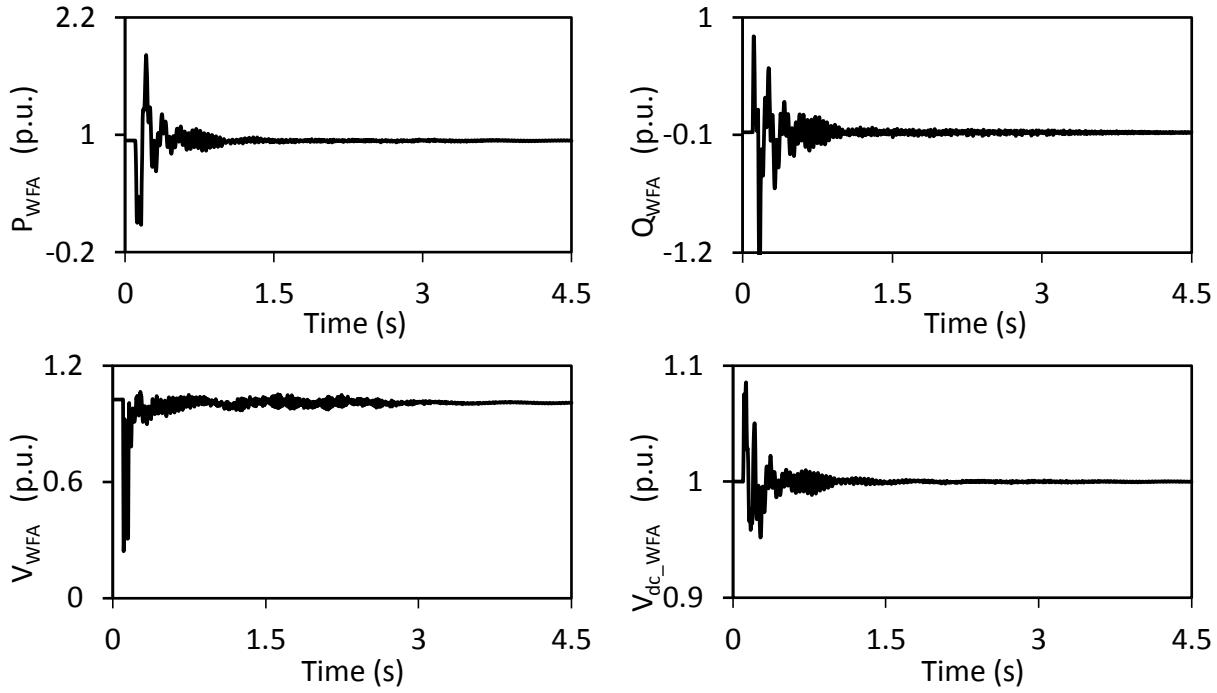

Figure 3.34: Wind farm A real and reactive powers, terminal voltage and dc capacitor voltage during and after clearing a 3-cycle, three-phase fault on Line 5 (60% compensation degree, supplemental control 1 is activated, Line 3 length = 200 km).

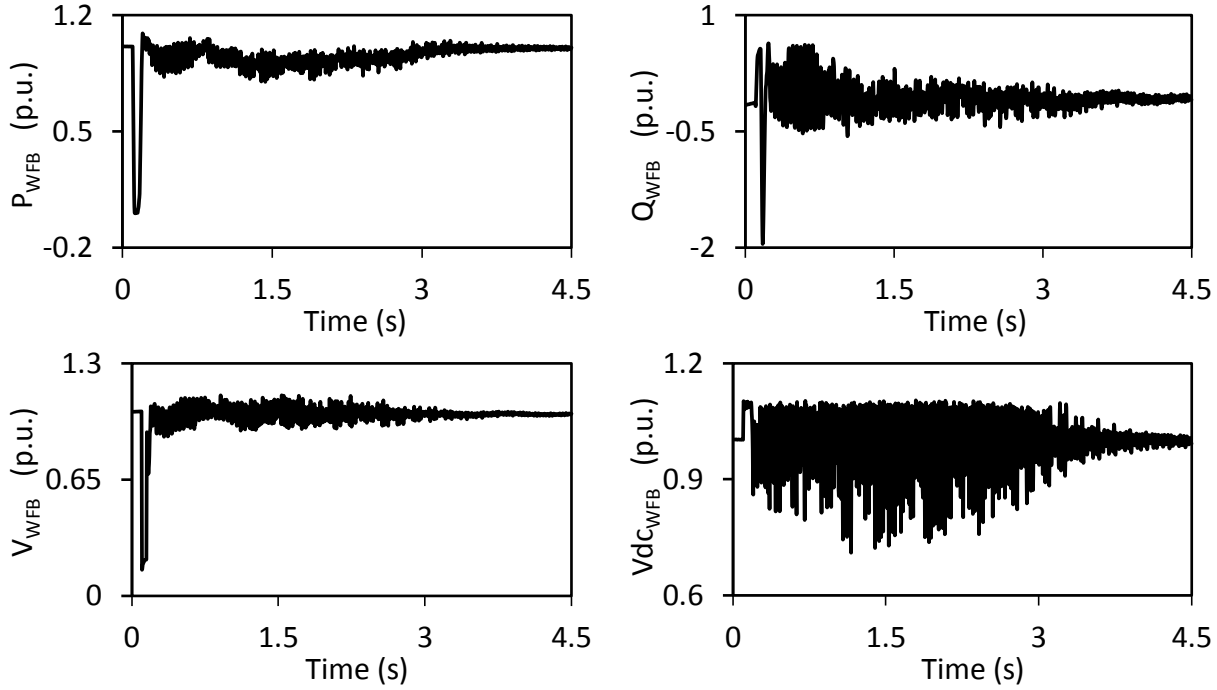

Figure 3.35: Wind farm B real and reactive powers, terminal voltage and dc capacitor voltage during and after clearing a 3-cycle, three-phase fault on Line 5 (60% compensation degree, supplemental control 1 is activated, Line 3 length = 200 km).

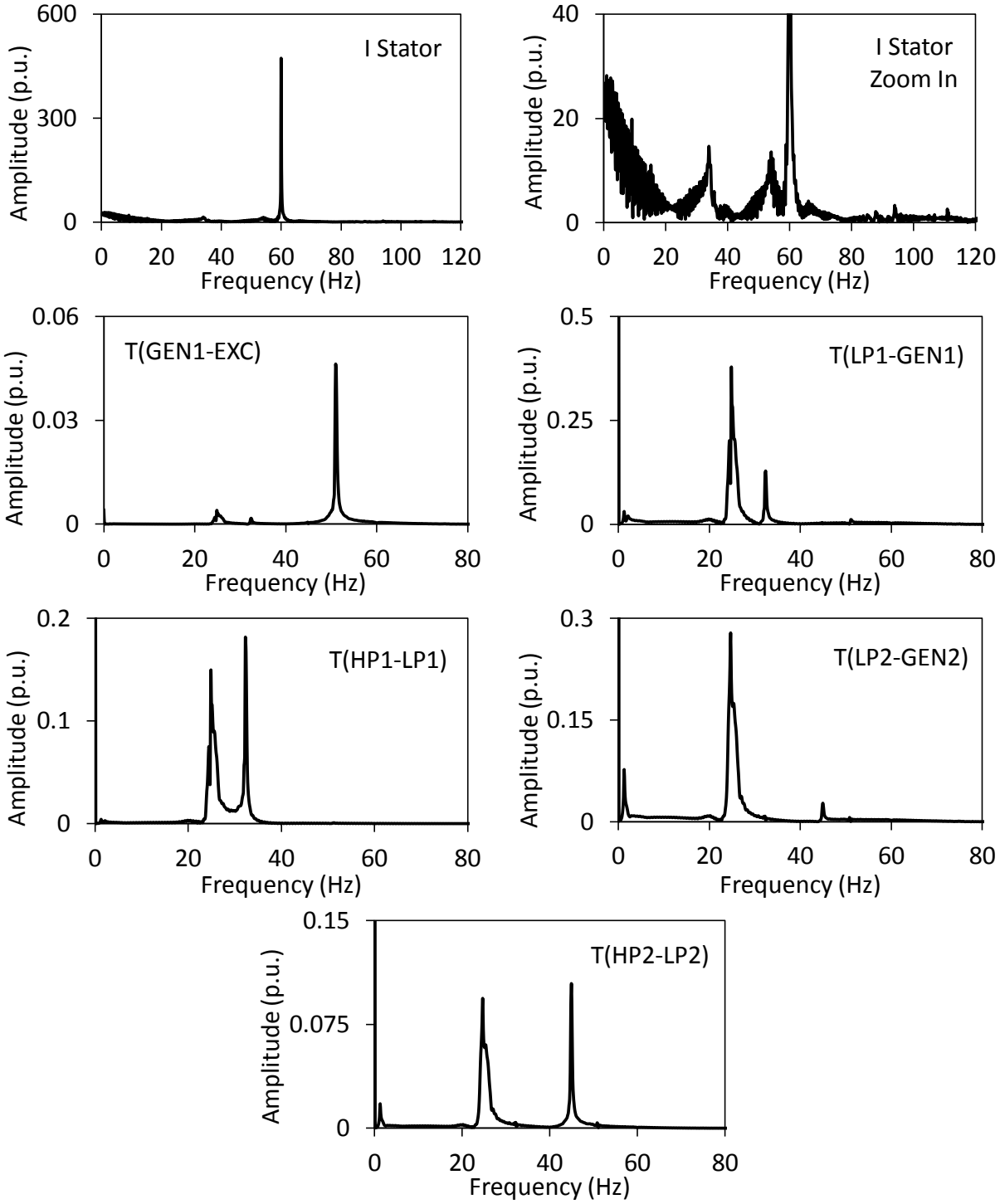

Figure 3.36: Frequency spectrums of the stator current of the DFIG wind turbine and the turbine-generator shaft torsional torques during and after clearing a 3-cycle, three-phase fault on Line 5 (60% compensation degree, supplemental control 1 is activated, Line 3 length = 200 km).

3.3.2 Effect of wind farm B rating

The effect of wind farm B rating on the performance of Supplemental control 1, is explored at two different ratings, namely 300 MW and 400 MW. The results of this study are presented in the following two groups of figures:

Group A: Wind farm B rating = 300 MW, (Figures 3.37, 3.38, 3.39, 3.40, 3.41, 3.42, 3.43, 3.44)

Group B: Wind farm B rating = 400 MW, (Figures 3.45, 3.46, 3.47, 3.48, 3.49, 3.50, 3.51, 3.52)

Table 3.4: Transfer functions of Supplemental control 1 for Group B (Wind farm B rating = 400 MW).

Modal speeds	Transfer function
G1, $\Delta_{\omega m0}$, G2, $\Delta_{\omega m0}$	0
G1, $\Delta_{\omega m1}$	$G_{\omega_1}(s) = 2.5\dfrac{0.1s + 300}{s + 1}$
G1, $\Delta_{\omega m2}$	$G_{\omega_2}(s) = -25\dfrac{0.01s + 1000}{10s + 1}$
G1, $\Delta_{\omega m3}$	$G_{\omega_3}(s) = 2.5\dfrac{s + 700}{s + 1}$
G2, $\Delta_{\omega m1}$	$G_{\omega_1}(s) = 25\dfrac{s + 250}{s + 1}$
G2, $\Delta_{\omega m2}$	$G_{\omega_2}(s) = 2.5\dfrac{0.01s + 500}{s + 1}$
Washout filter	$G(s) = \dfrac{s}{s + 10}$
Band-Pass filter	$G(s) = \dfrac{62.83s}{s^2 + 62.83s + 35500}$
Lead-Lag compensator	$G(s) = \dfrac{s + 250}{s + 1}$
U_{Total_max}, U_{Total_min}	0.33, -0.33

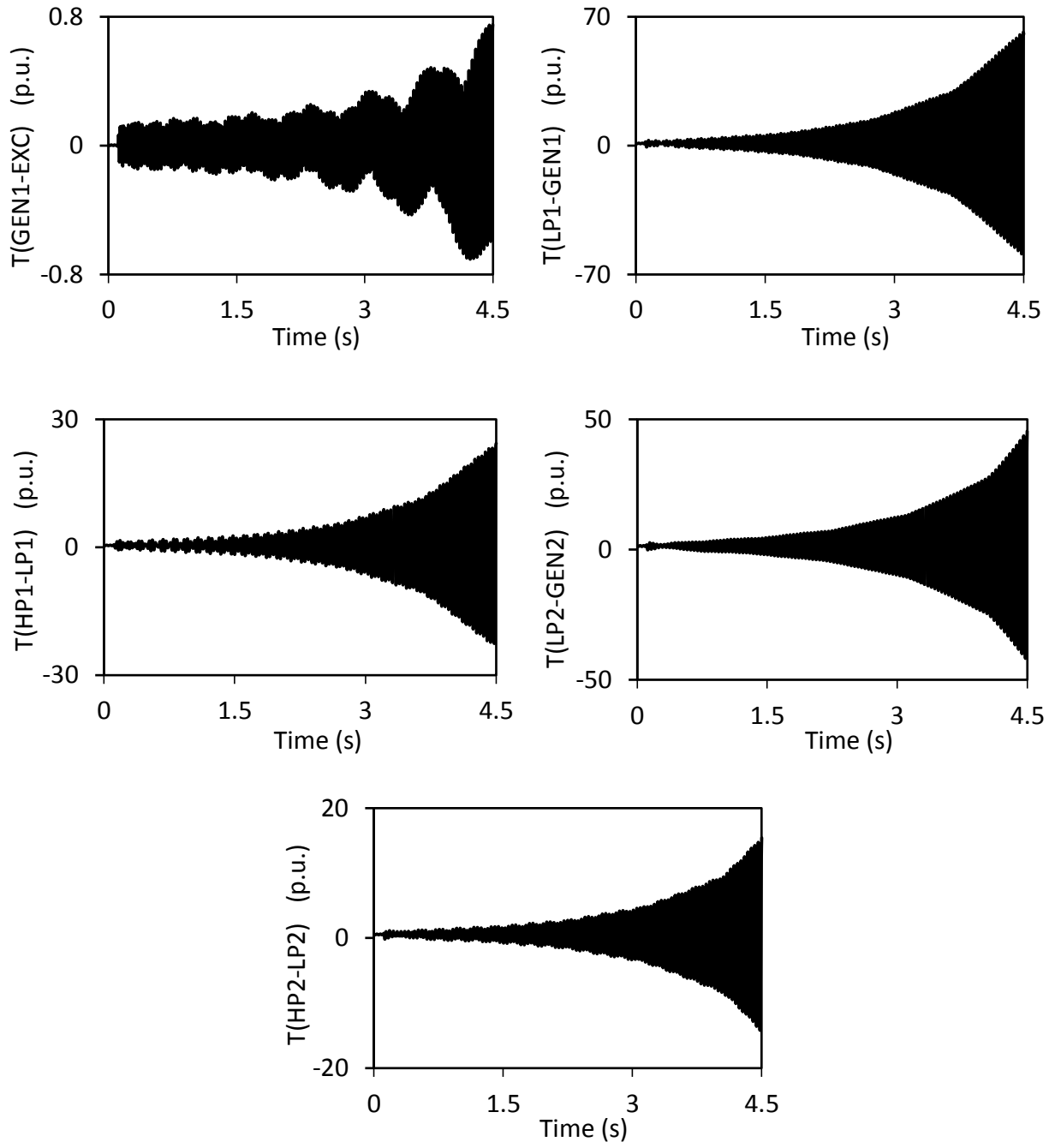

Figure 3.37: Turbine-generator shaft torsional torques during and after clearing a 3-cycle, three-phase fault on Line 5 (60% compensation degree, supplemental control 1 is not activated, wind farm B rating = 300 MW).

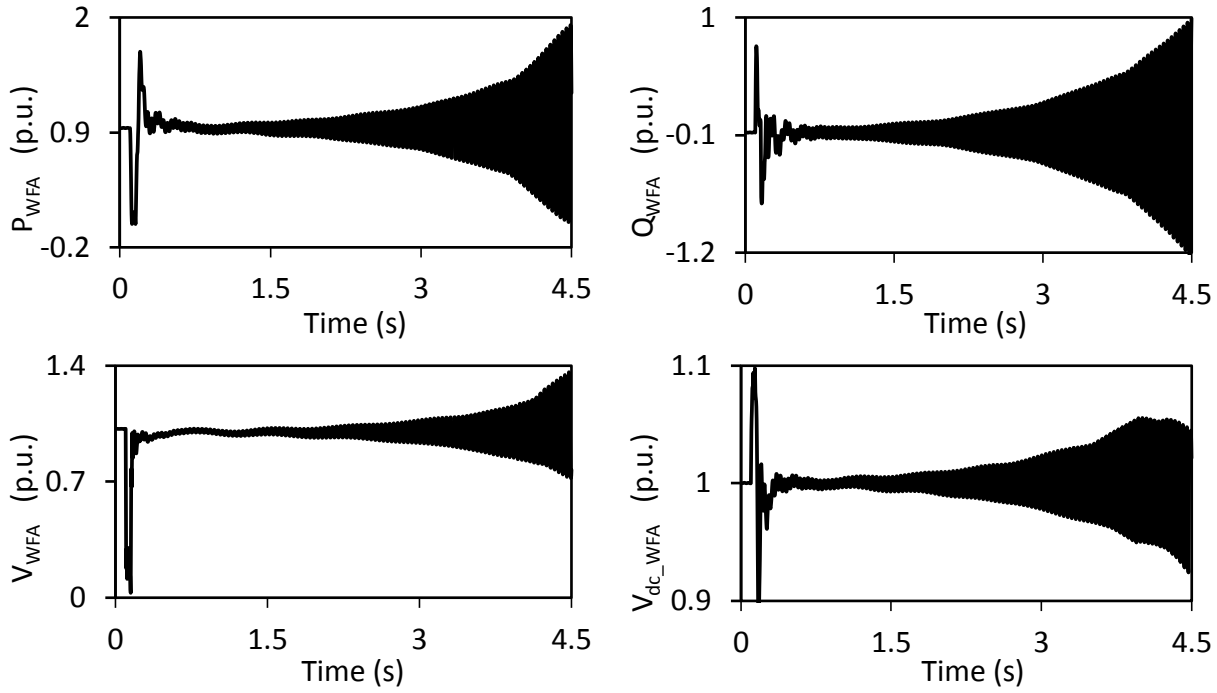

Figure 3.38: Wind farm A real and reactive powers, terminal voltage and dc capacitor voltage during and after clearing a 3-cycle, three-phase fault on Line 5 (60% compensation degree, supplemental control 1 is not activated, wind farm B rating = 300 MW).

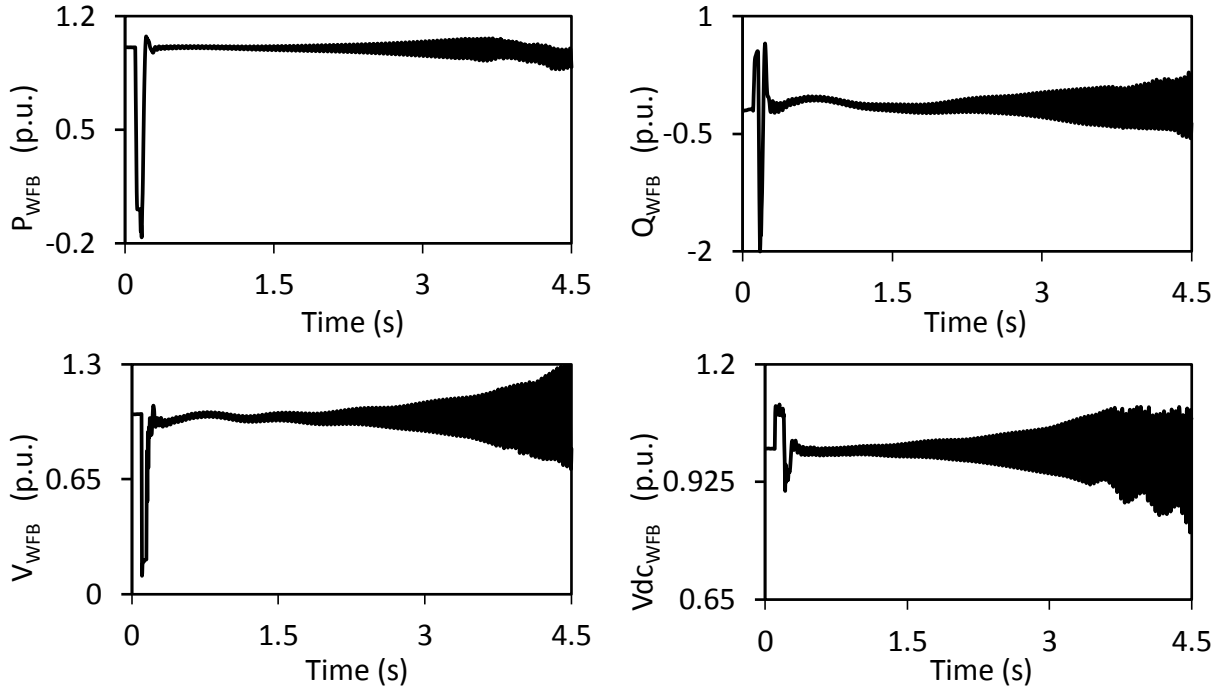

Figure 3.39: Wind farm B real and reactive powers, terminal voltage and dc capacitor voltage during and after clearing a 3-cycle, three-phase fault on Line 5 (60% compensation degree, supplemental control 1 is not activated, wind farm B rating = 300 MW).

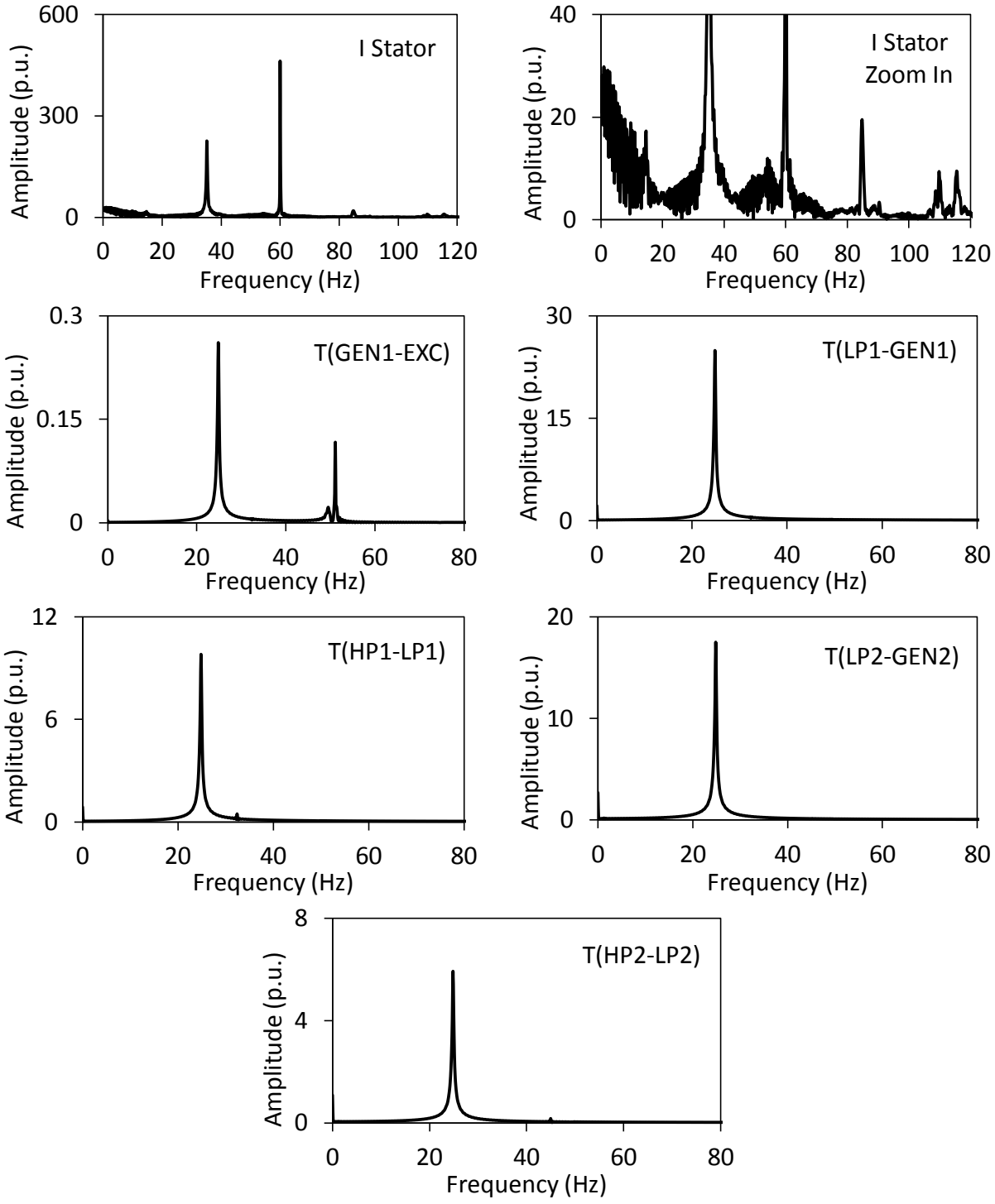

Figure 3.40: Frequency spectrums of the stator current of the DFIG wind turbine and the turbine-generator shaft torsional torques during and after clearing a 3-cycle, three-phase fault on Line 5 (60% compensation degree, supplemental control 1 is not activated, wind farm B rating = 300 MW).

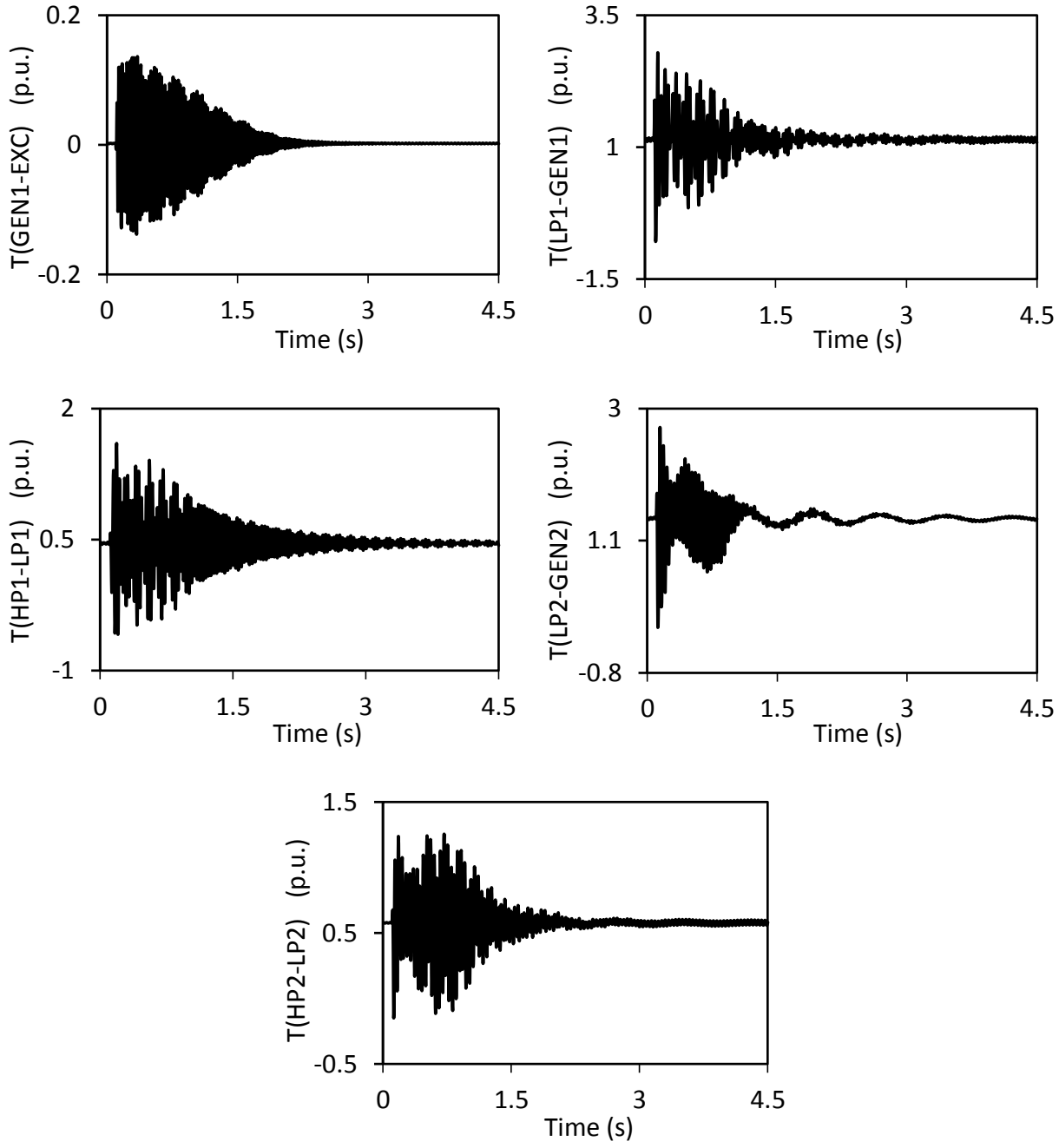

Figure 3.41: Turbine-generator shaft torsional torques during and after clearing a 3-cycle, three-phase fault on Line 5 (60% compensation degree, supplemental control 1 is activated, wind farm B rating = 300 MW).

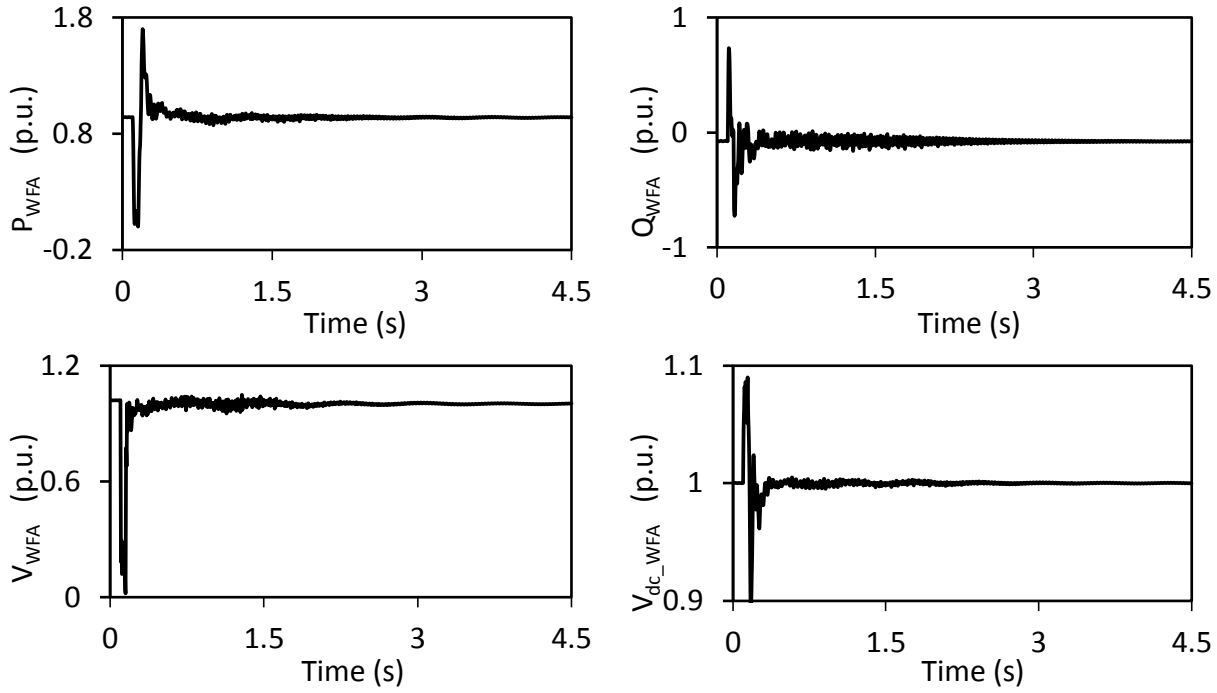

Figure 3.42: Wind farm A real and reactive powers, terminal voltage and dc capacitor voltage during and after clearing a 3-cycle, three-phase fault on Line 5 (60% compensation degree, supplemental control 1 is activated, wind farm B rating = 300 MW).

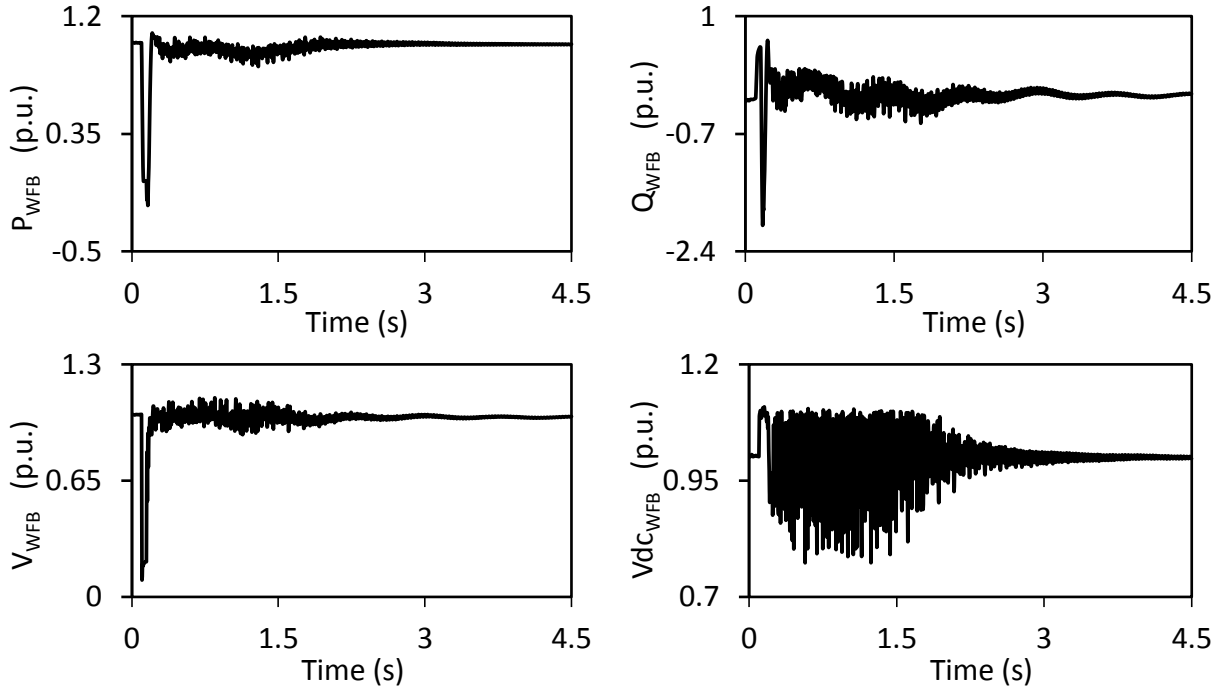

Figure 3.43: Wind farm B real and reactive powers, terminal voltage and dc capacitor voltage during and after clearing a 3-cycle, three-phase fault on Line 5 (60% compensation degree, supplemental control 1 is activated, wind farm B rating = 300 MW).

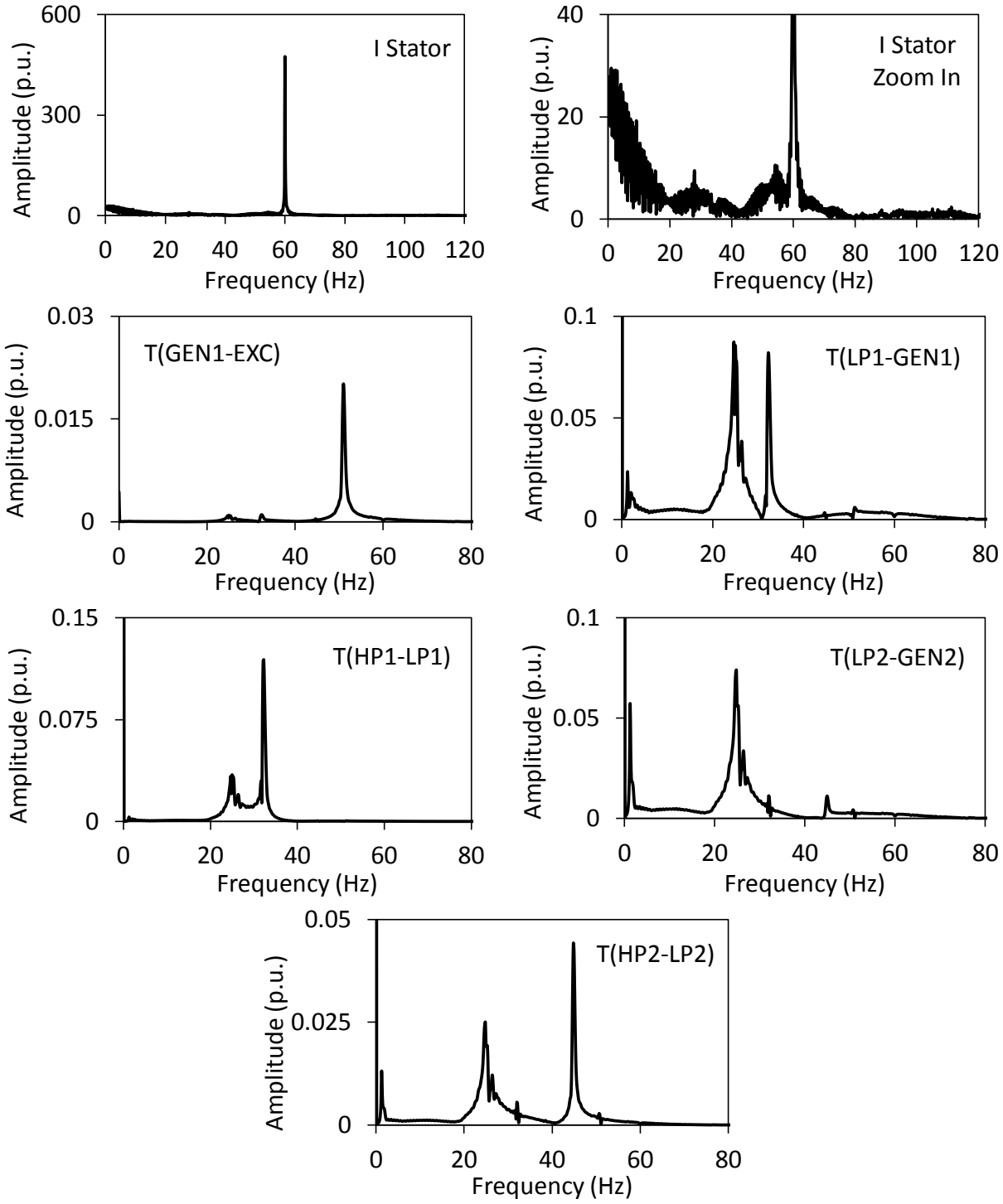

Figure 3.44: Frequency spectrums of the stator current of the DFIG wind turbine and the turbine-generator shaft torsional torques during and after clearing a 3-cycle, three-phase fault on Line 5 (60% compensation degree, supplemental control 1 is activated, wind farm B rating = 300 MW).

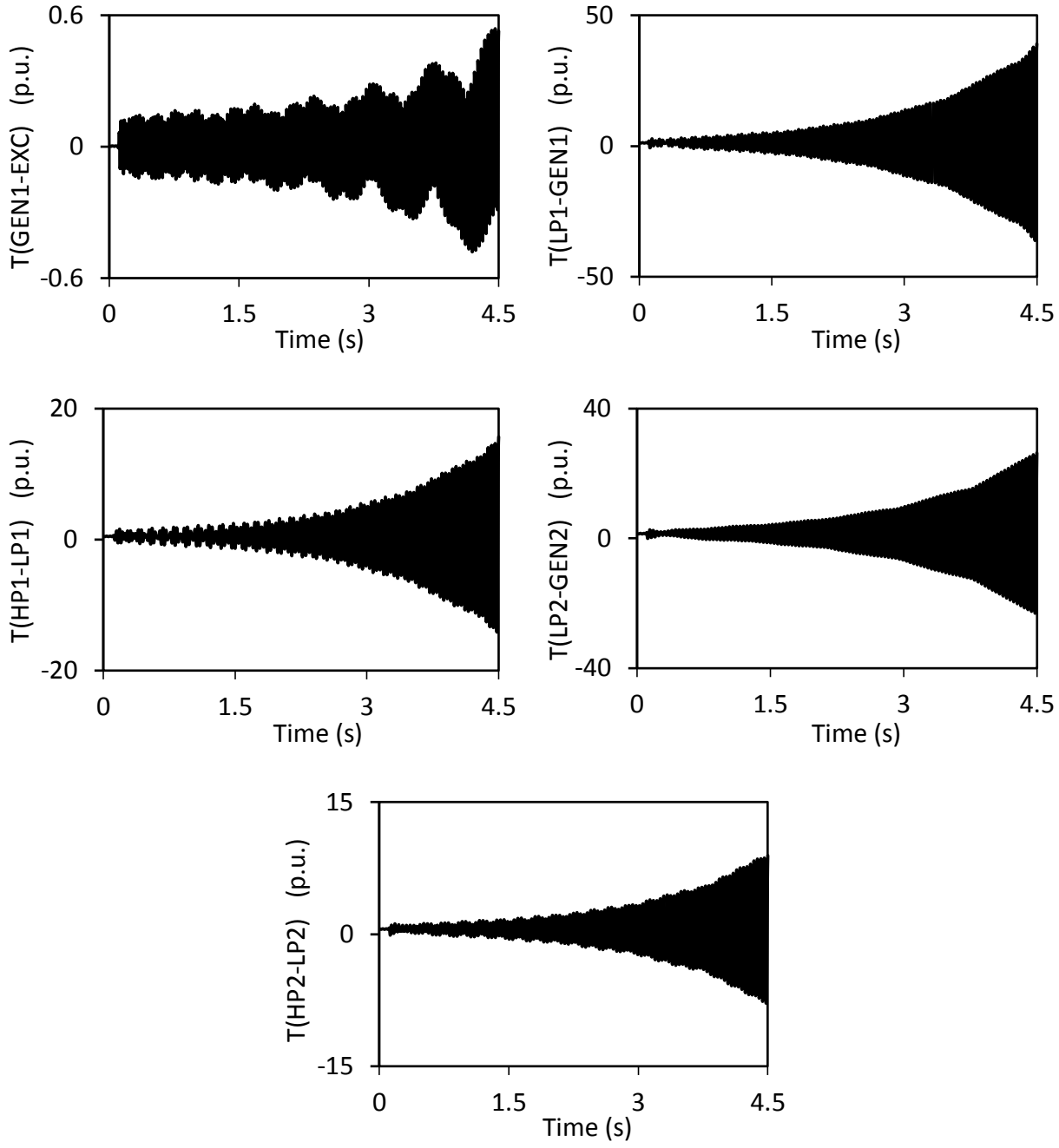

Figure 3.45: Turbine-generator shaft torsional torques during and after clearing a 3-cycle, three-phase fault on Line 5 (60% compensation degree, supplemental control 1 is not activated, wind farm B rating = 400 MW).

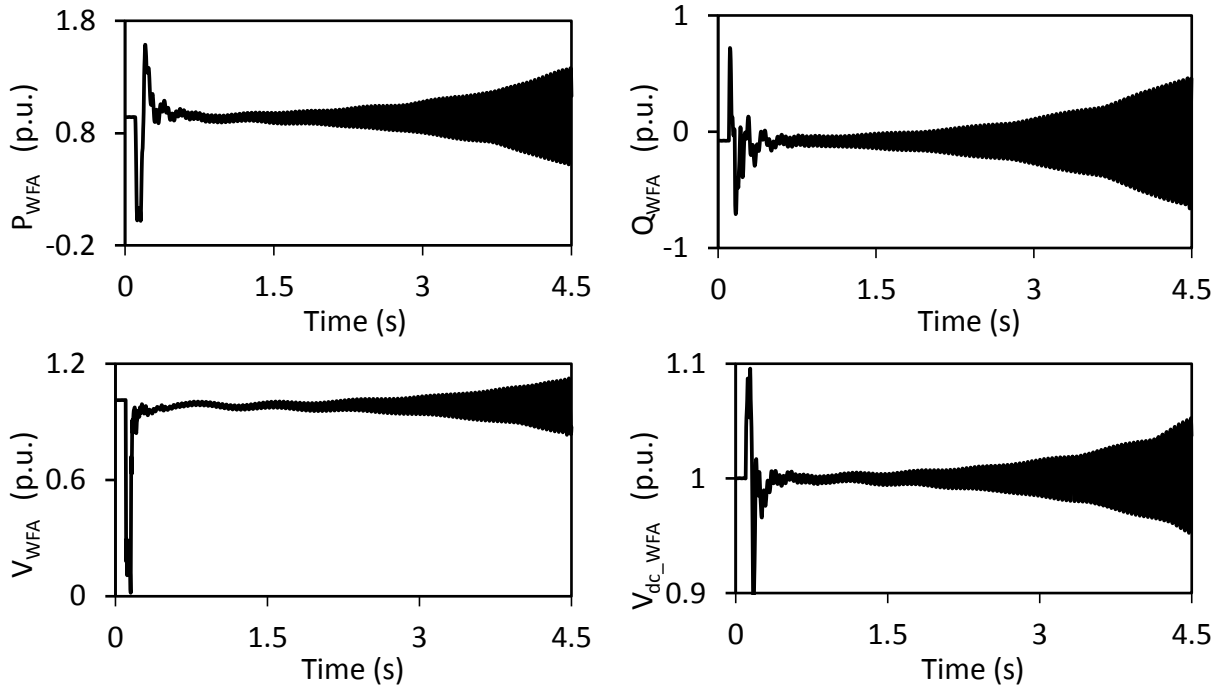

Figure 3.46: Wind farm A real and reactive powers, terminal voltage and dc capacitor voltage during and after clearing a 3-cycle, three-phase fault on Line 5 (60% compensation degree, supplemental control 1 is not activated, wind farm B rating = 400 MW).

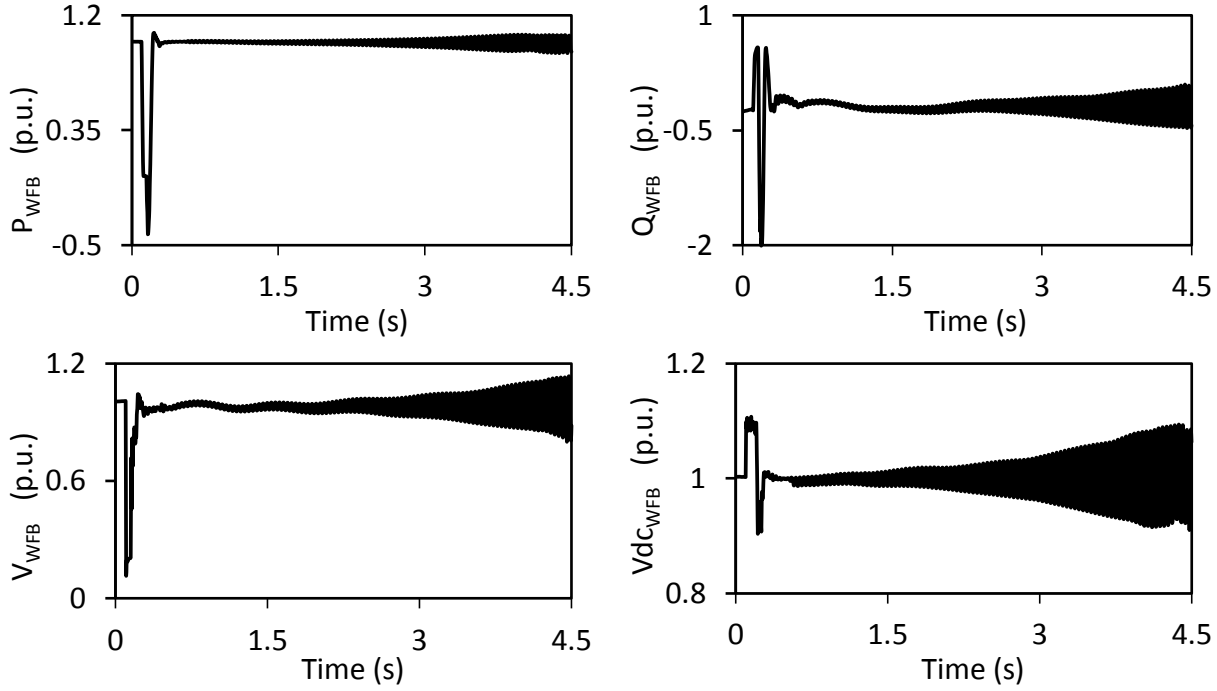

Figure 3.47: Wind farm B real and reactive powers, terminal voltage and dc capacitor voltage during and after clearing a 3-cycle, three-phase fault on Line 5 (60% compensation degree, supplemental control 1 is not activated, wind farm B rating = 400 MW).

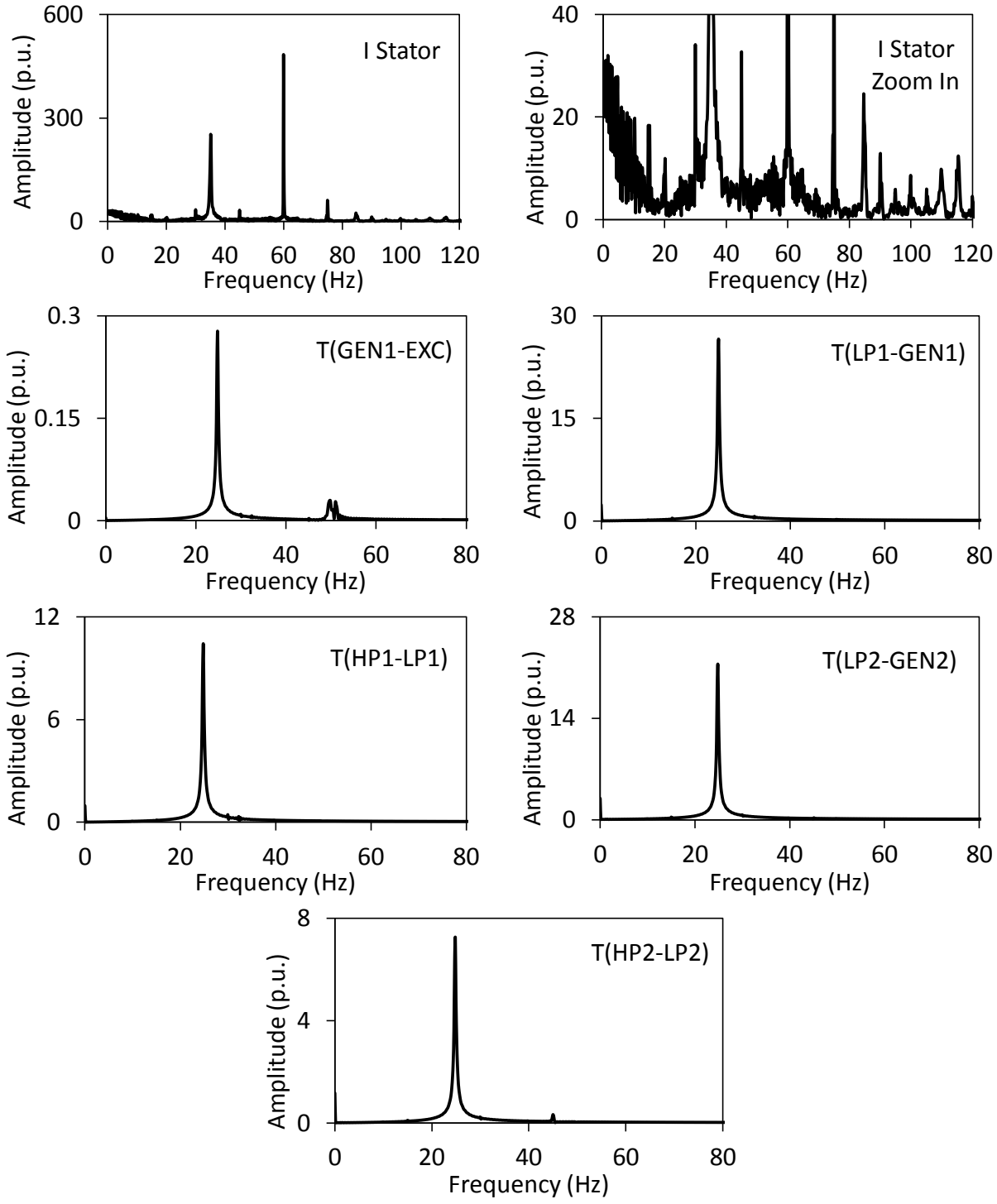

Figure 3.48: Frequency spectrums of the stator current of the DFIG wind turbine and the turbine-generator shaft torsional torques during and after clearing a 3-cycle, three-phase fault on Line 5 (60% compensation degree, supplemental control 1 is not activated, wind farm B rating = 400 MW).

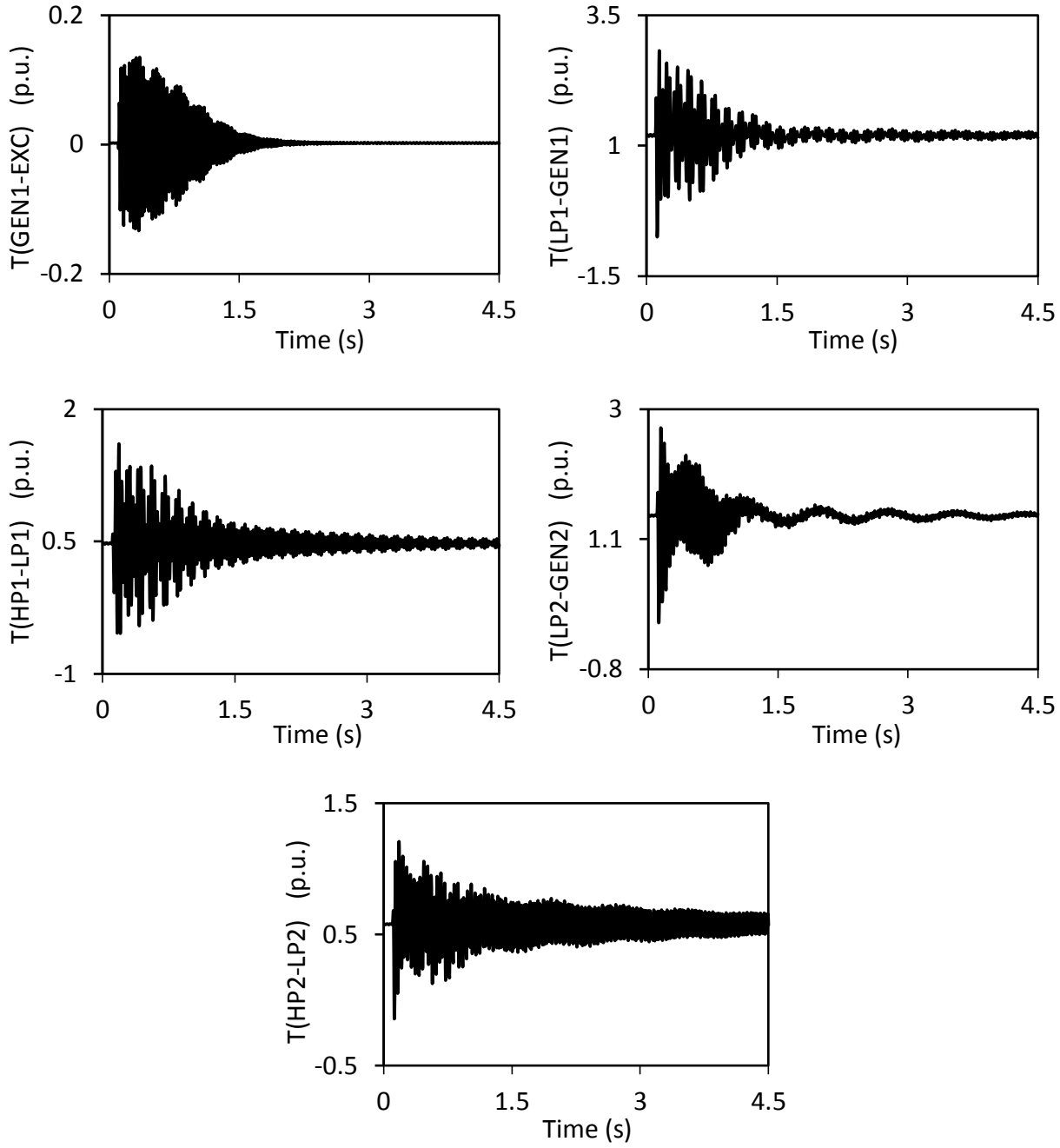

Figure 3.49: Turbine-generator shaft torsional torques during and after clearing a 3-cycle, three-phase fault on Line 5 (60% compensation degree, supplemental control 1 is activated, wind farm B rating = 400 MW).

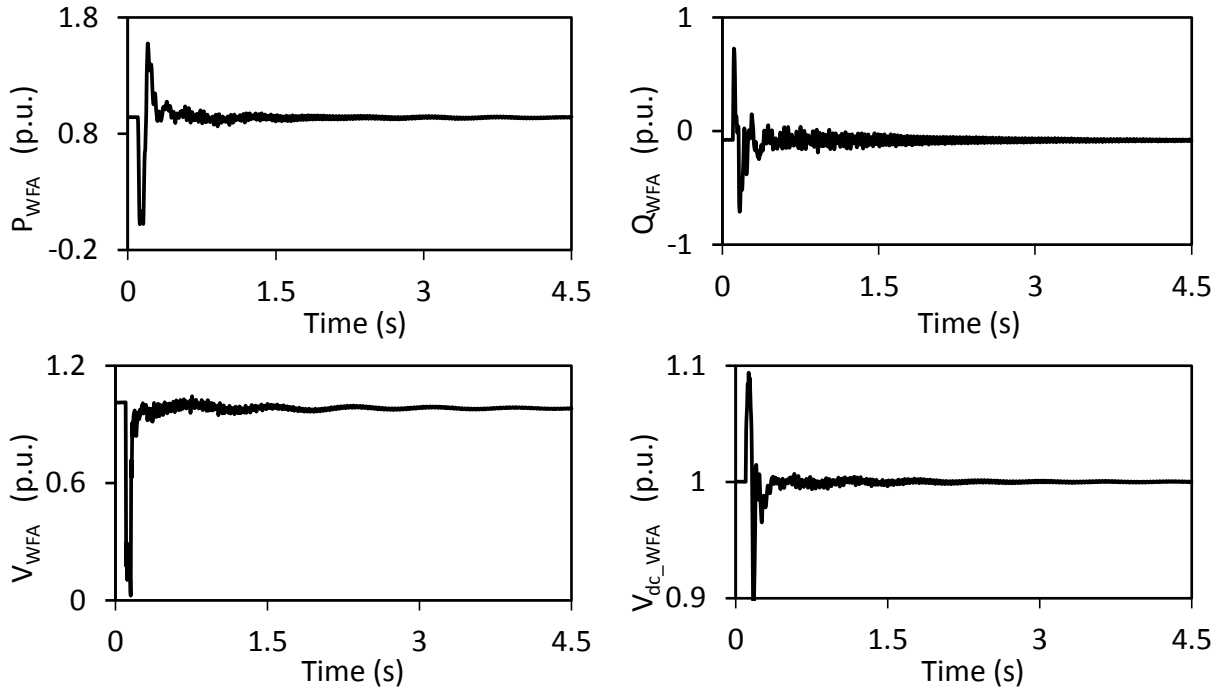

Figure 3.50: Wind farm A real and reactive powers, terminal voltage and dc capacitor voltage during and after clearing a 3-cycle, three-phase fault on Line 5 (60% compensation degree, supplemental control 1 is activated, wind farm B rating = 400 MW).

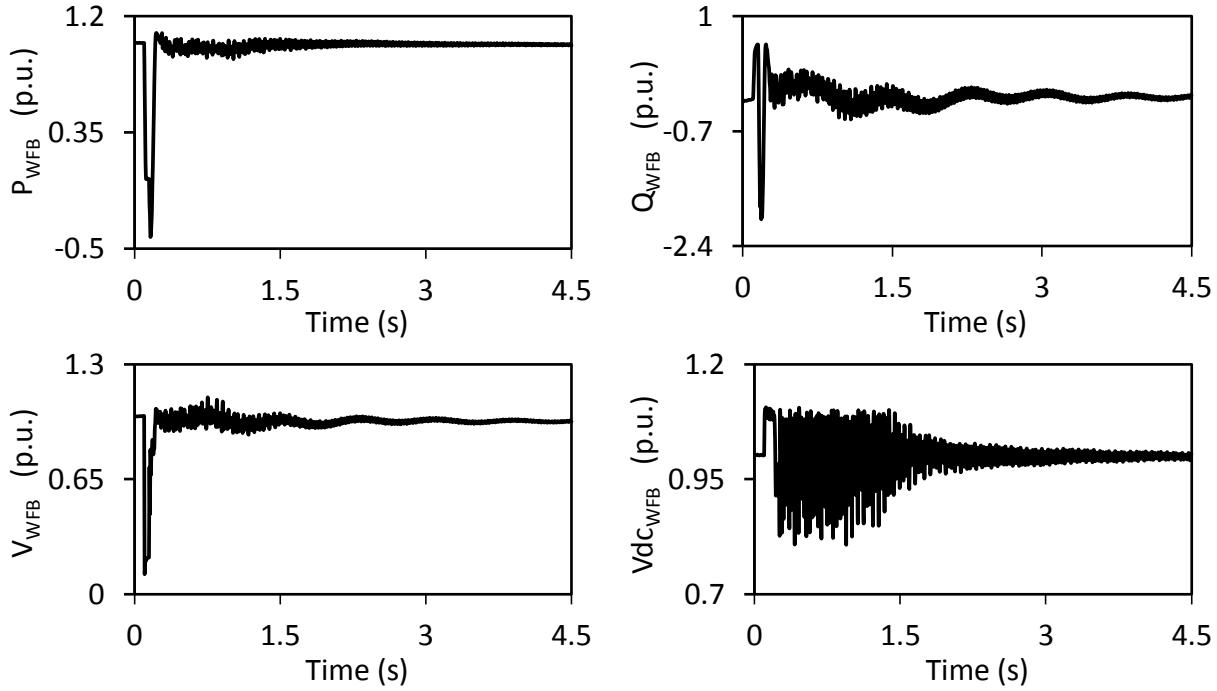

Figure 3.51: Wind farm B real and reactive powers, terminal voltage and dc capacitor voltage during and after clearing a 3-cycle, three-phase fault on Line 5 (60% compensation degree, supplemental control 1 is activated, wind farm B rating = 400 MW).

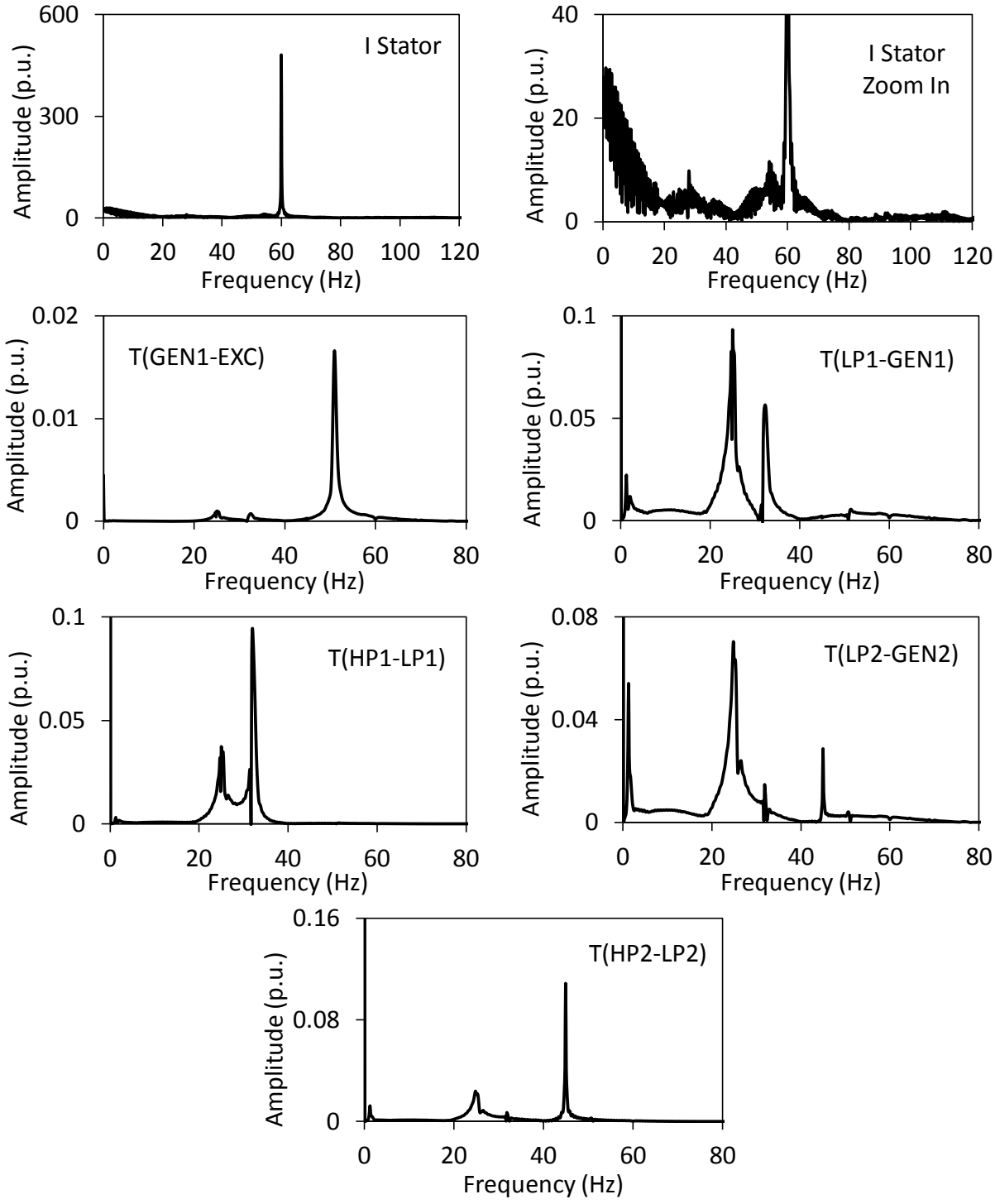

Figure 3.52: Frequency spectrums of the stator current of the DFIG wind turbine and the turbine-generator shaft torsional torques during and after clearing a 3-cycle, three-phase fault on Line 5 (60% compensation degree, supplemental control 1 is activated, wind farm B rating = 400 MW).

In each group, the turbine-generator shaft torsional torques, wind farms A and B active and reactive powers, terminal voltage and the BtB dc voltage as well as the frequency spectrums of the stator current of the DFIG wind turbines and the turbine-generator shaft torsional torques are shown for the cases when Supplemental control 1 is disabled and activated respectively. Moreover, the transfer functions of Supplemental control 1 in Group A are the same as those in Table 3.1. The transfer functions of Supplemental control 1 in Group B are given in Tables 3.4.

The comparisons between the two sets of figures (Set 1: Supplemental control 1 is disabled and Set 2: Supplemental control 1 is activated) in Groups A and B show the effectiveness of the supplemental control in mitigating SSR and SSI at different ratings of wind farm B.

3.3.3 Effect of the fault type

The effect of the fault type on the performance of Supplemental control 1 is examined by applying a ***double line-to-ground fault*** at the same fault location (Line 5). The results of this study are presented in the following two groups of figures:

Group A: Supplemental control 1 is disabled, (Figures 3.53, 3.54, 3.55, 3.56)

Group B: Supplemental control 1 is activated, (Figures 3.57, 3.58, 3.59, 3.60)

In each group, the turbine-generator shaft torsional torques, wind farms A and B active and reactive powers, terminal voltage and the BtB dc voltage as well as the frequency spectrums of the stator current of the DFIG wind turbines and the turbine-generator shaft torsional torques are shown. Moreover, the transfer functions of Supplemental control 1 in Group B are the same as those in Table 3.1.

The comparisons between the two sets of figures in Groups A and B (Set 1: Supplemental control 1 is disabled and Set 2: Supplemental control 1 is activated) demonstrate the effectiveness of the supplemental control in mitigating SSR and SSI during and after clearing an unsymmetrical fault. It is worth noting here that the comparison between Figures 3.5, 3.6, 3.7 and Figures 3.53, 3.54, 3.55 shows that the responses of the turbine-generator shaft torsional torques, wind farm A and B real and reactive powers as well as terminal voltages are “almost” the same during the three-phase and double line-to-ground faults.

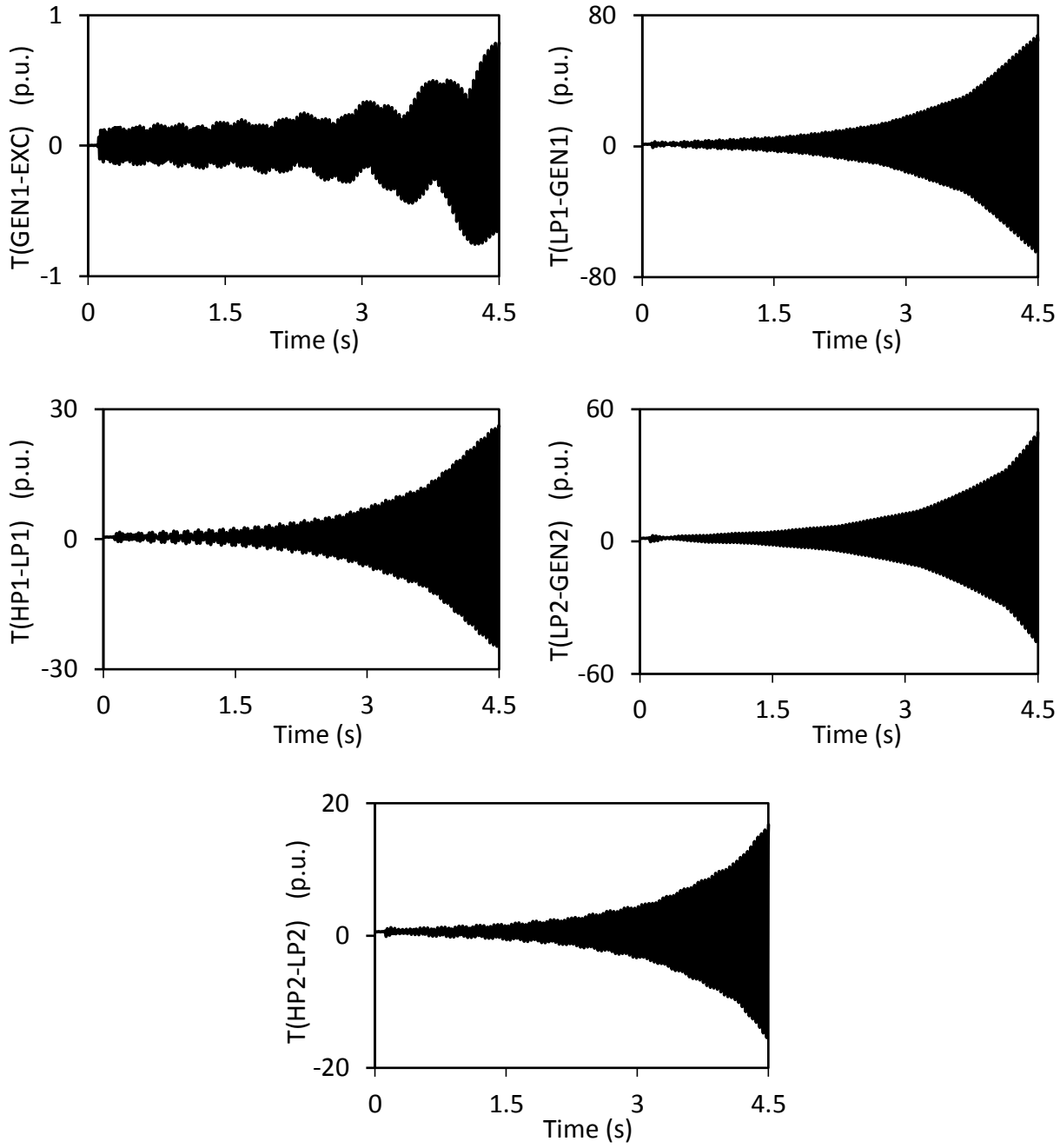

Figure 3.53: Turbine-generator shaft torsional torques during and after clearing a 3-cycle, double line-to-ground fault on Line 5 (60% compensation degree, supplemental control 1 is not activated).

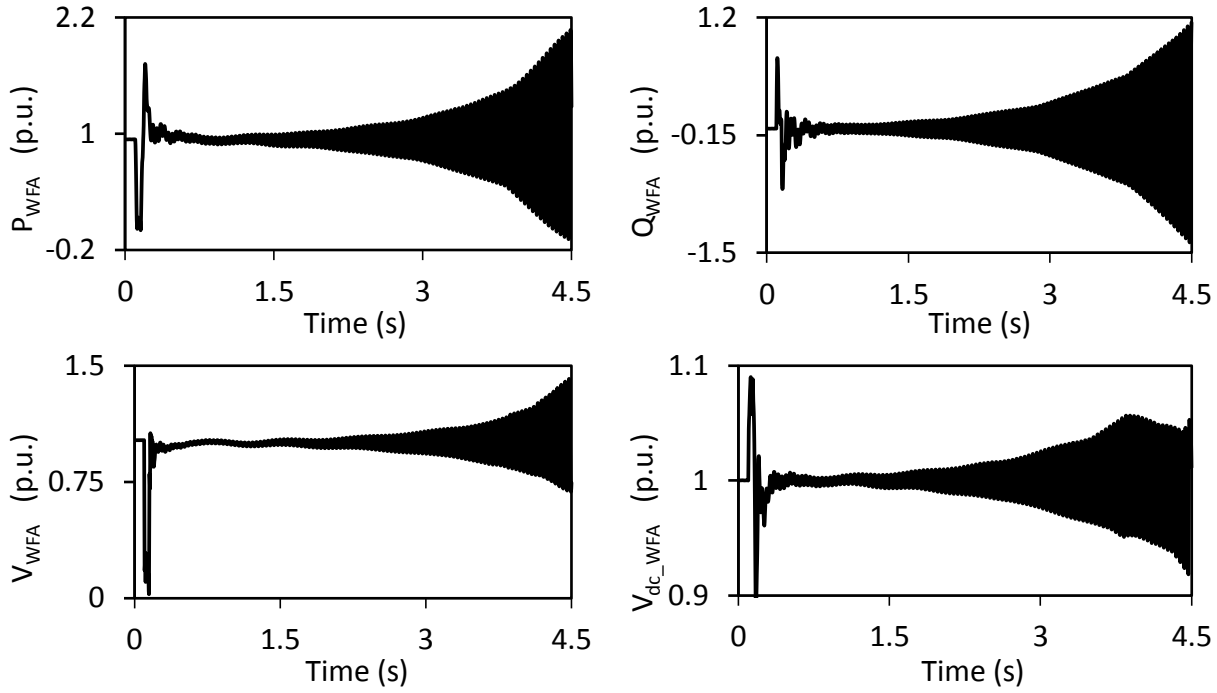

Figure 3.54: Wind farm A real and reactive powers, terminal voltage and dc capacitor voltage during and after clearing a 3-cycle, double line-to-ground fault on Line 5 (60% compensation degree, supplemental control 1 is not activated).

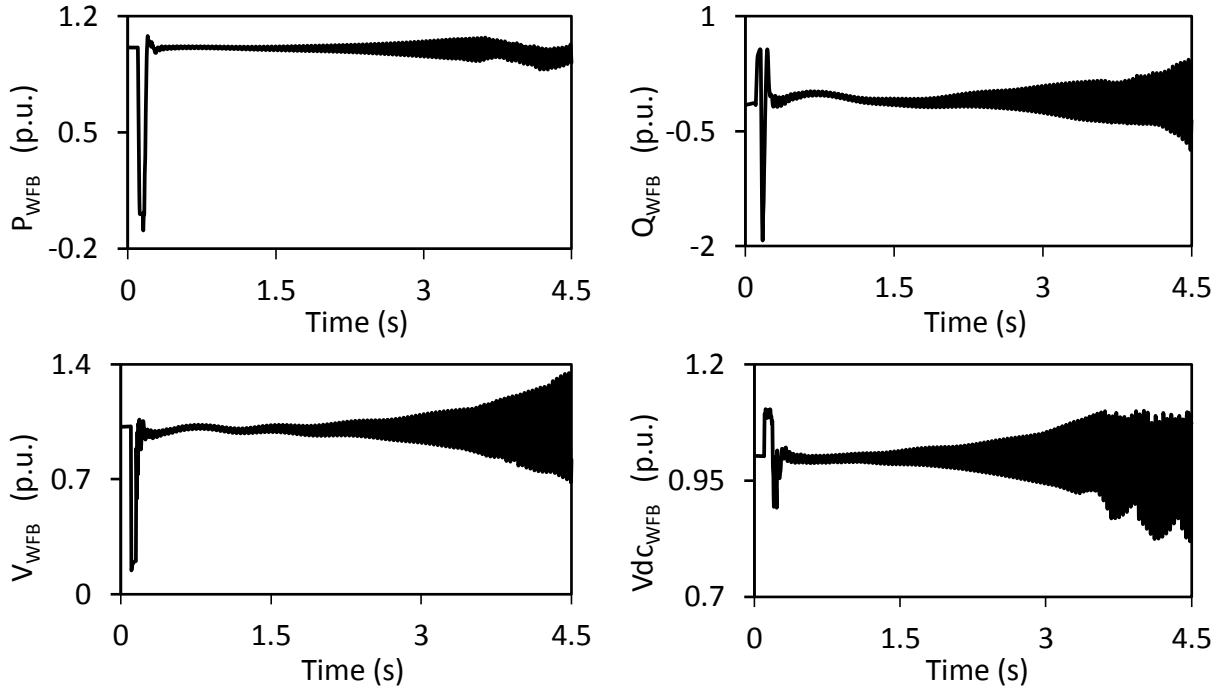

Figure 3.55: Wind farm B real and reactive powers, terminal voltage and dc capacitor voltage during and after clearing a 3-cycle, double line-to-ground fault on Line 5 (60% compensation degree, supplemental control 1 is not activated).

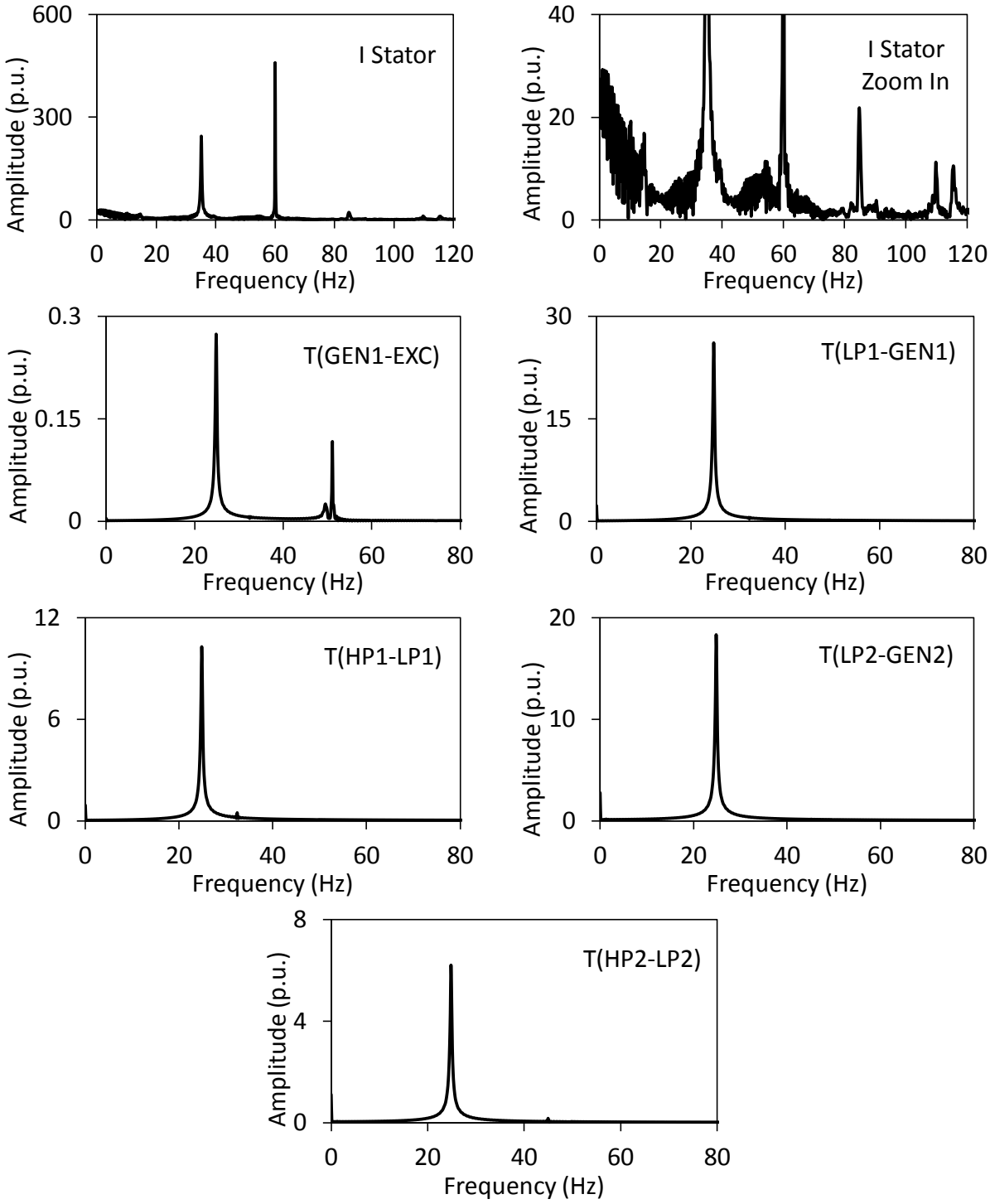

Figure 3.56: Frequency spectrums of the stator current of the DFIG wind turbine and the turbine-generator shaft torsional torques during and after clearing a 3-cycle, double line-to-ground fault on Line 5 (60% compensation degree, supplemental control 1 is not activated).

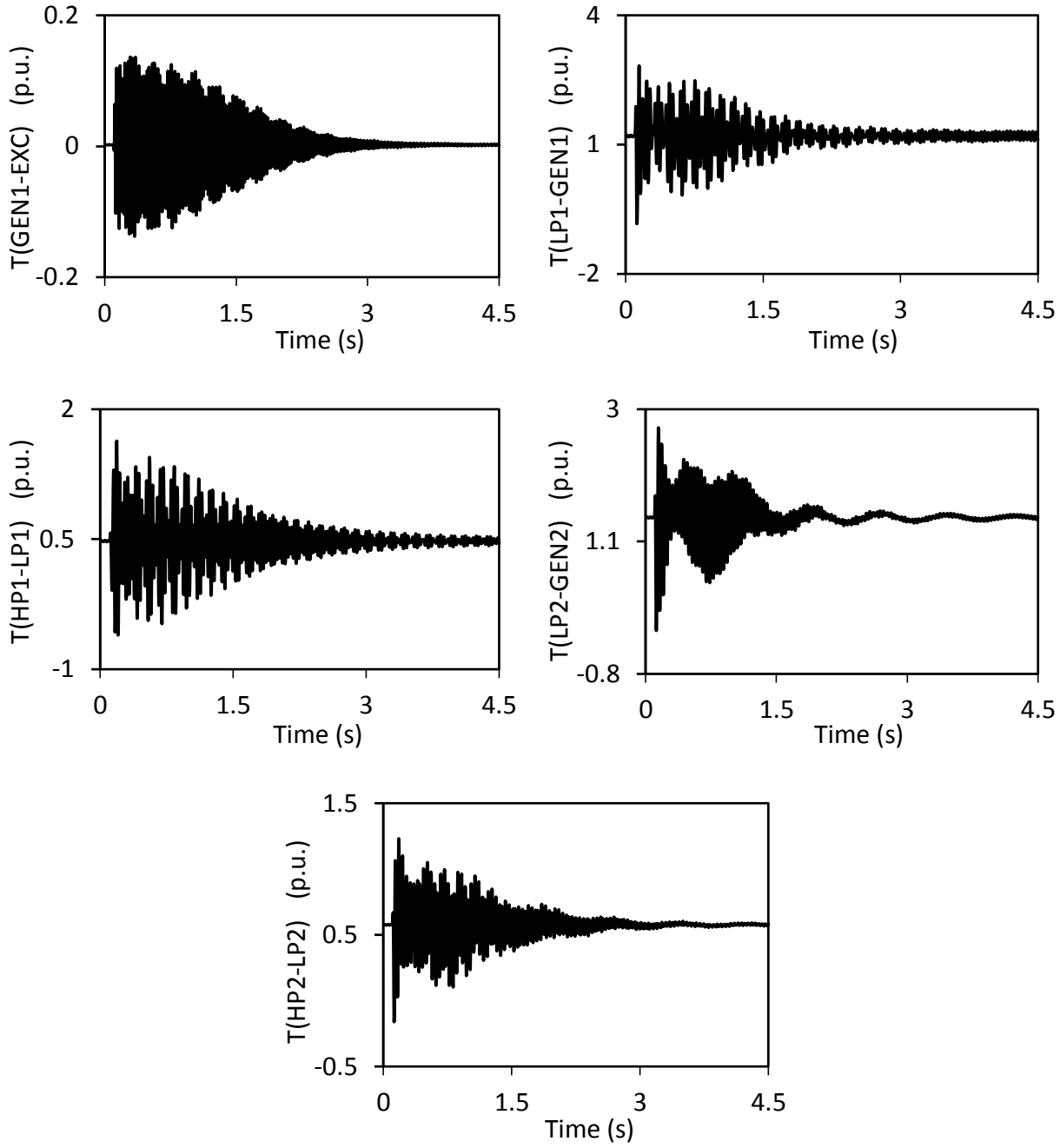

Figure 3.57: Turbine-generator shaft torsional torques during and after clearing a 3-cycle, double line-to-ground fault on Line 5 (60% compensation degree, supplemental control 1 is activated).

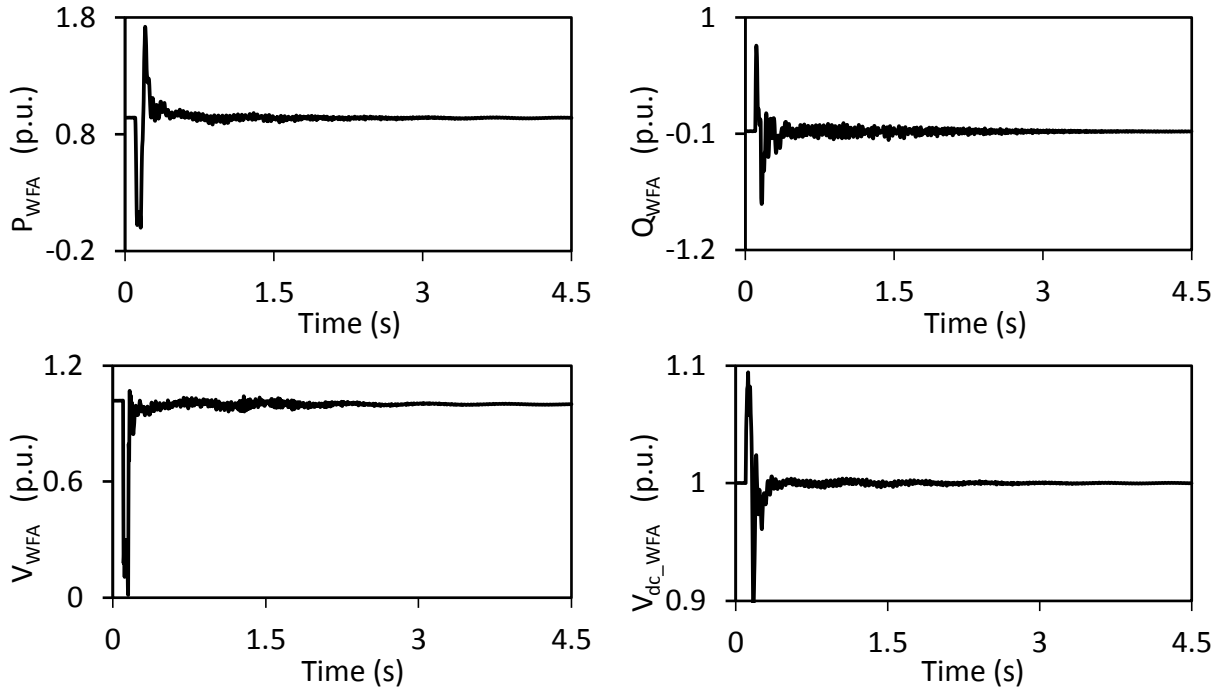

Figure 3.58: Wind farm A real and reactive powers, terminal voltage and dc capacitor voltage during and after clearing a 3-cycle, double line-to-ground fault on Line 5 (60% compensation degree, supplemental control 1 is activated).

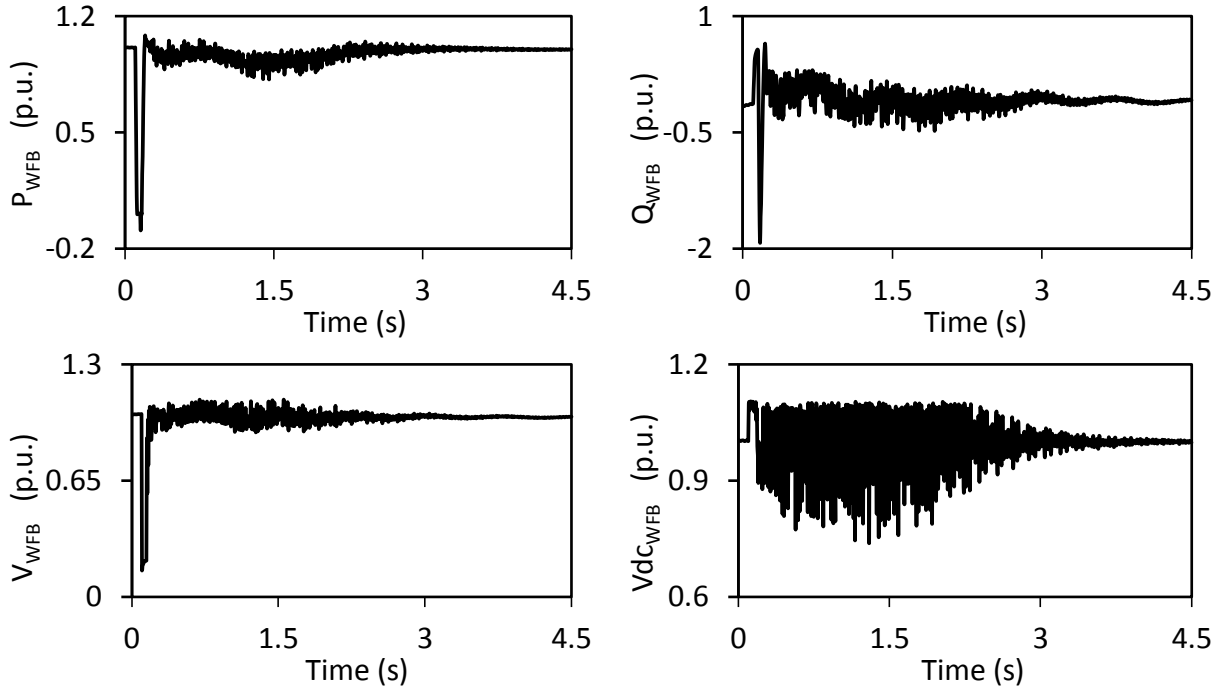

Figure 3.59: Wind farm B real and reactive powers, terminal voltage and dc capacitor voltage during and after clearing a 3-cycle, double line-to-ground fault on Line 5 (60% compensation degree, supplemental control 1 is activated).

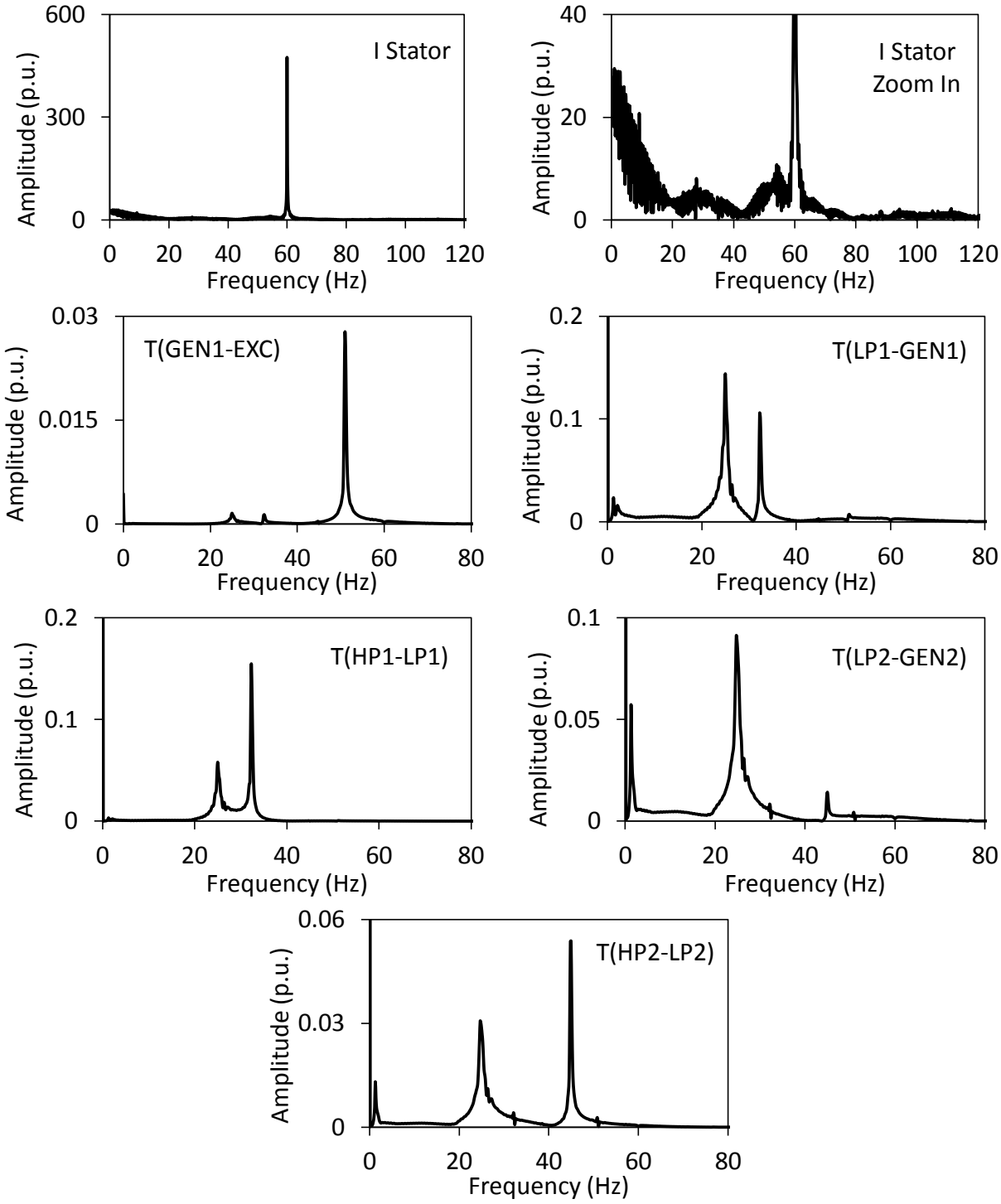

Figure 3.60: Frequency spectrums of the stator current of the DFIG wind turbine and the turbine-generator shaft torsional torques during and after clearing a 3-cycle, double line-to-ground fault on Line 5 (60% compensation degree, supplemental control 1 is activated).

3.4 Performance of Supplemental Control 2 in damping SSR and SSI Oscillations

Figure 3.61 shows the turbine-generator shaft torsional torque time responses during and after clearing a ***3-cycle, three-phase fault on line 5*** for the case when Supplemental control 2 is activated. Figures 3.62 and 3.62 illustrate respectively the time responses of wind farms A and B active and reactive powers, terminal voltage and the BtB dc voltage for the same case. Moreover, Figure 3.64 shows the frequency spectrums of the stator current of the DFIG wind turbines and the turbine-generator shaft torsional torques for the same study case. Furthermore, the transfer functions of Supplemental control 2 are the same as those in Table 3.1. The comparison between the two groups of figures (Figures 3.5, 3.6, 3.7, 3.8) and (Figures 3.61, 3.62, 3.63, 3.64) establishes the effectiveness of Supplemental control 2 in damping the torsional torques in all turbine-generator shaft sections as well as in mitigating SSI in wind farm A.

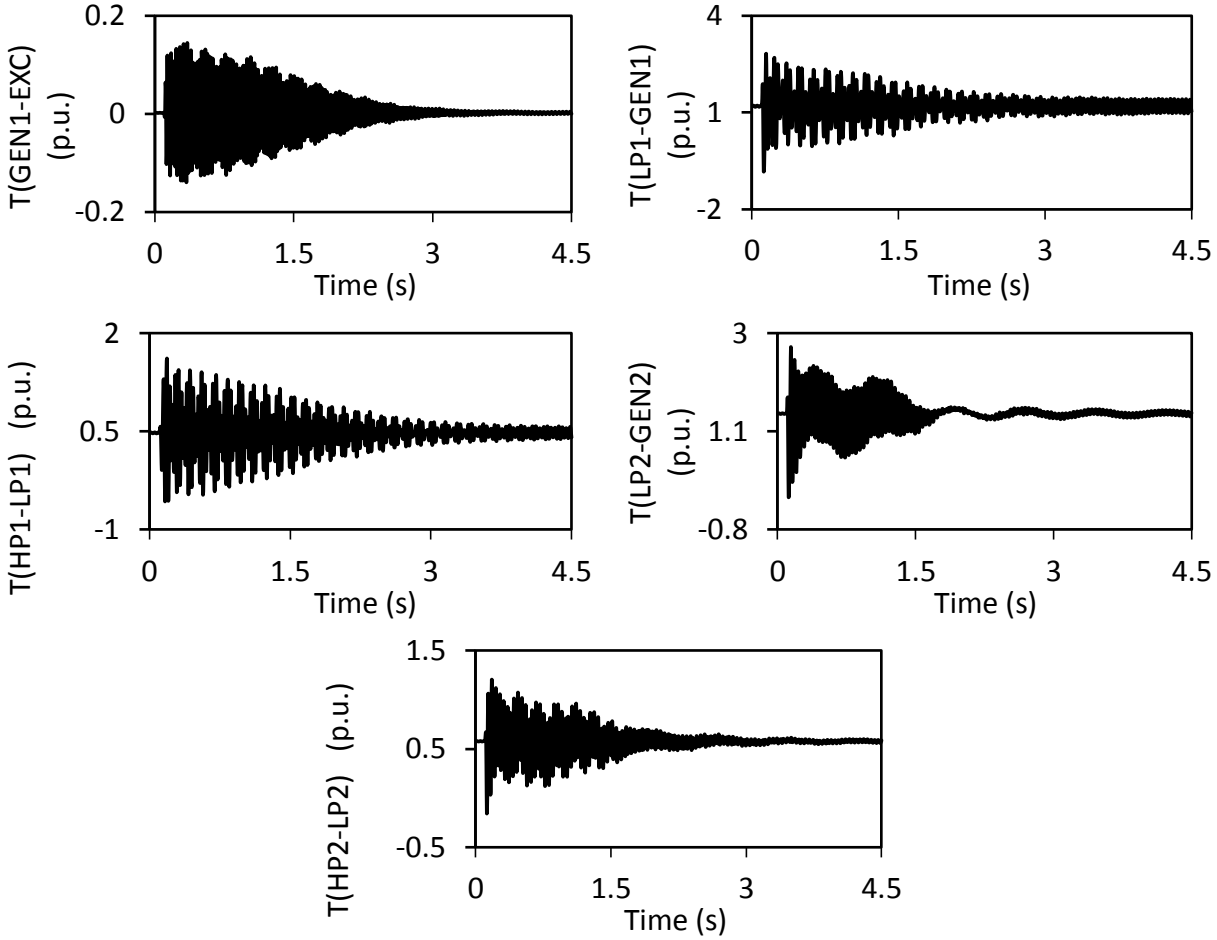

Figure 3.61: Turbine-generator shaft torsional torques during and after clearing a 3-cycle, three-phase fault on Line 5 (60% compensation degree, supplemental control 2 is activated).

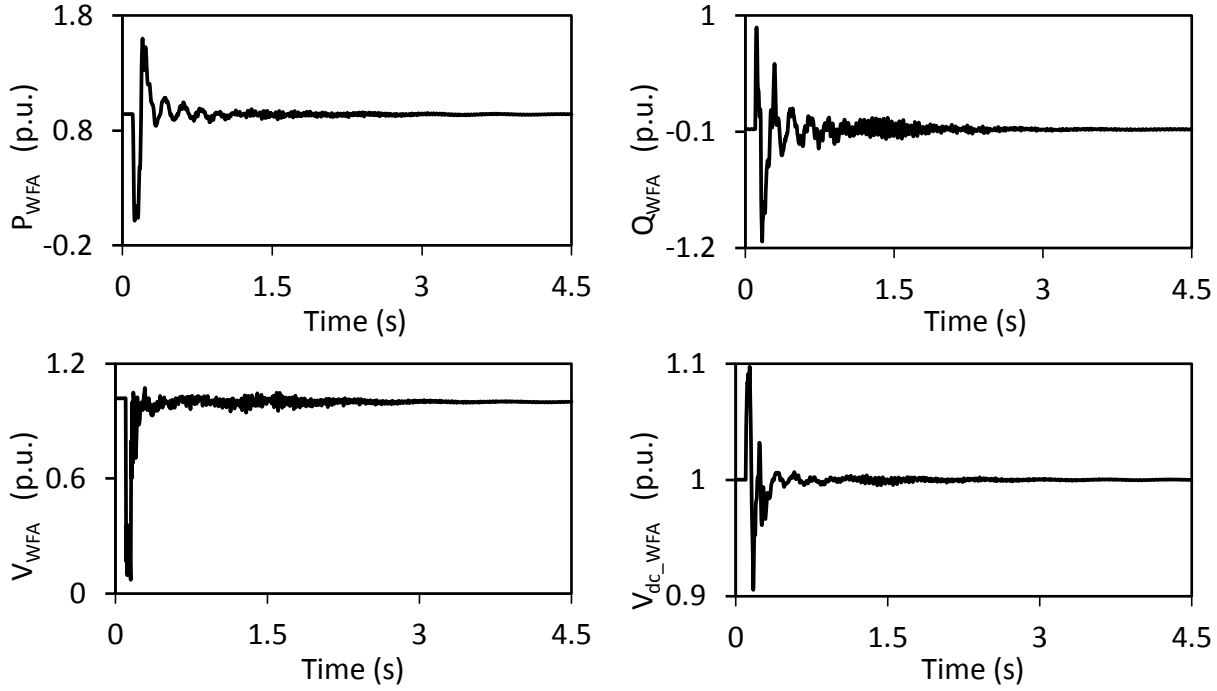

Figure 3.62: Wind farm A real and reactive powers, terminal voltage and dc capacitor voltage during and after clearing a 3-cycle, three-phase fault on Line 5 (60% compensation degree, supplemental control 2 is activated).

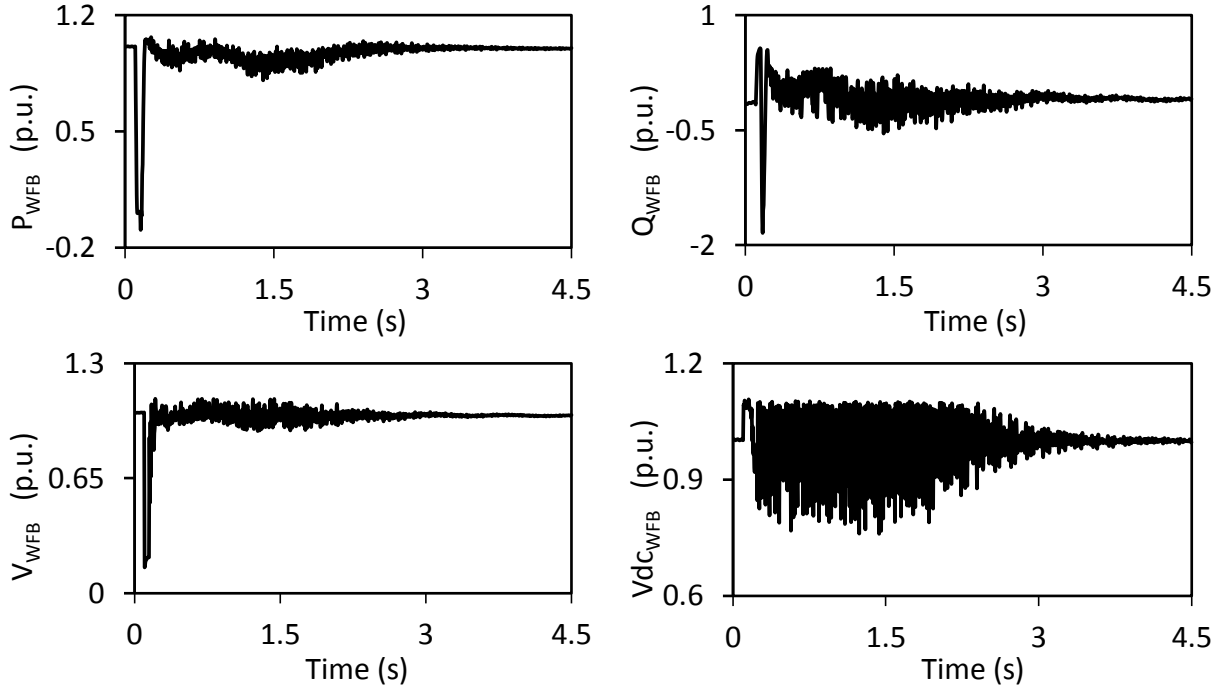

Figure 3.63: Wind farm B real and reactive powers, terminal voltage and dc capacitor voltage during and after clearing a 3-cycle, three-phase fault on Line 5 (60% compensation degree, supplemental control 2 is activated).

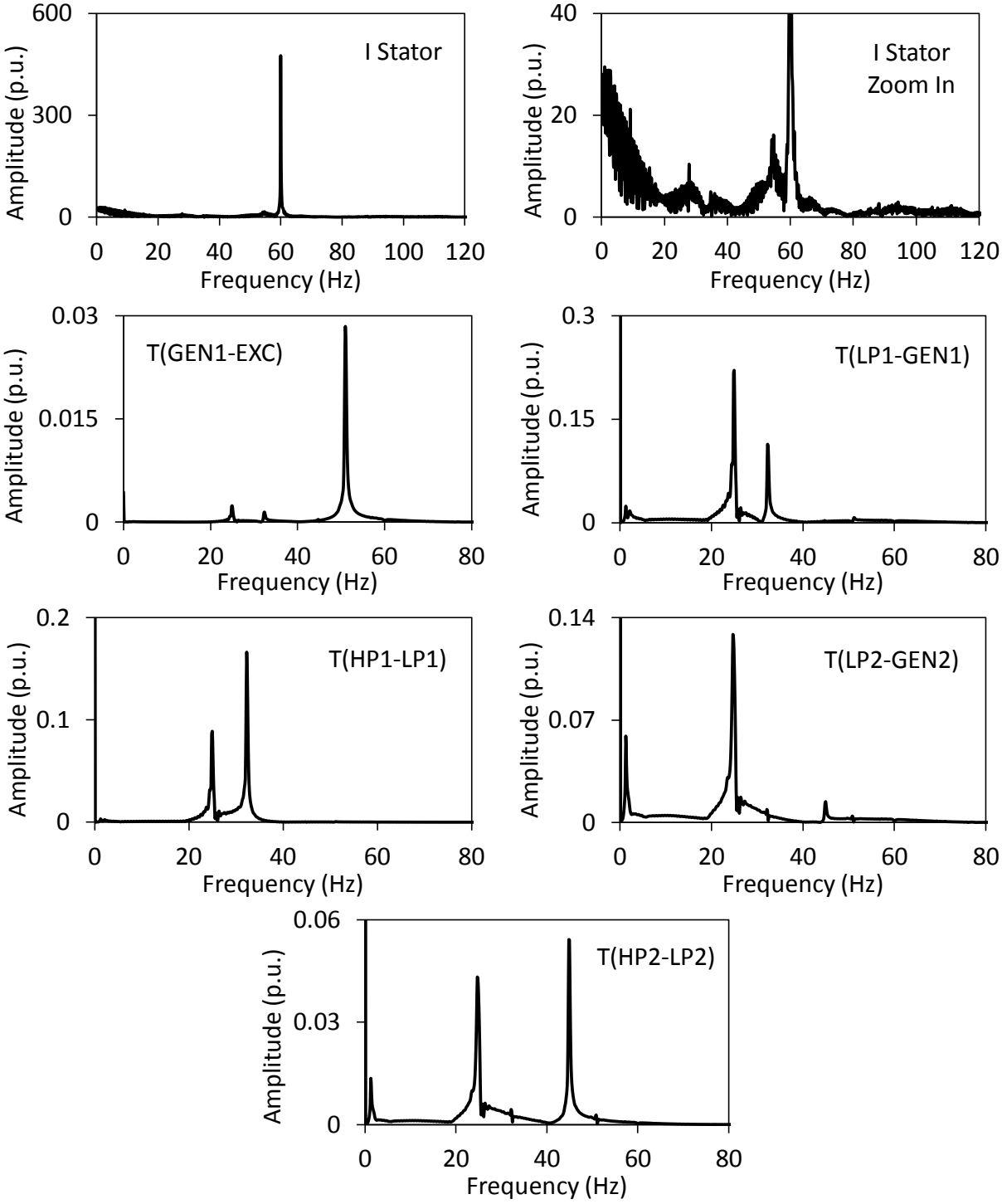

Figure 3.64: Frequency spectrums of the stator current of the DFIG wind turbine and the turbine-generator shaft torsional torques during and after clearing a 3-cycle, three-phase fault on Line 5 (60% compensation degree, supplemental control 2 is activated).

3.4.1 Effect of the fault location

The effect of the fault location on the performance of Supplemental control 2 is examined by applying a three-cycle, three-phase fault on Line 4. The results of this study are presented in the following two groups of figures:

Group A: Supplemental control 2 is disabled, (Figures 3.65, 3.66, 3.67, 3.68)

Group B: Supplemental control 2 is activated, (Figures 3.69, 3.70, 3.71, 3.72)

In each group, the turbine-generator shaft torsional torques, wind farms A and B active and reactive powers, terminal voltage and the BtB dc voltage as well as the frequency spectrums of the stator current of the DFIG wind turbines and the turbine-generator shaft torsional torques are shown. Moreover, the transfer functions of Supplemental control 2 in Group B are given in Table 3.5.

Table 3.5: Transfer functions of Supplemental control 2 (Wind farm B rating = 200 MW, three-phase fault on Line 4).

Modal speeds	Transfer function
G1, $\Delta_{\omega m0}$	0
G1, $\Delta_{\omega m1}$	$G_{\omega_1}(s) = 20000\dfrac{0.1s+1}{s+100}$
G1, $\Delta_{\omega m2}$	$G_{\omega_2}(s) = -2.5\dfrac{0.1s+100}{s+1}$
G1, $\Delta_{\omega m3}$	$G_{\omega_3}(s) = 25\dfrac{s+2000}{s+0.1}$
G2, $\Delta_{\omega m0}$	0
G2, $\Delta_{\omega m1}$	$G_{\omega_1}(s) = 20000\dfrac{0.1s+5}{s+100}$
G2, $\Delta_{\omega m2}$	$G_{\omega_2}(s) = -15000\dfrac{s+5}{s+1}$
Washout filter	$G(s) = \dfrac{s}{s+10}$
Band-Pass filter	$G(s) = \dfrac{62.83s}{s^2+62.83s+35500}$
Lead-Lag compensator	$G(s) = \dfrac{s+250}{s+1}$
U_{Total_max}, U_{Total_min}	0.33, -0.33 (same for both FFC and DFIG wind turbines)

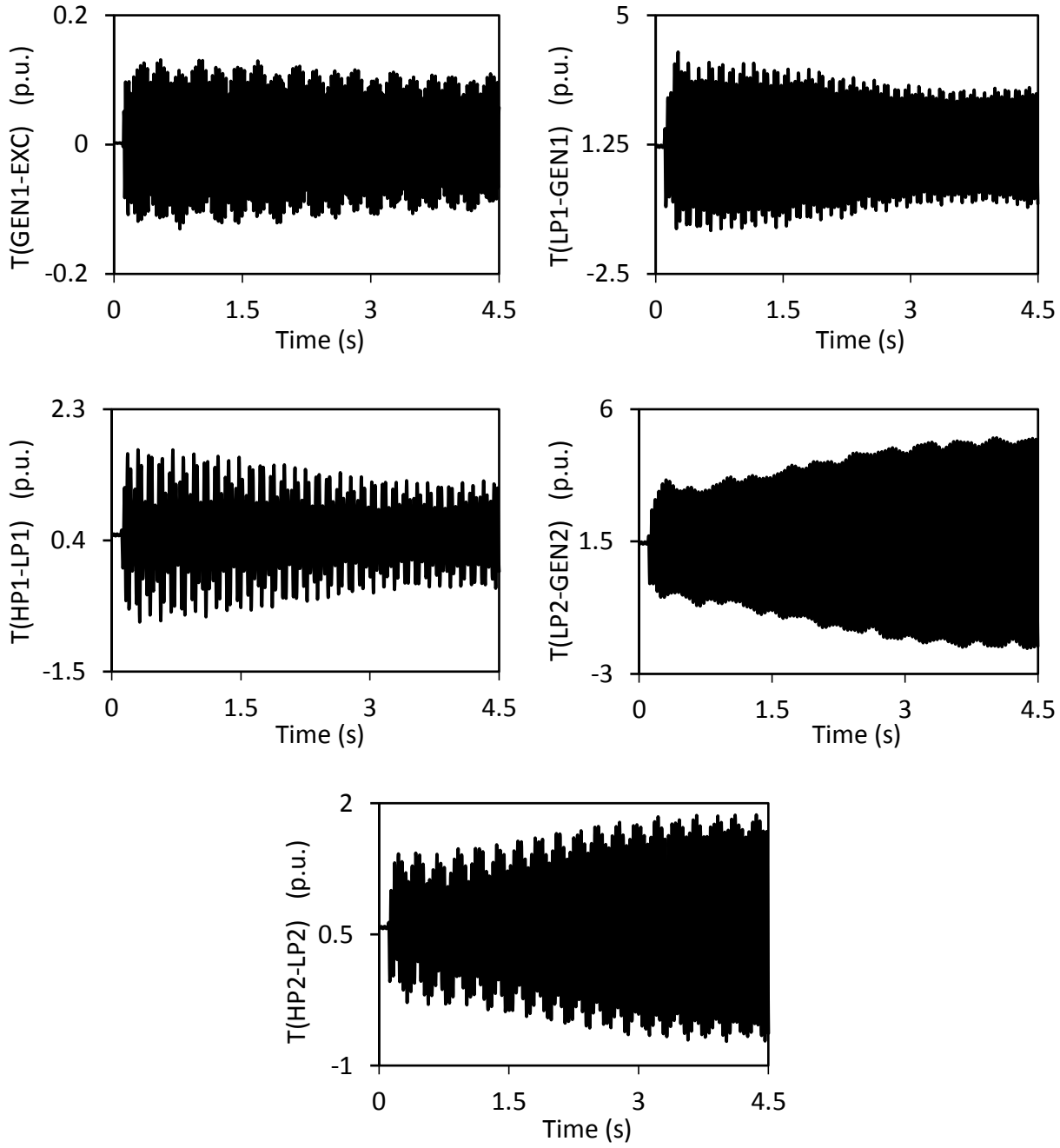

Figure 3.65: Turbine-generator shaft torsional torques during and after clearing a 3-cycle, three-phase fault on Line 4 (60% compensation degree, supplemental control 2 is not activated).

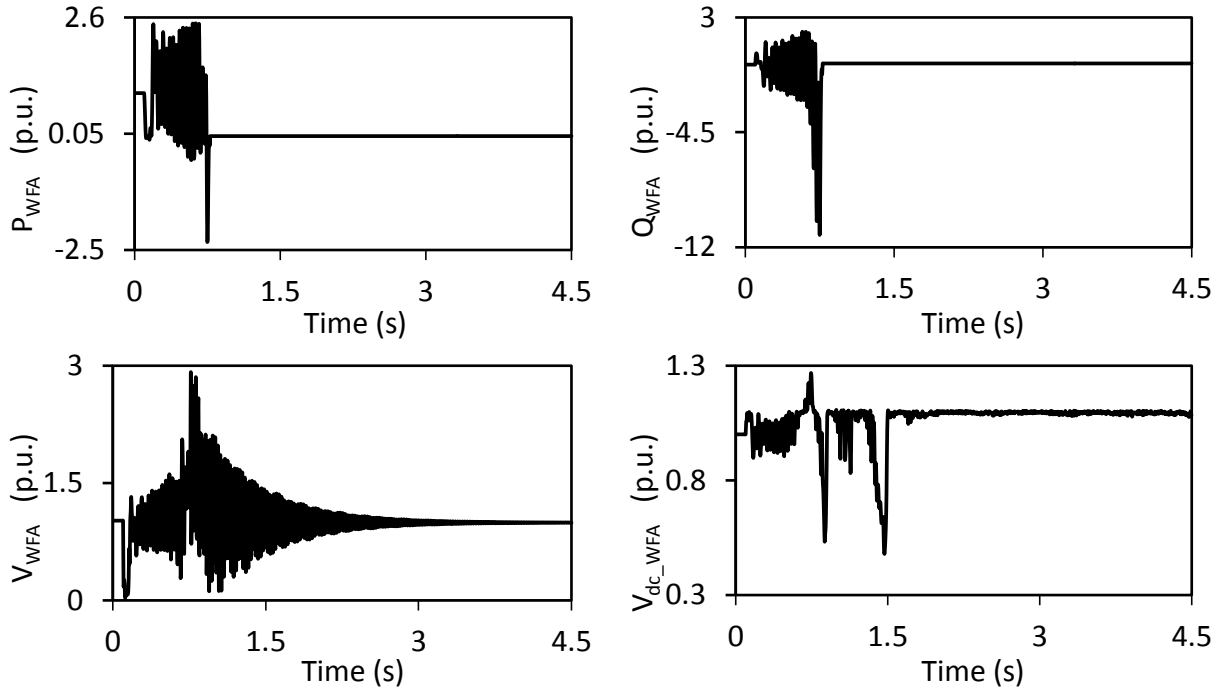

Figure 3.66: Wind farm A real and reactive powers, terminal voltage and dc capacitor voltage during and after clearing a 3-cycle, three-phase fault on Line 4 (60% compensation degree, supplemental control 2 is not activated).

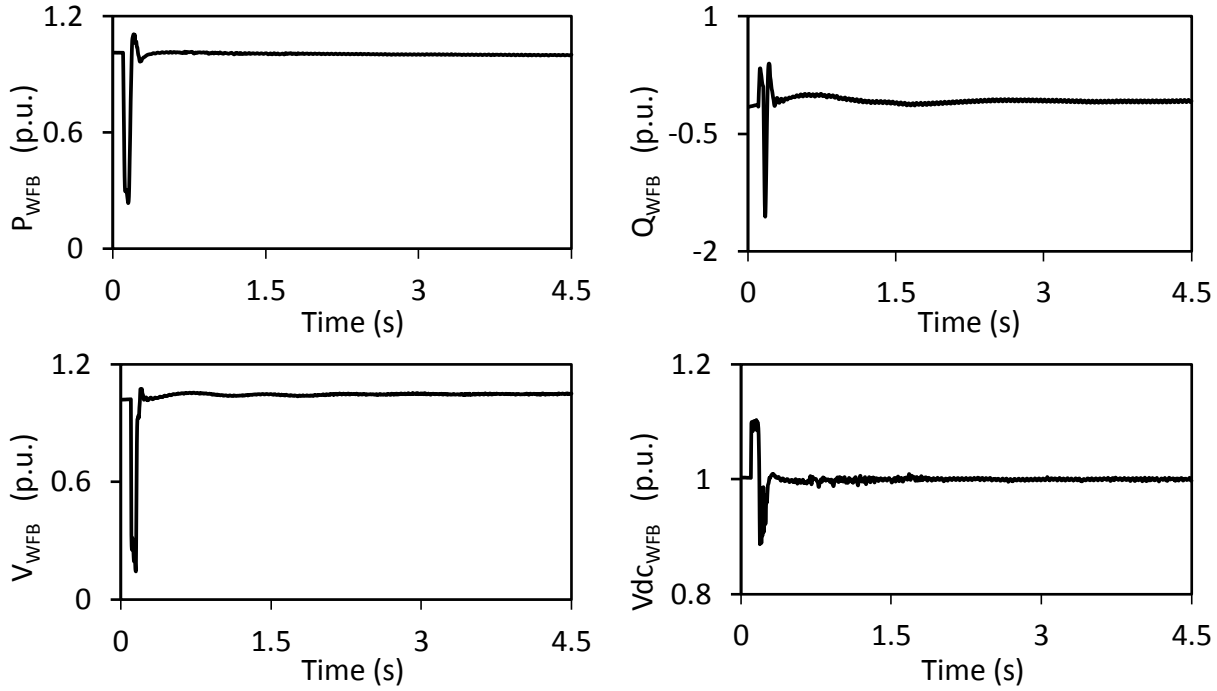

Figure 3.67: Wind farm B real and reactive powers, terminal voltage and dc capacitor voltage during and after clearing a 3-cycle, three-phase fault on Line 4 (60% compensation degree, supplemental control 2 is not activated).

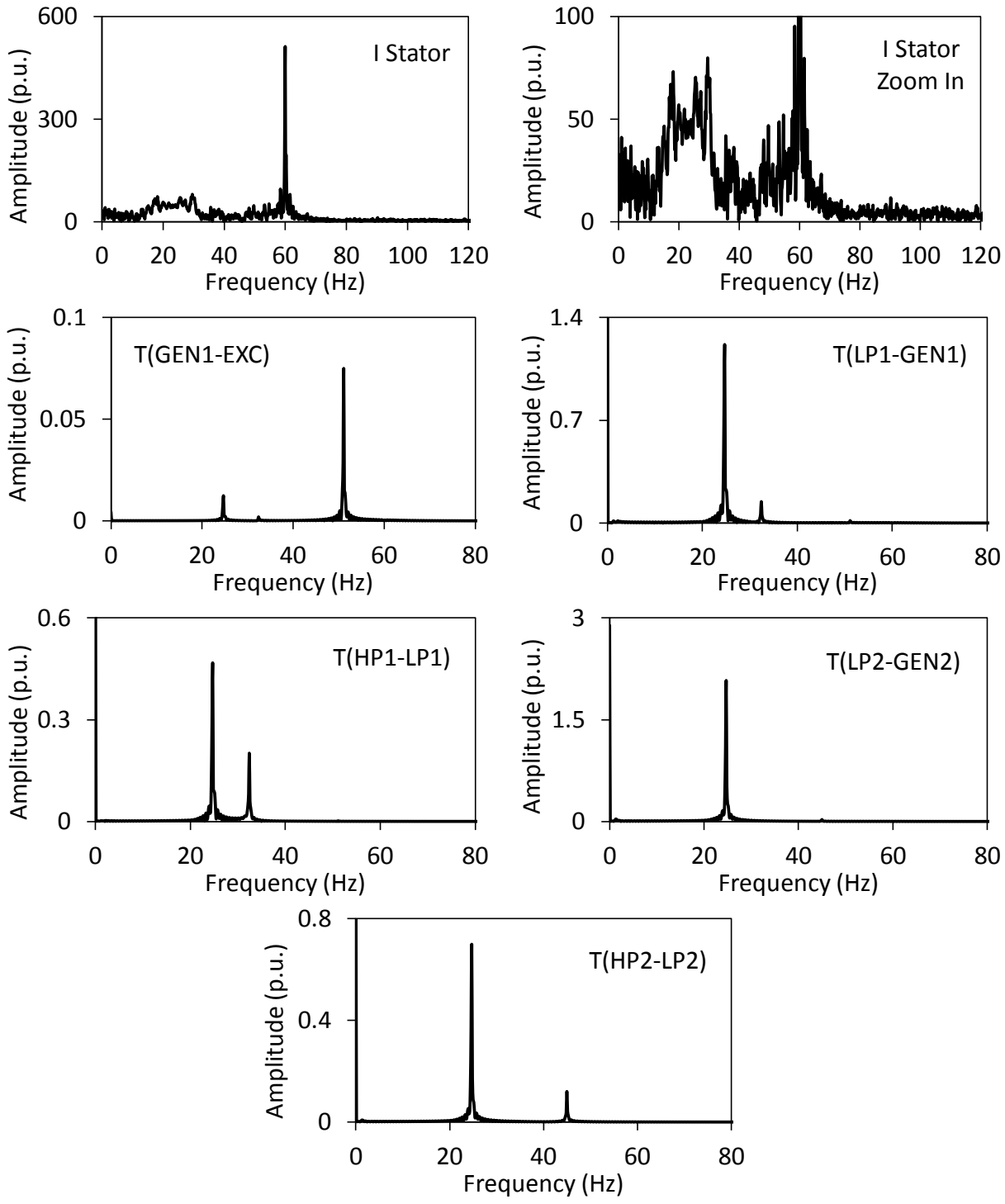

Figure 3.68: Frequency spectrums of the stator current of the DFIG wind turbine and the turbine-generator shaft torsional torques during and after clearing a 3-cycle, three-phase fault on Line 4 (60% compensation degree, supplemental control 2 is not activated).

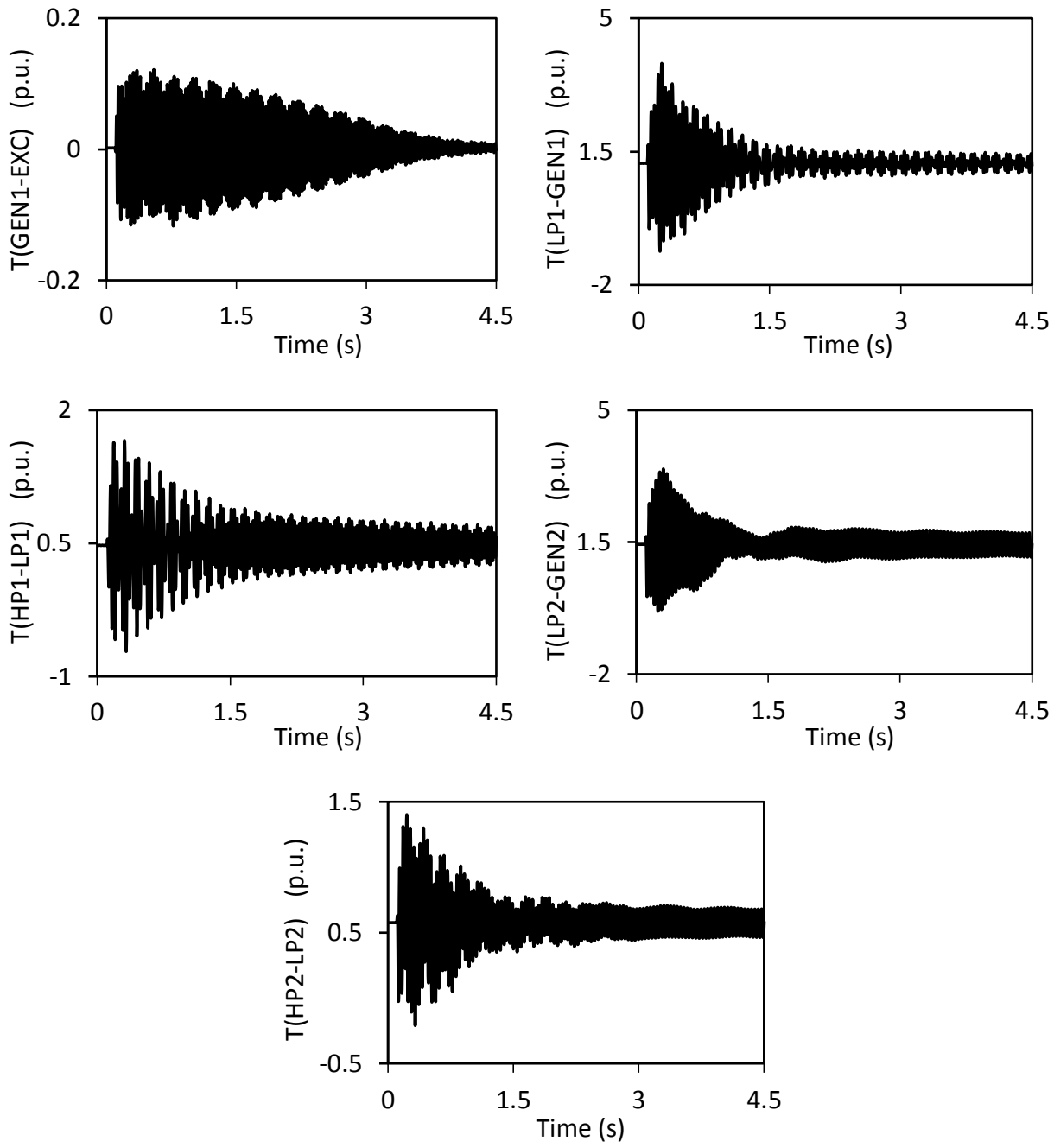

Figure 3.69: Turbine-generator shaft torsional torques during and after clearing a 3-cycle, three-phase fault on Line 4 (60% compensation degree, supplemental control 2 is activated).

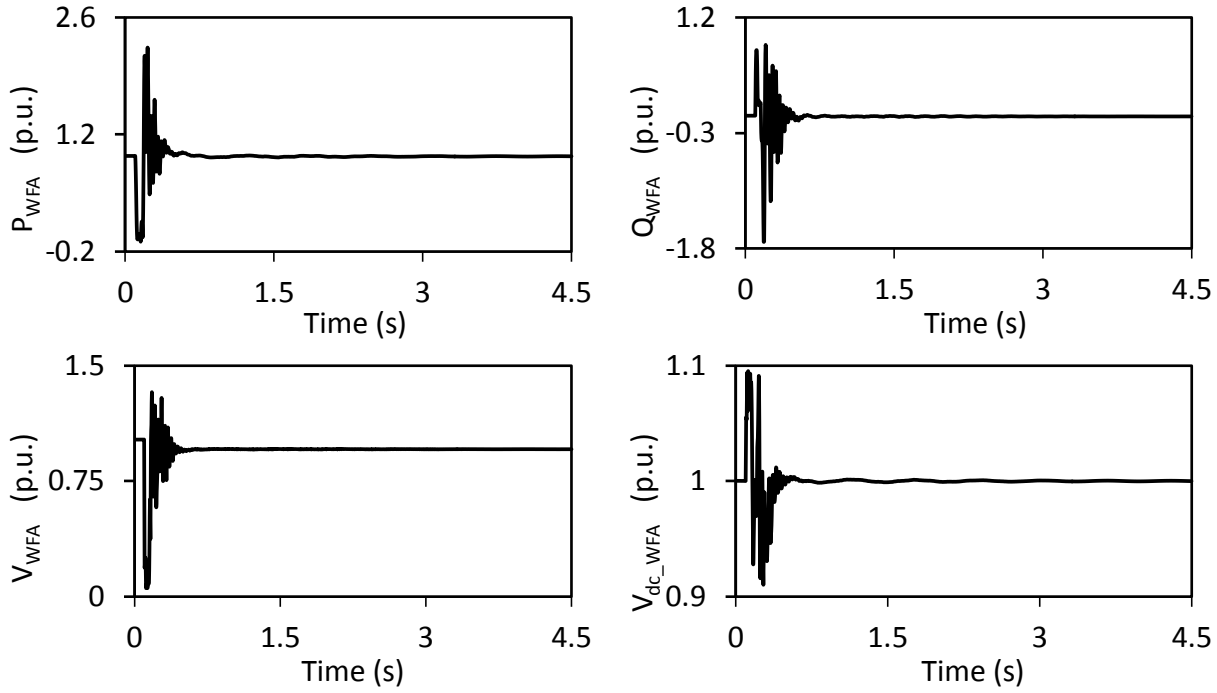

Figure 3.70: Wind farm A real and reactive powers, terminal voltage and dc capacitor voltage during and after clearing a 3-cycle, three-phase fault on Line 4 (60% compensation degree, supplemental control 2 is activated).

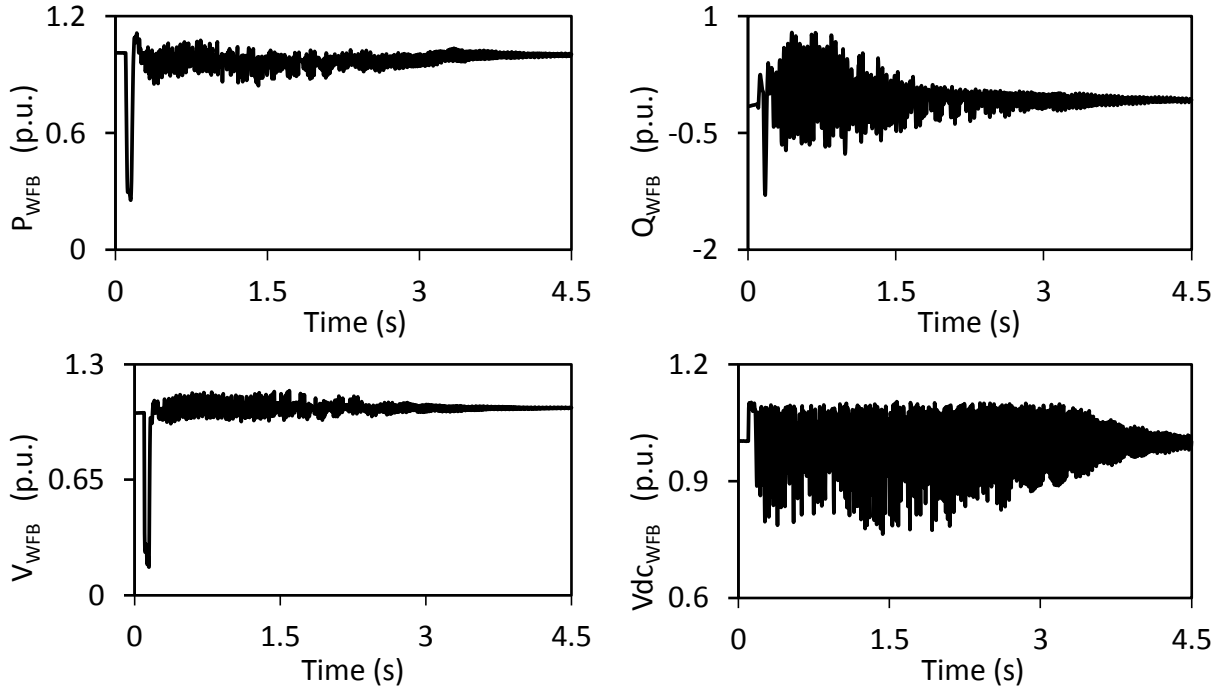

Figure 3.71: Wind farm B real and reactive powers, terminal voltage and dc capacitor voltage during and after clearing a 3-cycle, three-phase fault on Line 4 (60% compensation degree, supplemental control 2 is activated).

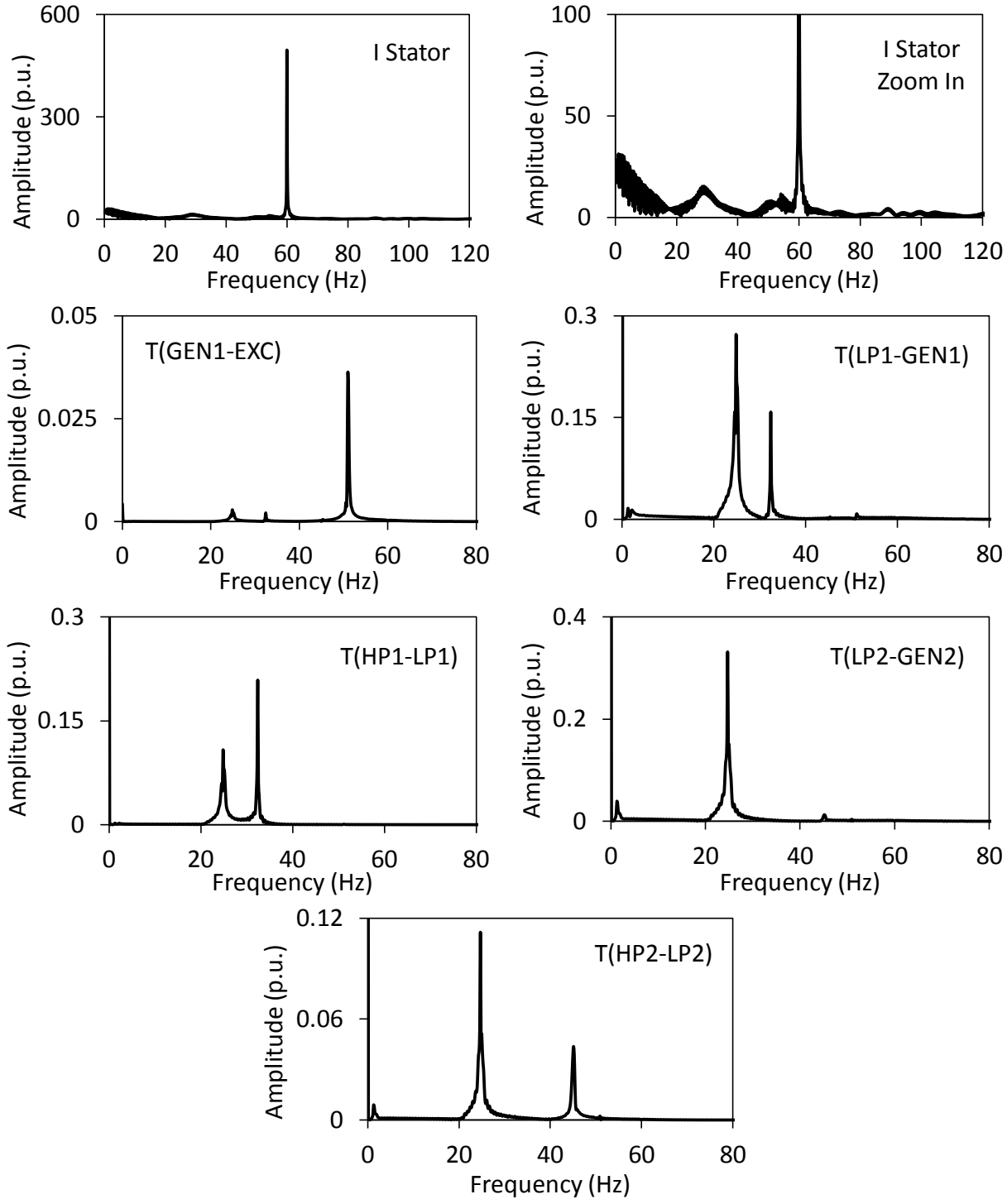

Figure 3.72: Frequency spectrums of the stator current of the DFIG wind turbine and the turbine-generator shaft torsional torques during and after clearing a 3-cycle, three-phase fault on Line 4 (60% compensation degree, supplemental control 2 is activated).

As it can be seen from Figure 2.1, clearing a system fault on line L4 "virtually" isolates wind farm A from wind farm B and the turbine-generators. Wind farm A is now radially connected to the infinite-bus system through a series capacitor compensated transmission line (Line 2). This is a favorable condition for the occurrence of SSI. As it can be seen from Figure 3.66, wind farm A real and reactive powers exhibit severe oscillations after fault clearing that result in the tripping of the wind farm by the protective system at t = 0.75 seconds.

Regarding the turbine-generator shaft torsional torques, Figure 3.65 shows that these torques exhibit either decaying, sustained or growing oscillations. These oscillations, however, have no adverse impact on the performance of wind farm B as it can be seen from Figure 3.67.

The comparison between the figures in Groups A and B demonstrates the effectiveness of Supplemental control 2 in mitigating SSR and SSI after clearing a three-phase fault at a different location.

3.4.2 Effect of the compensation degree

The effect of the compensation degree of transmission Lines 1 and 2 on the performance of Supplemental control 2 is examined by changing it from 60% to 50%. Moreover, the disturbance is a three-cycle, three-phase fault on Line 5. The results of this study are presented in the following two groups of figures:

Group A: Supplemental control 2 is disabled, (Figures 3.73, 3.74, 3.75, 3.76)

Group B: Supplemental control 2 is activated, (Figures 3.77, 3.78, 3.79, 3.80)

In each group, the turbine-generator shaft torsional torques, wind farms A and B active and reactive powers, terminal voltage and the BtB dc voltage as well as the frequency spectrums of the stator current of the DFIG wind turbines and the turbine-generator shaft torsional torques are shown. Moreover, the transfer functions of Supplemental control 2 in Groups B are given in Table 3.6.

The comparison between Figures 3.5, 3.8 and Figures 3.73, 3.76 shows that changing the series capacitive compensation degrees results in changing the contributions of the torsional modes to the induced torsional torques in the different shaft sections of the turbine-generators. As it can

be seen from Figure 3.73, some of the turbine-generator shaft torsional torques exhibit growing oscillations that indicate the presence of SSR. On the other hand, Figure 3.74 clearly shows the absence of SSI in wind farm A. Moreover, Figure 3.75 shows that the adverse impact of SSR is not extended to affect the performance of wind farm B. The comparison between the figures in Groups A and B demonstrates the effectiveness of the supplemental control in mitigating SSR at the 50% compensation degree of Lines 1 and 2.

Table 3.6: Transfer functions of Supplemental control 2 (Three-phase fault on Line 5, 50% compensation).

Modal speeds	Transfer function
G1, $\Delta_{\omega m0}$	0
G1, $\Delta_{\omega m1}$	$G_{\omega_1}(s) = 2.5\frac{s+2000}{s+1}$
G1, $\Delta_{\omega m2}$	$G_{\omega_2}(s) = -2.5\frac{s+1000}{s+1}$
G1, $\Delta_{\omega m3}$	$G_{\omega_3}(s) = 2.5\frac{s+1000}{s+1}$
G2, $\Delta_{\omega m0}$	0
G2, $\Delta_{\omega m1}$	$G_{\omega_1}(s) = 25\frac{s+500}{s+1}$
G2, $\Delta_{\omega m2}$	$G_{\omega_2}(s) = 25\frac{s+1250}{s+1}$
Washout filter	$G(s) = \frac{s}{s+10}$
Band-Pass filter	$G(s) = \frac{62.83s}{s^2+62.83s+35500}$
Lead-Lag compensator	$G(s) = \frac{s+250}{s+1}$
U_{Total_max}, U_{Total_min}	0.33, -0.33 (same for both FFC and DFIG wind turbines)

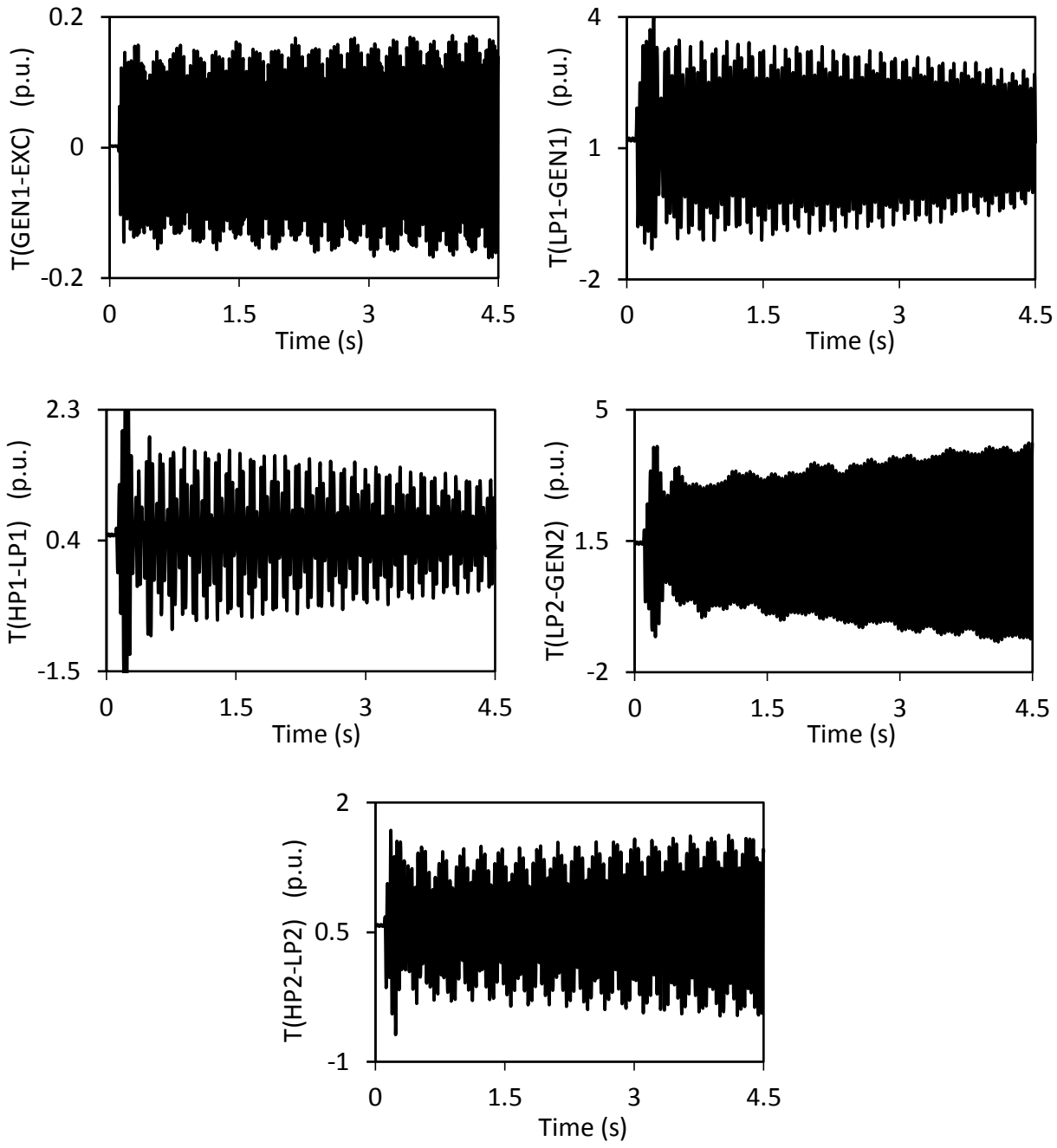

Figure 3.73: Turbine-generator shaft torsional torques during and after clearing a 3-cycle, three-phase fault on Line 5 (50% compensation degree, supplemental control 2 is not activated).

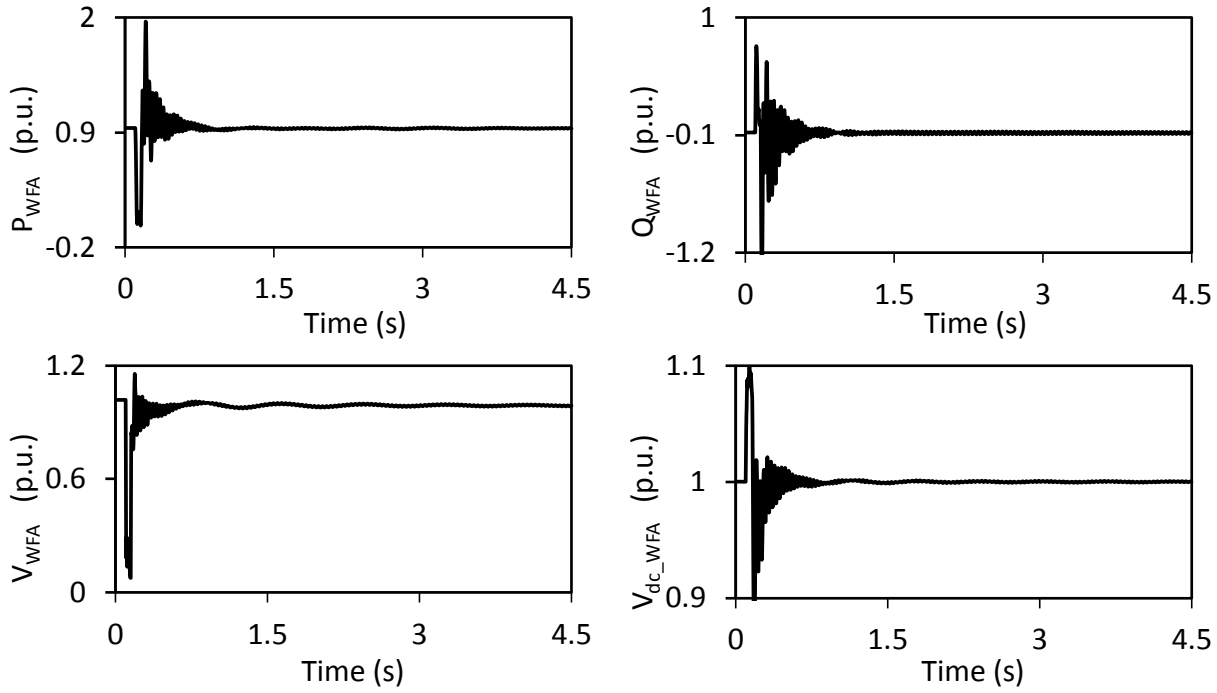

Figure 3.74: Wind farm A real and reactive powers, terminal voltage and dc capacitor voltage during and after clearing a 3-cycle, three-phase fault on Line 5 (50% compensation degree, supplemental control 2 is not activated).

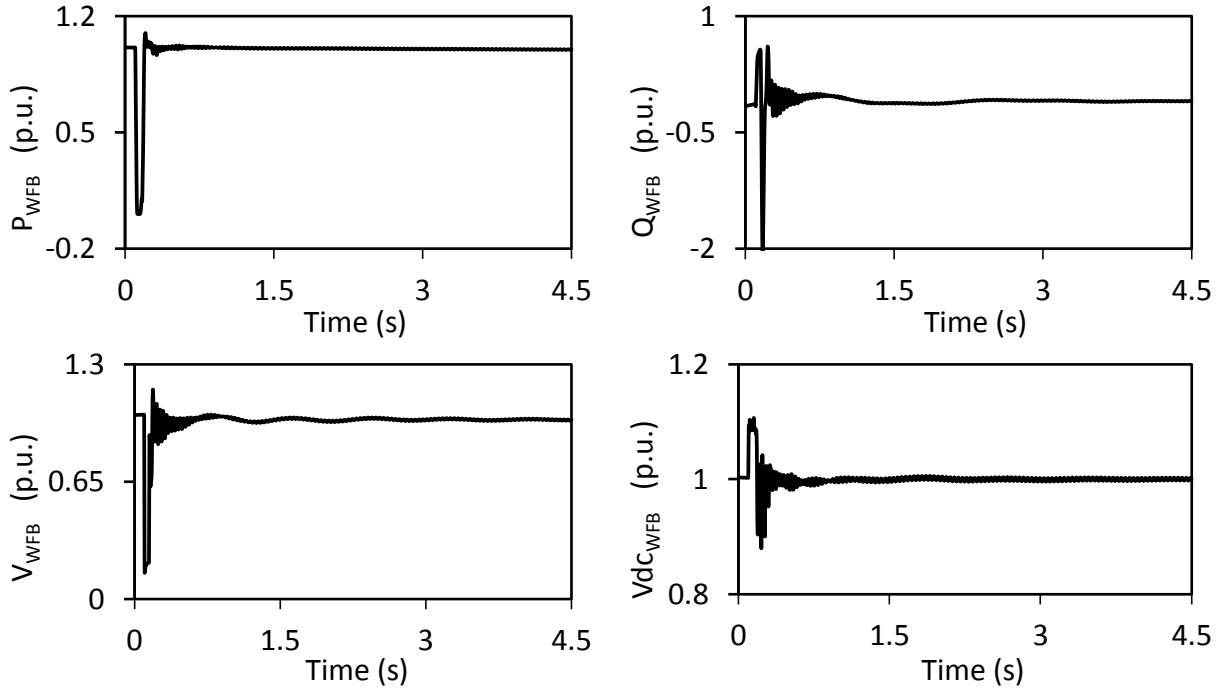

Figure 3.75: Wind farm B real and reactive powers, terminal voltage and dc capacitor voltage during and after clearing a 3-cycle, three-phase fault on Line 5 (50% compensation degree, supplemental control 2 is not activated).

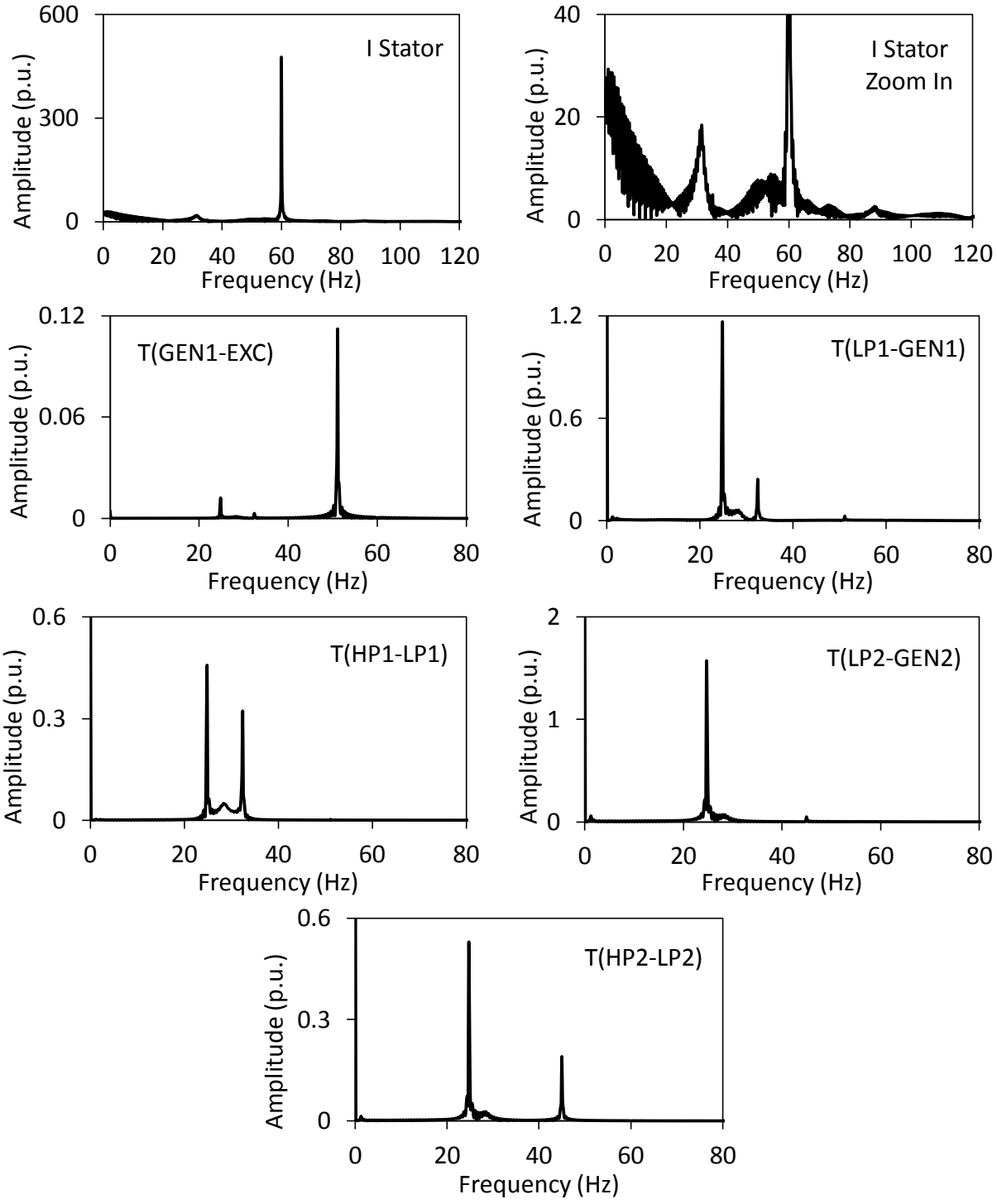

Figure 3.76: Frequency spectrums of the stator current of the DFIG wind turbine and the turbine-generator shaft torsional torques during and after clearing a 3-cycle, three-phase fault on Line 5 (50% compensation degree, supplemental control 2 is not activated).

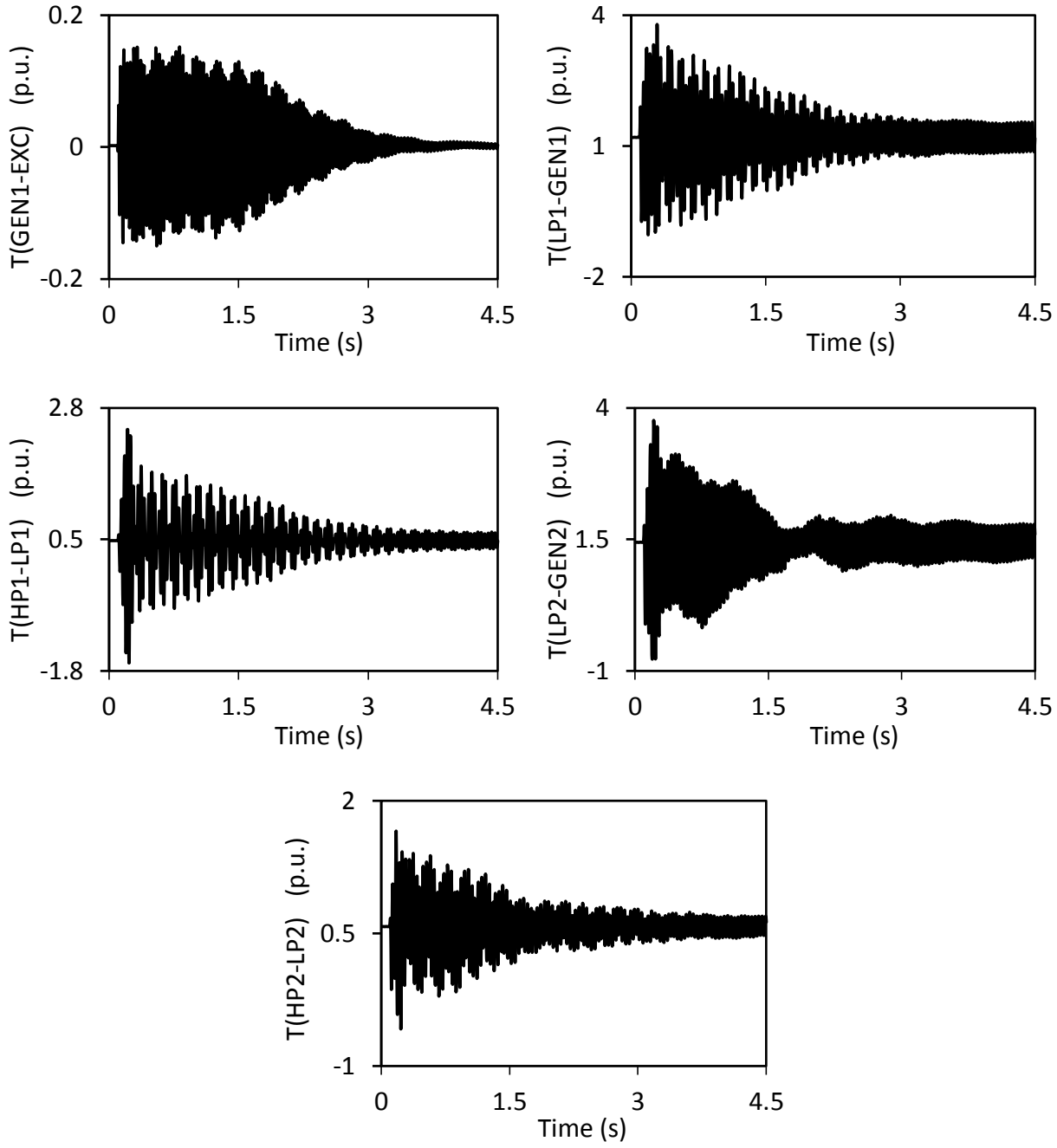

Figure 3.77: Turbine-generator shaft torsional torques during and after clearing a 3-cycle, three-phase fault on Line 5 (50% compensation degree, supplemental control 2 is activated).

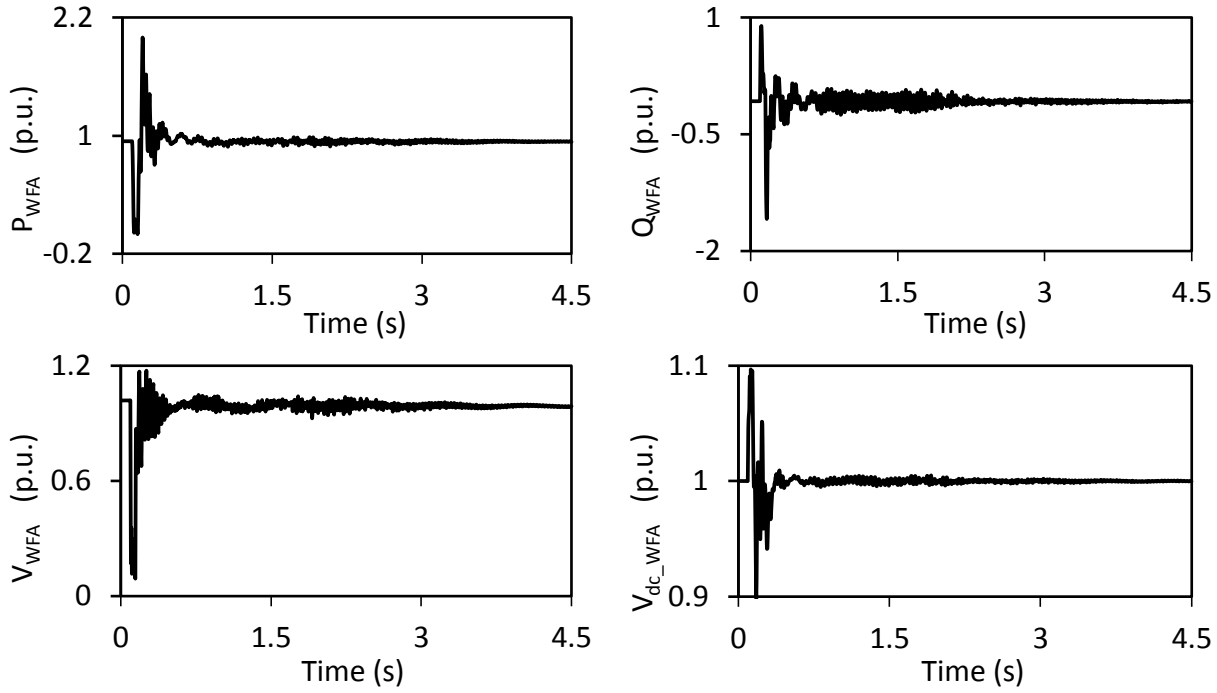

Figure 3.78: Wind farm A real and reactive powers, terminal voltage and dc capacitor voltage during and after clearing a 3-cycle, three-phase fault on Line 5 (50% compensation degree, supplemental control 2 is activated).

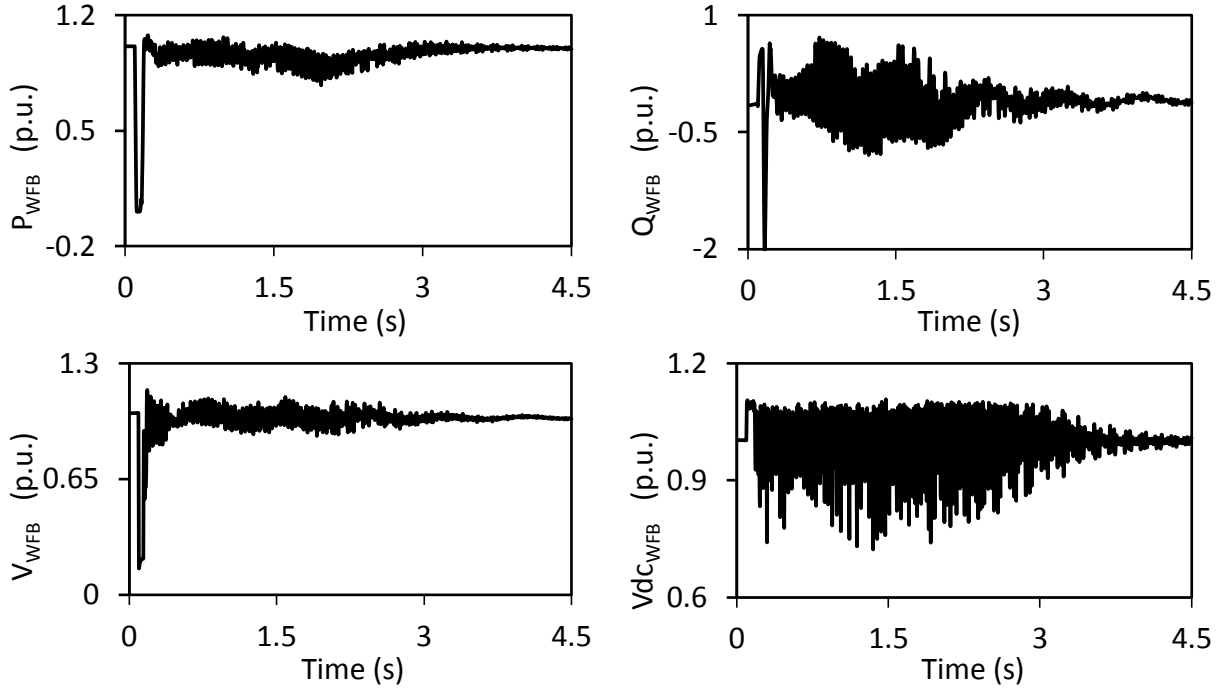

Figure 3.79: Wind farm B real and reactive powers, terminal voltage and dc capacitor voltage during and after clearing a 3-cycle, three-phase fault on Line 5 (50% compensation degree, supplemental control 2 is activated).

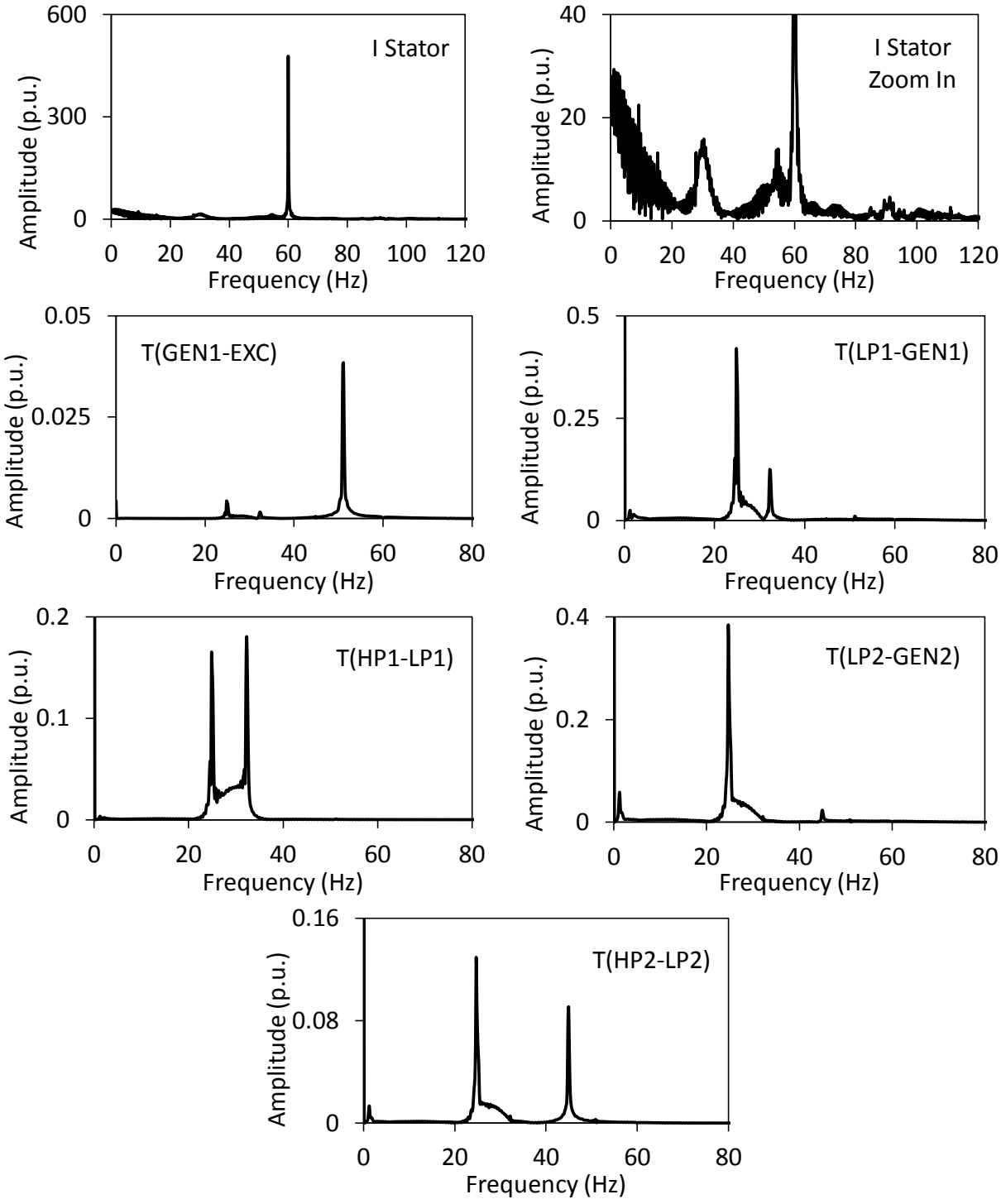

Figure 3.80: Frequency spectrums of the stator current of the DFIG wind turbine and the turbine-generator shaft torsional torques during and after clearing a 3-cycle, three-phase fault on Line 5 (50% compensation degree, supplemental control 2 is activated).

3.5 Summary

In this chapter, two supplemental controls of FFC- and DFIG-based wind farms for mitigating SSR and SSI are presented. The effectiveness of these controllers are investigated through several case studies of time-domain simulations for different fault type, fault location, transmission line compensation degrees as well as the rating and location of the FFC-based wind farm. The main conclusions drawn from the results of these studies are presented in the next chapter.

4. SUMMARY AND CONCLUSIONS

4.1 Summary

Transmission system capability limitations and the ways to overcome them are challenging problems facing power system engineers. The reasons for transmission system limitations extend from steady-state and thermal considerations to transient and dynamic stability of the power system. It can be due to unfavorable power flow pattern in the transmission system where some of the transmission lines may be very close to their thermal limits while other lines may have unnecessarily large thermal margins. Other reasons are transient and dynamic stability considerations, which impose limits on the power that can be transmitted while ensuring that the power system will be able to regain a new stable state following any expected disturbance. Due to these limitations, transmission lines are often loaded to levels below of their thermal capability and, in order to increase their loadability limit, some measures must be adopted.

Series capacitive compensation is the most economical way for increasing the transmission capacity and improving power system transient stability. However, subsynchronous resonance (SSR) is one of the major obstacles for the wide spread of high degrees (60% and higher) of series capacitor compensation. Recently, a new obstacle, namely subsynchronous interaction (SSI) has been added to the list after the Zorillo Gulf wind farm incident in Texas in October 2009. SSI is due to the interaction between large doubly fed induction generator (DFIG)-based wind farms and series capacitor compensated transmission systems.

In integrated power systems incorporating series capacitor compensated transmission lines and high penetration of wind energy conversion systems, especially DFIG-based wind farms, SSR and SSI could occur concurrently as a result of some system contingences. One solution to SSR and SSI is to avoid those series compensation degrees that excite the two phenomena. This is, however, a difficult to implement due to the large number of variables that impact SSR and SSI and may not be cost effective in view of reduced system capacity. Therefore, mitigating SSR

and SSI is an important area of research and development targeting at developing practical and effective countermeasures.

This thesis investigates the potential use of variable speed wind energy conversion systems (full-scale frequency converter (FFC) and doubly-fed induction generator (DFIG)-based wind farms) for concurrent mitigation of SSR and SSI. SSR and SSI damping is achieved by introducing supplemental control signals in the reactive power control loops of the grid side converters of the FFC and DFIG wind turbines of large wind farms.

Chapter 1 introduces some fundamental benefits of series compensation of transmission lines. Brief introductions to SSR and SSI are also presented. The objective of the research is also presented in this chapter.

In Chapter 2, the system used for the investigations conducted in this thesis is described and the detailed dynamic models of its individual components are also presented in this chapter. The results of the digital time-domain simulations of a case study for the system during a three-phase fault are presented at the end of this chapter.

Chapter 3 demonstrates the effectiveness of two supplemental controls in damping SSR and SSI oscillations through time-domain simulation studies. The supplemental controls performance at different system contingencies and operating conditions is also investigated.

4.2 Conclusions

The studies conducted in this thesis yield the following conclusions for the system under study:

1. Subsynchronous resonance and subsynchronous interaction do not necessarily occur simultaneously, at all high degrees (50% and higher) of transmission line series capacitive compensation.
2. The turbine-generator shaft torsional torques are not sinusoidal with a single frequency but contain contributions from all the torsional modes. Moreover, the shaft section between the generators and low-pressure turbines are subjected to the highest stresses.
3. Changing the series capacitive compensation degrees results in changing the contributions of the torsional modes to the induced torsional torques in the different shaft sections of the turbine-generators.

4. The adverse impacts of SSR are more severe than those of SSI. Although FFC wind turbines are "supposed" to be immune to SSI because their back-to-back converters virtually isolate them from the system dynamics, the studies have shown that SSR can cause FFC wind turbines to exhibit induction generator (IG) effect.
5. The electrical subsynchronous resonance frequency of the system (f_n) is a function of the capacitive reactances of Lines 1 and 2 and the equivalent inductive reactance of the system. The SSI mode is the complement of this frequency ($60 - f_n$). In all the reported case studies in this thesis except for the interruption of Line 4, SSI mode is found to be 24.5 Hz. In the case of the interruption of Line 4, SSI mode is 30.5 Hz. This is due to the change of f_e from 35.5 Hz to 29.5 Hz.
6. The proposed supplemental controls, namely Supplemental controls 1 and 2 have shown to be effective in mitigating SSR and SSI at different series capacitive compensation degrees, fault types and locations as well as wind farm B (FFC) ratings. Supplemental control 2 is, however, more effective in mitigating SSR and SSI in the case of system faults on Line 4 followed by subsequent line interruption as this action virtually splits the system into two subsystems.

This thesis is a stepping-stone in the direction of more research on the simultaneous mitigation of subsynchronous resonance and subsynchronous interaction. It is hoped that the research work documented in this thesis would provide useful guidance for conducting more studies and analyzing other technical issues that might be impacted by the simultaneous existence of the two phenomena.

REFERENCES

[1] Global Wind Energy Council, "Global Wind Report Annual market update 2012", April 2013.

[2] Wind power, Wikipedia, website: http://en.wikipedia.org/wiki/Wind_power

[3] P.M. Anderson, B.L. Agrawal and J.E. Van Ness, *Subsynchronous Resonance in Power Systems*, IEEE Press, 1990.

[4] B. Babak, S. Mandhir, Z. Yi, M. Dharshana and G. Aniruddha, "General Methodology for Analysis of Sub-Synchronous Interaction in Wind Power Plants," *IEEE Transactions on Power Systems*, Vol. 28, No. 2, May 2013, pp. 1858-1869.

[5] P.M. Anderson and R.G. Farmer, *Series Compensation of Power Systems*, PBLSH!, 1996.

[6] R. Billinton, M. Fotuhi-Firuzabad and S.O. Faried, "Power System Reliability Enhancement using a Thyristor Controlled Series Capacitor," *IEEE Transactions on Power Systems*, Vol. 14, No. 1, February 1999, pp. 369-374.

[7] IEEE Committee Report, "Proposed terms and definitions for subsynchronous oscillations," *IEEE Transactions on Power Apparatus and Systems*, Vol. PAS-99, No. 2, March 1980, pp. 506-511.

[8] IEEE Subsynchronous Resonance Working Group, "Terms, definitions and symbols for subsynchronous oscillations [power systems]," *IEEE Transactions on Power Apparatus and Systems*, Vol. PAS-104, No. 6, June1985, pp. 1325-1334.

[9] O. Anaya-Lara, N. Jenkins, J. Ekanayake, P. Cartwright, and M. Hughes, Wind Energy Generation: Modelling and Control, Wiley, 2009, John Wiley & Sons, Ltd.

[10] L. Fan, R. Kavasseri, Z. Lee Miao and C. Zhu, "Modeling of DFIG-Based Wind Farms for SSR Analysis," *IEEE Transactions on Power Delivery*, Vol. 25, No. 4, October 2010, pp. 2073-2082.

[11] A.R. Kashyap, "Direct-Drive Permanent Magnet Synchronous Generator Design for Hydrokinetic Energy Extraction", a thesis for master of science in electrical engineering, Missouri University of Science and Technology, Rolla, Missouri, United States, 2013.

[12] A.D. Hansen and G. Michalke, "Multi-pole permanent magnet synchronous generator wind turbines' grid support capability in uninterrupted operation during grid faults," *IET Renewable Power Generation*, Vol. 3, Issue 3, September 2009.

[13] Z. Miao, L. Fan, D. Osborn and S. Yuvarajan," Control of DFIG-Based Wind Generation to Improve Interarea Oscillation Damping," *IEEE Transactions on Energy Conversion*, Vol. 24, No. 2, June 2009, pp. 415-422.

[14] L. Fan, H. Yin and Z. Miao," On Active/Reactive Power Modulation of DFIG-Based Wind Generation for Interarea Oscillation Damping," *IEEE Transactions on Energy Conversion*, Vol. 26, No. 2, June 2011, pp. 513-521.

[15] N. Kshatriya, U.D. Annakkage, F.M. Hughes and A.M. Gole, "Optimized Partial Eigenstructure Assignment-Based Design of a Combined PSS and Active Damping Controller for a DFIG," *IEEE Transactions on Power Systems*, Vol. 25, No. 2, May 2010, pp. 866-876.

[16] T. Knuppel, J.N. Nielsen, K.H. Jensen, A. Dixon and J. Ostergaard, "Power Oscillation Damping Controller for Wind Power Plant Utilizing Wind Turbine Inertia as Energy Storage," in *2011 IEEE Power and Energy Society General meeting*, Detroit, MI, July 24-28, 2011, Paper No. 2011GM0059.

[17] S.O. Faried, I. Unal, D. Rai, and J. Mahseredjian, "Utilizing DFIG-Based Wind Farms for Damping Subsynchronous Resonance in Nearby Turbine-Generators," *IEEE Transaction on Power Systems*, Vol. 28, No. 1, February 2013, pp. 452-459.

[18] A.E. Leon, J.M. Mauricio and J.A. Solsona, "Subsynchronous Resonance mitigation Using Variable Speed Wind Energy Conversion Systems," *IET Generation, Transmission and Distribution*, Vol. 7, Issue 5, May 2013, pp. 511-525.

[19] E. Muljadi, C.P. Butterfield, A. Ellis, J. Mechenbier, J. Hochheimer, R. Young, N. Miller, R. Delmerico, R. Zavadil, and J.C. Smith, "Equivalencing the Collector System of a Large Wind Power Plant," in *Proceedings of the 2006 IEEE PES General Meeting*, Montreal, Quebec, Canada, June 18-22, 2006.

[20] P. Kundur, *Power System Stability and Control*, New York: McGraw-Hill, 1994.

[21] Y. Yu, *Electric Power System Dynamics*, New York, Academic Press, 1983.

[22] O.I. Elgerd, *Electrical Energy Systems Theory*, New York: McGraw-Hill, 1971.

[23] M.A. Poller, "Doubly-fed induction machine models for stability assessment of wind farms," in *Power Technology Conference*, Bologna, Italy, June 23-26, 2003, pp. 1-6.

[24] M. Lindholm, "Doubly fed drivers for variable speed wind turbines – a 40kW laboratory setup," PhD thesis, Technical University of Denmark, Kongens Lyngby, Denmark, 2004.

[25] L. Xu, L. Yao and C. Sasse, "Grid Integration of Large DFIG-Based Wind Farms Using VSC Transmission," *IEEE Transactions on Power Systems*, Vol. 22, No. 3, August 2007, pp. 976-984.

[26] W. Qiao, G. Harley and G.K. Venayamoorthy, "Coordinated Reactive Power Control of a Large Wind Farm and a STATCOM Using Heuristic Dynamic Programming," *IEEE Transactions on Energy Conversion*, Vol. 24, No. 2, June 2009, pp. 493-503.

[27] A.D. Hansen, G. Michalke, P. Sorensen, T. Lund and F. Iov, "Co-ordinated Voltage Control of DFIG Wind Turbines in Uninterrupted Operation during Grid Faults," *Wind Energy*, Vol. 10, No. 1, January/February 2007, pp. 51-68.

[28] A.D. Hansen and G. Michalke, "Modelling and fault ride-through capability of full-scale converter multipole PMSG wind turbines," in *European Wind Energy Conference EWEC*, Brussels, Belgium, March 31-April 3, 2008.

[29] EMTP-RV official website: http://emtp.com/

[30] R.M. Hamouda, M.R. Iravani and R. Hackam, "Coordinated Static VAR Compensators and Power System Stabilizers for Damping Power System Oscillations," *IEEE Transactions on Power Systems*, Vol. 2, No. 4, November 1987, pp. 1059-1067.

[31] R.M. Hamouda, M.R. Iravani and R. Hackam, "Torsional Oscillations of Series Capacitor Compensated AC/DC Systems," *IEEE Transactions on Power Systems*, Vol. 4, No. 3, August 1989, pp. 889-896.

[32] J.H. Chow and S. Ghiocel, "An Adaptive Wide-Area Power System Damping Controller using Synchrophasor Data", a chapter in, "Control and Optimization Theory for Electric Smart Grids", Editors: Aranya Chakrabortty and Marija D. Ilić, Springer, 2012.

APPENDIX A

DATA OF THE SYSTEM UNDER STUDY

A.1 Synchronous Generators

Table A.1: Synchronous generator data

	G_1	G_2
Rating, MVA	600	700
Rated voltage, kV	22	22
Armature resistance, r_a , p.u.	0.0045	0.0045
Leakage reactance, x_l , p.u.	0.14	0.12
Direct-axis synchronous reactance, x_d , p.u.	1.65	1.54
Quadrature-axis synchronous reactance, x_q , p.u.	1.59	1.50
Direct-axis transient reactance, x'_d , p.u.	0.25	0.23
Quadrature-axis transient reactance, x'_q , p.u.	0.46	0.42
Direct-axis subtransient reactance, x''_d , p.u.	0.20	0.18
Quadrature-axis subtransient reactance, x''_q , p.u.	0.20	0.18
Direct-axis transient open-circuit time constant, T'_{do} , s	4.50	3.70
Quadrature-axis transient open-circuit time constant, T'_{qo} ,s	0.67	0.43
Direct-axis subtransient open-circuit time constant, T''_{do} , s	0.04	0.04
Quadrature-axis subtransient open-circuit time constant, T''_{qo} ,s	0.09	0.06
Zero-sequence reactance, x_o , p.u.	0.42	0.36

A.2 Turbine-Generator Mechanical Shaft Data

Table A.2: Turbine-Generator 1

Mass	Shaft Section	Inertia M (p.u.)	Damping D (p.u./p.u. speed)	Spring Constant k (p.u./rad)
EXC		5.1953028	0.001382	
	GEN1-EXC			3.7414773
GEN1		661.91839	0.176111	
	LP1-GEN1			83.497161
LP1		1167.2677	0.310564	
	HP1-LP1			42.7159
HP1		187.49671	0.04988	

Turbine-Generator 2

Mass	Shaft Section	Inertia M (p.u.)	Damping D (p.u./p.u. speed)	Spring Constant k (p.u./rad)
GEN2		1078.3791	0.0573	
	LP2-GEN2			114.03409
LP2		1192.9066	0.0634	
	HP2-LP2			145.15423
HP2		353.93443	0.0188	

A.3 Transformers

Table A.3: Transformer data

	T_1 (Generator 1)	T_2 (Generator 2)	T_3 (Wind farm A)	T_4 (Wind farm B)
Rating, MVA	600	700	525	225
Rated voltage, kV	22/500	22/500	34.5/500	34.5/500
Resistance, r_T, p.u.	0.0012	0.0028	0.005	0.005
Leakage reactance, x_T, p.u.	0.12	0.28	0.15	0.15

A.4 Wind Farm A (DFIG-Based Wind Farm) and Wind Farm B (FFC-Based Wind Farm)

Table A.4: Wind farm A and B Parameters

	Wind Farm A	Wind Farm B
Number of wind turbine generators	300	100
System frequency, Hz	60	60
Rated capacity of each wind farm generator, MVA	1.67	2.22
Generator rated voltage, kV	0.575	0.575
DC nominal voltage, V	1150	1150
Number of poles	6	6
Average wind speed, m/s	11	15
Rated capacity of turbine, MW	1.5	2.0

A.5 Modal Speed Calculation Data

Turbine-Generator 1

$$\Delta\omega_m = (\Delta\omega_0 \quad \Delta\omega_1 \quad \Delta\omega_2 \quad \Delta\omega_3)^T$$

$$\Delta\omega = (\Delta\omega_{HP} \quad \Delta\omega_{LP} \quad \Delta\omega \quad \Delta\omega_{EXC})^T$$

$$Q_1 = \begin{bmatrix} 0.5 & -0.6306 & 0.8959 & -0.0005 \\ 0.5 & -0.1629 & -0.2514 & 0.0012 \\ 0.5 & 0.4611 & 0.1872 & -0.0097 \\ 0.5 & 0.6026 & 0.3148 & 1 \end{bmatrix}$$

Turbine-Generator 2

$$\Delta\omega_m = (\Delta\omega_0 \quad \Delta\omega_1 \quad \Delta\omega_2)^T$$

$$\Delta\omega = (\Delta\omega_{HP} \quad \Delta\omega_{LP} \quad \Delta\omega)^T$$

$$Q_2 = \begin{bmatrix} -0.9333 & -0.6592 & 0.5774 \\ 0.3499 & -0.3872 & 0.5774 \\ -0.0808 & 0.6446 & 0.5774 \end{bmatrix}$$

A.6 DFIG Data

1.5 MW, 0.575 kV, 60 Hz

R_s = 0.023 p.u., L_{ls} = 0.18 p.u., L_{md} = 2.9 p.u., L_{mq} = 2.9 p.u.,

R'_r = 0.016 p.u., L'_{lr} = 0.16 p.u., L_{lr} = 0.16 p.u., H_t = 4 sec, H_g = 0.71 sec, K_{shaft} = 1.2 $\frac{p.u.}{rad}$,

BtB dc capacitor = 0.01 F, dc voltage = 1.15 kV.

A.7 FFC Data

2 MW, 0.575 kV, 60 Hz

R_s = 0.002 p.u., X_l = 0.05 p.u., X_o = 0.05 p.u., X_d = 0.6 p.u., X_q = 0.6 p.u.,

H_t = 4 sec, H_g = 1 sec, K_{shaft} = 0.3 $\frac{p.u.}{rad}$,

BtB dc capacitor = 0.01 F, dc voltage = 1.15 kV.

A.8 Transmission Lines

All transmission lines have the same series impedance and shunt admittance per unit length.

$Z_{T.L.series}$= 0.0118+j0.3244 Ω/km

$Y_{T.L.shunt}$= 5.0512 $\mu s/km$

Transmission voltage = 500 kV

A.9 System Loads

Total Loads (L) = 300 MW + 150 MVAR

APPENDIX B

SUPPLEMENTAL CONTROL OUTPUT SIGNALS FOR THE CASE STUDIES

Figure B.1 to B.10 illustrate supplemental control 1 and 2 output signals U_{SSR}, U_{SSI} and U_S for the case studies reported in Chapters 2 and 3.

B.1 Supplemental Control 1 Output Signals

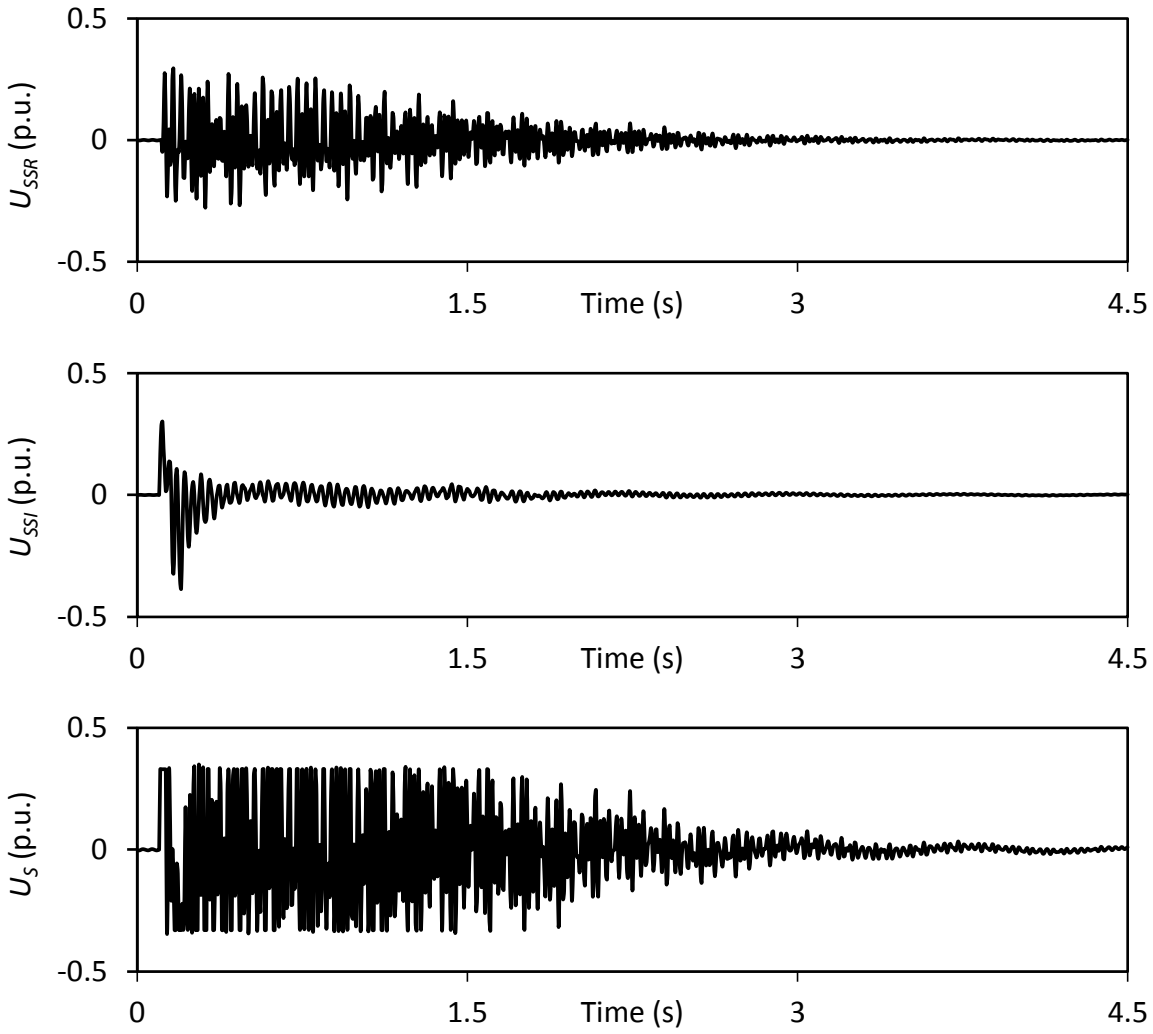

Figure B.1: Supplemental control 1 output signals during and after clearing a 3-cycle, three-phase fault on Line 5 (60% compensation degree, wind farm B rating = 200 MW).

B.2 Supplemental Control 1 Output Signals (Line 3 length = 50 km)

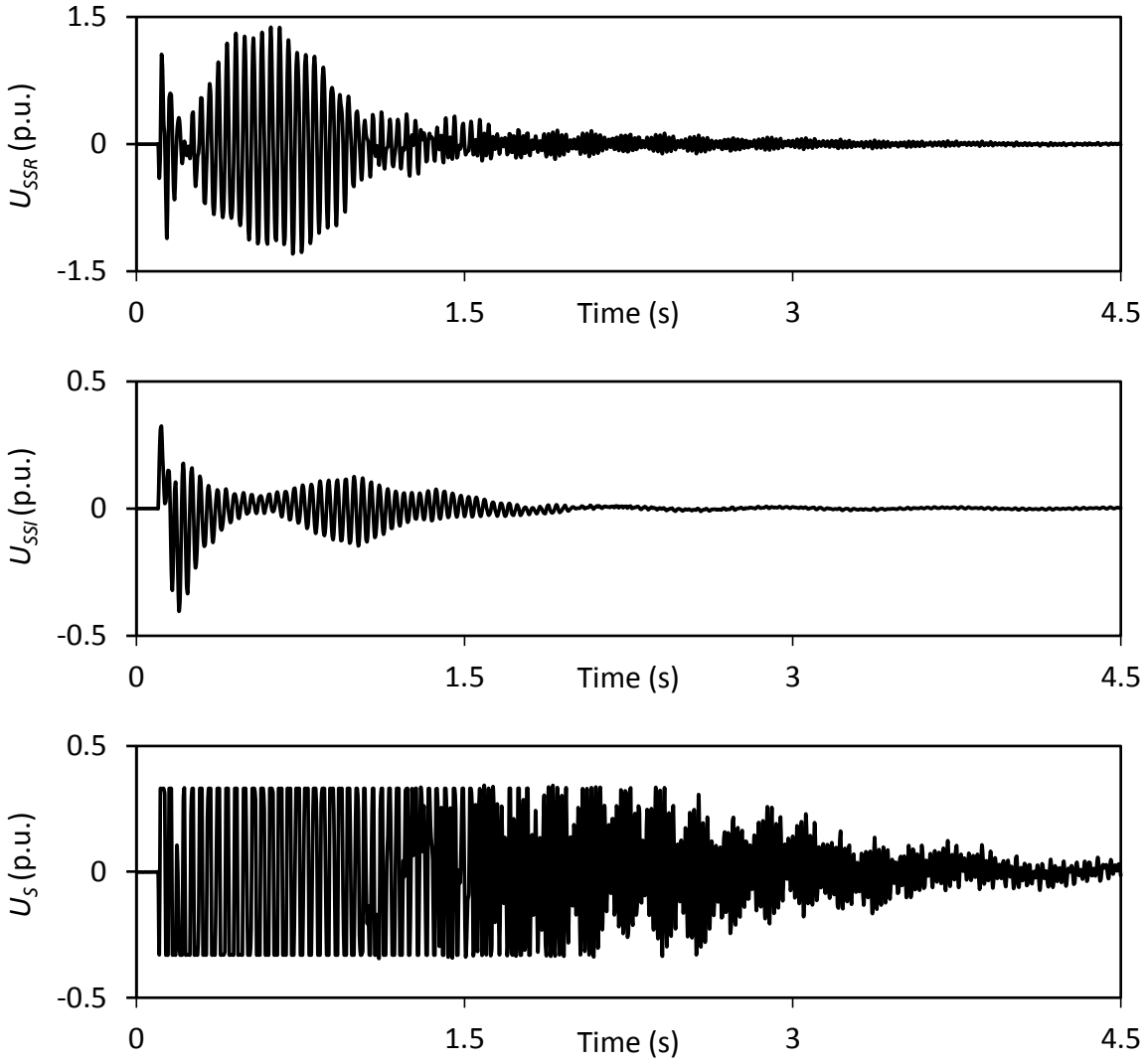

Figure B.2: Supplemental control 1 output signals during and after clearing a 3-cycle, three-phase fault on Line 5 (60% compensation degree, Line 3 length = 50 km).

B.3 Supplemental Control 1 Output Signals (Line 3 length = 100 km)

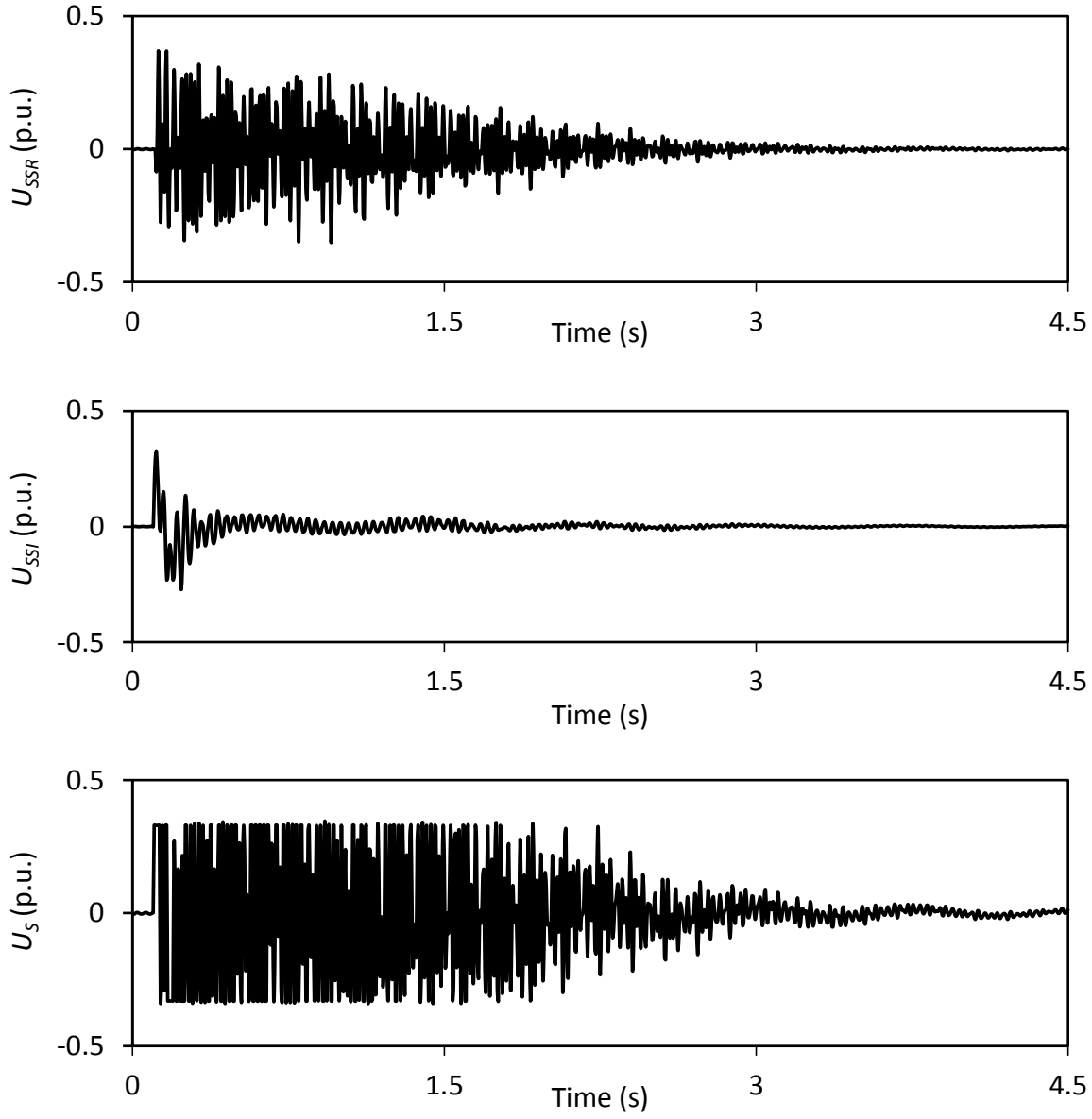

Figure B.3: Supplemental control 1 output signals during and after clearing a 3-cycle, three-phase fault on Line 5 (60% compensation degree, Line 3 length = 100 km).

B.4 Supplemental Control 1 Output Signals (Line 3 length = 200 km)

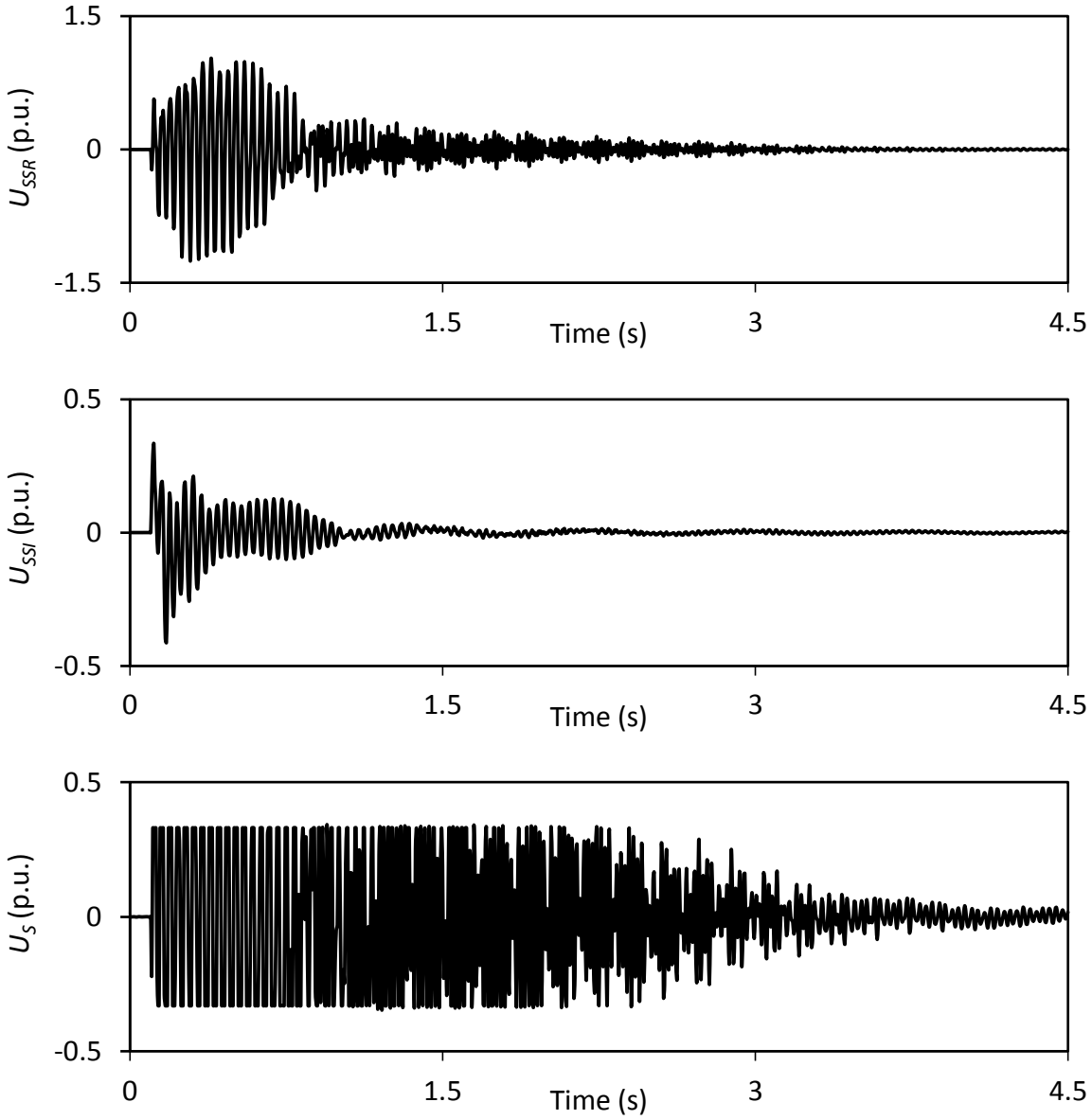

Figure B.4: Supplemental control 1 output signals during and after clearing a 3-cycle, three-phase fault on Line 5 (60% compensation degree, Line 3 length = 200 km).

B.5 Supplemental Control 1 Output Signals (Wind farm B rating = 300 MW)

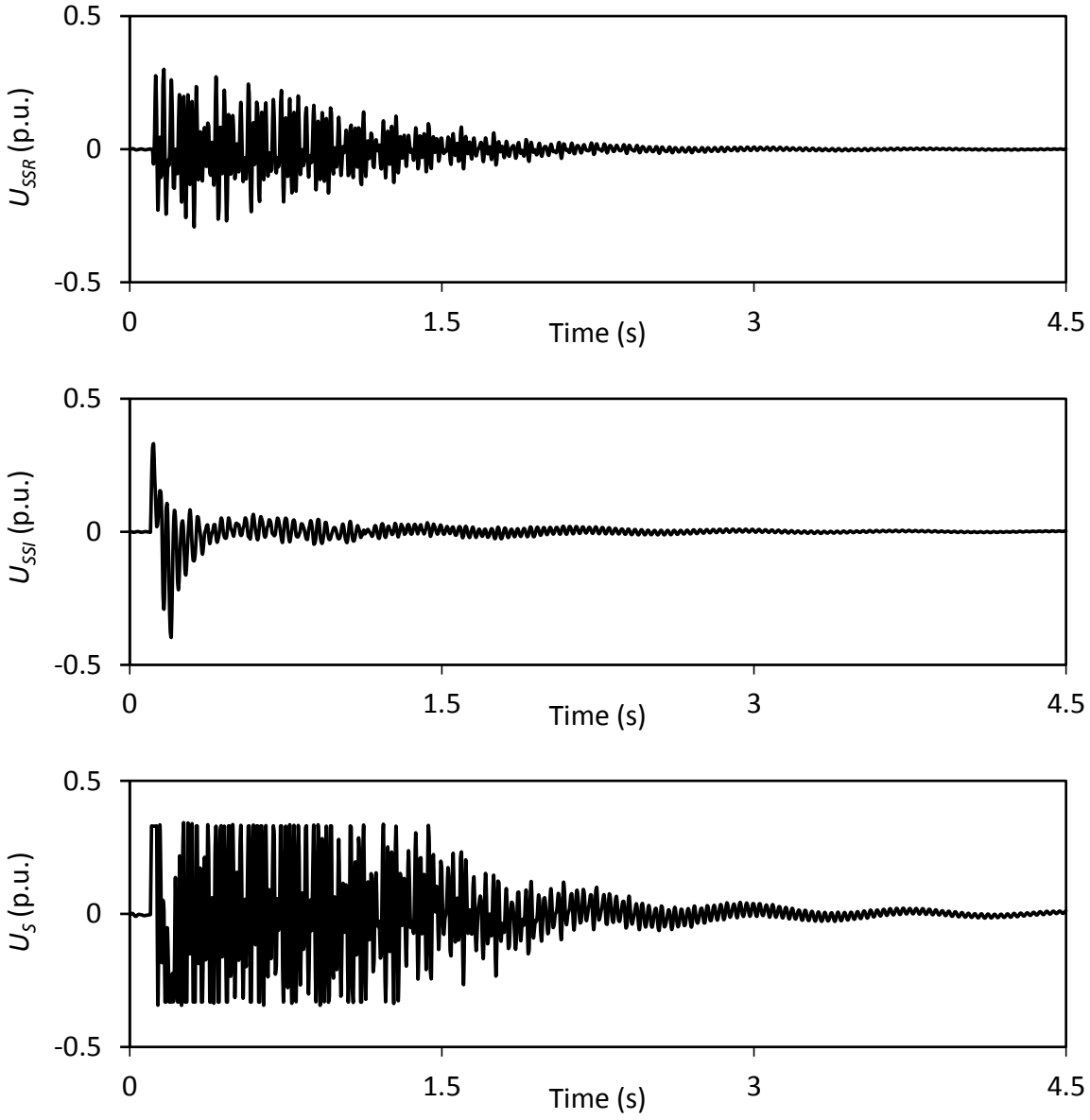

Figure B.5: Supplemental control 1 output signals during and after clearing a 3-cycle, three-phase fault on Line 5 (60% compensation degree, wind farm B rating = 300 MW).

B.6 Supplemental Control 1 Output Signals (Wind farm B rating = 400 MW)

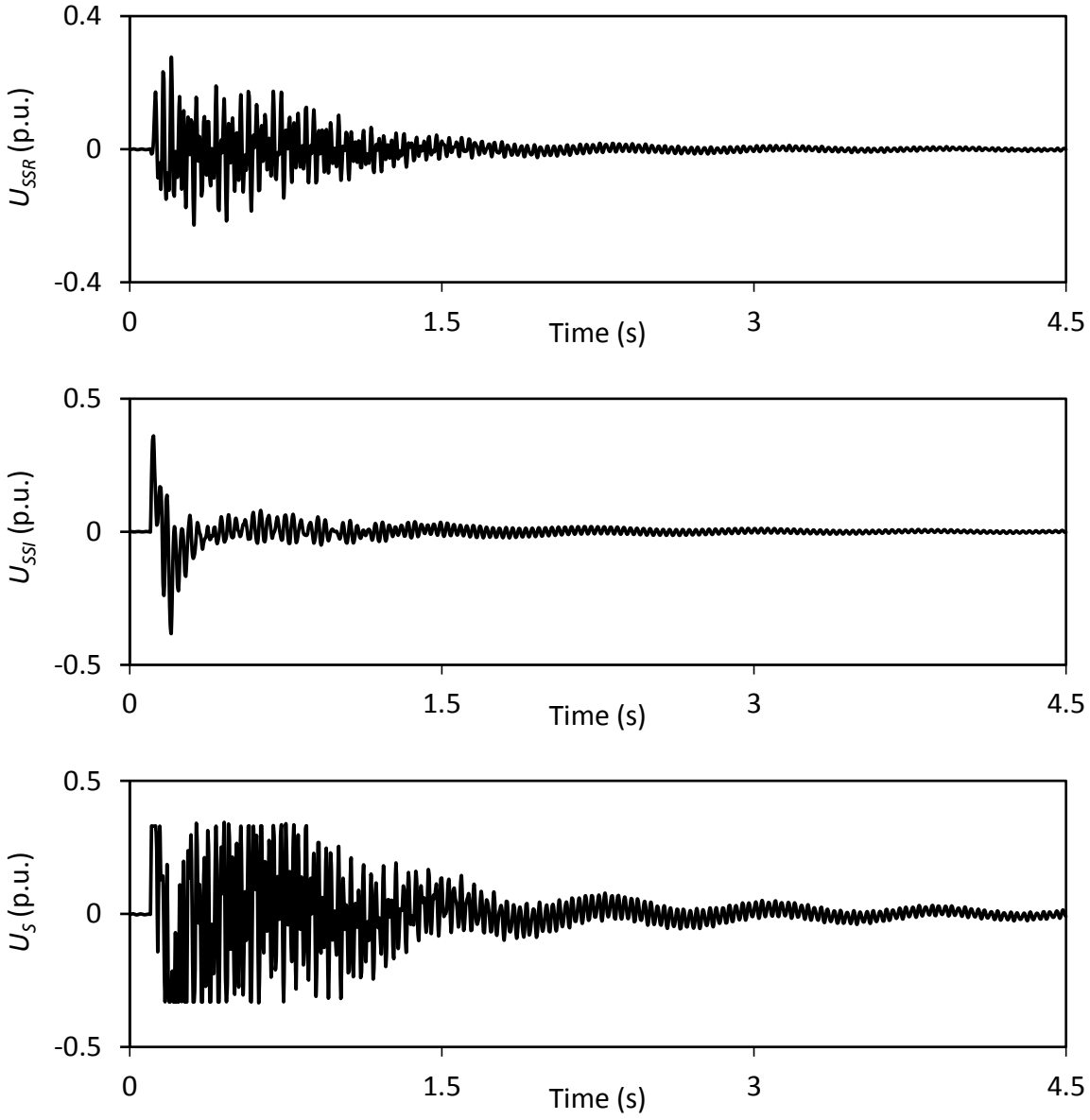

Figure B.6: Supplemental control 1 output signals during and after clearing a 3-cycle, three-phase fault on Line 5 (60% compensation degree, wind farm B rating = 400 MW).

B.7 Supplemental Control 1 Output Signals (Double Line-to-Ground Fault)

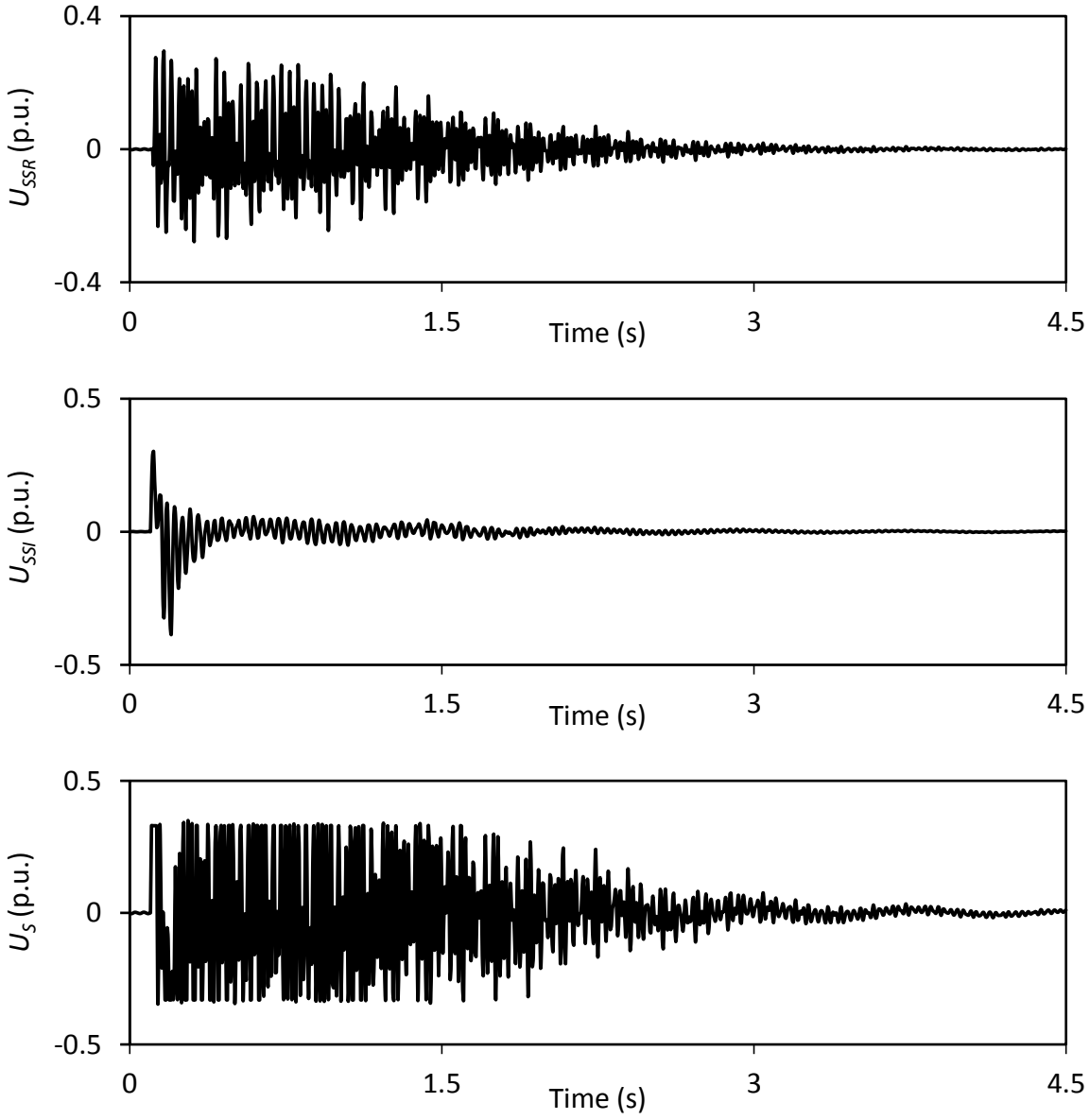

Figure B.7: Supplemental control 1 output signals during and after clearing a 3-cycle, L-L-G fault on Line 5 (60% compensation degree).

B.8 Supplemental Control 2 Output Signals

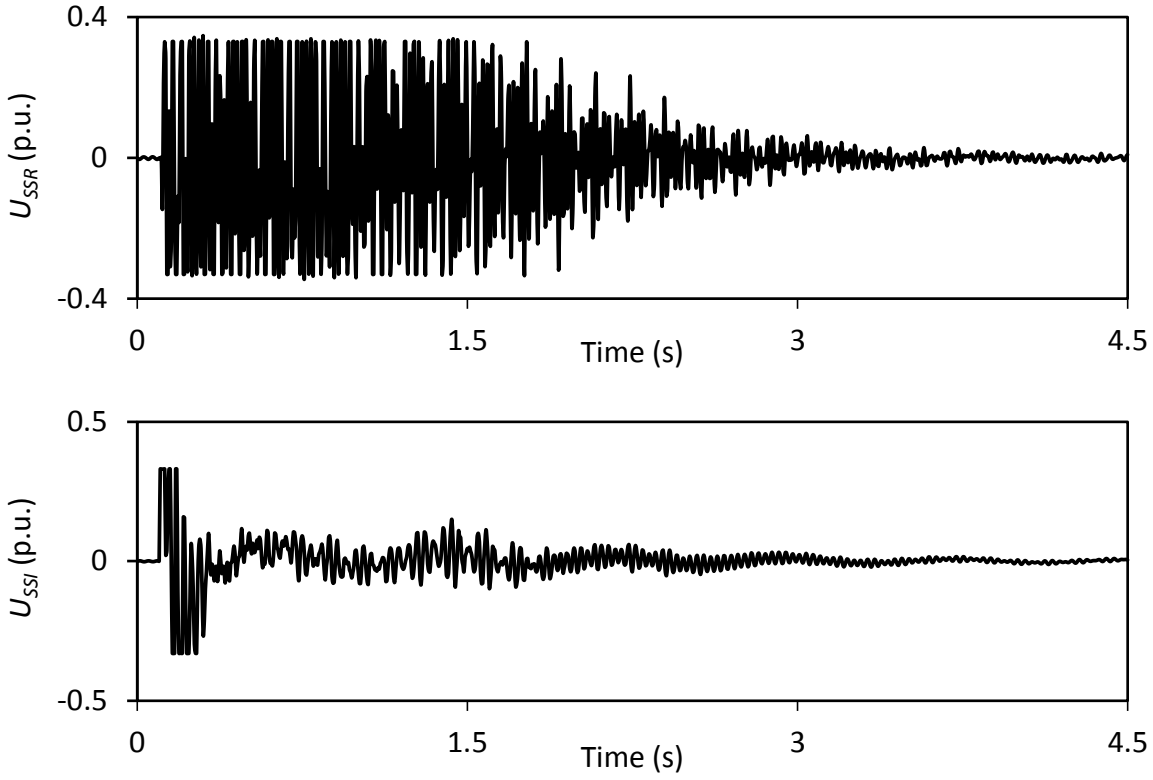

Figure B.8: Supplemental control 2 output signals during and after clearing a 3-cycle, three-phase fault on Line 5 (60% compensation degree).

B.9 Supplemental Control 2 Output Signals (Three-phase Fault on Line 4)

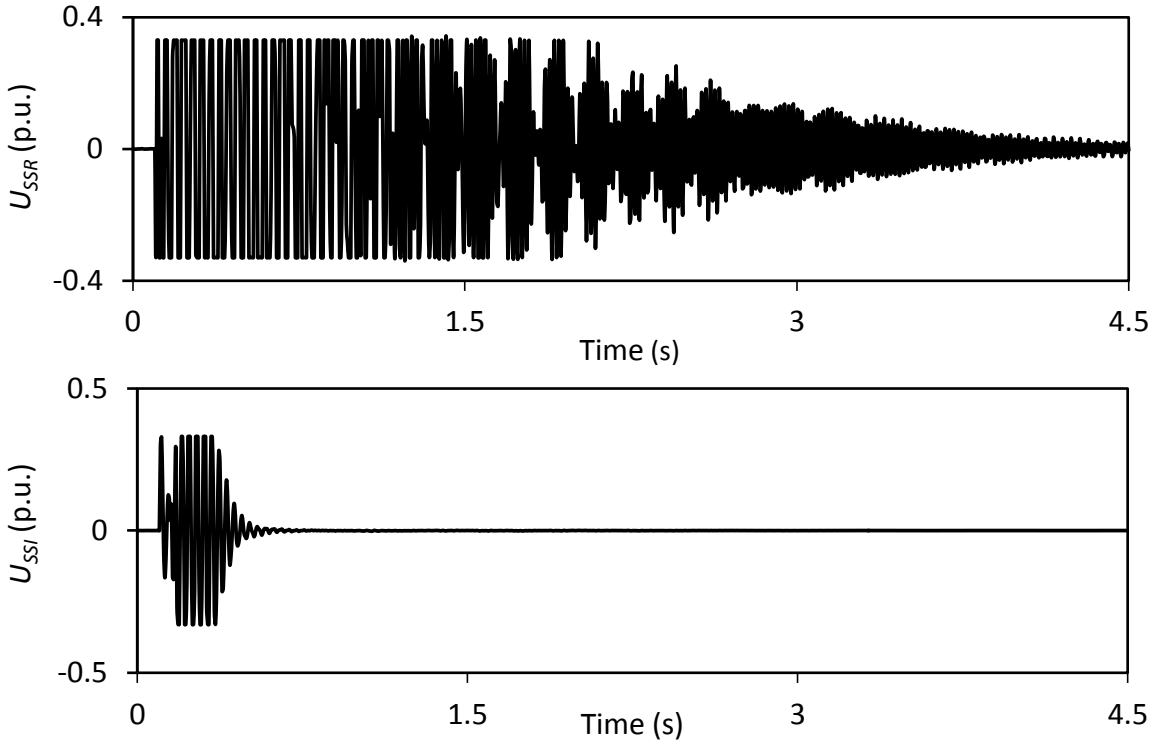

Figure B.9: Supplemental control 2 output signals during and after clearing a 3-cycle, three-phase fault on Line 4 (60% compensation degree).

B.10 Supplemental Control 2 Output Signals (50% Compensation)

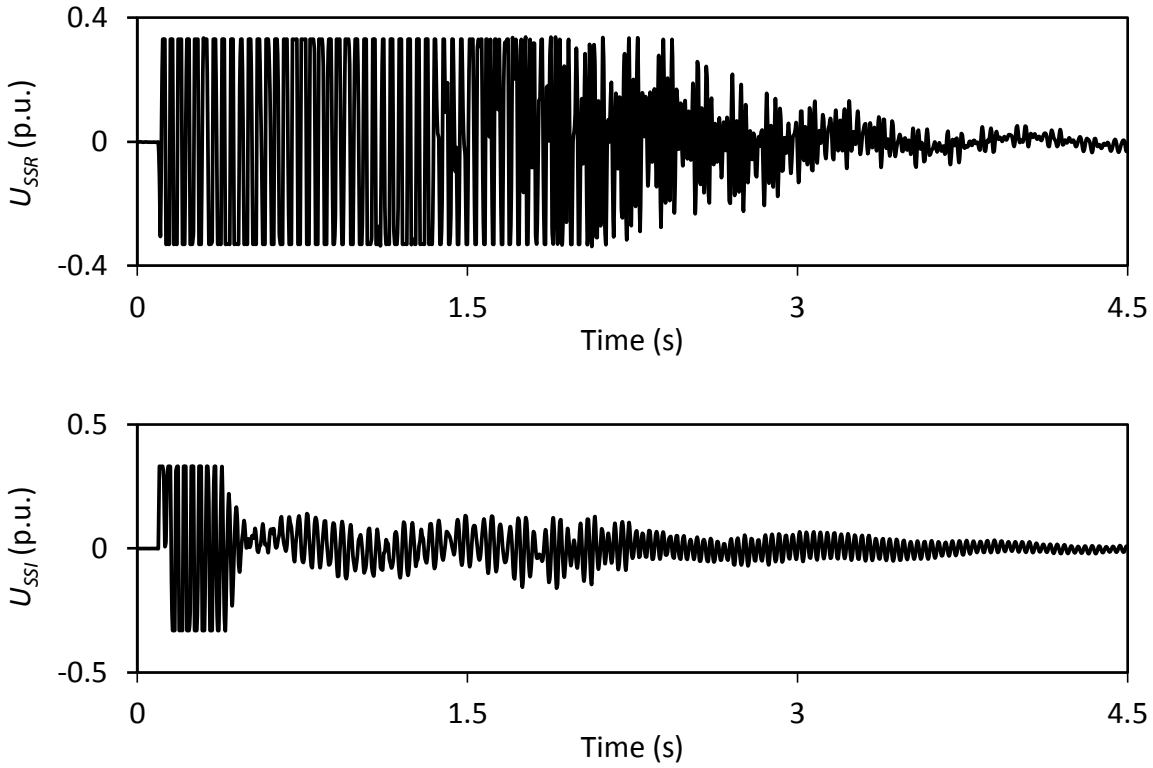

Figure B.10: Supplemental control 2 output signals during and after clearing a 3-cycle, three-phase fault on Line 5 (50% compensation degree).